

Nanostructures for Flexible Electronics and Drug Delivery

Lead Guest Editor: Chuanfei Guo

Guest Editors: Jian Zhong, Jinwei Gao, Siya Huang, and Liqian Gao





Nanostructures for Flexible Electronics and Drug Delivery

Journal of Nanomaterials

Nanostructures for Flexible Electronics and Drug Delivery

Lead Guest Editor: Chuanfei Guo

Guest Editors: Jian Zhong, Jinwei Gao, Siya Huang,
and Liqian Gao



Copyright © 2017 Hindawi. All rights reserved.

This is a special issue published in "Journal of Nanomaterials." All articles are open access articles distributed under the Creative Commons Attribution License, which permits unrestricted use, distribution, and reproduction in any medium, provided the original work is properly cited.

Editorial Board

- Domenico Acierno, Italy
Katerina Aifantis, USA
Nageh K. Allam, USA
Margarida Amaral, Portugal
Martin Andersson, Sweden
Raul Arenal, Spain
Ilaria Armentano, Italy
Vincenzo Baglio, Italy
Lavinia Balan, France
Thierry Baron, France
Andrew R. Barron, USA
Hongbin Bei, USA
Stefano Bellucci, Italy
Enrico Bergamaschi, Italy
Debes Bhattacharyya, New Zealand
Sergio Bietti, Italy
Giovanni Bongiovanni, Italy
Mohamed Bououdina, Bahrain
Philippe Caroff, Australia
Victor M. Castaño, Mexico
Albano Cavaleiro, Portugal
Bhanu P. S. Chauhan, USA
Shafiq Chowdhury, USA
Jin-Ho Choy, Republic of Korea
Yu-Lun Chueh, Taiwan
Elisabetta Comini, Italy
Giuseppe Compagnini, Italy
David Cornu, France
Miguel A. Correa-Duarte, Spain
P. Davide Cozzoli, Italy
Yong Ding, USA
Zehra Durmus, Turkey
Joydeep Dutta, Oman
Ovidiu Ersen, France
Claude Estournès, France
Andrea Falqui, KSA
Matteo Ferroni, Italy
Ilaria Fratoddi, Italy
Miguel A. Garcia, Spain
Siddhartha Ghosh, Singapore
Filippo Giubileo, Italy
Fabien Gasset, France
Jean M. Greneche, France
- Kimberly Hamad-Schifferli, USA
Simo-Pekka Hannula, Finland
Michael Harris, USA
Yasuhiko Hayashi, Japan
Michael Z. Hu, USA
Nay Ming Huang, Malaysia
Zafar Iqbal, USA
Balachandran Jeyadevan, Japan
Jeong-won Kang, Republic of Korea
Hassan Karimi-Maleh, Iran
Antonios Kelarakis, UK
Alireza Khataee, Iran
Ali Khorsand Zak, Iran
Philippe Knauth, France
Prashant Kumar, UK
Eric Le Bourhis, France
Jun Li, Singapore
Meiyong Liao, Japan
Shijun Liao, China
Silvia Licocchia, Italy
Nathan C. Lindquist, USA
Zainovia Lockman, Malaysia
Jim Low, Australia
Laura M. Maestro, Spain
Gaurav Mago, USA
Muhamamd A. Malik, UK
Francesco Marotti de Sciarra, Italy
Sanjay R. Mathur, Germany
Tony McNally, UK
Yogendra Mishra, Germany
Paulo Cesar Morais, Brazil
Paul Munroe, Australia
Jae-Min Myoung, Republic of Korea
Rajesh R. Naik, USA
Albert Nasibulin, Russia
Toshiaki Natsuki, Japan
Natalia Noginova, USA
Sherine Obare, USA
Won-Chun Oh, Republic of Korea
Abdelwahab Omri, Canada
Ungyu Paik, Republic of Korea
Piersandro Pallavicini, Italy
Edward A. Payzant, USA
- Alessandro Pegoretti, Italy
Oscar Perales-Pérez, Puerto Rico
Jorge Pérez-Juste, Spain
Alexey P. Popov, Finland
Helena Prima-García, Spain
Alexander Pyatenko, Japan
You Qiang, USA
Philip D. Rack, USA
Peter Reiss, France
Ilker S. Bayer, Italy
Sudipta Seal, USA
Shu Seki, Japan
Donglu Shi, USA
Bhanu P. Singh, India
Surinder Singh, USA
Vladimir Sivakov, Germany
Adolfo Speghini, Italy
Marinella Striccoli, Italy
Xuping Sun, KSA
Ashok K. Sundramoorthy, India
Angelo Taglietti, Italy
Bo Tan, Canada
Leander Tapfer, Italy
Valeri P. Tolstoy, Russia
Muhammet S. Toprak, Sweden
R. Torrecillas, Spain
Achim Trampert, Germany
Takuya Tsuzuki, Australia
Tamer Uyar, Turkey
Luca Valentini, Italy
Antonio Vassallo, Italy
Ester Vazquez, Spain
Ajayan Vinu, Australia
Ruibing Wang, Macau
Shiren Wang, USA
Yong Wang, USA
Magnus Willander, Sweden
Ping Xiao, UK
Zhi Li Xiao, USA
Yoke K. Yap, USA
William Yu, USA
Michele Zappalorto, Italy
Renyun Zhang, Sweden

Contents

Nanostructures for Flexible Electronics and Drug Delivery

Chuanfei Guo, Jian Zhong, Liqian Gao, Jinwei Gao, and Siya Huang
Volume 2017, Article ID 3516952, 2 pages

Reaction and Characterization of Low-Temperature Effect of Transition Nanostructure Metal Codoped SCR Catalyst

Ke Yang, Weiwei Xiao, Quan Xu, Jiaojiao Bai, Yan Luo, Hao Guo, Li Cao, Wei Cai, Peng Pu, and Lulu Cai
Volume 2017, Article ID 7901686, 10 pages

The Advances of Carbon Nanotubes in Cancer Diagnostics and Therapeutics

Zhou Chen, Aili Zhang, Xiaobing Wang, Jing Zhu, Yamin Fan, Hongmei Yu, and Zhaogang Yang
Volume 2017, Article ID 3418932, 13 pages

Synthesis of Fluorescent Carbon Dots by Gastrointestinal Fluid Treatment of Mongolia Har Gabur

Tegexibaiyin Wang, Wen Zhang, Xiaofeng Zhang, Xilin Qiqige, Wuhan Qimuge, Aodeng Qimuge, Hairong Wang, Bulin Baila, Alateng Qimuge, Ming Yuan, and Jun Ai
Volume 2017, Article ID 8575162, 7 pages

Application of Nanomaterials in Stem Cell Regenerative Medicine of Orthopedic Surgery

Su Pan, Hongmei Yu, Xiaoyu Yang, Xiaohong Yang, Yan Wang, Qinyi Liu, Liliang Jin, and Yudan Yang
Volume 2017, Article ID 1985942, 12 pages

Peptide Self-Assembled Nanostructures for Drug Delivery Applications

Taotao Fan, Xiaoyan Yu, Bing Shen, and Leming Sun
Volume 2017, Article ID 4562474, 16 pages

Optimal Zn-Modified Ca-Si-Based Ceramic Nanocoating with Zn Ion Release for Osteoblast Promotion and Osteoclast Inhibition in Bone Tissue Engineering

Jiangming Yu, Lizhang Xu, Ning Xie, Kai Li, Yanhai Xi, Xiling Liu, Xuebin Zheng, Xiongsheng Chen, Xiaojian Ye, and Daixu Wei
Volume 2017, Article ID 7374510, 9 pages

Study of the Dynamic Uptake of Free Drug and Nanostructures for Drug Delivery Based on Bioluminescence Measurements

Zhongjian Fang, Houchao Xu, Xiangjun Ji, Congbiao Liu, Kai Wang, Xiaoqing Qian, and Wencong Zhou
Volume 2017, Article ID 8542806, 12 pages

Functional Surface Coating on Cellulosic Flexible Substrates with Improved Water-Resistant and Antimicrobial Properties by Use of ZnO Nanoparticles

Xiaofei Tian, Yaping Li, Sikang Wan, Zhenqiang Wu, and Zhiwei Wang
Volume 2017, Article ID 9689035, 9 pages

Binding Affinity, Cellular Uptake, and Subsequent Intracellular Trafficking of the Nano-Gene Vector P123-PEI-R13

Yaguang Zhang, Hongmei Shu, Jing Hu, Min Zhang, Junweng Wu, Kehai Liu, and Qing Zhu
Volume 2016, Article ID 7064246, 8 pages



Recent Progress on Nanostructures for Drug Delivery Applications

Haijiao Lu, Jingkang Wang, Ting Wang, Jian Zhong, Ying Bao, and Hongxun Hao
Volume 2016, Article ID 5762431, 12 pages

Nanostructured Surface with Tunable Contact Angle Hysteresis for Constructing *In Vitro* Tumor Model

Kang Sun, Mingliang Yang, Yue Xu, Lelun Jiang, Rong Song, Yang Liu, Qing Jiang, and Chao Zhang
Volume 2016, Article ID 8275915, 5 pages

Editorial

Nanostructures for Flexible Electronics and Drug Delivery

Chuanfei Guo,¹ Jian Zhong,² Liqian Gao,³ Jinwei Gao,⁴ and Siya Huang⁵

¹*Southern University of Science and Technology, Shenzhen, Guangdong 518055, China*

²*Laboratory of Quality & Safety Risk Assessment for Aquatic Products on Storage and Preservation (Shanghai), Ministry of Agriculture, Shanghai Engineering Research Center of Aquatic-Product Processing & Preservation, College of Food Science & Technology, Shanghai Ocean University, Shanghai 201306, China*

³*School of Pharmaceutical Science (Shenzhen), Sun Yat-sen University (SYSU), Guangzhou, Guangdong 510275, China*

⁴*Institute for Advanced Materials (IAM), Academy of Advanced Optoelectronics, South China Normal University, Guangzhou, China*

⁵*Department of Physics and TcSUH, University of Houston, Houston, TX, 77204, USA*

Correspondence should be addressed to Chuanfei Guo; guocf@sustc.edu.cn

Received 22 June 2017; Accepted 22 June 2017; Published 1 October 2017

Copyright © 2017 Chuanfei Guo et al. This is an open access article distributed under the Creative Commons Attribution License, which permits unrestricted use, distribution, and reproduction in any medium, provided the original work is properly cited.

Nanostructures, including metal nanowires, semiconducting nanowires, carbon nanotubes, and graphene sheets, have been widely used as the building blocks or drug carriers for different applications (such as flexible photoelectronics, e-skins, soft machines, implantable electronics, drug delivery, health monitoring, and tissue engineering). In these applications, one of the emerging fields, flexible electronics, has attracted significant attention in both academic research and industrial applications during the past decade. Flexible electronic devices may also be implanted in the human body and combine with nanomedicine and drug delivery. Nanostructure based drug carriers allow for not only the delivery of small-molecule drugs, but also the delivery of peptides, nucleic acids, proteins, and so on. Targeting delivery of all these drug molecules to specific localization/area will reduce systemic side effects and allow for more efficient use of the drug. As fundamental research is called to fulfill the demands of industry and healthcare, the development of such nanotechnology and nanoscience has offered a good platform for flexible electronics and nanomedicine.

This special issue focuses on nanostructures for flexible electronics and their applications in drug delivery. This issue received seventeen submissions and finally accepted four exciting review papers and seven research papers. H. Lu et al. review the recent progress on nanostructures for drug delivery. T. Fan et al. summarize peptide self-assembled nanostructures for drug delivery applications. S. Pan et al.

introduce the application of nanomaterials in stem cell regenerative medicine of orthopedic surgery. Z. Chen et al. highlight the advance of carbon nanotubes in cancer diagnostics and therapeutics. K. Sun et al. fabricate nanostructured surface with tunable contact angle hysteresis for in vitro cell cultures of different tumor cells. Y. Zhang et al. investigate the binding affinity, cellular uptake, and subsequent intracellular trafficking of the nanogene vector P123-PEI-R13. X. Tian et al. develop functional surface coating on cellulosic flexible substrates with improved water-resistant and antimicrobial properties by the use of ZnO nanoparticles. Z. Fang et al. study dynamic uptake of free drug and nanostructures for drug delivery based on bioluminescence measurements. J. Yu et al. report optimal Zn-modified Ca-Si-based ceramic nanocoating with Zn ion release for osteoblast promotion and osteoclast inhibition in bone tissue engineering. K. Yang et al. analyze the reaction and characterization of low-temperature effect of transition nanostructure metal codoped SCR catalyst. T. Wang et al. synthesize fluorescent carbon dots by gastrointestinal fluid treatment of Mongolia Har Gabur. Unfortunately, we received few submissions on flexible electronics, especially those combined with both flexible electronic platforms and drug delivery. Hopefully, this crossing field can attract more attention in the near future.

By compiling these papers, we hope that this special issue provides the readers with some valuable information

and useful guides to the research field of nanostructures for flexible electronics and drug delivery.

*Chuanfei Guo
Jian Zhong
Liqian Gao
Jinwei Gao
Siya Huang*

Research Article

Reaction and Characterization of Low-Temperature Effect of Transition Nanostructure Metal Codoped SCR Catalyst

Ke Yang,¹ Weiwei Xiao,¹ Quan Xu,¹ Jiaojiao Bai,² Yan Luo,³ Hao Guo,⁴ Li Cao,¹ Wei Cai,¹ Peng Pu,¹ and Lulu Cai²

¹State Key Laboratory of Heavy Oil Processing, Beijing Key Laboratory of Biogas Upgrading Utilization, China University of Petroleum, Beijing 102249, China

²Personalized Drug Therapy Key Laboratory of Sichuan Province, Hospital of the University of Electronic Science and Technology of China and Sichuan Provincial, People's Hospital, Chengdu 610072, China

³Department of Chemical Engineering, West Virginia University, Morgantown, WV 26505, USA

⁴Chongqing Institute of Forensic Science, Chongqing 400021, China

Correspondence should be addressed to Quan Xu; xuquan@cup.edu.cn, Peng Pu; pupeng@hotmail.fr, and Lulu Cai; lzxlulu@126.com

Received 24 January 2017; Accepted 28 February 2017; Published 20 September 2017

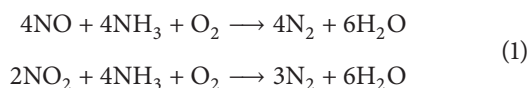
Academic Editor: Jinwei Gao

Copyright © 2017 Ke Yang et al. This is an open access article distributed under the Creative Commons Attribution License, which permits unrestricted use, distribution, and reproduction in any medium, provided the original work is properly cited.

Typical p-type semiconductor MnOx codoped with n-type semiconductors such as CeO₂ and V₂O₅ was reported to achieve high efficiency in catalytic NOx removal by NH₃. In this paper, we present novel Mn-Ce codoped V₂O₅/TiO₂ catalyst which exhibited an excellent NO conversion efficiency of 90% at 140°C. By using this codoped catalyst, the best low-temperature activity was greatly decreased when compared with single Mn- or Ce-doped catalyst. According to the characterization results from BET, XRD, and XPS, the codoped catalyst was composed of both CeO₂ and amorphous Mn. The electron circulation formed between doping elements is believed to promote the electron transfer, which may be one of the reasons for excellent low-temperature denitration performance.

1. Introduction

NOx is mainly derived from industrial emissions, traffic emissions, and living emissions. NOx gases react to form smog and acid rain as well as being central to the formation of tropospheric ozone. It especially can form small solid particles through the secondary chemical reactions that cause serious pollutions to the environment. Therefore, it is necessary to take a denitration treatment for flue gas after combustion. Selective catalytic reduction is the most widely used and effective methods for the removal of NOx in industrial at present. The main two reactions are presented in the following:



NH₃ and NO almost do not react in the absence of the catalyst; therefore, the catalyst is the key for the whole reaction. V₂O₅/TiO₂ and V₂O₅-WO₃/TiO₂ (anatase) catalysts operated at 350–400°C, with less than 1% V₂O₅ loading, have been widely accepted as commercial catalysts [1–3]. Currently, other doped companions such as Mn, Cu, Fe, Ce, W, and F [4–8] and morphological changes in the supports can be used to modify the catalyst to achieve high catalytic activity [9–12]. W or Mo doped V₂O₅/TiO₂, considered as the most effective commercial catalyst, is widely used for denitration in power plants and nitric acid plants [13, 14]. However, its narrow activity temperature window forces the selective catalytic reduction (SCR) unit to be installed upstream of the desulfurizer and electrostatic precipitator where high concentrations of SO₂ and particle matters can make the catalyst bed layer blocked, accelerating the deactivation of the catalyst [15]. Therefore, there is a rising interest in high

performance catalysts that can be used at low temperature. MnO_x has attracted significant attention because of its various types of labile oxygen species [16, 17]. Recently, Ce-doped catalyst has been found to reduce the reaction temperature significantly and has high catalytic activity and selectivity [18]. Mn-doped catalyst has shown excellent low-temperature activity, lower apparent active energy, and better ion dispersion than those of most previously reported SCR catalysts [17, 19]. This research committed to the development of low-temperature catalyst based on the V₂O₅/TiO₂ and V₂O₅-CeO₂/TiO₂ catalyst, which is the key of the selective catalytic reduction (SCR) to remove NO_x from effluent gas.

2. Materials and Methods

2.1. Materials. The low-temperature catalysts in the experiments were prepared with commercial anatase TiO₂ (Tianjin Guangfu Pharmaceutical) as carriers, with a specific surface area of 7.03 m²/g. Ammonium metavanadate (NH₄VO₃) was used as the precursor of vanadium, cerium nitrate (Ce(NO₃)₃·6H₂O) as the precursor of cerium, and oxalic acid solution as the precursor impregnation solution in the doping process. Manganese acetate (C₄H₆MnO₄·4H₂O), copper nitrate (Cu(NO₃)₂·3H₂O), cobalt nitrate (Co(NO₃)₂·6H₂O), ferric nitrate (Fe(NO₃)₃·9H₂O), and chromium nitrate (Cr(NO₃)₃·9H₂O) were selected to provide Mn, Cu, Co, Fe, and Cr, respectively. All these salts precursors were purchased from Tianjin Guangfu Technology Development Co., Ltd. and Aladdin Technology Co., Ltd.

2.2. Catalyst Preparation. The catalysts with different loadings of vanadium and cerium in the experiment were prepared by a conventional incipient-wetness impregnation method. Firstly, the oxalic acid was dissolved in deionized water and heated to dissolve completely, used as the precursor impregnation solution. Then, a certain quality of ammonium metavanadate was added to the oxalic acid solution and stirred until dissolved completely. A quantitative powder of cerium nitrate was added in the same way, finally, adding the TiO₂ powder to the above solution, stirring, and impregnating for 1 hour. The water was evaporated from the solution by a rotary evaporator and dried at 80°C for 24 hours. The dried samples were calcined at 500°C under the air atmosphere for 2 hours. Then the catalysts were ground and sieved to 20–40 mesh for catalytic performance evaluation. Other metals like Mn, Fe, Cr, etc. were doped in the same way as described above. Eventually, Ce-V₂O₅/TiO₂ catalyst with a fixed amount of 5% (wt%) V₂O₅ but different Ce loadings of 5%, 10%, 15%, 20%, 25%, and 30% (wt%) and other Bimetallic-doped V₂O₅/TiO₂ catalysts were prepared by the same impregnation method [20–22]. The catalysts prepared are denoted as xM-yCe-5V₂O₅/TiO₂. M represents the second metal, such as Mn, Fe, or Cu; x and y represent the loading of M (wt%) and Ce (wt%), respectively.

2.3. Catalytic Activity Test. The SCR activity measurement was performed on a fixed-bed stainless steel tube reactor with an inner diameter of 11 mm and the outer diameter of 14 mm.

Laboratory gas distribution was used to simulate the flue gas in the measurement. The feed gas mixture consisted of NH₃ 500 ppm, NO 500 ppm, 3% O₂ (volume fraction), and N₂ as the balance gas. The total flow rate was 1000 mL/min controlled by mass flow meters and the GHSV = 10,000 h⁻¹ in each reaction. The concentrations of NO_x were measured at the inlet and outlet by flue gas analyzer to calculate the conversion rate by the following:

$$\text{NO}_x \text{ conversion (\%)} = \frac{[\text{NO}_x]_{\text{in}} - [\text{NO}_x]_{\text{out}}}{[\text{NO}_x]_{\text{in}}} \times 100\%, \quad (2)$$

where [NO_x] = [NO] + [NO₂] and the in and out indicated the inlet and outlet concentration at steady state, respectively. The data was measured when the reaction reached the steady state (about 20–40 min) at each temperature, which could reduce the errors caused by instability.

2.4. Catalyst Characterization. The powder X-ray diffraction (XRD) measurements of the samples were recorded on a Bruker D8-Advance X-ray powder diffractometer using Cu K α radiation ($\lambda = 1.5406 \text{ \AA}$) with scattering angles (2θ) of 5–85° and a 0.0197 step size. The specific surface areas and pore size were measured by nitrogen adsorption at –196°C by the BET method using Micromeritics ASAP 2020 M surface areas and porosity analyzer. The samples were degassed at 200°C for 12 hours. The X-ray photoelectron spectroscopy (XPS) experiments were carried out on a Thermo Fisher Escalab 250Xi X-ray photoelectron spectrometer system equipped with a monochromatic Al K α X-ray source scanning from 0 to 5000 eV.

3. Results

3.1. Ce-Doped Effect of V₂O₅-TiO₂ Catalysts. NO_x conversions rate at various temperatures for the NH₃-SCR over Ce-doped V₂O₅/TiO₂ catalysts is shown in Figure 1. V₂O₅/TiO₂ shows above 80% NO_x conversion rate at a wide temperature range of 175°C to 375°C. The Ce doping can improve the catalytic activity effectively, especially from 160 to 450°C, due to the enhancement of electron transfer rate in catalyst. The 30Ce-V₂O₅/TiO₂ shows the highest NO_x conversion and widest temperature window with NO_x conversion above 90% from 160 to 400°C and the conversion rate could reach 99.83% at 200°C.

The catalytic activity with various Ce contents is shown in Figure 2. With the increase of Ce doping amount, the NO_x conversion firstly decreased and then increased at low-temperature zone (100–200°C) and high-temperature zone (350–450°C). 10Ce-5V₂O₅/TiO₂ shows the worst catalytic activity, the NO_x conversion even lower than the undoped 5V₂O₅/TiO₂ catalyst.

3.2. Low-Temperature Activity of X-Ce Codoped V₂O₅-TiO₂ Catalysts. Bimetal doped V₂O₅/TiO₂ catalyst was prepared on the basis of single Ce-doped catalyst. The Ce loadings were selected as 30 wt% based on the previous results and the cometal (Mn, Fe, Co, Cu, and Cr) loadings were varied

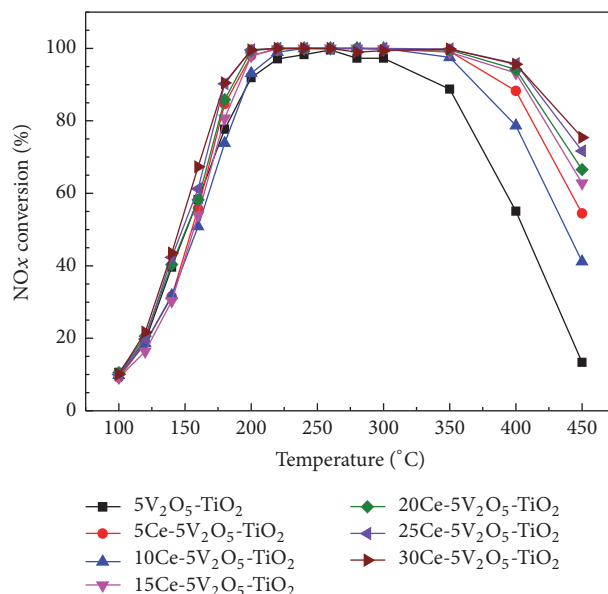


FIGURE 1: NO_x conversion over Ce-doped V₂O₅/TiO₂ catalysts with different Ce contents.

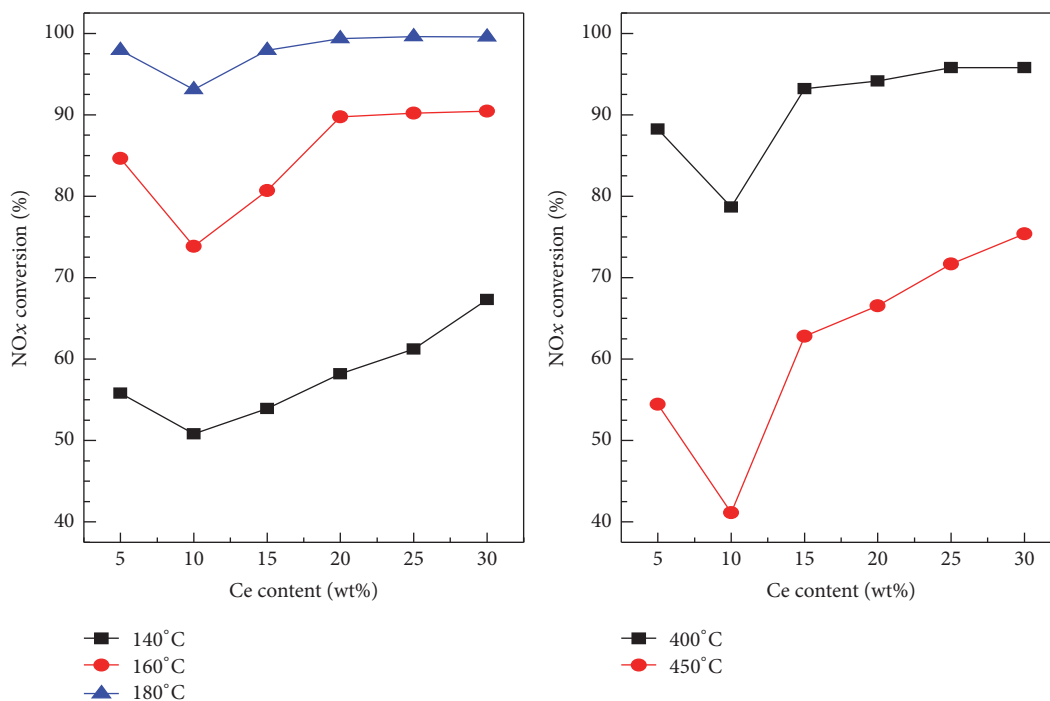


FIGURE 2: Effects of different Ce contents on NO_x conversion.

ranging from 10 to 30 wt%. The catalytic activity was tested on the fixed-bed reactor at different temperatures, and the results are shown in Figures 3 and 4. From the results we can observe that the catalytic effect of Fe-Ce codoped catalyst is slightly lower than single Ce-doped catalyst at the low-temperature zone. The Cu-Ce codoped catalyst shows the worst activity, even less than the based V₂O₅/TiO₂ catalyst. Co-Ce and Cr-Ce codoped catalyst can improve the catalytic activity at the low-temperature zone but drop rapidly at high-temperatures zone. With a narrower active temperature window that

cannot keep higher catalytic efficiency in a certain temperature range, Mn-Ce codoped V₂O₅/TiO₂ catalyst can improve the activity at low temperature effectively. It shows the best catalytic effect at low temperatures; the NO_x conversion can reach 95.69% at 140°C. The 20Mn-30Ce-V₂O₅/TiO₂ catalyst is the best as the effect of 20Mn-30Ce-V₂O₅/TiO₂ and 30Mn-30Ce-V₂O₅/TiO₂ is almost similar.

The NO_x conversion over X-Ce codoped V₂O₅/TiO₂ catalysts with loading contents of 20% at 160°C is shown in Figure 5. 20Mn-30Ce-V₂O₅/TiO₂ catalyst shows the best

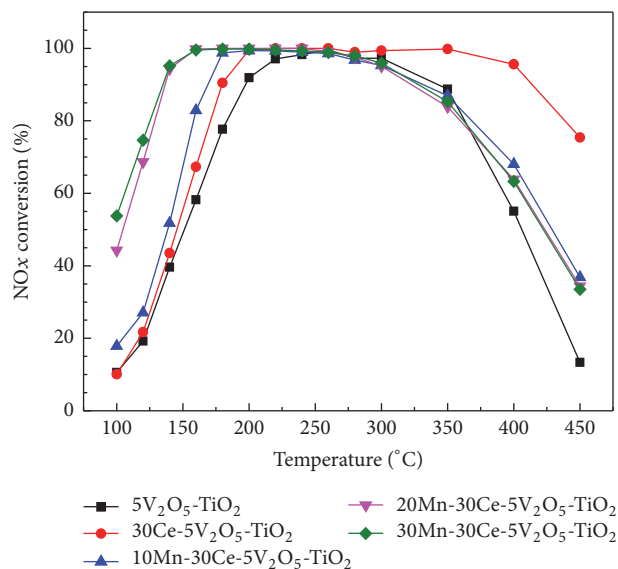


FIGURE 3: NO_x conversion over Mn-Ce-V₂O₅/TiO₂ catalysts with different Mn contents.

activity that the conversion rate can reach 99.58% which is nearly 30% higher than single Ce-doped. The catalytic activity over X-Ce codoped V₂O₅/TiO₂ catalysts is in the order of Mn-Ce > Co-Ce > Cr-Ce > Ce > Fe-Ce > Cu-Ce codoped.

3.3. Mn-Ce Codoped Effect. Initially, the single Mn- and Ce-doped V₂O₅/TiO₂ catalysts are prepared by the impregnation method to investigate the effect of single Mn or Ce, as compared to the Mn-Ce codoped catalyst. The result is shown in Figure 6. The NO_x conversion over Mn-Ce codoped V₂O₅/TiO₂ catalyst can reach more than 90% at 140°C, which is much higher than single doped catalyst. Mn-Ce codoped V₂O₅/TiO₂ catalysts have the best low-temperature activity that can drop to 80°C which is lower than Mn-doped catalyst and Ce-doped catalyst. However, the catalytic activity is difficult to maintain at high temperature. Single Ce-doped catalyst has the widest temperature window, but the low-temperature effect is not obvious. Mn-doped catalyst has neither good low-temperature activity nor wide temperature window. Relevant characterizations have been taken to the three kinds of catalysts in this experiment.

3.4. XRD. The X-ray powder diffraction patterns of the Mn-Ce codoped and single Ce- and Mn-doped V₂O₅/TiO₂ catalysts are shown in Figure 7. All the reflections provide typical diffraction patterns for the TiO₂ anatase phase. The characteristic peaks of Ce and Mn oxides appear, respectively, in single Ce- and Mn-doped catalyst. In the pattern of 30Ce-V₂O₅/TiO₂, the doped Ce exists mainly in the form of CeO₂ and part of CeVO₄. It was found that CeO₂ can effectively improve the catalytic activity and make the reaction temperature window wider [18]. However, the formation of CeVO₄ has a certain suppression to the improvement of catalytic activity [23]. A variety of diffraction peaks of Mn oxides appeared in the single Mn-doped catalyst, including Mn₂O₃, Mn₃O₄, and MnO₂. With the codoping of Mn-Ce, the diffraction peaks of TiO₂ become weak significantly and

CeO₂ crystal phase appears, but much weaker than single Ce-doped catalyst. The XRD results show that Mn, Ce, and TiO₂ have displayed a mutual influence by the codoping of Mn-Ce. The incorporation of Mn makes Ce exist in the form of CeO₂, but Mn is mostly in the amorphous state which can achieve a better low-temperature effect.

3.5. BET. The results of BET surface area, pore volume, and average pore diameter of each catalyst are shown in Table 1. Ce has a large particle diameter that the incorporation of Ce can improve the BET surface area effectively which is nearly five times more than original V₂O₅-TiO₂. Only a slight increase of the BET surface area has been achieved by the incorporation of Mn. But Mn-Ce codoped catalyst has the maximum surface area and minimum pore size. The change of BET surface area is consistent with the catalytic performance evaluation results in Figure 6.

3.6. XPS. The XPS spectra of Ce 3d of Mn-Ce codoped and single Ce-doped V₂O₅/TiO₂ catalyst are shown in Figure 8. The spectrum of Ce 3d contains eight peaks, in which *u*, *u*'', *u*'', *v*, *v*'', and *v*''' are the characteristic peaks of Ce⁴⁺ and *u*' and *v*' are the characteristic peaks of Ce³⁺. According to the intensity of the peak, Ce mainly exists as Ce⁴⁺ in both Mn-Ce codoped and single Ce-doped catalyst. The incorporation of Mn impacts the surface valence distribution of Ce that the Ce⁴⁺ increases significantly and Ce³⁺ reduces accordingly. The relative surface concentration of Ce⁴⁺ and Ce³⁺ calculated by the peak area is shown in Figure 9. The ratio of Ce⁴⁺/(Ce³⁺ + Ce⁴⁺) increased from 85% to 88.87% for Ce-V₂O₅/TiO₂ and Mn-doped Ce-V₂O₅/TiO₂ catalysts, respectively. These results suggest that the incorporation of Mn can convert part of the Ce³⁺ to Ce⁴⁺ and increase the proportion of Ce⁴⁺.

The XPS spectra of Mn 2p of Mn-Ce codoped and single Mn-doped V₂O₅/TiO₂ catalyst are shown in Figure 10. Mn 2p

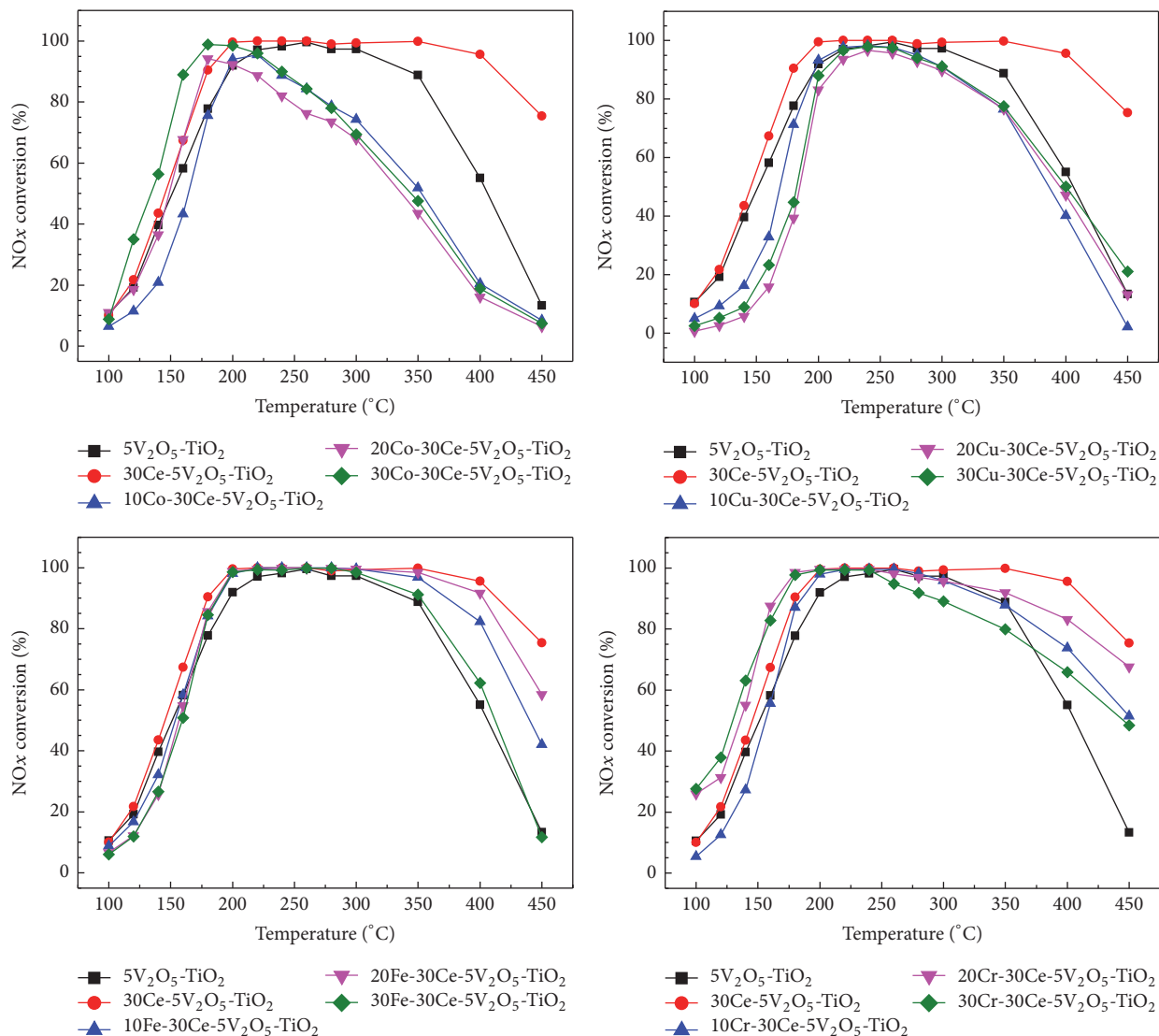


FIGURE 4: NOx conversion over Co-30Ce, Cu-30Ce, Fe-30Ce, and Cr-30Ce codoped V_2O_5/TiO_2 catalysts with different Co, Cu, Fe, and Cr loading contents.

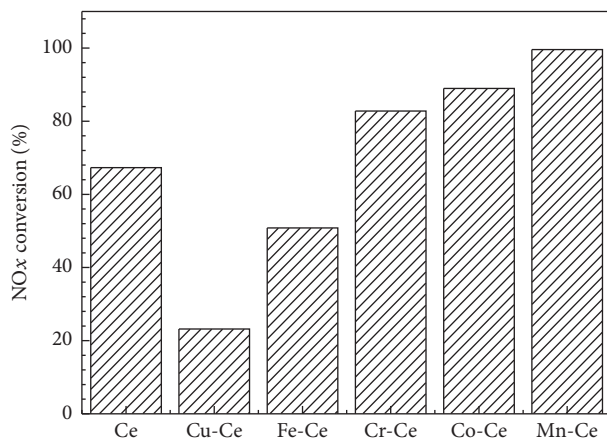


FIGURE 5: NOx conversion over X-Ce codoped V_2O_5/TiO_2 catalysts with different loading metals at 160°C.

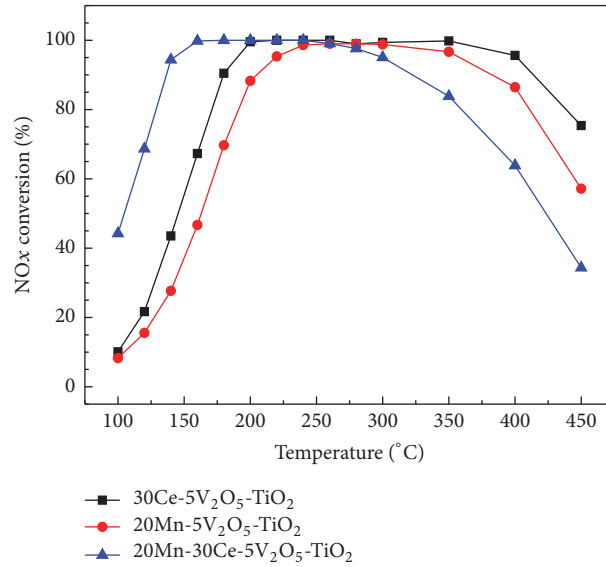


FIGURE 6: NO_x conversion over 20Mn-30Ce-5V₂O₅/TiO₂, 30Ce-5V₂O₅/TiO₂, and 20Mn-5V₂O₅/TiO₂ catalysts.

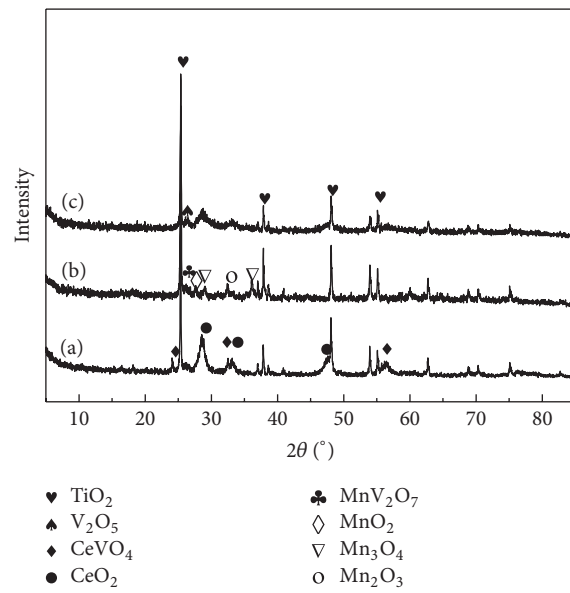


FIGURE 7: XRD profiles of (a) Ce-doped, (b) Mn-doped, and (c) Mn-Ce codoped V₂O₅/TiO₂ catalysts.

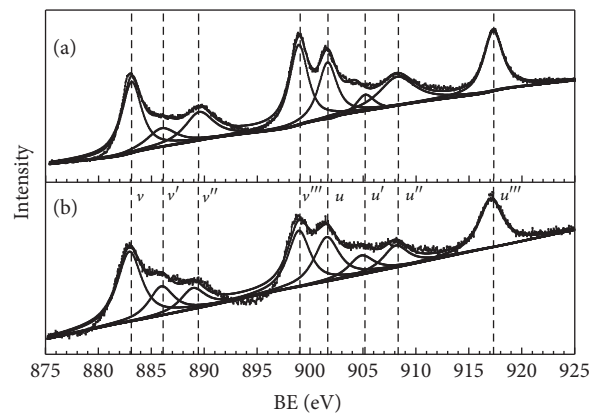
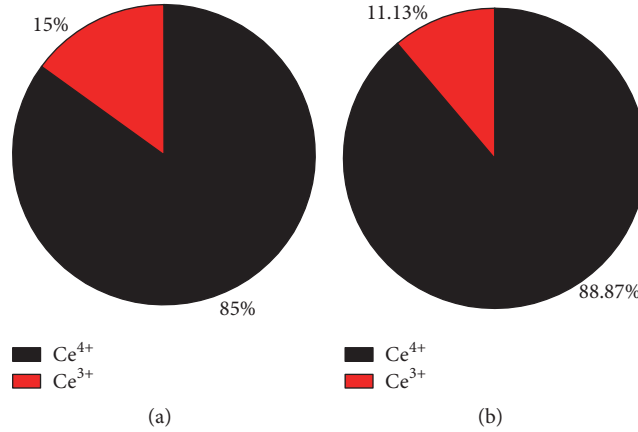
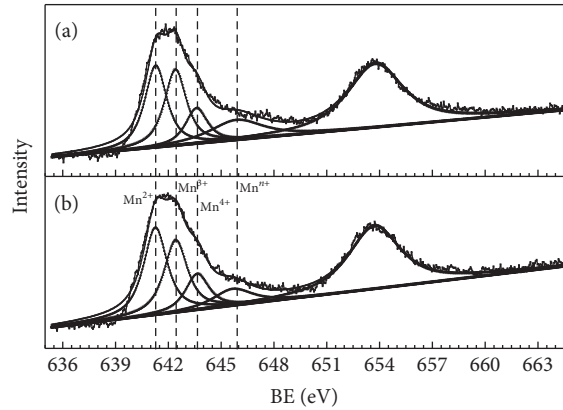


FIGURE 8: XPS spectra of Ce 3d of (a) Mn-Ce-V₂O₅/TiO₂ (20Mn-30Ce) and (b) Ce-V₂O₅/TiO₂ (30Ce) catalysts.

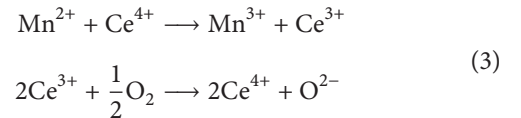
TABLE 1: Comparison of BET surface area, pore volume, and average pore diameter.

Samples	BET surface area (m ² /g)	Pore volume (cm ³ /g)	Average pore diameter (nm)
V ₂ O ₅ -TiO ₂	5.5022	0.025621	186.2567
Ce-V ₂ O ₅ -TiO ₂	28.7009	0.141243	196.8476
Mn-V ₂ O ₅ -TiO ₂	8.9057	0.061350	271.3350
Mn-Ce-V ₂ O ₅ -TiO ₂	33.5854	0.125967	150.0261

FIGURE 9: Surface atomic concentration ratio of Ce³⁺ and Ce⁴⁺. (a) 30Ce-5V₂O₅/TiO₂ and (b) 20Mn-30Ce-5V₂O₅/TiO₂.FIGURE 10: XPS spectra of Mn 2p of (a) Mn-Ce-V₂O₅/TiO₂ (20Mn-30Ce) and (b) Mn-V₂O₅/TiO₂ (20Mn) catalysts.

has two main peaks, Mn 2p_{1/2} (near 654 eV) and Mn 2p_{3/2} (near 642 eV), respectively. The characteristic peak of Mn 2p_{3/2} is superimposed from four peaks of Mn with different valence. Divide the characteristic peak into four subpeaks that Mn²⁺ (641.2–641.5 eV), Mn³⁺ (642.3–642.5 eV), Mn⁴⁺ (643.5–643.8 eV), and Mnⁿ⁺ (645.8–646.0 eV) can be achieved. The relative surface concentration of Mn²⁺, Mn³⁺, and Mn⁴⁺ calculated by the peak area is shown in Figure 11. Mn mostly exists in the form of Mn²⁺ in both Mn-Ce codoped and single Mn-doped catalyst. The higher the valence, the lower the atomic concentration. Under the interaction in Mn-Ce codoped system, a small part of the low-valence Mn²⁺ is oxidized to Mn³⁺. The incorporation of Mn can react with Ce which has a variable valence that can promote the electron transfer between active components. Some

chemical reactions may occur between the Mn²⁺ and Ce⁴⁺ as the following:



The XPS spectra of V 2p of Mn-Ce codoped and single Ce- and Mn-doped V₂O₅/TiO₂ catalyst are shown in Figure 12. The characteristic peak of V2p_{3/2} appears within 515~518 eV, which can be divided into two peaks, V⁴⁺ (516.7 eV) and V⁵⁺ (517.6 eV). The relative surface concentration of V⁴⁺ and V⁵⁺ calculated by the peak area is shown in Figure 13. The concentration of V⁵⁺ in a descending order of Mn-Ce codoped > Ce-doped > Mn-doped. V³⁺ is the active center of

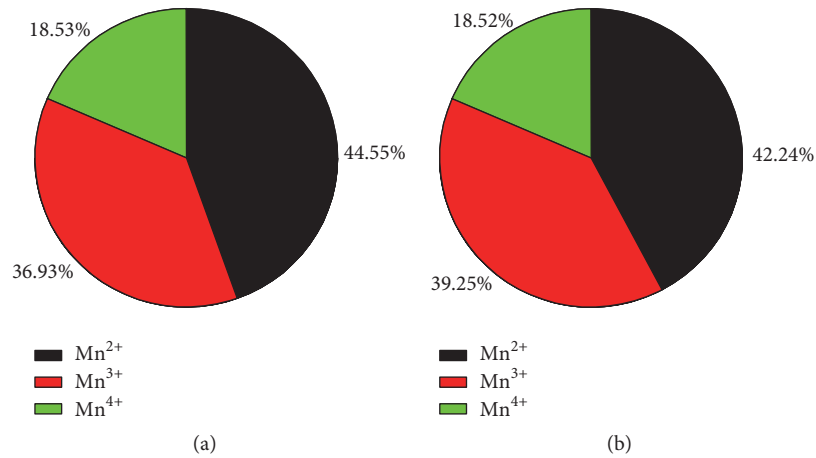


FIGURE 11: Surface atomic concentration ratio of Mn^{2+} , Mn^{3+} , and Mn^{4+} . (a) $\text{Mn-V}_2\text{O}_5/\text{TiO}_2$ and (b) $\text{Mn-Ce-V}_2\text{O}_5/\text{TiO}_2$.

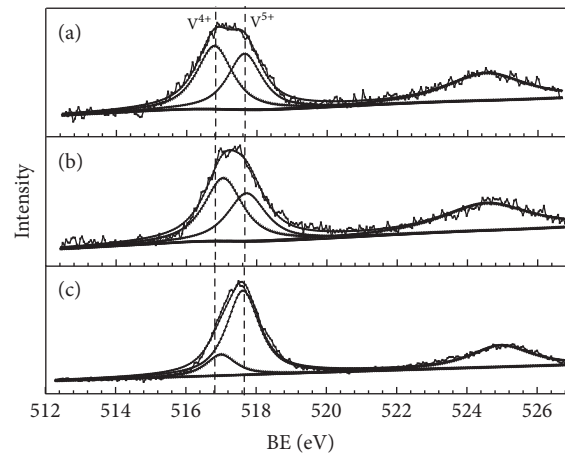


FIGURE 12: XPS spectra of V 2p of (a) $30\text{Ce-}5\text{V}_2\text{O}_5/\text{TiO}_2$ (30Ce), (b) $20\text{Mn-}5\text{V}_2\text{O}_5/\text{TiO}_2$ (20Mn), and (c) $20\text{Mn-}30\text{Ce-}5\text{V}_2\text{O}_5/\text{TiO}_2$ (20Mn-30Ce) catalysts.

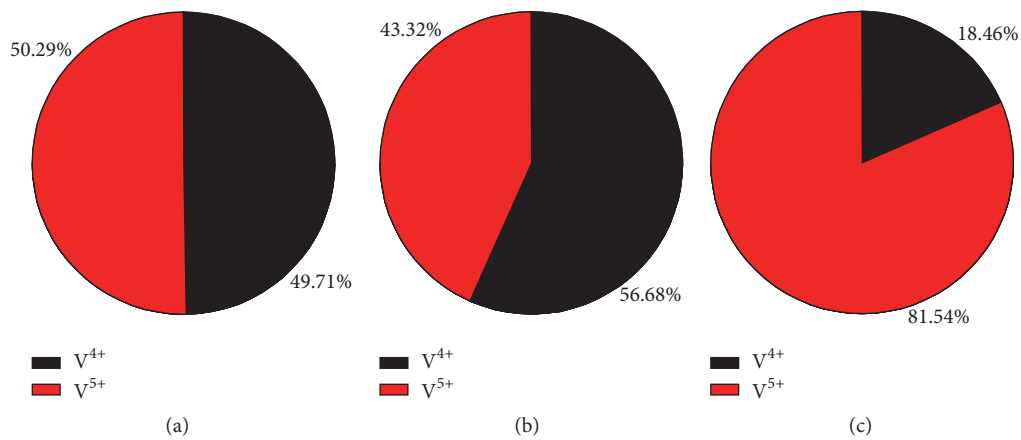


FIGURE 13: Surface atomic concentration ratio of V^{4+} and V^{5+} . (a) $20\text{Mn-}5\text{V}_2\text{O}_5/\text{TiO}_2$, (b) $30\text{Ce-}5\text{V}_2\text{O}_5/\text{TiO}_2$, and (c) $20\text{Mn-}30\text{Ce-}5\text{V}_2\text{O}_5/\text{TiO}_2$.

the denitration catalyst and NO and NH₃ can easily adsorb on the V⁵⁺ centers that promote the oxidation and reduction of NO. Under the effect of Mn and Ce, a lot of V⁴⁺ convert into more active V⁵⁺; the concentration of V⁵⁺ increased more than 30%.

The XPS results show that the Mn-Ce codoped catalysts promote the interaction among Mn, Ce, and V. The three kinds of atoms are moving to higher valence direction, which is beneficial for electron transformation and oxidation ability of the whole catalytic system. This is more conducive to the NO_x reduced by NH₃ at low temperatures.

4. Conclusions

Typical p-type semiconductor MnO_x codoped with n-type semiconductors such as CeO₂ and V₂O₅ achieved the excellent effect on NO removal by NH₃. Mn-Ce codoped vanadium-titanium catalyst system can effectively lower the reaction temperature and improve the efficiency. The NO_x conversion over Mn-Ce codoped V₂O₅/TiO₂ catalyst can reach more than 90% at 140 °C that is much higher than single doped catalyst. Mn-Ce codoped V₂O₅/TiO₂ catalyst has the best low-temperature activity that can drop to 80 °C which is lower than single Mn-doped catalyst and Ce-doped catalyst. The codoping of Mn-Ce makes Ce exist in the form of CeO₂, but Mn is mostly in amorphous state on the surface which can achieve better low-temperature effect. The incorporation of Mn can react with Ce which has a variable valence that can promote the electron transfer between the two active components to form an effective electron circulation in the presence of oxygen. The Mn, Ce, and V are moving to higher valence direction that the oxidation increased, which is more conducive to the NO_x reduced by NH₃. Thus even at low temperatures, it is possible to release O radical in the process of NO adsorption, which can be oxidized to NO₂ and then react with NH₃. All in all, Mn-Ce codoped V₂O₅/TiO₂ catalyst utilizes the electron transfer between Mn, Ce, and V effectively, and the denitration performance at low temperature is greatly improved. This finding may help scientists and engineers to development next generation smart surfaces [24, 25] with absorption functionality.

Conflicts of Interest

The authors declare that they have no conflicts of interest.

Authors' Contributions

Quan Xu, Peng Pu, and Li Cao conceived and designed the experiments; Ke Yang and Weiwei Xiao performed the experiments; Jiaojiao Bai, Li Cao, Yan Luo, and Hao Guo analyzed the data; Wei Cai contributed reagents/materials/analysis tools; Peng Pu and Quan Xu wrote the paper.

Acknowledgments

The authors thank Beijing Municipal Science and Technology Project (nos. Z161100001316010 and D141100002814001), National Key Research and Development Plan (no. 2016YFC0303701), Tribology Science Fund of State Key

Laboratory of Tribology (no. SKLTKF16A06), and Science Foundation of China University of Petroleum (nos. 2462014YJRC011, ZX20160056, and 201603) for the support.

References

- [1] R. M. Heck, "Catalytic abatement of nitrogen oxides—stationary applications," *Catalysis Today*, vol. 53, no. 4, pp. 519–523, 1999.
- [2] S. C. Wood, "Select the right IMO_x control technology," *Chemical Engineering Progress. Energy Technology Consultants*, p. 33, 1994.
- [3] M. F. H. Van Tol, M. A. Quinlan, F. Luck, G. A. Somorjai, and B. E. Nieuwenhuys, "The catalytic reduction of nitric oxide by ammonia over a clean and vanadium oxide-coated platinum foil," *Journal of Catalysis*, vol. 129, no. 1, pp. 186–194, 1991.
- [4] L. Chmielarz, P. Kuśrowski, R. Dziembaj, P. Cool, and E. F. Vansant, "Catalytic performance of various mesoporous silicas modified with copper or iron oxides introduced by different ways in the selective reduction of NO by ammonia," *Applied Catalysis B: Environmental*, vol. 62, no. 3–4, pp. 369–380, 2006.
- [5] Q. Li, H. Yang, F. Qiu, and X. Zhang, "Promotional effects of carbon nanotubes on V₂O₅/TiO₂ for NO_x removal," *Journal of Hazardous Materials*, vol. 192, no. 2, pp. 915–921, 2011.
- [6] P. S. Metkar, M. P. Harold, and V. Balakotaiah, "Selective catalytic reduction of NO_x on combined Fe- and Cu-zeolite monolithic catalysts: sequential and dual layer configurations," *Applied Catalysis B: Environmental*, vol. 111, pp. 67–80, 2012.
- [7] X. Wu, Z. Si, G. Li, D. Weng, and Z. Ma, "Effects of cerium and vanadium on the activity and selectivity of MnO_x-TiO₂ catalyst for low-temperature NH₃-SCR," *Journal of Rare Earths*, vol. 29, no. 1, pp. 64–68, 2011.
- [8] Z. Wu, R. Jin, H. Wang, and Y. Liu, "Effect of ceria doping on SO₂ resistance of Mn/TiO₂ for selective catalytic reduction of NO with NH₃ at low temperature," *Catalysis Communications*, vol. 10, no. 6, pp. 935–939, 2009.
- [9] M. Kang, J. Choi, Y. T. Kim et al., "Effects of preparation methods for V₂O₅-TiO₂ aerogel catalysts on the selective catalytic reduction of NO with NH₃," *Korean Journal of Chemical Engineering*, vol. 26, no. 3, pp. 884–889, 2009.
- [10] L. Xiong, Q. Zhong, Q. Chen, and S. Zhang, "TiO₂ nanotube-supported V₂O₅ catalysts for selective NO reduction by NH₃," *Korean Journal of Chemical Engineering*, vol. 30, no. 4, pp. 836–841, 2013.
- [11] Q. Li, X. Hou, H. Yang et al., "Promotional effect of CeO_x for NO reduction over V₂O₅/TiO₂-carbon nanotube composites," *Journal of Molecular Catalysis A: Chemical*, vol. 356, pp. 121–127, 2012.
- [12] J. Li, H. Chang, L. Ma, J. Hao, and R. T. Yang, "Low-temperature selective catalytic reduction of NO_x with NH₃ over metal oxide and zeolite catalysts—a review," *Catalysis Today*, vol. 175, no. 1, pp. 147–156, 2011.
- [13] J. M. García-Cortés, J. Pérez-Ramírez, M. J. Illán-Gómez, F. Kapteijn, J. A. Moulijn, and C. Salinas-Martínez de Lecea, "Comparative study of Pt-based catalysts on different supports in the low-temperature de-NO_x-SCR with propene," *Applied Catalysis B: Environmental*, vol. 30, no. 3–4, pp. 399–408, 2001.
- [14] H. Xu, Z. Qu, C. Zong, F. Quan, J. Mei, and N. Yan, "Catalytic oxidation and adsorption of Hg⁰ over low-temperature NH₃-SCR LaMnO₃ perovskite oxide from flue gas," *Applied Catalysis B: Environmental*, vol. 186, pp. 30–40, 2016.

- [15] M. Kang, E. D. Park, J. M. Kim, and J. E. Yie, "Manganese oxide catalysts for NO_x reduction with NH₃ at low temperatures," *Applied Catalysis A: General*, vol. 327, no. 2, pp. 261–269, 2007.
- [16] M. Wallin, S. Forser, P. Thormählen, and M. Skoglundh, "Screening of TiO₂-supported catalysts for selective NO_x reduction with ammonia," *Industrial & Engineering Chemistry Research*, vol. 43, no. 24, pp. 7723–7731, 2004.
- [17] G. Qi and R. T. Yang, "Performance and kinetics study for low-temperature SCR of NO with NH₃ over MnO_x-CeO₂ catalyst," *Journal of Catalysis*, vol. 217, no. 2, pp. 434–441, 2003.
- [18] W. Shan, F. Liu, Y. Yu, and H. He, "The use of ceria for the selective catalytic reduction of NO_x with NH₃," *Chinese Journal of Catalysis*, vol. 35, no. 8, pp. 1251–1259, 2014.
- [19] Z. Wu, B. Jiang, Y. Liu, W. Zhao, and B. Guan, "Experimental study on a low-temperature SCR catalyst based on MnO_x/TiO₂ prepared by sol-gel method," *Journal of Hazardous Materials*, vol. 145, no. 3, pp. 488–494, 2007.
- [20] L. Zhang, Q. Xu, J. Niu, and Z. Xia, "Role of lattice defects in catalytic activities of graphene clusters for fuel cells," *Physical Chemistry Chemical Physics*, vol. 17, no. 26, pp. 16733–16743, 2015.
- [21] Q. Xu, Y. Lv, C. Dong et al., "Three-dimensional micro/nano-scale architectures: fabrication and applications," *Nanoscale*, vol. 7, no. 25, pp. 10883–10895, 2015.
- [22] J. Liu, L. Yu, Z. Zhao et al., "Potassium-modified molybdenum-containing SBA-15 catalysts for highly efficient production of acetaldehyde and ethylene by the selective oxidation of ethane," *Journal of Catalysis*, vol. 285, no. 1, pp. 134–144, 2012.
- [23] Y. Huang, Z.-Q. Tong, B. Wu, and J.-F. Zhang, "Low temperature selective catalytic reduction of NO by ammonia over V₂O₅-CeO₂/TiO₂," *Journal of Fuel Chemistry and Technology*, vol. 36, no. 5, pp. 616–620, 2008.
- [24] Y. Wang and X. Gong, "Special oleophobic and hydrophilic surfaces: approaches, mechanisms, and applications," *Journal of Materials Chemistry A*, vol. 5, no. 8, pp. 3759–3773, 2017.
- [25] C. Zhang, D. A. Mcadams, and J. C. Grunlan, "Nano/micro-manufacturing of bioinspired materials: a review of methods to mimic natural structures," *Advanced Materials*, vol. 28, no. 30, pp. 6292–6321, 2016.

Review Article

The Advances of Carbon Nanotubes in Cancer Diagnostics and Therapeutics

**Zhou Chen,^{1,2} Aili Zhang,³ Xiaobing Wang,⁴ Jing Zhu,⁵ Yamin Fan,⁶
Hongmei Yu,⁷ and Zhaogang Yang⁶**

¹*School of Mechanical and Power Engineering, Nanjing Tech University, Nanjing, Jiangsu 211800, China*

²*Suzhou Yiheyongli New Energy Co., Ltd, Suzhou, Jiangsu 215400, China*

³*Department of Cancer Biology, Cleveland Clinic, Cleveland, OH 44195, USA*

⁴*Tumor Marker Research Center, Cancer Institute and Hospital, Chinese Academy of Medical Science and Peking Union Medical College, Beijing 100021, China*

⁵*College of Pharmacy, The Ohio State University, Columbus, OH 43210, USA*

⁶*Department of Chemical and Biomolecular Engineering, The Ohio State University, Columbus, OH 43210, USA*

⁷*China-Japan Union Hospital, Jilin University, Changchun, Jilin 130021, China*

Correspondence should be addressed to Hongmei Yu; yuhongm@jlu.edu.cn and Zhaogang Yang; yzhaogang@gmail.com

Received 1 February 2017; Revised 8 May 2017; Accepted 14 May 2017; Published 9 August 2017

Academic Editor: Jian Zhong

Copyright © 2017 Zhou Chen et al. This is an open access article distributed under the Creative Commons Attribution License, which permits unrestricted use, distribution, and reproduction in any medium, provided the original work is properly cited.

Carbon nanotubes (CNTs), one of the unique one-dimensional nanomaterials, have gained great attention because of their specific characters, versatile functionalization chemistry, and biological compatibility in the past few decades. CNTs can be functionalized via different methods to perform their specific functions. CNTs have been used in various areas of biomedicine as nanocarriers, including cancer diagnosis and therapy. Different molecules such as peptide, antigen, and nucleic acid can be delivered to cancer cells by CNTs with high efficiency. In this review, we summarized the properties of CNTs and the method of CNTs functionalization and illustrated their application in cancer diagnosis and therapy.

1. Introduction

Nanotechnology as one branch of engineering, which deals with the manipulation of individual molecules and atoms, has got much attention in recent years [1–8]. With the development of nanotechnology, many nanomaterials were developed and applied into industry [9–15]. Carbon nanotubes (CNTs) are one of the nanomaterials that are widely used in such area in recent years. They have got more and more attention because of their unique properties [16].

CNTs are more dynamic compared with other nanomaterials in their biological applications, and they are one of the most interesting nanocarriers in scientific studies. CNTs have displayed obvious prospect that they can cross the biological barriers as novel delivery systems. Compared with quantum dots which have been mainly used in cancer cell imaging, CNTs can also be applied in drug delivery and thermal

ablation [17]. They have the ability to enter cells, and this behavior is independent of cell type and functional group at their surface. Currently the detailed mechanisms of internalization (endocytosis or needle like penetration) have not been completely explained [18–20]. The high area of CNTs can provide multiple sites for attachment of different molecules, which makes polyvalent derivatization possible. In addition, based on the in vitro and in vivo results obtained from different research groups, a variety of chemically functionalized CNTs have the ability of biocompatibility with the biological environment. These results emphasized how the behavior of this material could be regulated via the degree and type of functionalization in vivo, and these two aspects need to be precisely managed [21–27]. CNTs possess some characters, including a high interfacial area with cellular membrane and unique capacity to incorporate multiple functionalizations. At the same time, CNTs also have the compatibility and

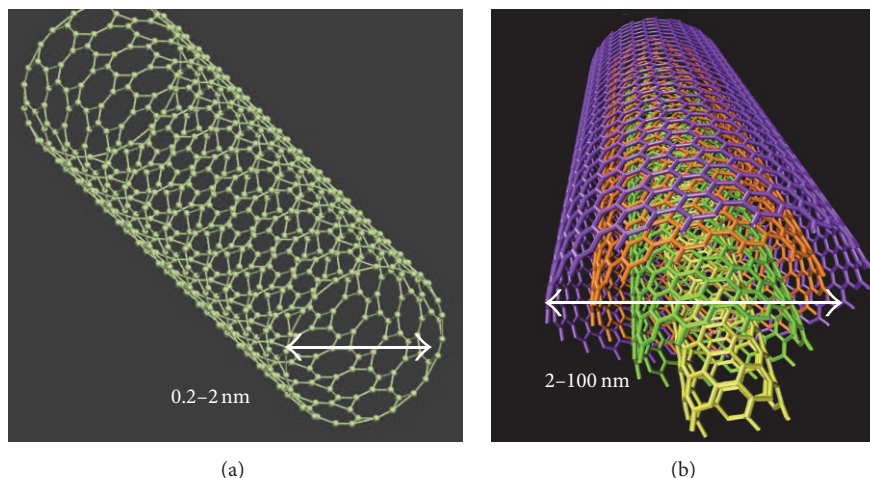


FIGURE 1: Conceptual diagrams of single-walled carbon nanotubes (SWCNTs) (a) and multiwalled carbon nanotubes (MWCNTs) (b).

transportability in biological fluids. These features make them a useful tool for all kinds of diagnosis and therapeutic as well as drug delivery application [28].

2. Character and Performance Properties of CNTs

CNTs were discovered in 1976 by Oberlin [29]. Currently, electric arc discharge, laser ablation, and thermal and plasma enhanced chemical vapor deposition (CVD) are the major technologies for the generating of CNTs [30]. CNTs can be divided into two broad classes based on their length, diameter, and structure. One is single-walled CNTs (SWCNTs) that consist of single sheet of cylindrical graphene, and the other is multiwalled carbon nanotubes (MWCNTs) which include several concentric graphene sheets [31, 32]. The structures of these two CNTs were indicated in Figure 1. Moreover, MWCNTs can be further divided into two subtypes: double-walled CNTs (DWCNTs) and triple-walled CNTs (TWCNTs) [33]. MWCNTs consist of several concentric layers of rolled graphite; these concentric layers have an inner diameter of 1 to 3 nm and an outer diameter of 2 to 100 nm [34]. The thickness of single cylindrical carbon layer in SWCNTs is from 0.2 to 2 nm [35]. SWCNTs have a higher ratio of length than that of diameter. MWCNTs have wider inner diameter compared to SWCNTs, and this characteristic can offer more space for high drug loading. It has also been suggested that the outer shell of MWCNTs can be functionalized while at the same time the side wall was not damaged [36].

CNTs can be modified to improve their solubility by efficient methods, which can be employed in several biological applications [37]. CNTs can be oxidized by strong acids, which results in the decrease of length and production of carboxylic groups. And these changes can improve their solubility in watery solutions [38]. Alternatively, the external walls and tips can have better solubility via the extra reactions to the CNTs [39, 40]. The solubility is a main property, which ensures the biocompatibility under physiological conditions [37]. Furthermore, virtually all kinds of active molecules

can be linked to the functionalized carbon nanotubes (f-CNTs), including peptides, proteins, nucleic acids, and other therapeutic agents. The physicochemical properties of CNTs mainly associate with several aspects, including an organized architecture with a high aspect ratio, surface area, mechanical strength, electrical and thermal conductivity, metallic or semimetallic behavior, and ultra-lightweight [41]. These advantages make CNTs the hopeful candidate material that possess enormous biomedical potentials [42]. However pristine CNTs (such as prepared and nonfunctionalized) are inherently hydrophobic, which have limited biomedical applications. Moreover, the nonfunctionalized CNTs exhibit high cytotoxicity, and it may be due to the insolubility of CNTs or the residual metal catalysts in CNTs. The toxicity of CNTs requires their functionalization, rendering them soluble and biocompatible so that they can be integrated into a biological system. Many molecules can be bound to CNTs (Figure 2) [31].

3. The Techniques of CNTs Functionalization

Even though CNTs have many advantages, their biomedical developments were limited. The purification of CNTs is still not well developed. Meanwhile, CNTs are difficult to dissolve in aqueous media, which limits their biomedical application, although this disadvantage can be overcome through functionalization [43]. In addition, CNTs are usually undissolved, and they also do not have good biocompatibility. In order to increase their biosolubility, two main techniques such as non-covalent functionalization and covalent functionalization are currently widely used. The covalently or noncovalently functionalized CNTs can be achieved via using different chemical groups [44]. CNTs can be divided into two zones according to their reactivity with functional groups, including tips and side walls. The tips are considered to have stronger functional groups bonding capabilities than the side walls.

3.1. Noncovalent Functionalization. Using the advantage of the conservation of the electronic structure of the nanotube aromatic, surfactants, peptide, polymer, nucleic acids,

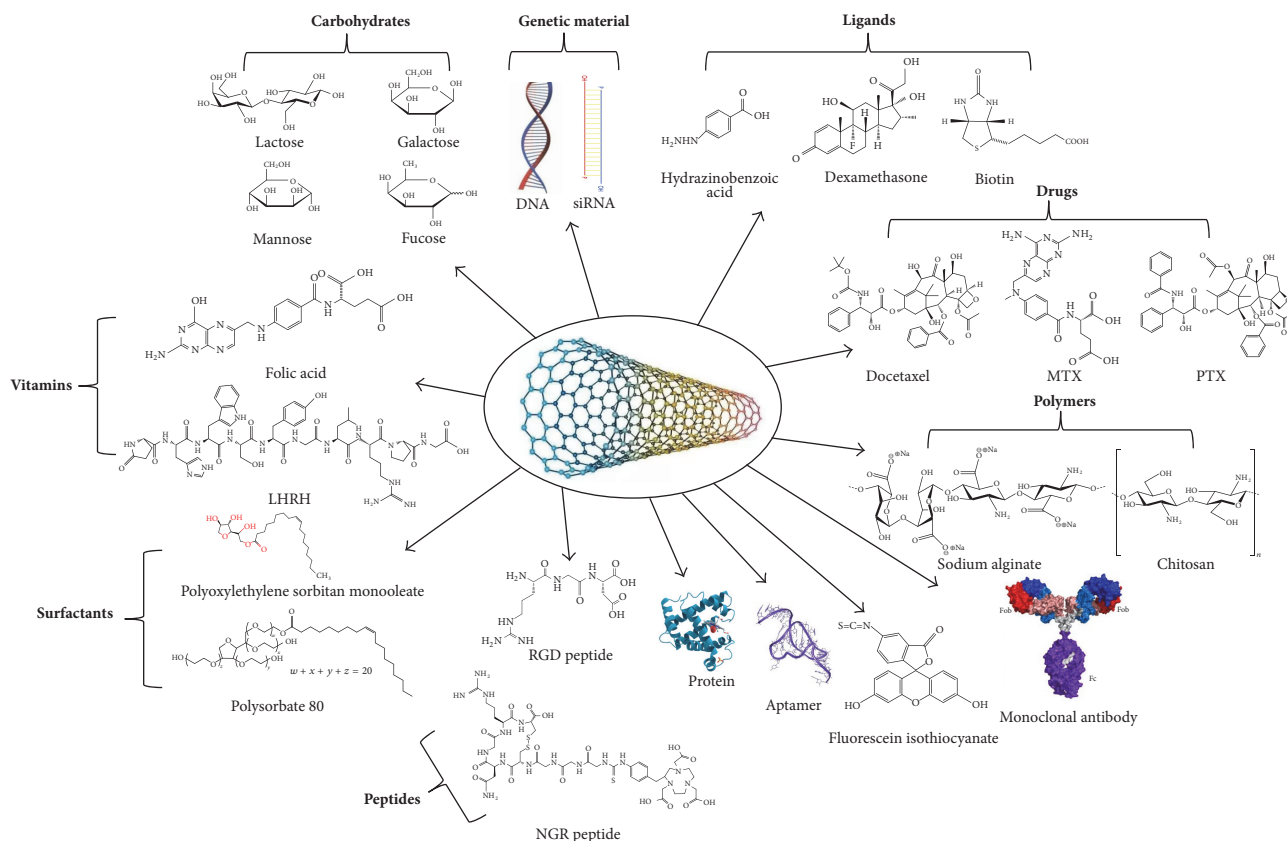


FIGURE 2: Examples of bioactive compounds conjugated through carbon nanotubes [31].

and oligomers can be bound to CNTs, which lead to the noncovalent functionalization of CNTs. The noncovalent functionalization of CNTs mainly related to the following several aspects, including pi stacking and Van der Waals and hydrophobic interactions. Hydrophobic or p-p interactions are necessary for noncovalent stabilization. The covalent functionalization of CNTs can be completed via the “ends and defects” and “side walls” functionalization. The ends and defects technique has higher specificity and reaction than side walls functionalization [45]. The surface of pristine CNTs can adsorb polymeric anticancer agents in a lot of cells. The interactions between the hydrophobic chains of the adsorbed molecules and the hydrophobic surface of CNTs can control the binding. In addition, p-p stacking interactions have also been considered to be related to such interactions [46]. The primary advantage of this kind of binding is to reduce the damage to the surface of CNTs to the minimal degree. According to some reports, the aromatic structure and electronic characteristics of CNTs can be preserved via noncovalent attachment. Due to chemical treatment, the emergence of charge on the surface of nanotube is able to adsorb the molecules via ionic interaction [35, 47, 48]. Some researchers have also been devoted to the debunching and solubilization of CNTs; they used nucleic acids and amphiphilic polymers on the basis of the p-p stacking interactions between the CNTs surface and aromatic bases/amino acids appearing in the structural backbone of these functional

biomolecules. Meanwhile, the noncovalent bond provides a weak strength for CNTs. These make it unsuitable for tumor-targeted drug delivery [49].

3.2. Covalent Functionalization. The covalent functionalization of CNTs can be achieved via the functionalization of “ends and defects” and “side walls.” The ends and defects technology has high specificity and reaction compared with the function of side walls [45]. The covalent functionalization of CNTs also can be finished via the bond between the surfaces of CNTs and the biocompatible groups. Using this way, the surface of CNTs has been modified by different techniques, and this modification provides an appropriate platform on the surface of these materials. At the same time, it also makes covalent biocompatible groups integrate with CNTs. The surface oxidation treatment is a usually way of originating covalent bonding [35]. The surface of CNTs can be cut via treatment with strong acid solutions and then lead to carboxylic group being exposed at the defect point, predominately on the open ends. CNTs in concentrated sulphuric and nitric acid have been treated and heated by ultrasonic wave. The side wall covalent functionalization can be achieved via this process, and carboxylic acid group can attach to CNTs and then make CNTs become water-soluble. CNTs can be cut and oxidized to produce a certain number of carboxylic groups and then be subsequently derivatized with different types of molecules. CNTs can be oxidized by the

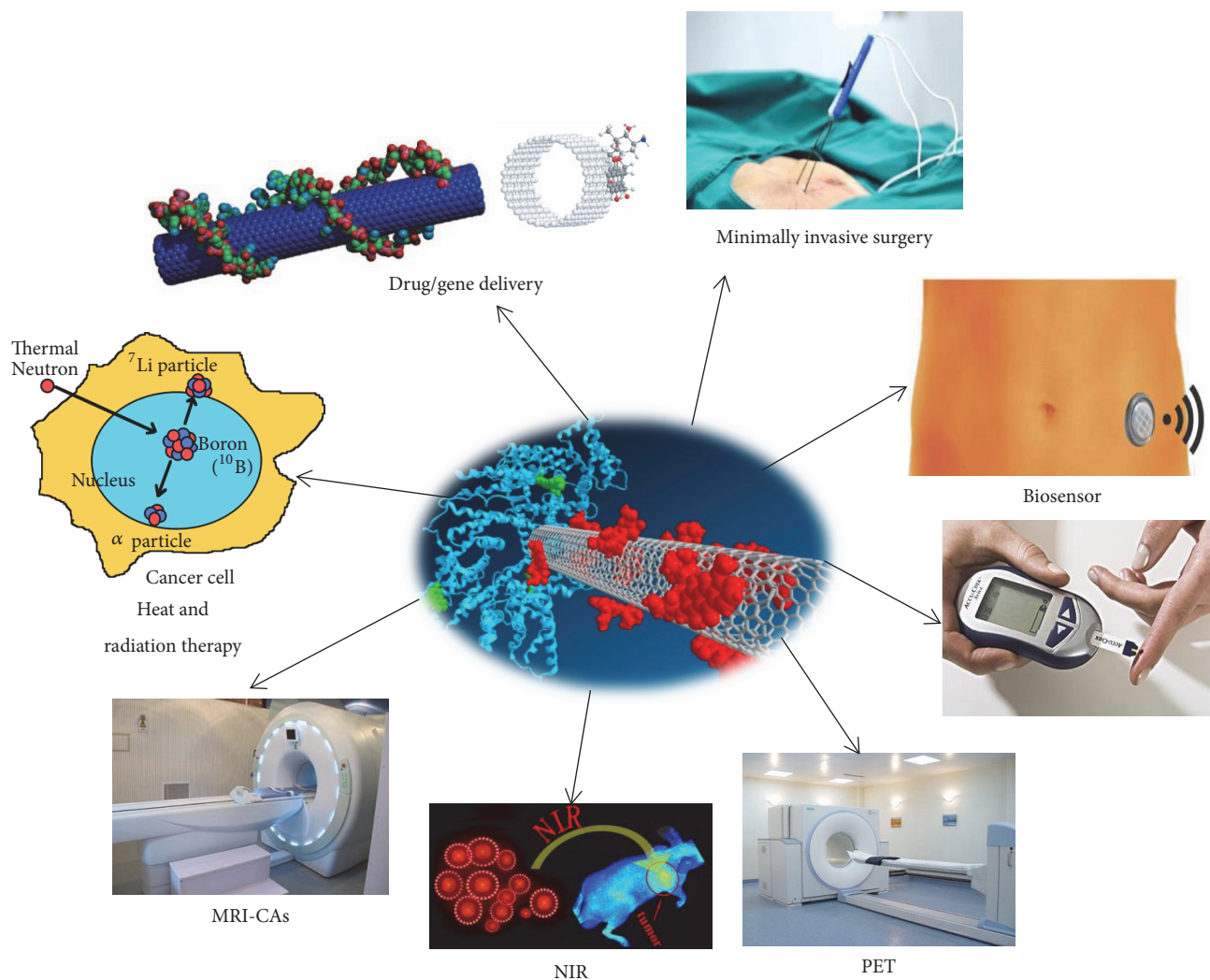


FIGURE 3: Biomedical applications of functionalized CNTs.

combination between nitric and sulphuric acid. Meanwhile, the biocompatibility of CNTs can be enhanced via the presence of a carboxylic group. According to extra reactions, the sidewalls of CNTs have been directly functionalized. The introductions of moieties with no the exterior surface of the nanotube produces exclusion between the nanotubes; this behavior makes them easily dispersible into the solvent [22, 50–54].

The carboxyl groups at the surface of CNTs can lead to a highly negative charge, which enhance the hydrophilicity of these materials [34, 35]. PEG is a hydrophilic substance, and it can cover the surface of CNTs and make oxidized CNTs more biostable [55]. The stable functionalized CNTs can be obtained via covalent coupling, which makes it become a more suitable tool for drug delivery. But during this process, the side wall of the CNTs has been damaged, which leads to the change of other properties of the CNTs [49, 56]. So the functionalization of CNTs should not be used in some applications, for example, imaging. Further, the function of CNTs can promote their applications (Table 1) [57]. These

functional features make CNTs a useful tool for biomedical applications (Figure 3).

4. The Applications of CNTs in Cancer Diagnostics

At the early stage of cancer, the effective method to treat cancer is the radical resection, so the early detection has become very important for the cancer therapy. However, the traditional imaging techniques for the treatment of clinical cancer (e.g., X-ray, CT, and MRI) cannot provide enough resolution for early diagnosis and assessment of prognosis. There are no obvious morphological changes appearing in most early neoplastic disorders, so the patient usually cannot be detected via these traditional imaging methods. Finding a reliable method to identify the presence of early biological molecular changes before any morphologic alterations has become more and more important. As an advanced imaging technology in the early detection of cancer, Positron emission tomography (PET) has better sensitivity and accuracy, and

TABLE 1: Summary of reviewed functionalization chemistries [57].

Types of association	Advantages	Disadvantages	Molecules attached	Potential applications
Noncovalent attachment	Higher loading than covalent approaches Chemistry of attached molecule is unaltered	Weaker binding and higher leaching than covalent approaches Limited to molecules with affinity for nanotube surface	Paclitaxel DNA Doxorubicin M13 phage	In vivo drug delivery for cancer therapeutics Detection of protein-protein interactions In vivo drug delivery for cancer therapeutics Tumor detection
Covalent attachment	Exhibits stronger/longer term binding Works for molecules which do not have a high affinity for the nanotube surface	Loading is limited to the number of available functional sites on nanotube surface Alters structure of molecule attached which might prove detrimental for the desired application	Lysostaphin AcT (perhydrolase) Protoporphyrin IX RNA aptamer Drug loaded liposomes	Antimicrobial nanocomposite films Glycoprotein detection In vivo drug delivery for cancer therapeutics

it is based on the biochemical and metabolic changes. Fluorodeoxyglucose (FDG) is one of the general radiopharmaceutical used in the medical imaging modality PET. It does not have the high specificity for cancer, but about 95% of the medical imaging technology is currently using it due to its promotion of metabolism [58–61]. It is urgent to find new methods for early cancer detection and diagnosis.

Some classic proteins are usually overexpressed in cancer cells, which can afford a chance for the early detection of the cancer. Clinically, several significant tumor markers have been widely used in the diagnosis of some cancers, including alpha-fetoprotein (AFP), carcinoma antigen 125 (CA125), carcinoembryonic antigen (CEA), human chorionic gonadotropin (hCG), carbohydrate antigen 19-9 (CA19-9), and prostate specific antigen (PSA). However, due to the low sensitivity and specificity for the early detection of cancer, these markers are only used in the following aspects, including deciding prognosis, predicting treatment responses, and keeping supervision for surgical treatment [62, 63]. On the other hand, due to their unique electronic, mechanical, and thermal properties, CNTs have been suggested as a hopeful tool for detecting the expression of typical biological molecules at early stage of cancer. The novel methods based on the CNTs have been achieved, which have high sensitivity and wide linear and ultralow detection. Moreover, the new system of CNTs can save time compared with the conventional ELISA commercial test kits while achieving the similar selectivity [64]. More importantly, this approach can provide handheld equipment with less expense compared with currently methods, such as immunoassays, test-strips, and kits [65]. In summary, the CNTs-based detection may be a selective way for cancer diagnosis and treatment in clinical analysis in the near future.

The discovery of biomarkers that can be used in the diagnosis of cancer has become an emergent work in recent years. Due to radical resection of the tumor being the only method to treat this disease at the early stage, the early screening and detection have become very important for the therapy of cancer. At the early stage most cancers has no obvious symptoms, and the traditional clinical cancer imaging technologies do not have enough resolution for early diagnosis and assessment of prognosis. The change of tissue properties is the basis for the diagnosis of cancer at the early stages, including optical absorption, mechanical properties, and RF absorption. It is very important to find new techniques for the early detection of cancer. Here, we provide a new view about how nanotubes have been used in the different diagnostic principles.

4.1. Photoacoustic Imaging. As a new imaging technology recently, photoacoustic imaging (PAI) was generally used in the different biomedical fields [66–69]. The theory of PAI is simple. Pulse laser is assimilated via absorptiometric molecule in the biological sample to produce heat, which can induce short-lived thermoelastic inflation, thereby resulting in broadband ultrasonic emission, and an ultrasound microphone can explore all these alterations; subsequently these detected signals were used to construct 2D or 3D images [66]. The primary advantage of PAI is to provide higher

spatial resolution and imaging of deeper tissues compared to the most optical imaging methods. The management of external photoacoustic contrast-mediums has become a necessary task. All kinds of nanomaterials have been applied as contrast-mediums in PAI, and these materials have strong capability to absorb light at near-infrared region (NIR) [66, 70–72]. Many contrast-mediums have been studied for PAI; however they cannot reach to the target site of disease in living subjects.

Due to MWNTs and SWNTs having strong NIR absorbance, they were used as a photothermal agent [73–75]. In addition, the property of firm NIR absorbance makes NTs become perfect contrast-mediums for PAI. Some reports have demonstrated the application of SWNTs in PAI, including in vitro and in vivo [76, 77]. SWNTs can offer more than twofold signal amplification in thermoacoustic tomography (TAT) and more than sixfold signal enlargement in photoacoustic tomography (PAT) compared with control. Due to SWNTs being able to give maximum signal compared with other carbon materials, fullerenes, and graphitic microparticles, this characteristic makes them applicable in the PAI as ideal contrast-mediums [78].

When SWNTs have ability to keep their integrity, they will be combined with other contrast-mediums in order to increase the photoacoustic signal of SWNTs. SWNTs have to be combined with some gold-coated layers or bioorganic molecules to improve their absorbance in the NIR areas. Gold coating can increase the inherent photoacoustic signal of SWNTs, so some researchers have developed “golden nanotubes” (GNTs) [79]. Moreover, some NIR dyes such as indocyanine green (IGG) molecules [80] can be loaded on PEGylated SWNTs to improve the optical density, which result in the presence of multiplexed PAI probes [81].

Hence, CNTs that possess strong NIR absorbance have become a hopeful contrast agent in PAI. Other than the application of their innate optical absorbance, CNTs can also be combined with other absorptivity nanomaterials in order to enhance or multiplex PAI, which make CNTs also a universal nanoplatform. Now majority of CNTs-based PAI probes depended on SWNTs; MWNTs can also be helpful for this imaging technique.

4.2. Fluorescence Imaging. Fluorescence imaging (FI) performs important functions for medical diagnosis. But the penetration depth has limited their further application in fluorescence imaging [82]. In order to solve this problem, some researchers have been to continually advance and improve fluorescence probes. These probes can be excited and sent wavelengths reach to the biological transparent NIR window [83].

As synthesized SWNTs, only a small number can produce fluorescence after laser stimulation; meanwhile most of SWNTs have not generated fluorescence under the excitation of laser wavelength, and these no fluorescent SWNTs are dark field images. So once polarization-purified SWNTs are applied, most of nanotubes injected into animal can lead to significant decrease. Van Hoff singularities (VHSs) can provide a good character for the density of states (DOS), and VHSs have limited narrow energy bands with high DOS

[84, 85]. The energy band gap is in the order of 1 eV between every semiconducting SWNTs, this character can ensure the fluorescence in the NIR-II region under the stimulation in the NIR-I region [85]. Furthermore, the large Stoke-shift between the excitation at 550–850 nm and emission at 900–1600 nm would dramatically lower the autofluorescence of biological tissues during imaging, and this condition can improve the sensitivity of imaging *in vivo* [86].

Robinson et al. have constructed a well functionalized SWNTs formulation; this formulation has a half-life of 30 h in blood circulation *in vivo*, thus leading to more than ~30% inject dose (% ID/g) drug accumulated [87]. High fluorescent video rate imaging and principle component analysis (PCA) have been applied to monitor the fluorescent signals in tumors and other organs at the first time. After 20 s injection they have seen the obvious fluorescent signals in tumor, and the fluorescence signal can be kept up to 72 h. Furthermore, they have also seen the colocalization between tumor vasculatures and SWNTs in tumor inside via using technology of 3D reconstruction of NIR-II fluorescence signals. This discovery indicated that the effect of permeability and retention (EPR) may play vital role in mediating the tumor accumulation of nanotubes.

Hence, the SWNTs-based NIR-II FI has enormous potential in the field of biomedical diagnostics, and its peculiar advantages have been proved compared with other existing imaging technologies. Furthermore, different SWNTs have different excitation and emission wavelengths, and this feature makes them become potentially useful material for multicolor NIR-II fluorescence imaging. In other fluorescence enlargement technologies, such as based on surface resonance, the gold substrate can enhance the fluorescence of SWNT [88], and maybe these technologies can combine to further improve the sensitivity of imaging and detection.

4.3. Raman Image. Raman scattering is a photon scattering process, which refers to emission of photons with shifted wavelengths under light stimulation. The inherent Raman scattering signals of molecules do not involve enhancement mechanism such as surface enhanced Raman scattering (SERS) and are usually rather weak. SWNTs have various Raman peaks, which include the radical breathing mode (RBM, 100–300 cm^{-1}) and tangential G band (~1580 cm^{-1}). These Raman peaks accord with the oscillation of carbon atoms in the radial direction and in the tangential direction, respectively. Because Raman spectroscopy can provide particular information on the chemical composition of cells and tissues, it has been studied in the application of biomedical diagnostics. It is very easy to distinguish the autofluorescence background due to the sharp and narrow Raman peaks of SWCNTs. The Raman excitation and scattering photons of SWCNTs can reach to the NIR region, and this is a transparent window for *in vivo* imaging. Dai and coworker have found various Raman imaging of live cells with isotopically modified SWCNTs [89]. In this work, SWCNTs with different isotope (^{12}C and/or ^{13}C) compositions (which have distinct Raman G band peaks) have been studied, while different cancer cells with different surface receptors were applied to receptor-specific targeting. Each targeting ligand

can recognize its specific receptor, which led to the multicolor Raman imaging of cells in a multiplexed manner. When pure ^{12}C - and ^{13}C -SWCNTs are conjugated by different antibodies, multiplexed Raman detection of different proteins can be proved.

5. The Application of Carbon Nanotubes in Cancer Therapeutics

At the early stage, the only effective method of cancer treatment is radical resection. In recent years, some methods for cancer therapy have appeared with the development of biotechnology; however, a more efficient method for specific target delivery of chemodrugs still needs to be developed [90, 91]. In the past decades, various drug delivery systems were evaluated in order to deliver some chemicals to tumors, for example, doxorubicin (DOX) and paclitaxel (PTX). These delivery systems include liposome, natural/synthetic polymers, and nanoparticles. In these methods, liposomes and polymeric materials are widely used. Unfortunately, the inorganic materials, which have unique physiochemical properties, are largely ignored. CNTs have unique properties, which make them suitable carriers for target-specific drug-loadable delivery. CNTs have specific advantages as drug-carriers, which include thermal conductivity, rigid structural properties capable of postchemical modification, sufficient surface-to-volume ratio, and excellent biocompatibility.

In addition, the drugs with water insolubility, antigens, antibodies, and nucleic acids can also be delivered into tumor cells via these carbon-based materials, and the unloading of therapeutic molecules is also very safe in tumor cells; then anticancer activity was efficiently enhanced. In this review, we have summarized the application of CNTs in cancer treatment from several aspects.

5.1. CNTs in Cancer Chemotherapy. Medicine for the treatment through a series of biologic obstacles is the first step, which is a vital link for the effect of chemotherapy. These obstacles include hepatic and renal clearance, hydrolysis, enzymolysis, endocytosis, and lysosomal degradation. Some chemotherapeutic drugs have poor solubility, low stability, and high toxicity for normal cells and tissues, which have a serious influence on their efficiency. However, CNTs-based carriers can enhance the biodistribution and prolong blood circulation of therapeutics; then the pharmaceutical efficacy can be increased and the usage dose can be decreased. In view of the fact that the biocompatible SWNT, Liu et al. [92], made DOX loaded onto branched PEG-functionalized SWNTs designed in order to prolong blood circulation time, they have injected the SWNT-DOX complex to tumor mice. They found that DOX can be delivered into tumors, and SWNT can be cleared from systemic blood circulation via renal excretion. However, physical loading for PTX is very difficult due to its poor solubility in aqueous solution. In order to overcome this hurdle, Lay et al. produced both PEG-graft single-walled CNTs (PEG-gSWNTs) and PEG-graft multiwalled CNTs (PEG-gMWNTs) to enhance loading ability [93]. They found that the delivery of PTX can be sustained over 40 days *in vitro*. With the development of technology, some researchers

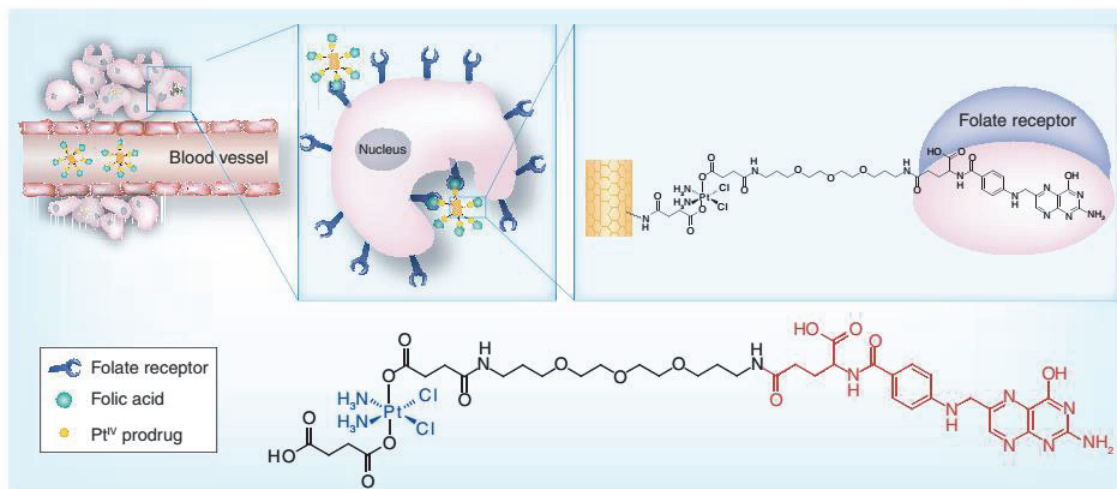


FIGURE 4: Folate-mediated cancer targeting using single-walled carbon nanotubes conjugated with platinum-containing anticancer drug and its subsequent endocytosis [27].

have modified SWNTs carrier to improve their efficiency of delivery, such as the epidermal growth factor- (EGF-) mediated SWNT delivery of an anticancer agent cisplatin [94]. In addition, MWNTs can be used for thermal ablation as a carbon-based nanomaterial, which results in hyperthermia for destroying cancer cells.

5.2. CNTs in Drug Delivery. The systemic toxicity of chemotherapeutic agents is often neglected due to the lack of selectivity conventional administration. Furthermore, these agents have limited solubility and inability to pass through cellular barriers [95], especially the clinical routines which are lacking for overcoming multidrug resistant (MDR) cancer [96]. In recent years, these problems have been studied by researchers all over the world. Several novel targeted therapies have been discovered, which are based on CNTs materials. These delivery systems usually include three portions, and they are functional CNTs, targeted ligands, and anticarcinogen. Many drugs, polypeptides and nucleonic acid, can be integrated into CNTs because of their unique ultrahigh surface area. Due to the existence of endocytosis and other mechanisms, the functional CNTs can pass through the membrane of mammalian cells [94, 97, 98]. They have the unique ability to identify the specific surface receptors when drug delivery systems (NDDs) interact with cancer cells, which can result in receptor-mediated endocytosis. Anticancer drugs can effectively reach the cells via the CNTs-based delivery system, and these advantages make CNTs become ideal candidates for drug delivery. The cancer cells can effectively and specifically absorb the CNTs complex, and the chemotherapeutic agents can be released into intracellular space; then these drugs can more effectively curb the spread of cancer cells than uncontrolled drugs. In addition, the cytotoxicity was decreased by using this novel approach, and the severe side-effects could be avoided [94]. SWNTs can offer higher ability of drug loading compared with the traditional liposomes and dendrimer drug carries due to their extremely

high specific surface area [49]. Figure 4 indicates a delivery system that SWCNTs medicated, which can deliver drugs for treatment of cancer. Overall, these advantages clearly indicated that CNTs can be used for targeted delivery system in the future.

5.3. Photothermal Therapy. While thermotherapy has been applied in treatment of tumor patients for long time [99], photothermal therapy is still considered to be one of the best methods to treat cancer. Recently, some researchers have been reported indicating the possibility of heating CNTs injected into cancer cells and thus induce their death. Photothermal therapy as a noninvasive, uninjurious and effective therapeutic technology can be heated locally just to the tumor tissues via NIR, and then tumor cells have been destroyed [55, 100, 101]. In addition, the side-effects on other parts can be decreased to the minimum by using this method [102–106]. The CNTs have good light absorption performance under NIR and radio-frequency radiation [107, 108]. Furthermore, the length of nanotubes is a very vital element, and it decides the capacity of heat transmission and cancer cell erosion [109]. The CNTs-based photothermal therapy systems can combine with chemotherapy and gene treatment techniques to obtain more efficiency for treating cancer [55, 110].

To enhance the selectivity in the treatment of cancer and to reduce the side-effects to normal cells, the targeted CNTs can be achieved via covalent or noncovalent coating with cell-bound ligands, for example, monoclonal antibodies (MAbs) or peptides [55, 104, 110, 111]. In view of photothermal transduction influence, nanotubes have been supposed and developed as photothermal agents for killing cancer, and this function can be achieved via heating the nanotube to 50–70°C through sustaining laser irradiation at high power density (3.5–35 W/cm²) for a long time (3–4 min) [112]. Furthermore, photothermal therapy is based on absorption properties of antibody-conjugated nanomaterials, and this therapy method

has been confirmed having selective ability to kill tumor cells, but the healthy cells will not be affected [113–115].

5.4. Delivery of Immunotherapeutics. The antitumor immunotherapy with CNTs-based has been studied. Tumor cell vaccines (TCV) were used in this method and the immune response of the patient against the tumor itself was triggered by inactivated cancer cells or dendritic cells presenting tumor antigens [116]. In order to enhance the efficacy of TCV, the oxidized MWCNTs can be covalently coupled with tumor lysate proteins by an amide bond. On the other hand, Villa et al. have developed the capacity of SWCNTs to act as antigen presenting carries to increase the response to weak immunogenic peptides [117]. The Wilms tumor protein (WT1) was covalently conjugated with SWCNTs, and this modification makes it become a vaccine target for many human cancers. In their study, SWCNTs-WT1 can be rapidly uptaken by APC in vitro, which is also dependent of dose. In addition, they used SWCNTs-WT1 adjuvant to immune mice and found that mice can cause a specific humoral immune reaction, and they do not see other response against the peptide alone against the peptide mixed with the adjuvant. These results suggested that SWCNTs can be a new tool to deliver poorly immunogenic peptides to the immune system, thus enhancing the efficiency of vaccine treatment.

6. Conclusion

In recent years, nanotechnology has dramatically drawn attention and interest in medicine and biology. Carbon nanotubes are one of the nanomaterials, which include two forms. CNTs have been functionalized via covalent and noncovalent interaction. Functionalized CNTs can be used as carriers to play their roles in delivery system. The research of their biomedical applications just has been less than twenty years. The CNTs have better biocompatibility and multimodal functions after their surfaces were modified; therefore the therapeutic effect was better than before, especially for the treatment of cancer. Carriers CNTs have many advantages, including high load of drugs, good penetrability, photothermal ablation, and inherent diagnostic capability. These advantages are the key elements for making them as appropriate nanocarriers in tumor treatment. CNTs have the ability to deliver biologically active molecules to cytoplasm, and they need to bypass many biological barriers and play as a cellular needle during this process. Furthermore, CNTs have more surface areas and internal antrums, which can be loaded with targeted ligands and filled with diagnostic or therapeutic agents. In addition, CNTs also have unparalleled electrical and thermal conductivity characters. These advantages make their clinical application possible. Despite CNTs having great promise for the treatment of cancer, we cannot neglect their nonbiodegradable nature and cytotoxicity in clinical use. The emergence of new techniques for surface functionalization may help reduce these disadvantages. We believe that this novel CNT based platform can provide us with a safer and more effective way for the cancer therapy in the near future.

Conflicts of Interest

The authors declare that they have no conflicts of interest.

Authors' Contributions

Zhou Chen, Aili Zhang, and Xiaobing Wang contributed equally to this work.

Acknowledgments

This work is supported by the Priority Academic Program Development of Jiangsu Higher Education Institutions.

References

- [1] S. Y. Madani, F. Shabani, M. V. Dwek, and A. M. Seifalian, "Conjugation of quantum dots on carbon nanotubes for medical diagnosis and treatment," *International Journal of Nanomedicine*, vol. 8, pp. 941–950, 2013.
- [2] Z. Yang, L. Chang, C.-L. Chiang, and L. J. Lee, "Micro-/nanoelectroporation for active gene delivery," *Current Pharmaceutical Design*, vol. 21, no. 42, pp. 6081–6088, 2015.
- [3] Z. Yang, B. Yu, J. Zhu et al., "A microfluidic method to synthesize transferrin-lipid nanoparticles loaded with siRNA LOR-1284 for therapy of acute myeloid leukemia," *Nanoscale*, vol. 6, no. 16, pp. 9742–9751, 2014.
- [4] C. Zhou, Z. Yang, and L. Teng, "Nanomedicine based on nucleic acids: pharmacokinetic and pharmacodynamic perspectives," *Current Pharmaceutical Biotechnology*, vol. 15, no. 9, pp. 829–838, 2015.
- [5] X. Yang, S. Yang, H. Chai et al., "A novel isoquinoline derivative anticancer agent and its targeted delivery to tumor cells using transferrin-conjugated liposomes," *PLoS ONE*, vol. 10, no. 8, Article ID e0136649, 2015.
- [6] B. Yu, X. Wang, C. Zhou et al., "Insight into mechanisms of cellular uptake of lipid nanoparticles and intracellular release of small RNAs," *Pharmaceutical Research*, vol. 31, no. 10, pp. 2685–2695, 2014.
- [7] J. Xie, L. Teng, Z. Yang et al., "A polyethylenimine-linoleic acid conjugate for antisense oligonucleotide delivery," *BioMed Research International*, vol. 2013, Article ID 710502, 7 pages, 2013.
- [8] J. Xie, Z. Yang, C. Zhou, J. Zhu, R. J. Lee, and L. Teng, "Nanotechnology for the delivery of phytochemicals in cancer therapy," *Biotechnology Advances*, vol. 34, no. 4, pp. 343–353, 2016.
- [9] Z. Chen, A. Zhang, J. Hu, X. Wang, and Z. Yang, "Electrospun nanofibers for cancer diagnosis and therapy," *Biomaterials Science*, vol. 4, no. 6, pp. 922–932, 2016.
- [10] Z. Chen, M. Cong, J. Hu, Z. Yang, and Z. Chen, "Preparation of functionalized TiO₂ nanotube arrays and their applications," *Science of Advanced Materials*, vol. 8, no. 6, pp. 1231–1241, 2016.
- [11] Z. Yang, J. Xie, J. Zhu et al., "Functional exosome-mimic for delivery of siRNA to cancer: in vitro and in vivo evaluation," *Journal of Controlled Release*, vol. 243, pp. 160–171, 2016.
- [12] L. Sha, Z. Chen, Z. Chen, A. Zhang, and Z. Yang, "Polylactic acid based nanocomposites: Promising safe and biodegradable materials in biomedical field," *International Journal of Polymer Science*, vol. 2016, Article ID 6869154, 11 pages, 2016.

- [13] C. Kang, Y. Sun, J. Zhu et al., "Delivery of nanoparticles for treatment of brain tumor," *Current Drug Metabolism*, vol. 17, no. 8, pp. 745–754, 2016.
- [14] Z. Chena, A. Zhang, Z. Yang et al., "Application of DODMA and derivatives in cationic nanocarriers for gene delivery," *Current Organic Chemistry*, vol. 20, no. 17, pp. 1813–1819, 2016.
- [15] L. J. Lee, Z. Yang, M. Rahman et al., "Extracellular mRNA detected by tethered lipoplex nanoparticle biochip for lung adenocarcinoma detection," *American Journal of Respiratory & Critical Care Medicine*, vol. 193, no. 12, pp. 1431–1433, 2016.
- [16] N. G. Sahoo, H. Bao, Y. Pan et al., "Functionalized carbon nanomaterials as nanocarriers for loading and delivery of a poorly water-soluble anticancer drug: a comparative study," *Chemical Communications*, vol. 47, no. 18, pp. 5235–5237, 2011.
- [17] P. Utreja, S. Jain, and A. K. Tiwary, "Novel drug delivery systems for sustained and targeted delivery of anti-cancer drugs: current status and future prospects," *Current Drug Delivery*, vol. 7, no. 2, pp. 152–161, 2010.
- [18] K. Kostarelos, L. Lacerda, G. Pastorin et al., "Cellular uptake of functionalized carbon nanotubes is independent of functional group and cell type," *Nature Nanotechnology*, vol. 2, no. 2, pp. 108–113, 2007.
- [19] N. W. Kam, Z. Liu, and H. Dai, "Carbon nanotubes as intracellular transporters for proteins and DNA: an investigation of the uptake mechanism and pathway," *Angewandte Chemie*, vol. 118, no. 4, pp. 591–595, 2006.
- [20] C. Fabbro, H. Ali-Boucetta, T. D. Ros, K. Kostarelos, A. Bianco, and M. Prato, "Targeting carbon nanotubes against cancer," *Chemical Communications*, vol. 48, no. 33, pp. 3911–3926, 2012.
- [21] R. Singh, D. Pantarotto, L. Lacerda et al., "Tissue biodistribution and blood clearance rates of intravenously administered carbon nanotube radiotracers," *Proceedings of the National Academy of Sciences of the United States of America*, vol. 103, no. 9, pp. 3357–3362, 2006.
- [22] L. Lacerda, H. Ali-Boucetta, M. A. Herrero et al., "Tissue histology and physiology following intravenous administration of different types of functionalized multiwalled carbon nanotubes," *Nanomedicine*, vol. 3, no. 2, pp. 149–161, 2008.
- [23] L. Lacerda, M. A. Herrero, K. Venner, A. Bianco, M. Prato, and K. Kostarelos, "Carbon-nanotube shape and individualization critical for renal excretion," *Small*, vol. 4, no. 8, pp. 1130–1132, 2008.
- [24] M. R. McDevitt, D. Chattopadhyay, J. S. Jaggi et al., "PET imaging of soluble yttrium-86-labeled carbon nanotubes in mice," *PLoS ONE*, vol. 2, no. 9, article no. e907, 2007.
- [25] Z. Liu, C. Davis, W. Cai, L. He, X. Chen, and H. Dai, "Circulation and long-term fate of functionalized, biocompatible single-walled carbon nanotubes in mice probed by Raman spectroscopy," *Proceedings of the National Academy of Sciences of the United States of America*, vol. 105, no. 5, pp. 1410–1415, 2008.
- [26] K. Kostarelos, A. Bianco, and M. Prato, "Promises, facts and challenges for carbon nanotubes in imaging and therapeutics," *Nature Nanotechnology*, vol. 4, no. 10, pp. 627–633, 2009.
- [27] A. Ruggiero, C. H. Villa, E. Bander et al., "Paradoxical glomerular filtration of carbon nanotubes," *Proceedings of the National Academy of Sciences of the United States of America*, vol. 107, no. 27, pp. 12369–12374, 2010.
- [28] P. C. B. D. Faria, L. I. D. Santos, J. P. Coelho et al., "Oxidized multiwalled carbon nanotubes as antigen delivery system to promote superior CD8+ T Cell response and protection against Cancer," *Nano Letters*, vol. 14, no. 9, pp. 5458–5470, 2014.
- [29] A. Jemal, S. S. Devesa, P. Hartge, and M. A. Tucker, "Recent trends in cutaneous melanoma incidence among whites in the United States," *Journal of the National Cancer Institute*, vol. 93, no. 9, pp. 678–683, 2001.
- [30] Y. Yan, M. B. Chan-Park, and Q. Zhang, "Advances in carbon-nanotube assembly," *Small*, vol. 3, no. 1, pp. 24–42, 2007.
- [31] P. Kesharwani, V. Mishra, and N. K. Jain, "Validating the anticancer potential of carbon nanotube-based therapeutics through cell line testing," *Drug Discovery Today*, vol. 20, no. 9, pp. 1049–1060, 2015.
- [32] D. S. Bethune, C. H. Kiang, M. S. de Vries et al., "Cobalt-catalysed growth of carbon nanotubes with single-atomic-layer walls," *Nature*, vol. 363, no. 6430, pp. 605–607, 1993.
- [33] N. K. Mehra, V. Mishra, and N. K. Jain, "A review of ligand tethered surface engineered carbon nanotubes," *Biomaterials*, vol. 35, no. 4, pp. 1267–1283, 2014.
- [34] E. Bekyarova, Y. Ni, E. B. Malarkey et al., "Applications of Carbon Nanotubes in Biotechnology and Biomedicine," *Journal of Biomedical Nanotechnology*, vol. 1, no. 1, pp. 3–17, 2005.
- [35] C. Klumpp, K. Kostarelos, M. Prato, and A. Bianco, "Functionalized carbon nanotubes as emerging nanovectors for the delivery of therapeutics," *Biochimica et Biophysica Acta—Biomembranes*, vol. 1758, no. 3, pp. 404–412, 2006.
- [36] S. Y. Madani, N. Naderi, O. Dissanayake, A. Tan, and A. M. Seifalian, "A new era of cancer treatment: carbon nanotubes as drug delivery tools," *International Journal of Nanomedicine*, vol. 6, pp. 2963–2979, 2011.
- [37] A. Bianco, K. Kostarelos, and M. Prato, "Applications of carbon nanotubes in drug delivery," *Current Opinion in Chemical Biology*, vol. 9, no. 6, pp. 674–679, 2005.
- [38] J. Liu, A. G. Rinzler, H. Dai et al., "Fullerene pipes," *Science*, vol. 280, no. 5367, pp. 1253–1256, 1998.
- [39] D. Tasis, N. Tagmatarchis, V. Georgakilas, and M. Prato, "Soluble carbon nanotubes," *Chemistry - A European Journal*, vol. 9, no. 17, pp. 4000–4008, 2003.
- [40] V. Georgakilas, K. Kordatos, M. Prato, D. M. Guldi, M. Holzinger, and A. Hirsch, "Organic functionalization of carbon nanotubes," *Journal of the American Chemical Society*, vol. 124, no. 5, pp. 760–761, 2002.
- [41] Z. Chen, W. Wu, Z. Chen, X. Cong, and J. Qiu, "Microstructural characterization on ZrC doped carbon/carbon composites," *Ceramics International*, vol. 38, no. 1, pp. 761–767, 2012.
- [42] A. Bianco, K. Kostarelos, C. D. Partidos, and M. Prato, "Biomedical applications of functionalised carbon nanotubes," *Chemical Communications*, no. 5, pp. 571–577, 2005.
- [43] P. Kesharwani, R. Ghanghoria, and N. K. Jain, "Carbon nanotube exploration in cancer cell lines," *Drug Discovery Today*, vol. 17, no. 17–18, pp. 1023–1030, 2012.
- [44] I. D. Rosca, F. Watari, M. Uo, and T. Akasaka, "Oxidation of multiwalled carbon nanotubes by nitric acid," *Carbon*, vol. 43, no. 15, pp. 3124–3131, 2005.
- [45] S. Vardharajula, S. Z. Ali, P. M. Tiwari et al., "Functionalized carbon nanotubes: biomedical applications," *International Journal of Nanomedicine*, vol. 7, pp. 5361–5374, 2012.
- [46] V. S. Thakare, M. Das, A. K. Jain, S. Patil, and S. Jain, "Carbon nanotubes in cancer theragnosis," *Nanomedicine*, vol. 5, no. 8, pp. 1277–1301, 2010.
- [47] R. M. Lucente-Schultz, V. C. Moore, A. D. Leonard et al., "Antioxidant single-walled carbon nanotubes," *Journal of the American Chemical Society*, vol. 131, no. 11, pp. 3934–3941, 2009.

- [48] N. Jia, Q. Lian, H. Shen, C. Wang, X. Li, and Z. Yang, "Intracellular delivery of quantum dots tagged antisense oligodeoxynucleotides by functionalized multiwalled carbon nanotubes," *Nano Letters*, vol. 7, no. 10, pp. 2976–2980, 2007.
- [49] Z. Liu, X. Sun, N. Nakayama-Ratchford, and H. Dai, "Supramolecular chemistry on water-soluble carbon nanotubes for drug loading and delivery," *ACS Nano*, vol. 1, no. 1, pp. 50–56, 2007.
- [50] A. Hirsch, "Functionalization of single-walled carbon nanotubes," *Angewandte Chemie - International Edition*, vol. 41, no. 11, pp. 1853–1859, 2002.
- [51] G. Pastorin, W. Wu, S. Wieckowski et al., "Double functionalisation of carbon nanotubes for multimodal drug delivery," *Chemical Communications*, no. 11, pp. 1182–1184, 2006.
- [52] Y.-J. Lu, K.-C. Wei, C.-C. M. Ma, S.-Y. Yang, and J.-P. Chen, "Dual targeted delivery of doxorubicin to cancer cells using folate-conjugated magnetic multi-walled carbon nanotubes," *Colloids and Surfaces B: Biointerfaces*, vol. 89, no. 1, pp. 1–9, 2012.
- [53] N. Karousis, N. Tagmatarchis, and D. Tasis, "Current progress on the chemical modification of carbon nanotubes," *Chemical Reviews*, vol. 110, no. 9, pp. 5366–5397, 2010.
- [54] V. Mishra, P. Kesharwani, and N. K. Jain, "SiRNA nanotherapeutics: a Trojan horse approach against HIV," *Drug Discovery Today*, vol. 19, no. 12, pp. 1913–1920, 2014.
- [55] N. W. S. Kam, M. O'Connell, J. A. Wisdom, and H. Dai, "Carbon nanotubes as multifunctional biological transporters and near-infrared agents for selective cancer cell destruction," *Proceedings of the National Academy of Sciences of the United States of America*, vol. 102, no. 33, pp. 11600–11605, 2005.
- [56] S. Niyogi, M. A. Hamon, H. Hu et al., "Chemistry of single-walled carbon nanotubes," *Accounts of Chemical Research*, vol. 35, no. 12, pp. 1105–1113, 2002.
- [57] R. V. Mundra, X. Wu, J. Sauer, J. S. Dordick, and R. S. Kane, "Nanotubes in biological applications," *Current Opinion in Biotechnology*, vol. 28, pp. 25–32, 2014.
- [58] S.-R. Ji, C. Liu, B. Zhang et al., "Carbon nanotubes in cancer diagnosis and therapy," *Biochimica et Biophysica Acta—Reviews on Cancer*, vol. 1806, no. 1, pp. 29–35, 2010.
- [59] R. P. Levy, "PET-CT: evolving role in hadron therapy," *Nuclear Instruments and Methods in Physics Research, Section B: Beam Interactions with Materials and Atoms*, vol. 261, no. 1–2, pp. 782–785, 2007.
- [60] D. Papanthassiou, C. Bruna-Muraille, J.-C. Liehn, T. D. Nguyen, and H. Curé, "Positron emission tomography in oncology: present and future of PET and PET/CT," *Critical Reviews in Oncology/Hematology*, vol. 72, no. 3, pp. 239–254, 2009.
- [61] D. Delbeke, H. Schöder, W. H. Martin, and R. L. Wahl, "Hybrid imaging (SPECT/CT and PET/CT): improving therapeutic decisions," *Seminars in Nuclear Medicine*, vol. 39, no. 5, pp. 308–340, 2009.
- [62] M. J. Duffy, "Role of tumor markers in patients with solid cancers: a critical review," *European Journal of Internal Medicine*, vol. 18, no. 3, pp. 175–184, 2007.
- [63] L. K. Rogers, M. Robbins, D. Dakhlallah et al., "Attenuation of MIR-17~92 cluster in bronchopulmonary dysplasia," *Annals of the American Thoracic Society*, vol. 12, no. 10, pp. 1506–1513, 2015.
- [64] N. V. Panini, G. A. Messina, E. Salinas, H. Fernández, and J. Raba, "Integrated microfluidic systems with an immunosensor modified with carbon nanotubes for detection of prostate specific antigen (PSA) in human serum samples," *Biosensors and Bioelectronics*, vol. 23, no. 7, pp. 1145–1151, 2008.
- [65] J.-A. A. Ho, Y.-C. Lin, L.-S. Wang, K.-C. Hwang, and P.-T. Chou, "Carbon nanoparticle-enhanced immunoelectrochemical detection for protein tumor marker with cadmium sulfide biotracers," *Analytical Chemistry*, vol. 81, no. 4, pp. 1340–1346, 2009.
- [66] H. Gong, R. Peng, and Z. Liu, "Carbon nanotubes for biomedical imaging: the recent advances," *Advanced Drug Delivery Reviews*, vol. 65, no. 15, pp. 1951–1963, 2013.
- [67] X. Wang, Y. Pang, G. Ku, X. Xie, G. Stoica, and L. V. Wang, "Noninvasive laser-induced photoacoustic tomography for structural and functional in vivo imaging of the brain," *Nature Biotechnology*, vol. 21, no. 7, pp. 803–806, 2003.
- [68] G. Ku and L. V. Wang, "Deeply penetrating photoacoustic tomography in biological tissues enhanced with an optical contrast agent," *Optics Letters*, vol. 30, no. 5, pp. 507–509, 2005.
- [69] C. G. A. Hoelen, F. F. M. De Mul, R. Pongers, and A. Dekker, "Three-dimensional photoacoustic imaging of blood vessels in tissue," *Optics Letters*, vol. 23, no. 8, pp. 648–650, 1998.
- [70] K. Yang, L. Hu, X. Ma et al., "Multimodal imaging guided photothermal therapy using functionalized graphene nanosheets anchored with magnetic nanoparticles," *Advanced Materials*, vol. 24, no. 14, pp. 1868–1872, 2012.
- [71] G. Ku, M. Zhou, S. Song, Q. Huang, J. Hazle, and C. Li, "Copper sulfide nanoparticles as a new class of photoacoustic contrast agent for deep tissue imaging at 1064 nm," *ACS Nano*, vol. 6, no. 8, pp. 7489–7496, 2012.
- [72] A. Agarwal, S. W. Huang, M. O'Donnell et al., "Targeted gold nanorod contrast agent for prostate cancer detection by photoacoustic imaging," *Journal of Applied Physics*, vol. 102, no. 6, Article ID 064701, 2007.
- [73] J. T. Robinson, K. Welscher, S. M. Tabakman et al., "High performance in vivo near-IR (>1 μm) imaging and photothermal cancer therapy with carbon nanotubes," *Nano Research*, vol. 3, no. 11, pp. 779–793, 2010.
- [74] X. Liu, H. Tao, K. Yang, S. Zhang, S.-T. Lee, and Z. Liu, "Optimization of surface chemistry on single-walled carbon nanotubes for in vivo photothermal ablation of tumors," *Biomaterials*, vol. 32, no. 1, pp. 144–151, 2011.
- [75] H. K. Moon, S. H. Lee, and H. C. Choi, "In vivo near-infrared mediated tumor destruction by photothermal effect of carbon nanotubes," *ACS Nano*, vol. 3, no. 11, pp. 3707–3713, 2009.
- [76] P. K. Avti, S. Hu, C. Favazza et al., "Detection, mapping, and quantification of single walled carbon nanotubes in histological specimens with photoacoustic microscopy," *PLoS ONE*, vol. 7, no. 4, Article ID e35064, 2012.
- [77] L. Wu, X. Cai, K. Nelson et al., "A green synthesis of carbon nanoparticles from honey and their use in real-time photoacoustic imaging," *Nano Research*, vol. 6, no. 5, pp. 312–325, 2013.
- [78] M. Pramanik, M. Swierczewska, D. Green, B. Sitharaman, and L. V. Wang, "Single-walled carbon nanotubes as a multimodal-thermoacoustic and photoacoustic-contrast agent," *Journal of Biomedical Optics*, vol. 14, no. 3, Article ID 034018, 2009.
- [79] J.-W. Kim, E. I. Galanzha, E. V. Shashkov, H.-M. Moon, and V. P. Zharov, "Golden carbon nanotubes as multimodal photoacoustic and photothermal high-contrast molecular agents," *Nature Nanotechnology*, vol. 4, no. 10, pp. 688–694, 2009.
- [80] A. D. L. Zerda, Z. Liu, S. Bodapati et al., "Ultrahigh sensitivity carbon nanotube agents for photoacoustic molecular imaging in living mice," *Nano Letters*, vol. 10, no. 6, pp. 2168–2172, 2010.
- [81] A. De La Zerda, S. Bodapati, R. Teed et al., "Family of enhanced photoacoustic imaging agents for high-sensitivity

- and multiplexing studies in living mice," *ACS Nano*, vol. 6, no. 6, pp. 4694–4701, 2012.
- [82] X. He, J. Gao, S. S. Gambhir, and Z. Cheng, "Near-infrared fluorescent nanoprobe for cancer molecular imaging: status and challenges," *Trends in Molecular Medicine*, vol. 16, no. 12, pp. 574–583, 2010.
- [83] B. Chance, "Near-infrared images using continuous, phase-modulated, and pulsed light with quantitation of blood and blood oxygenation," *Annals of the New York Academy of Sciences*, vol. 838, pp. 29–45, 1998.
- [84] H. Kuzmany, B. Burger, M. Fally, A. G. Rinzler, and R. E. Smalley, "Effect of dimensionality in polymeric fullerenes and single-wall nanotubes," *Physica B: Condensed Matter*, vol. 244, pp. 186–191, 1998.
- [85] A. Jorio, M. A. Pimenta, A. G. S. Filho, R. Saito, G. Dresselhaus, and M. S. Dresselhaus, "Characterizing carbon nanotube samples with resonance Raman scattering," *New Journal of Physics*, vol. 5, article 139, 2003.
- [86] G. Hong, J. C. Lee, J. T. Robinson et al., "Multifunctional in vivo vascular imaging using near-infrared II fluorescence," *Nature Medicine*, vol. 18, no. 12, pp. 1841–1846, 2012.
- [87] J. T. Robinson, G. Hong, Y. Liang, B. Zhang, O. K. Yaghi, and H. Dai, "In vivo fluorescence imaging in the second near-infrared window with long circulating carbon nanotubes capable of ultrahigh tumor uptake," *Journal of the American Chemical Society*, vol. 134, no. 25, pp. 10664–10669, 2012.
- [88] G. Hong, S. M. Tabakman, K. Welsher, H. Wang, X. Wang, and H. Dai, "Metal-enhanced fluorescence of carbon nanotubes," *Journal of the American Chemical Society*, vol. 132, no. 45, pp. 15920–15923, 2010.
- [89] Z. Liu, X. Li, S. M. Tabakman, K. Jiang, S. Fan, and H. Dai, "Multiplexed multicolor raman imaging of live cells with isotopically modified single walled carbon nanotubes," *Journal of the American Chemical Society*, vol. 130, no. 41, pp. 13540–13541, 2008.
- [90] B. Haley and E. Frenkel, "Nanoparticles for drug delivery in cancer treatment," *Urologic Oncology: Seminars and Original Investigations*, vol. 26, no. 1, pp. 57–64, 2008.
- [91] D. M. Webster, P. Sundaram, and M. E. Byrne, "Injectable nanomaterials for drug delivery: carriers, targeting moieties, and therapeutics," *European Journal of Pharmaceutics and Biopharmaceutics*, vol. 84, no. 1, pp. 1–20, 2013.
- [92] Z. Liu, A. C. Fan, K. Rakhra et al., "Supramolecular stacking of doxorubicin on carbon nanotubes for *in vivo* cancer therapy," *Angewandte Chemie*, vol. 48, no. 41, pp. 7668–7672, 2009.
- [93] C. L. Lay, H. Q. Liu, H. R. Tan, and Y. Liu, "Delivery of paclitaxel by physically loading onto poly(ethylene glycol) (PEG)-graftcarbon nanotubes for potent cancer therapeutics," *Nanotechnology*, vol. 21, no. 6, Article ID 065101, 2010.
- [94] A. A. Bhirde, V. Patel, J. Gavard et al., "Targeted killing of cancer cells *in vivo* and *in vitro* with EGF-directed carbon nanotube-based drug delivery," *ACS Nano*, vol. 3, no. 2, pp. 307–316, 2009.
- [95] E. Heister, V. Neves, C. Tilmaciu et al., "Triple functionalisation of single-walled carbon nanotubes with doxorubicin, a monoclonal antibody, and a fluorescent marker for targeted cancer therapy," *Carbon*, vol. 47, no. 9, pp. 2152–2160, 2009.
- [96] L. S. Jabr-Milane, L. E. van Vlerken, S. Yadav, and M. M. Amiji, "Multi-functional nanocarriers to overcome tumor drug resistance," *Cancer Treatment Reviews*, vol. 34, no. 7, pp. 592–602, 2008.
- [97] N. Sinha and J. T.-W. Yeow, "Carbon nanotubes for biomedical applications," *IEEE Transactions on Nanobioscience*, vol. 4, no. 2, pp. 180–195, 2005.
- [98] X. Zhang, L. Meng, Q. Lu, Z. Fei, and P. J. Dyson, "Targeted delivery and controlled release of doxorubicin to cancer cells using modified single wall carbon nanotubes," *Biomaterials*, vol. 30, no. 30, pp. 6041–6047, 2009.
- [99] S. B. Field and N. M. Bleehen, "Hyperthermia in the treatment of cancer," *Cancer Treatment Reviews*, vol. 6, no. 2, pp. 63–94, 1979.
- [100] X. Huang, I. H. El-Sayed, W. Qian, and M. A. El-Sayed, "Cancer cell imaging and photothermal therapy in the near-infrared region by using gold nanorods," *Journal of the American Chemical Society*, vol. 128, no. 6, pp. 2115–2120, 2006.
- [101] A. M. Gobin, M. H. Lee, N. J. Halas, W. D. James, R. A. Drezek, and J. L. West, "Near-infrared resonant nanoshells for combined optical imaging and photothermal cancer therapy," *Nano Letters*, vol. 7, no. 7, pp. 1929–1934, 2007.
- [102] Z. Liu and R. Peng, "Inorganic nanomaterials for tumor angiogenesis imaging," *European Journal of Nuclear Medicine and Molecular Imaging*, vol. 37, no. 1, pp. S147–S163, 2010.
- [103] S. Ghosh, S. Dutta, E. Gomes et al., "Increased heating efficiency and selective thermal ablation of malignant tissue with DNA-encased multiwalled carbon nanotubes," *ACS Nano*, vol. 3, no. 9, pp. 2667–2673, 2009.
- [104] R. Marches, P. Chakravarty, I. H. Musselman et al., "Specific thermal ablation of tumor cells using single-walled carbon nanotubes targeted by covalently-coupled monoclonal antibodies," *International Journal of Cancer*, vol. 125, no. 12, pp. 2970–2977, 2009.
- [105] H. Park, J. Yang, J. Lee, S. Haam, I.-H. Choi, and K.-H. Yoo, "Multifunctional nanoparticles for combined doxorubicin and photothermal treatments," *ACS Nano*, vol. 3, no. 10, pp. 2919–2926, 2009.
- [106] N. H. Levi-Polyachenko, E. J. Merkel, B. T. Jones, D. L. Carroll, and J. H. Stewart IV, "Rapid photothermal intracellular drug delivery using multiwalled carbon nanotubes," *Molecular Pharmaceutics*, vol. 6, no. 4, pp. 1092–1099, 2009.
- [107] C. J. Gannon, P. Cherukuri, B. I. Jakobson et al., "Carbon nanotube-enhanced thermal destruction of cancer cells in a noninvasive radiofrequency field," *Cancer*, vol. 110, no. 12, pp. 2654–2665, 2007.
- [108] M. J. O'Connell, S. H. Bachilo, C. B. Huffman et al., "Band gap fluorescence from individual single-walled carbon nanotubes," *Science*, vol. 297, no. 5581, pp. 593–596, 2002.
- [109] S. V. Torti, F. Byrne, O. Whelan et al., "Thermal ablation therapeutics based on CNx multi-walled nanotubes," *International Journal of Nanomedicine*, vol. 2, no. 4, pp. 707–714, 2007.
- [110] P. Chakravarty, R. Marches, N. S. Zimmerman et al., "Thermal ablation of tumor cells with antibody-functionalized single-walled carbon nanotubes," *Proceedings of the National Academy of Sciences of the United States of America*, vol. 105, no. 25, pp. 8697–8702, 2008.
- [111] N. Shao, S. Lu, E. Wickstrom, and B. Panchapakesan, "Integrated molecular targeting of IGF1R and HER2 surface receptors and destruction of breast cancer cells using single wall carbon nanotubes," *Nanotechnology*, vol. 18, no. 31, Article ID 315101, 2007.
- [112] B. Kang, D. Yu, Y. Dai, S. Chang, D. Chen, and Y. Ding, "Cancer-cell targeting and photoacoustic therapy using carbon nanotubes as 'bomb' agents," *Small*, vol. 5, no. 11, pp. 1292–1301, 2009.

- [113] C. Loo, A. Lowery, N. Halas, J. West, and R. Drezek, "Immuno-targeted nanoshells for integrated cancer imaging and therapy," *Nano Letters*, vol. 5, no. 4, pp. 709–711, 2005.
- [114] I. H. El-Sayed, X. Huang, and M. A. El-Sayed, "Selective laser photo-thermal therapy of epithelial carcinoma using anti-EGFR antibody conjugated gold nanoparticles," *Cancer Letters*, vol. 239, no. 1, pp. 129–135, 2006.
- [115] Z. Liu, W. B. Cai, L. N. He et al., "In vivo biodistribution and highly efficient tumour targeting of carbon nanotubes in mice," *Nature Nanotechnology*, vol. 2, no. 1, pp. 47–52, 2007.
- [116] J. Meng, J. Duan, H. Kong et al., "Carbon nanotubes conjugated to tumor lysate protein enhance the efficacy of an antitumor immunotherapy," *Small*, vol. 4, no. 9, pp. 1364–1370, 2008.
- [117] C. H. Villa, T. Dao, I. Ahearn et al., "Single-walled carbon nanotubes deliver peptide antigen into dendritic cells and enhance IgG responses to tumor-associated antigens," *ACS Nano*, vol. 5, no. 7, pp. 5300–5311, 2011.

Research Article

Synthesis of Fluorescent Carbon Dots by Gastrointestinal Fluid Treatment of Mongolia Har Gabur

Tegexibaiyin Wang,¹ Wen Zhang,¹ Xiaofeng Zhang,¹
Xilin Qiqige,¹ Wuhan Qimuge,¹ Aodeng Qimuge,¹ Hairong Wang,¹
Bulin Baila,¹ Alateng Qimuge,¹ Ming Yuan,² and Jun Ai³

¹Pharmacy Laboratory, Inner Mongolia International Mongolian Hospital, 83 Daxuedong Road, Hohhot 010065, China

²Agricultural Nanocenter, School of Life Sciences, Inner Mongolia Agricultural University, 306 Zhaowuda Road, Hohhot 010018, China

³College of Chemistry and Environmental Science, Inner Mongolia Normal University, 81 Zhaowuda Road, Hohhot 010022, China

Correspondence should be addressed to Tegexibaiyin Wang; tegexibaiyin@yeah.net

Received 30 January 2017; Revised 6 April 2017; Accepted 24 April 2017; Published 9 July 2017

Academic Editor: Jian Zhong

Copyright © 2017 Tegexibaiyin Wang et al. This is an open access article distributed under the Creative Commons Attribution License, which permits unrestricted use, distribution, and reproduction in any medium, provided the original work is properly cited.

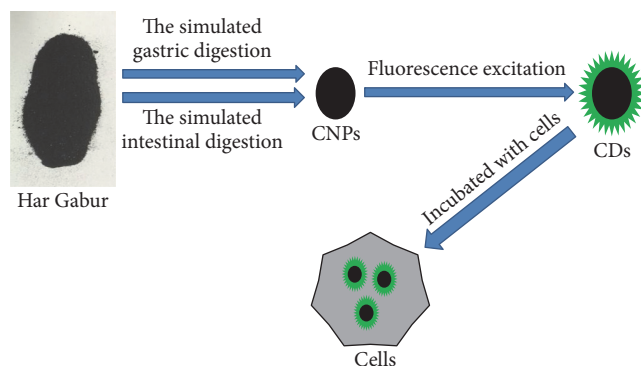
Har Gabur is the carbide obtained from pig manure by burning. The fluorescent carbon dots (CDs) of Har Gabur were successfully synthesized through simulating the digestion process of human gastrointestinal tract. Transmission Electron Microscope (TEM) analysis showed that the average size of the prepared Har Gabur CDs was 4 nm, with good solubility in water and strong fluorescence under UV irradiation. The X-ray and Raman results showed that the Har Gabur CDs were mainly composed of oxygen “O” and carbon “C” elements, in the forms of “C=O” and “C-O.” The bond energy results showed that the nitrogen “N” atom presented as “C-N” form, which indicated that Har Gabur CDs also contain “N.” In photobleaching assay, Har Gabur CDs showed excellent light stability compared with ordinary organic dye, fluorescein, and Rhodamine B. The fluorescence intensity of Har Gabur CDs was fairly stable within a wide pH range of 3–10. When L-lysine and L-cysteine were applied for the passivation stage, the relative quantum yields were improved by 1.53 and 3.68 times, respectively. Finally, the fluorescence properties of Har Gabur CDs were tested in cells and zebrafish, illustrating that Har Gabur CD has potential in the application of biological labeling and imaging.

1. Introduction

As one of the most important natural elements, carbon is not only involved in human body but also found to play critical role in the field of medicine [1]. For instance, the charcoal ash is a typical carbonized traditional Mongolian medicine [2]. As a matter of fact, the carbonized medicine is made up of carbon. The traditional Mongolian medicine applies anaerobic burning of a variety of drugs to get the biological carbon powder. The medicines made by these carbon powders are finally ingested through gastrointestinal tracts to function. Clinically, carbonized traditional Mongolian medicine is used for the treatment of esophageal diseases, gastrointestinal diseases, and tumors due to its significant effect. In recent years, the carbon molecules including

the most famous molecules fullerene, grapheme, and CD have become the topics of innovative scientific research [3, 4].

The CD is also called carbon quantum dot (CQD). It is mainly made up of nanocarbon particles of grapheme quantum dots (GQDs) and CQDs with diameter smaller than 10 nm. The discovery of CDs is mainly through the purification of the single layer nanotube used in early preparative electrophoresis assay and the laser ablation of graphite powder and cement. The diversity of composition and structure of CDs define their different properties. The carboxyl groups on the surface of CDs enable them to have excellent water solubility and biocompatibility. In addition, the physical properties of CDs can be enhanced by chemically modifying the surface structure, for example, by applying a



SCHEME 1: Synthesis scheme of carbon dots derived from Har Gabur.

variety of organic, inorganic, and even biological molecules [5–7].

As an innovative fluorescence nanomaterial, CDs have palmary photoluminescence, chemical inertness, and biocompatibility [8, 9]. Based on the previous studies, CDs would cause no abnormality, damage, and toxicity to tissues, organs, and even genes. Furthermore, the unique optic and biological features of CD give it outstanding advantages and prominent future on the optic imaging, tumor diagnosis, and treatment [2, 8, 10]. There are several kinds of raw materials for CDs, such as ginger, straw, coffee, egg, candle ash, and grapheme [11, 12]. The CDs prepared have been found to have good inhibitory effects on the growth of and antioxidation of hepatocellular carcinoma, lung cancer, breast cancer, and human cervical cancer [2, 13].

The preparation methods of CDs have been developed and summarized into several particular refined methodologies including the synthetic, electrochemical, laser ablation, acid dissolution, and hydrothermal method [14, 15]. In this study, an innovative biological method for CDs preparation has been discussed. This method has a close correlation with the absorption and digestion process of traditional charcoal medicine in human body [16]. In addition, this method could possibly improve the pharmacological effects of CDs [17]. Based on this enzymatic method, the surface of nanostructured CDs is full of organic groups, which enable CDs to have good dispersibility and water solubility [18, 19]. Moreover, the structure of the CDs obtained through this way would benefit the functional modification and biological coupling labeling that allow medicine to have good biocompatibility.

In this study, Har Gabur CD was used for the first time as a raw material for CD preparation due to its characteristics of simple composition and cheap price. In this study, we simulate the digestion process in human body through mixing Har Gabur CDs with biological enzyme *in vitro*. These CDs have better water solubility, fluorescence characteristics, and biocompatibility (Scheme 1). Study on Har Gabur CDs not only has great significance for the preparation method of the fluorescent CDs but also has important research value on understanding the physiological mechanism of Har Gabur CDs. In addition to its foundation build up, it has profound significance on the application of drug delivery and targeting.

2. Materials and Methods

2.1. Materials. Muffle furnace (Beijing Cinit Electric Co., China) and U-3010 UV-visible spectrophotometer (Hitachi, Japan) were applied to the absorption measurement of carbon solution. F-2500 fluorescence spectrophotometer (Hitachi, Japan) was used for measuring fluorescence excitation and emission spectra. Zetasizer Nano (Malvern Instruments Ltd., UK) was applied for carbon hydrate particle size and surface charge determination. X-ray photoelectron spectroscopy ESCALAB 250X (Thermo, USA) was used for the determination of CD composition and C is spectrum. SpectrumGX infrared transform spectroscopy (PerkinElmer, America) and LabRAMHR800 Raman spectrometer (Joe Pingyi Feng company, France) were used to characterize the surface structure and other characteristics of carbon dots; fluorescence lifetime points by FL-TCSPC (fluorescence spectrometer Joe Feng Pingyi company, France) were measured; PHS-3C (Chengdu ark Technical Developing Company, China) was used for the acidity measurement.

2.2. Preparation of CD

2.2.1. Preparation of Gastric Liquid. 0.2 g of NaCl, 0.32 g of pepsin (2330 U/mg prot, Sigma), and 0.7 ml concentrated hydrochloric acid were dissolved in distilled water up to 100 ml after adjusting pH to 1.2.

2.2.2. Preparation of Intestinal Liquid. The intestinal tract liquid was prepared by dissolving 0.68 g of KH_2PO_4 into 25 ml distilled water. NaOH was applied for pH adjustment (pH 7.5) and additional 19 ml distilled water was added. Then, 1 g of trypsin (10010 U/mg prot, Sigma) was added, and NaOH was applied again. Distilled water was added up to 100 ml finally.

2.2.3. Preparation of Fluorescent CD from Har Gabur CD Powder. 1.0 g of Har Gabur CD powder was added to a falcon flask containing prepared simulated gastric acid liquid. The falcon flask was set in the 37°C oil bath pot, allowing magnetic stirring for 12 hrs. Then, the nonreacted substances were collected through centrifugation. The supernatant was transferred into a dialysis bag (USA Viskase MWCO 1000D) and left in distilled water for 2-3 days, by changing the water once in 1 h until the pH reached neutral. After dialysis, the liquid was centrifuged at 1.6×10^2 rpm for 30 min and the supernatant was stored at 4°C . The pellets collected through gastric acid digestion were then recycled for CD particles. They were mixed with distilled water and centrifuged for 10 min at 1.6×10^4 rpm, and this step was repeated twice. The pellets were mixed with the simulated intestinal acid liquid and the flask was left in the oil bath for 12 hrs stirring. After reaction, the supernatant was repeatedly done as the above method, putting into a dialysis bag for dialysis reaction and the final liquid was stored at 4°C .

The collected supernatants from either gastric or intestinal acid liquid treatment were mixed and condensed to 25 ml. Then, the condensed liquid was microwaved for 5 min at

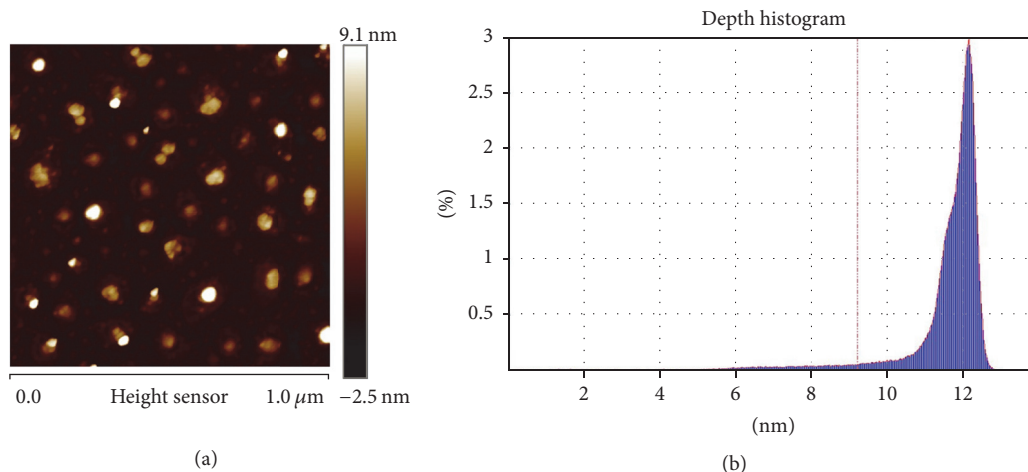


FIGURE 1: Direct acquisition of 3D image of C-dots by atomic force microscopy. (a) The AFM height mode image of C-dots obtained in air, the upper and bottom bars indicate the dots' height and scale, respectively. (b) The AFM cross-sectional analysis of (a). An average hydrodynamic size of 3.6 ± 0.102 nm with a PDI of 0.422 was obtained from the DLS measurement.

50 Hz. The liquid was then freeze dried and the certain amount of distilled water was added to dissolve it. The final CDs were collected through 1 min centrifugation and sent for fluorescence activity detection or stored at 4°C .

2.3. Surface Passivation of CD. 100 ml of prepared CDs liquid (0.5 mg/ml) was mixed with 1 g surface passivation agent (pH 7.25) and sent for ultrasonic treatment for 5 min. The mixture was heated up to 110°C and polylysine (PLL) and cysteine were applied for CDs surface passivation through removal of extra polylysine (PLL) and cysteine and keeping molecules of 500 Da inside of dialysis bag. Passivation using PLL was achieved through filtration. Passivation based on chitosan was also done by filtration and the extra chitosan was removed by precipitation in ethanol.

2.4. Characterizations. Transmission electron microscopy (TEM) was performed using a FEI Tecnai G²Spirit at an acceleration voltage of 120 kV. Nano-ZS90 Zetasizer (Malvern Instruments, Malvern, UK) was used to determine the zeta potential. Absorption and fluorescence spectra were recorded at room temperature on UV-2550 UV-Vis spectrophotometry (Shimadzu, Japan) and Luminescence Spectrometer 55 (PerkinElmer), respectively. XPS spectra were used to characterize the chemical composition using an Escalab 250 Xi X-ray photoelectron spectrometer (Thermo Scientific).

2.5. Fluorescence Quantum Yield Measurements. The fluorescence quantum yield was measured and calculated based on previous studies [19, 20]. $\Phi_x = \Phi_{\text{std}} I_x A_{\text{std}} \eta_x^2 / I_{\text{std}} A_x \eta_{\text{std}}^2$ was applied and I_x and I_{std} were the fluorescence strength of CDs and control. A_x and A_{std} were the optical density of CDs and control. The absorbencies of all the samples in 1.0 cm cuvette were kept under 0.1 at the excitation wavelength to minimize reabsorption effects.

2.6. Cell Experiments. HepG2 cells were inoculated in 24-well culture plate (1000 cells/well). After 12 h, 1 mg/ml of prepared CDs was added to cells and cells were cultivated for extra 2 h. PBS was applied to wash cells and formalin was used for cell fixing. Cell imaging was performed through Nikon Ti-U inverted fluorescence microscope, and the excitation wavelengths were 380–420 nm and 450–490 nm for blue and green color, respectively [21, 22].

2.7. Ex Vivo Zebrafish Experiment. Zebrafish was raised in a standardized light cycled system with a cycle of 14 h light and 10 h dark at 28°C . The imaging system for zebrafish was performed using Cri Maestro. The adult fish was cultivated into a water system with CDs (5 mg/ml) for 10 min and washed with distilled water for imaging.

3. Results and Discussion

3.1. Size and Zeta Potential. The 3D image of CDs was obtained by atomic force microscopy (Atomic Force, AFM) (Figure 1(a)). An average hydrodynamic size of 3.6 ± 0.102 nm with a PDI of 0.422 was obtained from the Dynamic Light Scattering (DLS) measurement. By contrast, the cross-sectional analysis of the AFM image performed in air revealed a typical topographic height of approximately 1.40 nm, which is less than that found by the DLS results, because of the AFM imaging mode in air. According to the analysis of the image, we can get the three-dimensional size of the particle (Figure 1(b)). The CDs were evaluated by DLS and atomic force microscopy image analysis for the first time in our study.

3.2. Optical Property. UV-Vis absorption and photoluminescence (PL) emission spectra for CDs were examined. Figure 2(a) shows the detection of CDs surface passivation applying UC spectroscopy and photoluminescence spectroscopy. Fluorescence image of the CD labeled image, its control,

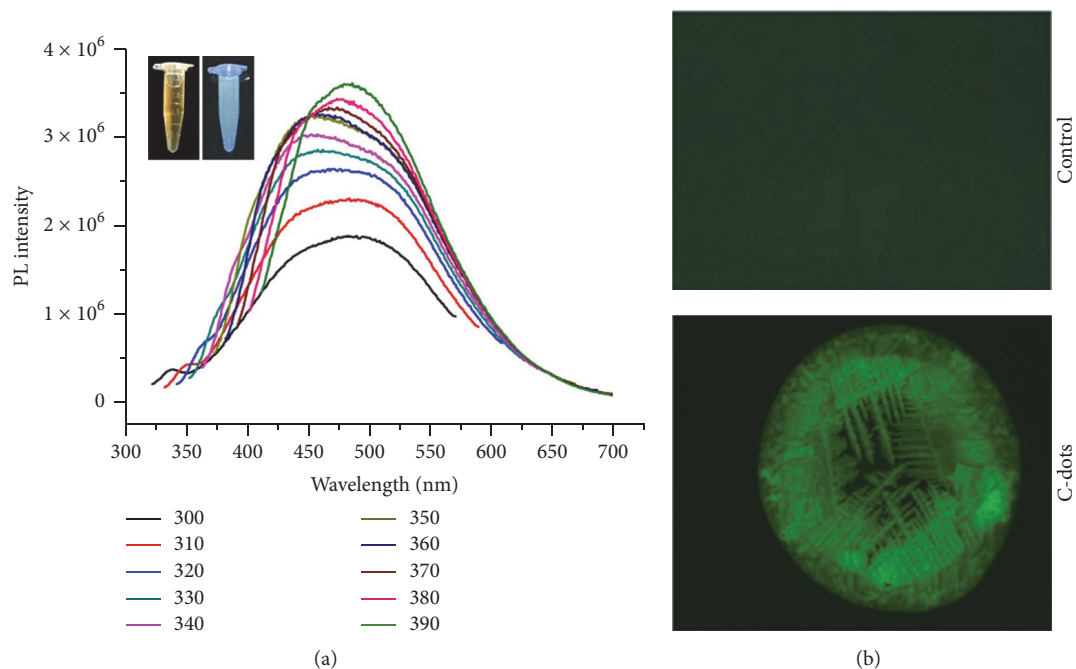


FIGURE 2: UV-Vis absorption and photoluminescence (PL) emission spectra for C-dots. (a): photograph of the C-dots excited by a UV lamp (365 nm). PL emission spectra (excitation wavelength from 325 nm to 445 nm in 20 nm increments). (b) Fluorescence image of the C-dot labeled image, its control, and bare C-dots measured with fluorescence microscope imaging system.

and bare CDs were measured with fluorescence microscope imaging system (Figure 2(b)). The one with applying UV spec did not show obvious peaks, which are consistent with the commercial CDs. CQDs corresponding emissions covering the ultraviolet wavelength range from ultraviolet (~ 430 nm) yellow to green (~ 550 nm). The position of CDs emission shifts from the peak to longer wavelength and the intensity increases with the gradually decreased excitation wavelength. By selecting quinine sulfate in $0.1\text{ M H}_2\text{SO}_4$ as the standard, the measured relative fluorescence quantum yield (QY) of the bare CDs was 0.72%. This value was equal to the value of the carbon point from the candle soot and was greater than the value of the CDs from the soot of the natural gas. The luminescence mechanism of CDs is still not clearly understood, and the proposed reason may be radiative recombination. The green luminescence of CDs can be attributed to the surface energy trap, and the blue emission of CDs can be attributed to the Z locus, because of the graphene molecules embedded in the CDs.

3.3. Structure and Constituents. In order to obtain detailed structural and compositional information on the prepared carbon points, we also measured their X-ray diffraction (XRD) and X-ray photoelectron spectroscopy (XPS). XRD data showed that our CDs were amorphous, similar to that reported in other reports. As the wide spectrum XPS scanning shown in Figure 3, 284.74 represents SP2 hybrid graphite. The 288.09 and 286.25 represent “C=O” and “C-O” bonds, which are the two representatives of graphene oxide structure (Figure 3(b)). The samples mainly contain “C” and “O” elements (Figure 3(a)). Linking this result with “CIs”

peak analysis, the samples were composed of graphene and graphene oxide (GO). According to the binding energy, the “N” atom presented in the form of “C-N.” Our result proved that the graphite in the sample contains some nitrogen doped graphene (NG). According to the binding energy, the “Si” atom presented in the form of “Si-O” bond, while “P” and “Na” existed in the form of NaH_2PO_4 (Figure 3(b)).

Three strong peaks at 285.4, 400, and 532.5 eV were attributed to oxygen, nitrogen, and carbon. Therefore, the main elements of the prepared CQDs are “C” (60.8%), “O” (25%), and “N” (7.2%) (see Table 1). CIs spectrum (Figure 3(b)) shows three peaks at 284.9, 286, and 288.9 eV, which were attributed to “C-C,” “C=O,” and “C-N.” XPS and Raman spectra showed that the “O” and “C” elements were the main elements in the sample. The “O/C” atoms were in “C=O” and “C-O” forms, which are two representative graphene oxide (GO) structures (Figure 3(c)).

3.4. Cell Imaging. The potential applications of the fluorescent CDs derived from plant soot were evaluated in HepG2 cells imaging. The HepG2 cells incubated with PLL-passivated CDs in Figure 4 become bright when existing at the wavelength of 450–490 nm. This indicates that PLL passivation of HepG2 can be labeled CDs cells in a simple incubator. In addition, no quenching effect was observed in the continuous excitation of cell imaging in 15 minutes.

3.5. Ex Vivo Zebrafish Imaging. For organism imaging, we chose a small guppy, which is one of the vertebrates which can be used in Maestro imaging system to observe the

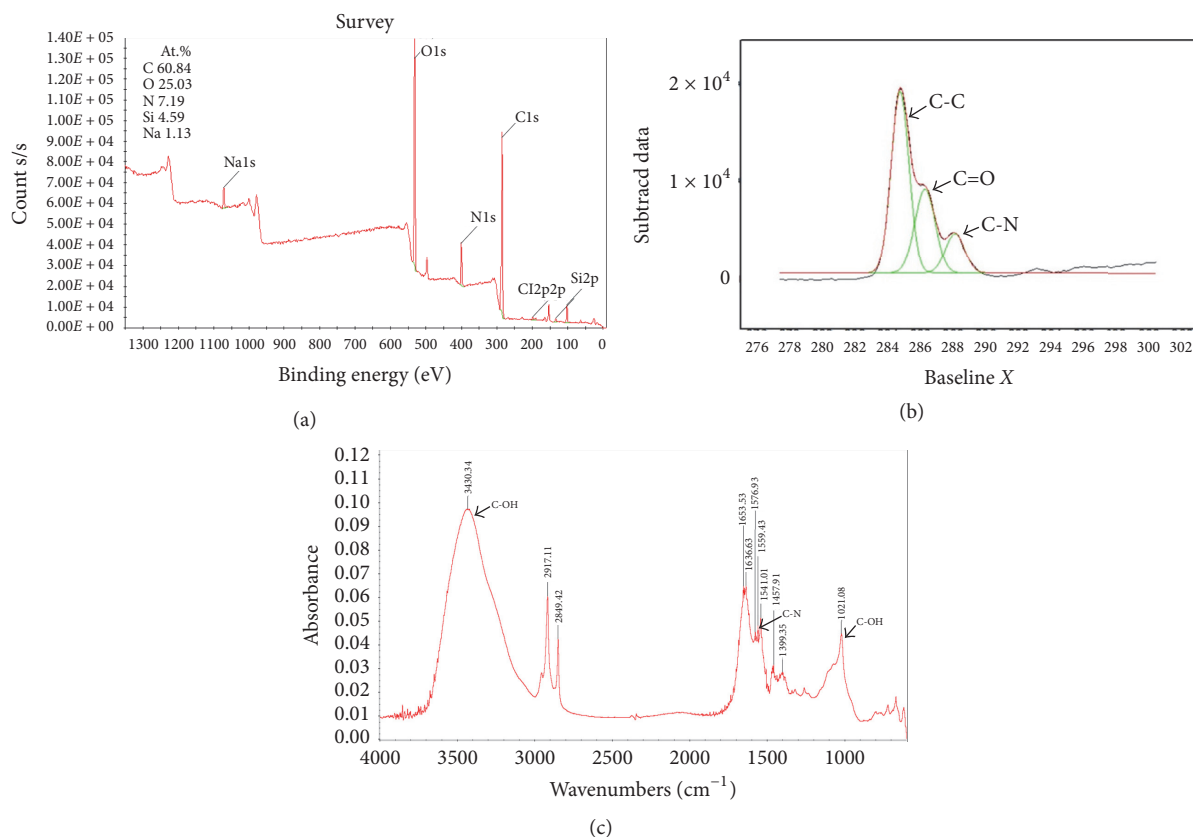


FIGURE 3: XPS and FTIR spectra and zeta potential. (a) The element detection. (b) XPS C1s spectrum. (c) FTIR spectra of as-prepared C-dots.

TABLE 1: X-ray photoelectron spectroscopy (XPS) spectra of the C-dots.

Name	Start BE	Peak BE	End BE	Height	CPS area (P)	CPS.eV	Atomic %
C1s	2.9×10^2	2.8×10^2	2.8×10^2	8.4×10^4	3.5×10^5		60.8
O1s	5.4×10^2	5.3×10^2	5.2×10^2	1.0×10^5	3.6×10^5		25.0
N1s	4	4×10^2	3.9×10^2	1.9×10^4	6.5×10^4		7.2
Si2p	1.1×10^2	1×10^2	0.9×10^2	8×10^3	2.5×10^4		4.6
Na1s	1.1×10^3	1.1×10^3	1.1×10^2	9.8×10^3	3.8×10^4		1.1
Cl2p	2×10^2	2×10^2	1.9×10^2	1.4×10^3	7.8×10^3		0.5
P2p	1.4×10^2	1.3×10^2	1.3×10^2	1.7×10^3	6×10^3		0.7
C1s	3×10^2	2.8×10^2	2.8×10^2	2×10^4	5×10^4		0

fluorescence signal. As shown in Figure 5, the CD labeled zebrafish clearly showed enhanced luminescence compared with its control. Fluorescence spectra analysis confirmed that the fluorescence signal came from the passivation of CDs in zebrafish. This result indicates that the passivation of CDs may have potential for imaging of vertebrate animals.

4. Conclusions

In conclusion, through simulating human gastrointestinal absorption digestion process, we successfully synthesized highly fluorescence and biological activated carbon using gastric and intestinal juice to simply process traditional carbon black borneol. These CDs show multicolor fluorescence, excellent light stability, and their suitability used in various

pH conditions. The black synthetic borneol, the dry stool carbonization of wild boars belonging to pig families, is one of the typical carbonized Mongolian medicines with the effects of invigorating the stomach and promoting the digestion and so forth. The black synthetic borneol also named Har Gabur in Mongolian is the most distinctive carbon herbs for the treatment of gastrointestinal diseases and can be mixed with other drugs used in a variety of formulations. So far, a lot of black borneol function was not clear. It needs more in-depth study and exploration.

Through the literature research we found that the current researchers have developed a variety of preparation methods of CDs, such as synthetic method, electrochemical method, laser ablation method, acid dissolution method, and hydrothermal method, in which CDs are synthesized

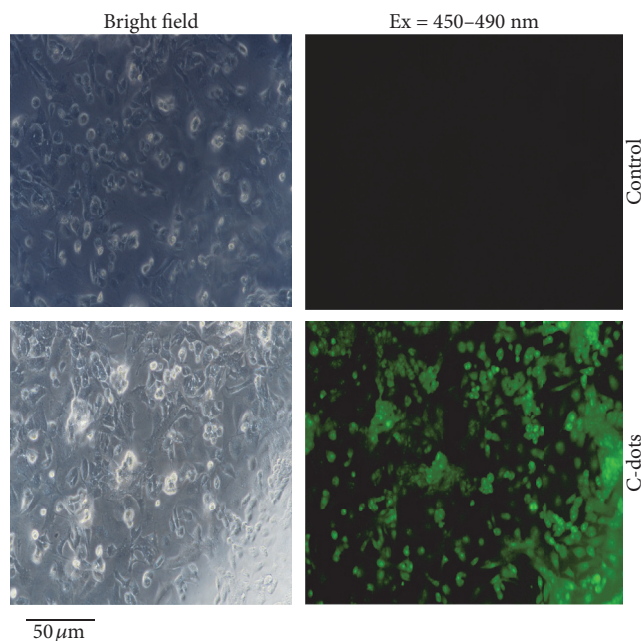


FIGURE 4: Bright filed and fluorescence microphotographs of HepG2 cells incubated with PLL-passivated C-dots (C-dots) and without C-dots (Control) with an excitation filter of 450–490 nm for green color, respectively.

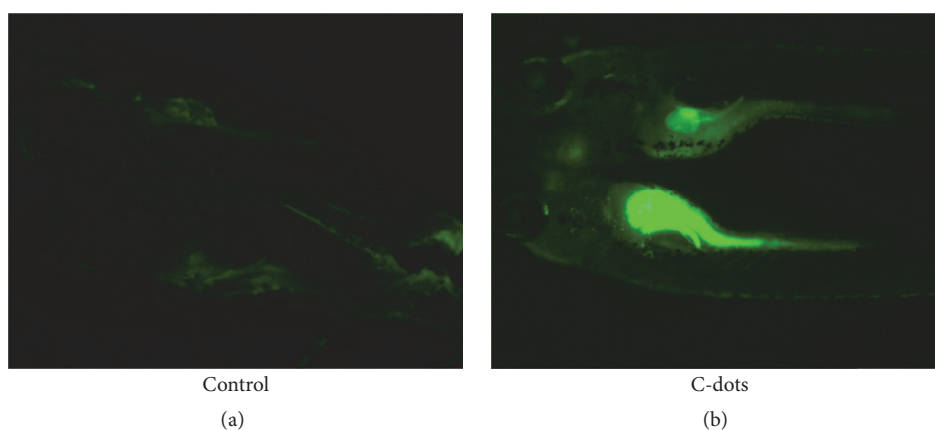


FIGURE 5: *Ex vivo* zebrafish imaging. Photograph of the C-dot labeled zebrafish (C-dots) and its control (control) (a) and fluorescence image (b) of the C-dot labeled zebrafish, its control, and bare C-dots measured with fluorescence microscope imaging system. Fluorescence spectra comparison of the C-dots and their control.

using physical and chemical methods at the great costs of labor force and money. However, an important preparation method, enzyme digestion method, has not yet been applied to the preparation of CDs. More importantly, there is close relationship between this method and traditional medicine digestion in the human body and carbon absorption in the human body. Thus prepared CDs completely dissolve in the human body without any security risks and even do good to improve immunity and have other health effects.

In enzyme digestion method, Har Gabur was processed by intestinal fluid to prepare CDs. Following the heat treatment in 37°C water, pepsin or trypsin will first attack the defect area of the surface of the carbon particles, “cutting”

or “dividing” those carbon particles, forming the smaller size quantum dots, ice sheet fluorescent CDs.

The surface of ice sheet fluorescent CDs prepared by such method is rich in amino functional organic groups, which makes it not only have good dispersibility, water solubility, easy functionalization, and biological coupling markers but also have good biocompatibility. We will model ice sheet fluorescent nano-CDs to explore the relationship between chemical properties and biological properties of nanomaterials in the field of cells. Choosing the most suitable carbon for preparation and biological safety detection is also our next plan. It will help to carry out the new fluorescent nanomaterials development and application of optical imaging studies. Ice sheet fluorescent CDs provide

valuable information for optical imaging in tumor diagnosis, especially early diagnosis and imaging research.

Conflicts of Interest

The authors declare that they have no conflicts of interest.

Authors' Contributions

Jun Ai provided technical support.

Acknowledgments

This work was supported by the project “The Innovative Research Team of the New Drug Research and the Industrialization of Mongolian Medicine” of “Prairie Talents” Engineering, no. NEI ZU TONG ZI[2015]56, and the Program of Hospital Project of Inner Mongolia International Mongolian Hospital (Grant no. 2016YJS22).

References

- [1] M. Tan, L. Zhang, R. Tang et al., “Enhanced photoluminescence and characterization of multicolor carbon dots using plant soot as a carbon source,” *Talanta*, vol. 115, pp. 950–956, 2013.
- [2] C.-L. Li, C.-M. Ou, C.-C. Huang et al., “Carbon dots prepared from ginger exhibiting efficient inhibition of human hepatocellular carcinoma cells,” *Journal of Materials Chemistry B*, vol. 2, no. 28, pp. 4564–4571, 2014.
- [3] H. Wang, C. Sun, X. Chen et al., “Excitation wavelength independent visible color emission of carbon dots,” *Nanoscale*, vol. 9, no. 5, pp. 1909–1915, 2017.
- [4] K. Yang, S. Wang, Y. Wang, H. Miao, and X. Yang, “Dual-channel probe of carbon dots cooperating with gold nanoclusters employed for assaying multiple targets,” *Biosensors and Bioelectronics*, vol. 91, no. 15, pp. 566–573, 2017.
- [5] Y. Yeon, M. Y. Lee, S. Y. Kim et al., “Production of quasi-2D graphene nanosheets through the solvent exfoliation of pitch-based carbon fiber,” *Nanotechnology*, vol. 26, no. 37, Article ID 375602, 2015.
- [6] Q. Wang, C. Zhang, G. Shen, H. Liu, H. Fu, and D. Cui, “Fluorescent carbon dots as an efficient siRNA nanocarrier for its interference therapy in gastric cancer cells,” *Journal of Nanobiotechnology*, vol. 12, no. 1, article 58, 2014.
- [7] H. Liu, Q. Wang, G. Shen et al., “A multifunctional ribonuclease A-conjugated carbon dot cluster nanosystem for synchronous cancer imaging and therapy,” *Nanoscale Research Letters*, vol. 9, no. 1, pp. 1–11, 2014.
- [8] X. Yang, Y. Wang, X. Shen et al., “One-step synthesis of photoluminescent carbon dots with excitation-independent emission for selective bioimaging and gene delivery,” *Journal of Colloid and Interface Science*, vol. 492, pp. 1–7, 2017.
- [9] P. Namdari, B. Negahdari, and A. Eatemadi, “Synthesis, properties and biomedical applications of carbon-based quantum dots: an updated review,” *Biomedicine & Pharmacotherapy*, vol. 87, pp. 209–222, 2017.
- [10] A. S. Minin, A. V. Belousova, L. T. Smolyuk, M. V. Ulitko, M. A. Uimin, and I. V. Byzov, “Interactions of bimodal magnetic and fluorescent nanoparticles based on carbon quantum dots and iron-carbon nanocomposites with cell cultures,” *Bulletin of Experimental Biology and Medicine*, vol. 162, no. 2, pp. 248–251, 2016.
- [11] J. Wang, C.-F. Wang, and S. Chen, “Amphiphilic egg-derived carbon dots: rapid plasma fabrication, pyrolysis process, and multicolor printing patterns,” *Angewandte Chemie—International Edition*, vol. 51, no. 37, pp. 9297–9301, 2012.
- [12] J. Fan and P. K. Chu, “Group IV nanoparticles: Synthesis, properties, and biological applications,” *Small*, vol. 6, no. 19, pp. 2080–2098, 2010.
- [13] W. Li, Z. Zhang, B. Kong et al., “Simple and green synthesis of nitrogen-doped photoluminescent carbonaceous nanospheres for bioimaging,” *Angewandte Chemie - International Edition*, vol. 52, no. 31, pp. 8151–8155, 2013.
- [14] H. Liu, T. Ye, and C. Mao, “Fluorescent carbon nanoparticles derived from candle soot,” *Angewandte Chemie International Edition*, vol. 46, no. 34, pp. 6473–6475, 2007.
- [15] C. Wan, Z. Bao, L. Que, N. Song, and Z. G. Tang, “The effect of piper longum. L on blood pressure and body weight in insulin resistance syndrome rats,” *Journal of Medicine & Pharmacy of Chinese Minorities*, vol. 5, no. 5, pp. 23–26, 2009.
- [16] M. Yuan, R. Zhong, H. Gao et al., “One-step, green, and economic synthesis of water-soluble photoluminescent carbon dots by hydrothermal treatment of wheat straw, and their bio-applications in labeling, imaging, and sensing,” *Applied Surface Science*, vol. 355, pp. 1136–1144, 2015.
- [17] J. Ai, J. Li, L. Ga, G. Yun, L. Xu, and E. Wang, “G-quadruplex/protoporphyrin IX-functionalized silver nanoconjugates for targeted cancer cell photodynamic therapy,” *RSC Advances*, vol. 6, no. 99, pp. 96942–96945, 2016.
- [18] J. Ai, J. Li, Ga. Lu, GH. Yun, and Li. Xu, “Multifunctional near-infrared fluorescent nanoclusters for simultaneous targeted cancer imaging and photodynamic therapy,” *Sensors Actuators B Chemical*, pp. 222–918, 2015.
- [19] W. Li, W. Zhang, X. Dong et al., “Porous heterogeneous organic photocatalyst prepared by HIPE polymerization for oxidation of sulfides under visible light,” *Journal of Materials Chemistry*, vol. 22, no. 34, pp. 17445–17448, 2012.
- [20] W. Li, L. Li, H. Xiao et al., “Iodo-BODIPY: A visible-light-driven, highly efficient and photostable metal-free organic photocatalyst,” *RSC Advances*, vol. 3, no. 32, pp. 13417–13421, 2013.
- [21] W. Li, M. Jiang, Y. Cao et al., “Turning ineffective transplatin into a highly potent anticancer drug via a prodrug strategy for drug delivery and inhibiting cisplatin drug resistance,” *Bioconjugate Chemistry*, vol. 27, no. 8, pp. 1802–1806, 2016.
- [22] R. Du, H. Xiao, G. Guo et al., “Nanoparticle delivery of photosensitive Pt(IV) drugs for circumventing cisplatin cellular pathway and on-demand drug release,” *Colloids and Surfaces B: Biointerfaces*, vol. 123, pp. 734–741, 2014.

Review Article

Application of Nanomaterials in Stem Cell Regenerative Medicine of Orthopedic Surgery

Su Pan,^{1,2} Hongmei Yu,³ Xiaoyu Yang,¹ Xiaohong Yang,² Yan Wang,³
Qinyi Liu,¹ Liliang Jin,⁴ and Yudan Yang^{3,5}

¹Department of Orthopedics, The Second Hospital of Jilin University, Changchun, Jilin, China

²Jilin University School of Pharmaceutical Sciences, Changchun, Jilin, China

³China-Japan Union Hospital of Jilin University, Changchun, Jilin, China

⁴Department of Pathobiological Sciences, Louisiana State University, Baton Rouge, LA, USA

⁵State Key Laboratory on Integrated Optoelectronics, College of Electronic Science and Engineering, Jilin University, Changchun, Jilin, China

Correspondence should be addressed to Yudan Yang; yangyudan@jlu.edu.cn

Received 27 January 2017; Accepted 8 March 2017; Published 6 July 2017

Academic Editor: Jian Zhong

Copyright © 2017 Su Pan et al. This is an open access article distributed under the Creative Commons Attribution License, which permits unrestricted use, distribution, and reproduction in any medium, provided the original work is properly cited.

Regenerative medicine aims to achieve functional rehabilitation of tissue or cells injured through wound, disease, or aging. Recent findings suggest that nanotechnology provides advanced biomaterials with specified morphologies which can create a nanoscale extracellular environment capable of promoting the adhesion and proliferation of stem cells and accelerating stem cell differentiation in a controlled manner in tissue engineering. This review summarizes the biological effects of nanomaterials and their regenerative medicine applications in orthopedic surgery research, including bone, cartilage, tendons, and nerve tissue engineering.

1. Introduction

Stem cell is a special class of cells which can self-renew and differentiate into specific types of functional cell (such as cardiac cells, pancreatic islet cells, and nerve cells), and then these cells are transplanted into the patient to replace damaged tissue, and it is the basic principle of regenerative medicine. Stem cells and regenerative medicine is a new biomedical field in recent years with significantly clinical value, which promotes wound healing of body and can be used in treatment of disease through stem cell transplantation, differentiation, and tissue regeneration. With more and more trauma and increasing aging population, an incremental number of orthopedic procedures are performed with orthopedic implants annually. However, there are many complications for traditional orthopedic implants, such as infection, poor host tissue conformity, and implant loosening resulting in treatment failure.

Nowadays, nanotechnology and nanomaterials are heavily employed in various biomedical fields [1–11]. Among

them, regeneration therapy using stem cells and nanometer technology both belong to the latest conduits of biotechnological research. One of the main objectives for a successful implementation of regenerative medicine treatment is to control the preservation and proliferation of stem cells and to accelerate their differentiation in a managed manner. The development of nanometer technology has provided an access for unambiguous comprehension of stem cell therapy in vivo by mimicking the environments of extracellular matrix in the culture, and nanotechnology seems to adapt a great possibility in providing new outlook for stem cell research. Nanotechnology carries in its innovation of dynamic three-dimensional nanoenvironments or nanoscaffolds with patterned nanomorphologies and different bioactive molecular substrates for preservation, proliferation, and differentiation of stem cells required for advancement of tissue engineering. Novel regenerative medicine methods combine different scaffold biomaterials with stem cells to provide biological implant or substitutes that can repair and eventually improve tissue functions.

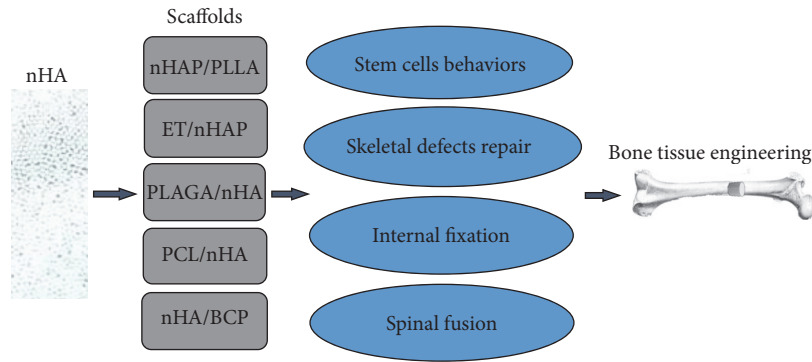


FIGURE 1: The application of nHA scaffolds in bone tissue engineering.

This review will discuss the biological effects of nanomaterials and their regenerative medicine applications in orthopedic surgery research, including bone, cartilage, tendons tissue, and nerve tissue engineering.

2. Bone Tissue Engineering

Currently, bone compositions fabricated according to the fundamental of tissue engineering are being regarded as an ideal selection for the functional restoration of segmental deossification. Biomaterials used for bone tissue engineering include nanohydroxyapatite, titanium, calcium phosphate, graphene oxide, carbon nanotubes, or the compound of them [12–14]. The surfaces or three-dimensional nanostructures of implant which better mimic the naturalistic environments of bone extracellular matrix in the culture, naturally nanocompound tissue, can promote the osteogenic differentiation of stem cell which is important for bone tissue engineering.

2.1. Nanohydroxyapatite. Hydroxyapatite is the principal inorganic mineral component of animal and human teeth and bones which is difficult to be dissolved in a solution and to be utilized in various applications. If nanometer size hydroxyapatite (nHA) particles can be made, it will exhibit a range of unique properties (Figure 1).

2.1.1. Effect on Biological Behavior of Stem Cells. Three different shapes of nHAP/PLLA scaffolds were prepared, such as needle structure, spherical structure, and rod structure, on which passaged-3 rat MSCs were cultured in three-dimensional scaffolds, and it was demonstrated that needle nHAP/PLLA scaffolds appeared to provide the most proportionate environment for bone regeneration using MSCs. It was demonstrated that a novelly fabricated eri-tasar silk fibroin nanofibrous scaffold (ET) scaffold hybridized with nHA deposition by a surface precipitation method stimulated osteogenic differentiation in the absence of any growth factors due to the improved properties of it in physical chemistry and biology. It may offer effectual and profitable biomaterials for bone tissue engineering in orthopedic surgery by promoting stem cell differentiation on ET/nHAP scaffold without any growth factor additive in stem cell culture [15]. A fibrous structure and synergistic action of collagen and nHA with

high molecular weight poly-L-lactide (PLLA) played a crucial role in stimulating human mesenchymal stem cells (hMSCs) differentiation towards osteogenic lineages, indicating its possibility for bone defect repair based on stem cell therapies [16].

Conventional biphasic calcium phosphate (BCP) ceramics with porous structure, displaying superior bone conduction and biocompatibility without intrinsically osteoinductive, were coated with nHA due to supernal osteoinductive potentiality of it. The new nHA coating BCP scaffolds were demonstrated to be more suitable for the adhesion and proliferation of stem cell and MSCs osteogenic differentiation as compared with the conventional BCP scaffolds, indicating the property of nHA conducive for osteoinduction making this scaffolds more adaptive for applications in bone regeneration [17]. The proliferation, osteogenic phenotypic markers expression, and mineral deposition were elevated when hMSCs were seeded on a new three-dimensional, porous poly (D,L-lactide-co-glycolide) (PLAGA)/nHA scaffold suitable for high-aspect ratio vessel (HARV) bioreactor applications, and the degradation pattern of the scaffold was not altered by nHA incorporation and maintained its mechanical integrity for 6 weeks in the dynamic culture environment, which can be used as a potential tissue engineering matrix allowing for the generation of bone tissue [18]. Upon culturing hMSCs on a bioactive nanofiber scaffold made of poly-caprolactone (PCL) and nHA, it was demonstrated that the mineral phase existence increased alkaline phosphatase (ALP) activity and mRNA expression levels of genes related to osteoblast without any osteogenous composition, and it was suggested that the architecture of this novel nanofibrous scaffolds and its chemical constituent could regulate hMSCs osteogenic differentiation [19]. In conclusion, nanofibrous scaffolds composed of nHA manufactured to different shape or hybridized with various nanomaterials will have favourable effect on biological behavior of stem cells and then enhance osteoinductive potential of it by some molecular biology mechanism.

2.1.2. Skeletal Defects Repair. Successful clinical repair of nonhealing bone defects relies on artificial bone with robust efficiency of osteoinduction and outstanding biomechanical stability. Allogenic BMSCs seeded on the nHA/polyamide

6 (nHA/PA6) composite scaffolds used as porous matrices were implanted in the 8 mm diameter calvarial defect of rats, and this showed good biocompatibility and osteoinduction which enhanced bone inductivity at the initial stage after implantation [20]. A composite scaffold composed of nHA-type I collagen beads, BMSCs, and platelet rich plasma (PRP) enhanced significantly the new bone formation which could generate transplants with effectively meliorative bone tissue reorganization promising skeletal defects restoration [21]. It was used to repair successfully the nodulated skeletal defectiveness by eight weeks after operation of novel nHA/collagen/PLLA/chitin fibers (nHACP/CF) scaffolds with goat bone mesenchymal stem cells (BMSCs) cultured and autograft bone. Furthermore, the results revealed that the level of ALP and DNA in goat BMSCs cultured on it was markedly increased. It was demonstrated that this novel scaffold could be a proper graft for bone defects repair [22]. In conclusion, in cases of large bone defects resulting from trauma, infection, tumors, osteomyelitis surgical debridement, and a variety of congenital diseases, tissue-engineered structures may provide alternatives to traditional bone substitute by culturing autogeneic stem cells of patients with nHA composite scaffolds in culture system.

2.1.3. Internal Fixation. Bone plate set and screws for bone fractures therapy by internal fixation methods showed excellent biocompatibility and biomechanical properties. The nHA/polyamide 66/glass fiber compound with good biocompatibility and biomechanical properties was demonstrated to enhance the attachment and proliferation of MSCs without any negative effect on the mineralization of matrix and MSCs osteogenesis. This new compound might be used for operations by internal fixation [23].

2.1.4. Spinal Fusion. Spinal fusion surgery performed with an autologous osseous graft obtained from the crest of ilium is a conventional treatment in therapy spondylolisthesis in children or lumbago derived from intervertebral discs degeneration. However, the procedure is foregone to have several shortcomings, such as nearthrosis, ache, or the adverse reactions of blood transfusion. It has been demonstrated that a novel graft material comprised of a new matrix of mineralized collagen and nHA integrated with autogeneic adipose-derived mesenchymal stem cells (ADMSCs) had effective impact on rabbit posterolateral spinal fusion [24].

In conclusion, nanohydroxyapatite scaffold has both nanomaterials properties and good biocompatibility which render it a very broad application prospect in bone regenerative medicine, including the regulation of stem cell biological behavior (such as proliferation and differentiation), the improvement of bone tissue regeneration promising skeletal defects repair, internal fixation surgery, and spinal fusion in orthopedic surgery.

2.2. Ti. Osteogenic cells belong to anchorage-dependent cells in which the increase of adhesion and cytoskeleton changes in early stage is imperative to stimulate osteogenesis and to accomplish a more expedient osseointegration of

implant materials surfaces in vivo. Metallic implant materials including titanium and its alloys are conventionally used in orthopedic applications due to their superior mechanical functions and biological unreactiveness.

2.2.1. Effect of Topography and Measurement. It was presumed that the original progenitor cells morphology on the nanoscale surface topography might have effect on the succedent stem cell functions [25].

Stem cells were cultured onto titanium discs with different structures, such as sandblasted, sandblasted and large-grit acid etched, and full contact coverage (FCC). The results showed that the FCC titanium surface on which osteoblast-like cells matured most rapidly might have a crucial effect on the primeval phase of bone union course [26]. Different micro- and nanostructure of a new nanosized oxidized titanium graft enhanced the adhesion and osteogenic differentiation of BMSC plated onto the oxidative surfaces which exhibited a greater tanglesome micro- and nanosized structures and had increased levels of coarseness parameters contrasting to the convention alone [27]. Titanium surface features were controlled as subnano-, nano-, and submicron scales which could activate integrin-ligand proteins interactions, and then the results showed that osteoblast differentiation of primary mouse BMSC was accelerated significantly only on the surface of titanium with nano- and submicron hybrid after 2 weeks. Furthermore rapid cytoskeletal reorganization of BMSC on the transparent surface of titanium with nanoscale was demonstrated, which definitively induced increased genes expression level of osteoblast dominant form after three weeks [28]. It was observed that oxidized titanium nanotubes with a diameter of 70 nm was the optimal dimension for the osteogenic differentiation in adipose-derived stem cells of human (hASCs). Furthermore the results revealed that the nanotopography of oxidized titanium nanotubes directs stem destiny by upregulating methylation level of histone H3 at lysine 4 in the promoter regions of osteogenic genes Runx2 and osteocalcin, by inhibiting demethylase retinoblastoma binding protein [15, 29].

2.2.2. Titanium Surfaces Modification. Human bone ECM is comprised of collagen nanofibers and nanostructured hydroxyapatite particles in nanometer dimension improving cells growth in its nanofibrous porous structure, so the biomimetic and bioactive titanium surface with nanostructured coating might control stem cell adhesion and osseointegration (Figure 2). It was demonstrated that the adhesion and proliferation of osteoblast and MSCs were enhanced on titanium treated with nHA/carbon nanotubes [30]. The stem cells cultured on titanium nanostructure coated with ECM components exhibited faster osteoblastic differentiation and more efficient deposition of mineralized matrix as compared with uncoated structure. Heatedly oxidative Ti-6Al-4V coating with biomimetic chitosan/alginate film containing nanoscale silver particles enhanced significantly the morphology, viability, and proliferation of BMSC. Furthermore, the composite film restrained the multiplication of *Escherichia coli* and *Staphylococcus aureus* and upregulated significantly the expression of ALP [31].

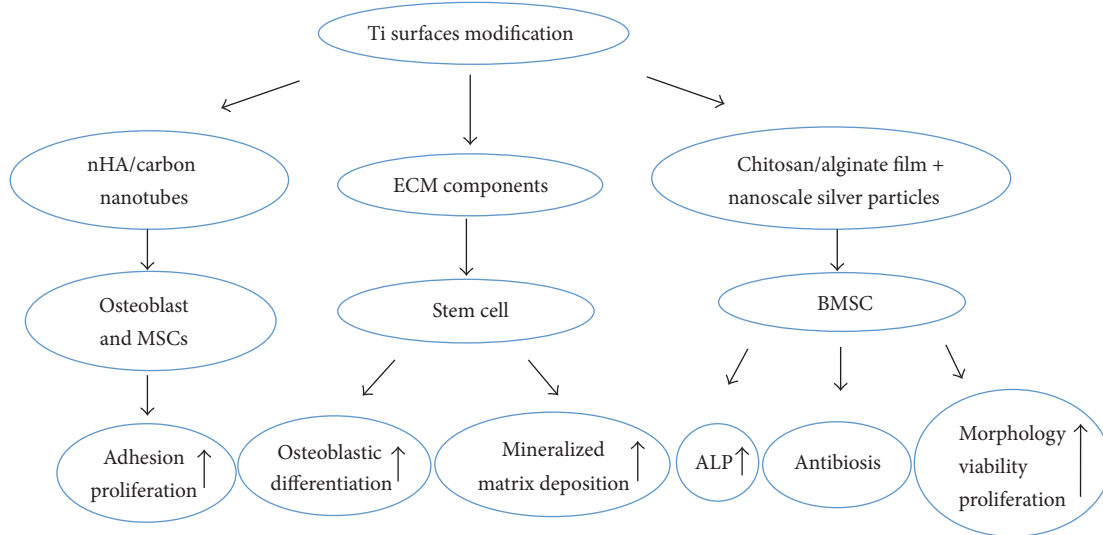


FIGURE 2: The effect of titanium surfaces modification on stem cell.

Overall, these studies present a towardly stratagem to improve biocompatibility and potential of these novel nanostructured materials for orthopedic applications.

2.3. Calcium Phosphate. Nanostructured calcium phosphate (CaP) biomaterials/scaffolds are of particular interest to meet the increasing need for osteoanagenesis, because they share chemical/crystallographic analogies to inorganic components of bone. It was demonstrated that the MSCs proliferation was enhanced when cultured on the nanosized three methods-biomimetic discs coated with CaP as compared with the uncoated or galvano-chemically coated structures [32]. Novel porous Cap-Ti6Al4V (Cap-Ti) hybrids with conspicuous physical and chemical properties regulated the propagation, osteogenous differentiation, and matrix mineralization of human periosteum derived cells (hPDCs), such as regulating osteoclast formation by CaP coating absorption of hPDCs, decreasing gene expression level of osteoprotegerin, and promoting multinucleated giant cells aggregation near to the Cap-Ti hybrids surface. Furthermore, Cap-Ti compound induced heterotopic bone formation during hypodermic implantation by a manner depending on cell density [33].

Calcium phosphate cement (CPC) possesses superior osteoconductivity and it is easy to be assimilated or replaced by regenerative bone tissue, so CPC is suitable to be injected in bone defect position to form powered supports. It was demonstrated that umbilical cord mesenchymal stem cells of human (hUCMSCs) attaching to high-strength CPC showed superior propagation or osteogenous differentiation. The results revealed that hUCMSCs transported by CPC might be a probable alternative in orthopedic treatment [34]. However, CPC is limited to non-stress-bearing repairs due to the low strength of it that can be reinforced by chitosan incorporation. It was reported that MSCs differentiated to osteoblasts cell lines and expressed ALP in high level which is a bone marker on the CPC and chitosan scaffolds with increased strength as compared to CPC [35]. Magnesium phosphate

cement (MPC) was combined with CPC to develop novel calcium-magnesium phosphate cement (CMPC) which was implanted into bone defects in rabbits. It was demonstrated that CMPC has a shorter setting time and markedly better mechanical properties than either CPC or MPC. Furthermore, the histological evaluation showed that the introduction of MPC into CPC enhanced the efficiency of new bone formation, and the CMPC also exhibited good biocompatibility, biodegradability, and osteoconductivity with host bone in vivo [35].

2.4. Graphene. Polymeric material composed of graphene is developed for biomedical applications, such as biosensing for the increased electrical conductivity of the graphene composite material. Furthermore, soft biomaterials can be reinforced by graphene incorporated to polymer. Graphene oxide (GO) is a broadly investigated form of grapheme. GO is rich in oxygen, including functional groups, such as epoxide carboxyl and hydroxyl groups. It is important for bone regeneration therapy to control the propagation and differentiation of stem cells in a controlled manner. It was proved that osteogenic differentiation of stem cell is increased when cultured on mechanically stiff substrates. Graphene could provide a towardly biocompatible scaffold to accelerate the specific differentiation of hMSCs into bone cells without hampering their proliferation [36]. GO flakes conjugated to collagen sponges which were clinically approved scaffolds to provide soft microenvironment for bone regeneration increased the scaffold stiffness 3-fold without cytotoxicity and enhanced significantly osteogenic differentiation of hMSCs, so this novel 3D GO-collagen scaffolds could offer a novel platform for stem cell study and bone regeneration [37]. PCL compound of GO, reduced GO (RGO), and amine-functionalized GO (AGO) were prepared at various filling material components. The results demonstrated that AGO and GO particles significantly enhanced hMSCs proliferation, and AGO was most effectual in modulating the osteogenic differentiation of stem cell leading to mineralization [38].

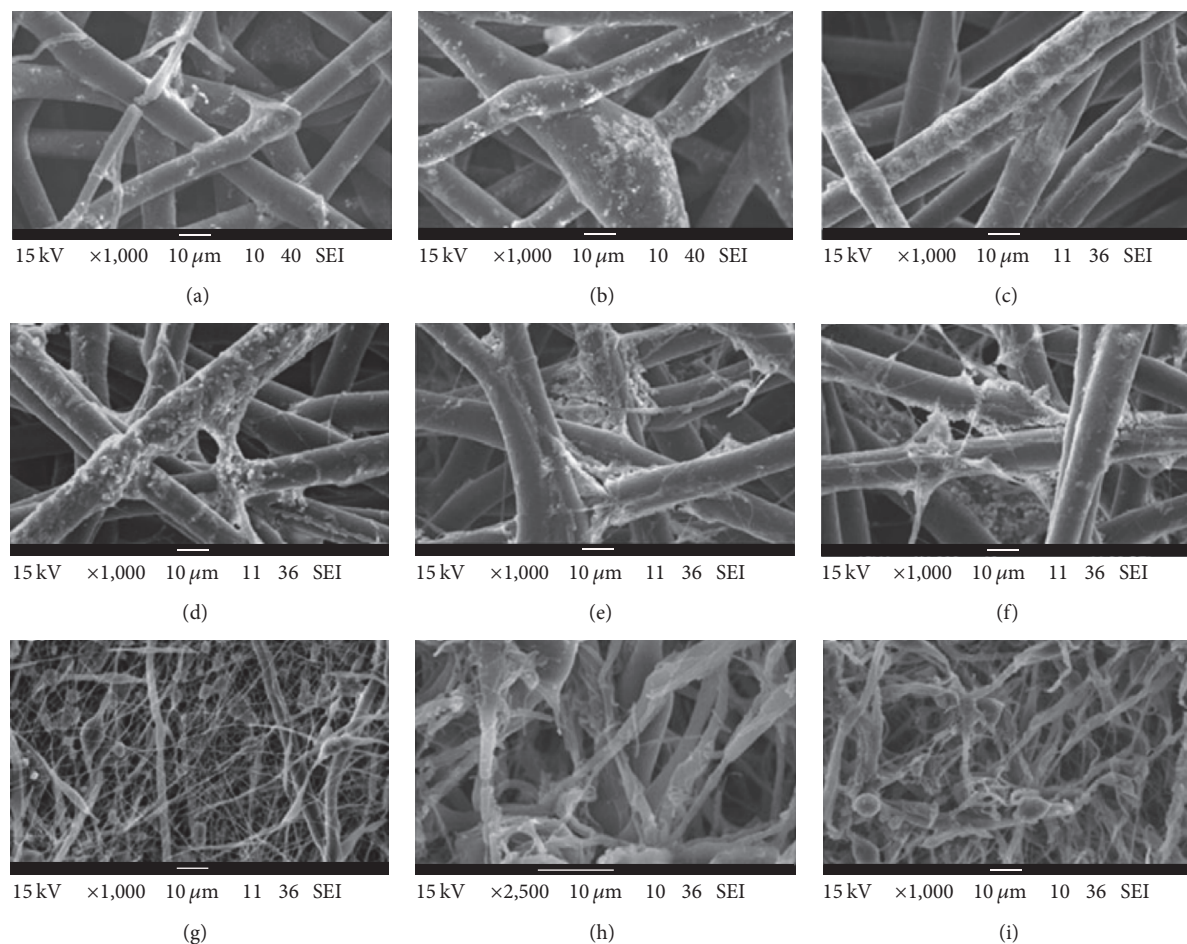


FIGURE 3: SEM image showing biominerzation in untreated (a, d, g), argon-treated (b, e, h), and nitrogen-treated (c, f, i) microfibers (a–c), micro/nanofibers (d–f), and nanofibers (g–i). Figure 3 is from [40].

2.5. Topography of Nanomaterial Surface. One important goal in tissue engineering is to understand and control the factors directing cell proliferation and differentiation into a special cell lineage in the nanoscale environment, and it is a useful method to control cell biological behaviors by material surface. It was demonstrated that the adhesion and differentiation of MSC were enhanced by ion beam irradiation (10 keV He⁺) which induced negligible surface smoothening and various nanostructured surface of PCL [39]. Micro-hybrid, micro/nanohybrid, and nano-PCL fibers were subjected to plasma treatment with argon and nitrogen in low pressure, by which PCL scaffold with superhydrophobicity converted to hydrophilic scaffolds with modified biominerzation (Figure 3). Furthermore, it was demonstrated that cell spreading, elongation, attachment, proliferation, and protein adsorption were increased remarkably on micro- and micro/nanofibers with plasma treatment, cell attachment was enhanced significantly on plasma-treated nanofibers, and differentiation towards osteoblast lineage was accelerated in fibers with plasma treatment [40].

The biological behavior of stem cells can be controlled by physical factors such as the micro- and nanotopography of the extracellular matrix. It was demonstrated that

nanofibrous combinatorial scaffolds can influence the fate of human BMSC without chemical treatments or cellular reprogramming by mimicking the extracellular matrix topographical environment [43]. Changing the depth of biomaterial surface structures enhanced hMSCs adhesion and induced specific differentiation into osteoblast-like cells without osteogenic medium which was dictated by stress through focal-adhesion-induced restructuring of F-actin filaments [44]. Another investigation demonstrated that different forms of biomaterials control osteogenic differentiation and growth of stem cell by differential activation focal adhesion kinase [45].

These studies have fundamental implication for comprehension of the architectural effects of extracellular matrix microenvironment and also for the regenerative medicine of orthopedic surgery using stem cells.

3. Cartilage Tissue Engineering

Nanostructured cartilage tissue is traditionally difficult to regenerate because of its extremely poor inherent regenerative capacity and perplexing hierarchical structures. Traditionally medical treatments are not noninvasive and may

cause many complications. Nanomaterials fabrication committed to producing useful biologically scaffolds of tissue-engineered cartilage used to promote the chondrification of stem cells. Several novel 3D biomimetic nanostructured scaffolds were studied which was fabricated by PLLA polymers and multiwalled carbon nanotubes treated with hydrogen. The scaffolds embedded by multiwalled carbon nanotubes exhibited a vigorous enhancement in shatter strength with a compressed Young's modulus accordant to human cartilage. It was demonstrated that MSCs was preferred to attach on smaller fiber diameter structure and increasing chondrogenic differentiations were induced by combination of plasma-treated multiwalled carbon nanotubes and PLLA [46].

Another investigation demonstrated that the attachment, distribution, viability, and propagation of stem cells cultured in vitro in the 3D nHA coated poly(lactide-co-glycolide) scaffolds were increased as compared with poly(lactide-co-glycolide) one. Furthermore, it was demonstrated that the osteochondral defects of rats knees treated by three-dimensional poly(lactide-co-glycolide)/nHA scaffold combining with MSCs were stuffed with crystalline cartilage. Furthermore, there was affluent mucopolysaccharide and collagen type II sedimentation after surgery. The results suggested that the poly(lactide-co-glycolide)/nHA-MSCs compound might have probable utilization in tissue-engineered cartilage [47]. Traditionally, chondrogenic differentiation is accomplished by stem cells culturing with chondrogenic factors in the culture medium, such as the protein transforming growth factor-beta 3. However, cell-to-cell interaction and diffusional limitation of transforming growth factor-beta 3 mainly provided by pellets may restrain stem cells differentiation to restrain. It was demonstrated that a novel GO could be used as substrates for adhesion of stem cells and delivered growth factor during the stem cell differentiation to cartilage. GO used to adsorb fibronectin and transforming growth factor-beta 3 was incorporated in pellets of hASCs to obtain a hybrid pellets of hASC-GO sheets (size = 0.5–1 μm) which promoted the hASCs differentiation to cartilage through increasing the interaction of cell with fibronectin and providing transforming growth factor-beta 3 efficiently. The novel hASC-GO sheets may offer novel methods for hASC culture to obtain tissue-engineered cartilage [48].

4. Tendons Tissue Engineering

The reconstructive articulation usually tends to fail at the tendon-to-bone insertion site, so an orthobiologic material is formidably required to provide a stable transition from hard bone to soft ligament tissue.

A nanostructured material using PLLA mineralized with hydroxyapatite and magnesium nanoparticles was developed to regenerate the tendon-to-bone insertion site which was fashioned in the shape of an o-ring to recover functionality to injured entheses, the graded transition of mineralized fibrous cartilage connecting ligament to bone. Tendon stem cells are useful in effectual restoration or regeneration of wounded tendons. The destiny of tendon stem cells is not unambiguous during the implantation. It was demonstrated that tagging tendon stem cells with super-paramagnetic iron oxide (SPIO)

nanomaterials was a practicable method for tracing tendon stem cells used to determine the feasibility of it. This novel SPIO labeled tendon stem cells provide a noninvasive approach to wounded tendons observe restoration [49].

5. Nerve Tissue Engineering

Spinal cord injury is defined as the direct or indirect factors that cause spinal cord damage, in the corresponding segment of the injury, associated with motor, sensory and sphincter dysfunction, muscle tension abnormalities and pathological changes, and so on. The extent and clinical manifestations of spinal cord injury depend on the location and nature of the primary injury. Spinal cord injury is the most serious complication of spinal injury, which often leads to severe dysfunction of the injured segment following limb. Infection, tumor, spinal degenerative disease, scoliosis, myelochisis, spondylolisthesis, and various types of spinal fractures and dislocations caused by indirect external forces can lead to spinal cord injury. The nerve repair of spinal cord injury is a difficult and important problem in regenerative medicine, and more and more research is used to repair the nerve along with the depth of people's understanding in the nerve biology and material science.

5.1. Effect of Surface Topography. Conclusive extracellular environment has a crucial impact in cell life by regulation of cell morphology, proliferation, survival, and differentiation into a specific cell line. A main restraint in the clinical application of stem cell technique is the lack of available regulate of its biological behavior, such as attachment, multiplication, and differentiation. Current in vitro studies have indicated that biological materials with nanosurfaces morphology can affect cell behavior. Thus, confirmation of biological materials supporting adequate ES cell adhesion, proliferation, and differentiation into special cell lineage is a fascinating measure to investigate. Current medicinal cell therapy, using the special ability of stem cells in differentiating to nerve corpuscles which is loaded by polymer materials, focuses on the restoration of the central nervous system damage.

A thin film of gold with different roughness of surface morphology was fabricated by the conjugation of microfabrication technology. Then the biomimetic possibility of the thin film was investigated, compared with glass coverslips and plastic tissue culture materials, for regulating the differentiation of neural precursor derived from ES cell. It was demonstrated that the neural precursors derived from ES cells which were cultured for five days had the best adhesion on the gold films and were carried out with the maximum differentiation on gold films with surface roughness of standard deviation 21 nm without any conventional diffuent neurotrophic factor. In addition, the influence of the grating axis on the axons growth direction is observed when the neural precursors derived from ES cell were seeded in a conjunction of microscale trenches and nanoscale surface roughness. These data suggest that biological material design can maximize the differentiation and organization of neural precursors derived from ES cells, and it can be found to be useful as a synergistic supplement of diffuent neurotrophic

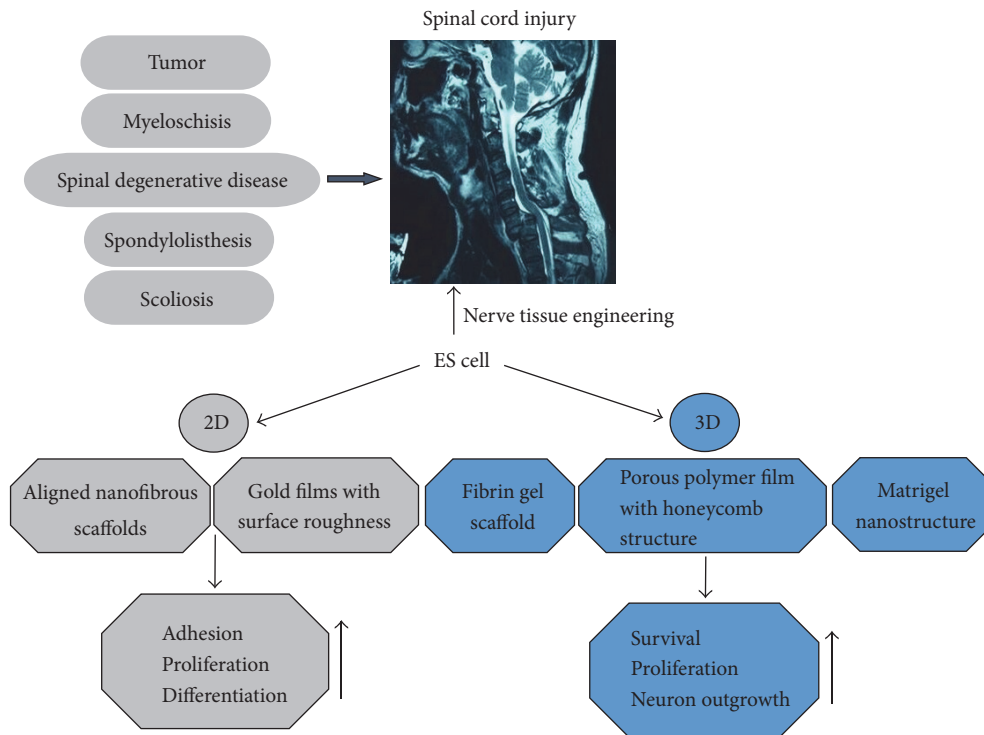


FIGURE 4: The application of stem cell on 2D or 3D scaffold for spinal cord injury.

factor usually used to stimulate and model the differentiation of ES cell in vitro. This basal pattern of gold thin films may be used in the nerve prosthesis with the need for directed induction [50].

The multipotency P19 embryonic cancer cells were cultured on poly(lactic-co-glycolic acid) nanofibrous scaffolds which were fabricated by random and aligned; subsequently it was investigated that the effect of surface morphology of nanofibrous scaffold on the proliferation and retinoic acid induced neural differentiation of P19 cancer cells. It was demonstrated that the surface of aligned nanofibrous scaffolds provided compatible interface for normal cellular functioning and promoted cell proliferation due to their resemblance with naturalistic extracellular matrix [51].

5.2. Effect of Three-Dimensional Scaffold. Nerve tissue engineering belongs to the most towardly approaches to recover the health of the central nervous system damage. Stem cell technique integrated with surface topology of nanofiber scaffolds offers a novel and more effective method for inducing stem cell differentiation and thus to be used for central nervous system functional reconstruction. The goal of 3D cell culture moulds in vitro is to fill in gaps in the normal 2D cellular research and the in vivo extracellular matrix (Figure 4). 3D scaffold made up by nanofibers with poriferous structure provides 3D environment for cell distribution, proliferation, and differentiation which has clinical application prospect for tissue engineering. In particular, for nerve historegeneration which is very small regeneration ability, 3D moulds are fundamental in providing support to mimic ECM which is convenient for naturalistic circulation of oxygen, nutriment,

and nerve factors and might be beneficial to nerve cell regeneration.

The neuron-like cells derived from human endometrial stem cells (hEnSCs) were cultured in a novel fibrin gel scaffold to control cell behaviors such as survival, proliferation, and neuron outgrowth and to investigate the interactions between cell and matrix. The mechanical characters of the newly prepared fibrin gel scaffolds were investigated which showed the suitable materials, and a good conformity between cell and fibrin gel scaffolds was detected by SEM and TEM. Cell was seeded and cultured on fibrin gel scaffolds for 6 days, and the result showed good expansion and integration of the neuronal network by immunofluorescence assay. Furthermore, the survival, proliferation, and nerve growth of the neuron-like cells were compared between 2D culture and 3D culture, and the results showed that 3D culture has positive influence. These results demonstrated that the novel 3D fibrin gel scaffolds were applied to promote the survival and outgrowth of nerve cell for nerve injury repair [52]. It was demonstrated that neural progenitors (NPs) derived from hEnSCs can express correlative markers such as Pax6, Nidogen, and Sox1 and it might experience pluripotency differentiation to neuroglial and neurons. A composite, random orientation, 3D nanofibrils matrix consisting of polyamine nanofibers prepared by electrospinning methods was adopted to evaluate the behavior of NPs cultured on it. The results showed that the immigration, proliferation, morphology, and neurapophysis length of NPs cell were enhanced when cultured on 3D scaffolds as compared with 2D structure [53].

The nanostructure scaffold design originated in self organization is the focus of study when looking for novel

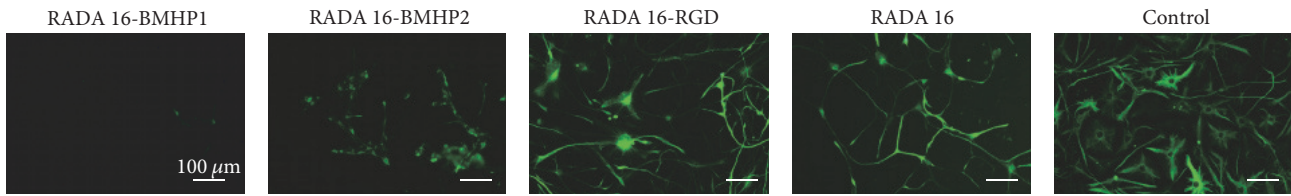


FIGURE 5: The immunofluorescence image of NSCs after 7 days of differentiation. NSCs had been proliferating for 7 days in each of the self-assembling peptides in analysis. Glial fibrillary acidic protein positive cells are shown as control. RADA16, 16-residue peptide; BMHP, bone marrow homing peptide; RGD, Arg-Gly-Asp. Figure 5 is from [41].

biological materials and biosensor, and the new nanostructure scaffold has many kinds of probable utilization for tissue regeneration and iatrical implantation. 3D nanostructures in proportionate aperture and porousness and with coadjacent pores are necessary to promote the agglutination, proliferation, differentiation of stem cells, and ultimate tissue engineering. A new porous polymer film with high regularity in honeycomb structure was fabricated through self-organized formation which had a strong influence in cell biological behavior, such as proliferation, macula adheres, and cell morphology. The results suggested that the biological behavior of neural stem cell and progenitor cells could be affected by honeycomb-patterned polymer film aperture, and this novel honeycomb film is expected to be used for biological material in nerve tissue engineering without any nutrilitie in stem cell proliferation. Another novel 3D nanostructured culture system for neural stem cells was fabricated with matrigel biomaterial at different concentrations by self-assembling which possess the formation of a complex and biologically activated matrix displaying exceptionally premeditated serviceable subjects for Arg-Gly-Asp, bone marrow homing peptide 1, and bone marrow homing peptide 2. Neural stem cells were embedded in the 3D scaffolds and detected by microscopy, and the results exhibited that the survival, proliferation, and differentiation of neural stem cells in the 3D nanostructured scaffold were in good condition which indicated that this novel self-assembling 3D matrigel scaffold could be potentially used to create particular premeditated peptides for nerve stem cell lines (Figure 5) [41].

5.3. Effect of Graphene Biomaterial. Although graphene based nanomaterial is still in its infancy, as a novel type of biocompatible biomaterials, it has high performance for biomedical applications in tissue engineering and regenerative medicine because of the good electric conductivity, flexibility, and high molecular absorption of it. In neural tissue engineering and regenerative medicine, research is focused on the exploration of graphene characteristics which can enhance the bioeffect and the application of it on neural cells and stem cells [54].

5.3.1. Two-Dimensional Graphene. It was reported that nanostructure hybrid scaffold of graphene composite material can directionally induce the neural stem cells differentiated into myelinating cells in central nervous system, such as mature oligodendrocytes. In addition, the procedure could be promoted in absence of any differentiation inducing agents in

stem cell nutrient medium, and it could be a potentially biological material for neural tissue engineering (Figure 6) [42]. It was demonstrated that human neural stem cells seeded on hybrid scaffold of graphene nanoparticles exhibited a distinctive behavior that the neurite of differentiated neural stem cells showed increased growth and arrangement. Furthermore, it was demonstrated that the orientation of axons was largely owing to graphene and the radical nanometer particle monostratum leading to the increased differentiation of human neural stem cells into neuron which could be potentially used in nerve tissue engineering [55]. It was reported that fluorinated graphene accelerated the differentiation of MSCs into neuron lines; furthermore, cell alignment caused by fluorinated graphene with typographic dimethyl silicone polymer tunnel arrays obviously strengthened MSCs neuroinduction without any chemic inductors [56].

5.3.2. Three-Dimensional Graphene. Neural regeneration is a promising method for nerve injury repair with neural stem cells in clinical, for which 3D nanostructure scaffolds are necessary to offer culture microhabitats and collaboratively proportionate direction cues for the stem cells. A novel 3D poriferous scaffold was manufactured by graphene foam used for neural stem cell culture. It was demonstrated that the 3D graphene foam could sustain the growth of stem cell cultured on it as compared with 2D nanostructure, and the 3D graphene foam could maintain the proliferation of neural stem cell by promoting the gene expression of Ki67. At the same time, it was found that neural stem cell differentiated to stellate cells and particularly neurons by phenotype essay. Meanwhile, it was demonstrated that there was a superior electric coupling between stem cells which was differentiated with 3D nanostructure of graphene foams for effectual electrostimulation. These results indicated that 3D graphene foams might provide a novel terrace for nerve regeneration medicine [57].

5.3.3. Graphene Oxide. Nanoparticles are more likely to pass through cell membrane which is used as an ideal platform with biocompatibility and mechanically stability in regulating stem cell biological behavior. Transplant comprised of nanostructure biological material and stem cells is considered to be a clinical treatment in various neurological diseases. In light of recent developments, it was demonstrated that artificial synthesis of biological material based on carbon including carbon nanotubes and graphene could be used for enhancing the adhesion and differentiation of stem cell.

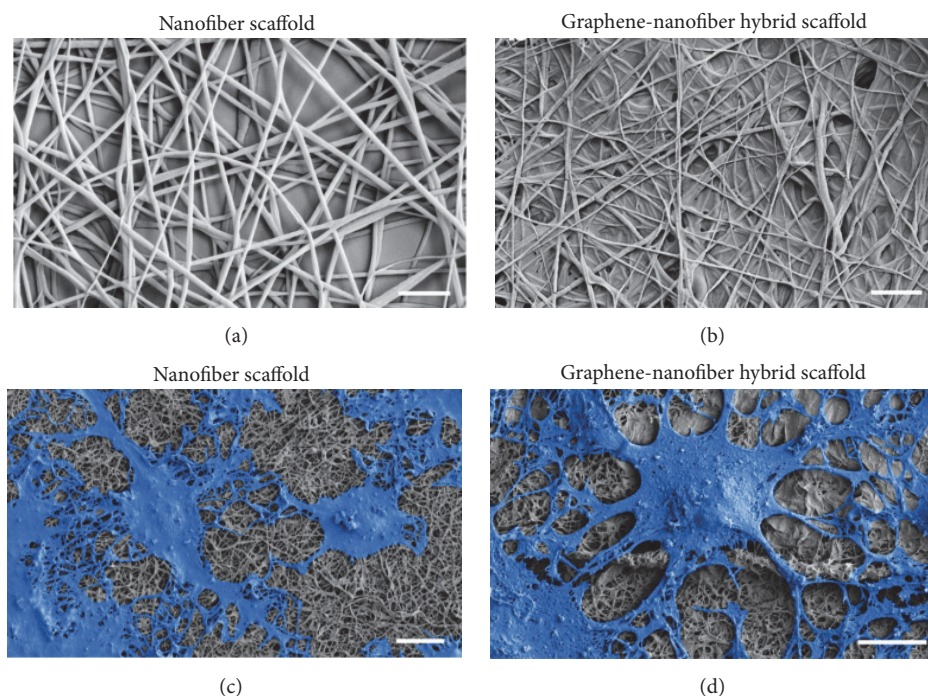


FIGURE 6: The morphology of nanofibrous scaffolds and cultured NSCs on the scaffolds. FE-SEM images of nanofibers (a) and graphene-nanofibers hybrid scaffolds (b). FE-SEM of differentiated NSCs cultured on nanofiber scaffolds (c) and graphene-nanofiber hybrid scaffolds (d). The cells are pseudocolored blue for contrast. The differentiated cells on the grapheme-nanofiber hybrid scaffolds (d) show a clear morphological difference in terms of process extension compared with the nanofiber scaffolds alone (c). Figure 6 is from [42].

A research was carried out to investigate the function of different kinds of carbon nanomaterials on biological behaviors of dopamine neural stem cells including graphene, graphene oxide, and carbon nanotubes. The results showed that merely graphene oxide efficaciously advanced the differentiation of dopamine neurons and the expression of correlative gene, and it indicated that graphene oxide could be promisingly used for neural stem cell therapy [58].

5.3.4. Mechanism of Graphene Biological Function. One of the main problems in nerve tissue regeneration is the development of biomaterials with powerful functions for managing the behavior of a particular cell and forming useful neural net. Surface topology structure of nanomaterial substrates provides opportunity to regulating the neural stem cell physiologic functions on molecular level. Grapheme is considered as a towardly candidate for nerval surfaces because of the unique properties of it in electrochemistry and machinery, while there is seldom understanding in the neural net structures on graphene as a biomaterial for nanostructures in regenerative medicine. Microarray research was carried out to explain the possible mechanism for the enhancement of human neural stem cell attachment and differentiation into neurons on grapheme substrate, and it was demonstrated that graphene electrodes can enhance differentiation of stem cells by electrical stimulation (Figure 7) [59]. The change in neural net combination of neural stem cell when cultured on graphene scaffold surface was investigated, and the results showed that graphene improved the serviceable neural

circuits construction and enhanced the nerval behavior and electrophysiological signal of neural net which provided a further comprehension of interactions between neural stem cells with nanobiomaterial surface of grapheme, so it pointed out the great possibility of graphene as nerval separatrix in nerve tissue regeneration medicine [60].

6. Conclusion

In summary, stem cell research based on nanotechnology has obtained a lot of achievement in the field of regenerative medicine of orthopedic surgery, showing good prospects in clinical applications. But nanotechnology applied to stem cell research is still in its early stages, and there are a number of key issues to be solved. The objective of tissue engineering research with stem cell is to develop a system to accurately simulate the in vivo microenvironment system in vitro; however, the mechanism is not very clear regarding how nanomaterials similar to extracellular matrix in morphology affect the function of stem cells.

Biomaterials and their scaffold used for tissue engineering in orthopedic surgery can be manufactured by nanohydroxyapatite, titanium, calcium phosphate, graphene oxide, carbon nanotubes, or the compound of them. These composite scaffolds have both nanomaterials properties and good biocompatibility and low toxicity which render it a very broad application prospect in orthopedic surgery regenerative medicine by some nanoscale surface topography or molecular biology mechanism, including the regulation of

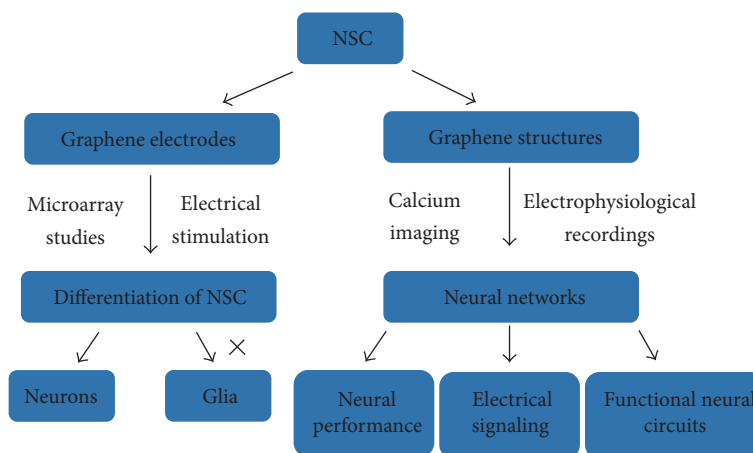


FIGURE 7: The mechanism of graphene biological function to NSCs.

stem cell biological behavior (such as attachment, proliferation, and differentiation), the improvement of bone tissue regeneration promising skeletal defects repair, internal fixation surgery, and spinal fusion in orthopedic surgery, the potential application in cartilage tissue engineering and recovery at tendon-to-bone insertion site, and the nerve tissue engineering for spinal cord injury.

Although the research of stem cell nanotechnology is facing many difficulties in regenerative medicine of orthopedic surgery, its potential applications have caused great concern. With the development of nanotechnology and stem cell research, the investigation of stem cell based on nanotechnology will be studied more in depth and will provide new methods for stem cell therapy and tissue engineering in regenerative medicine of orthopedic surgery.

Conflicts of Interest

The authors declare that there are no conflicts of interest regarding the publication of this paper.

Acknowledgments

This work was supported by the National Natural Science Foundation of China (Grant nos. 81301289 and 8167090834), the Youth Research Fund Project of Jilin Province Science and Technology Development Plan (Grant nos. 20130522032JH and 20130522039JH), and the Projects of International Cooperation of Jilin Provincial Science & Technology Department (Grant no. 20150101175JC).

References

- [1] Z. Yang, J. Xie, J. Zhu et al., "Functional exosome-mimic for delivery of siRNA to cancer: in vitro and in vivo evaluation," *Journal of Controlled Release*, vol. 243, pp. 160–171, 2016.
- [2] J. Xie, Z. Yang, C. Zhou, J. Zhu, R. J. Lee, and L. Teng, "Nanotechnology for the delivery of phytochemicals in cancer therapy," *Biotechnology Advances*, vol. 34, no. 4, pp. 343–353, 2016.
- [3] Z. Chen, Z. Chen, A. Zhang, J. Hu, X. Wang, and Z. Yang, "Electrospun nanofibers for cancer diagnosis and therapy," *Biomaterials Science*, vol. 4, no. 6, pp. 922–932, 2016.
- [4] L. J. Lee, Z. Yang, M. Rahman et al., "Extracellular mRNA detected by tethered lipoplex nanoparticle biochip for lung adenocarcinoma detection," *American Journal of Respiratory and Critical Care Medicine*, vol. 193, no. 12, pp. 1431–1433, 2016.
- [5] C. Kang, Y. Sun, J. Zhu et al., "Delivery of nanoparticles for treatment of brain tumor," *Current Drug Metabolism*, vol. 17, no. 8, pp. 745–754, 2016.
- [6] Z. Yang, L. Chang, C.-L. Chiang, and L. J. Lee, "Micro-/nanoelectroporation for active gene delivery," *Current Pharmaceutical Design*, vol. 21, no. 42, pp. 6081–6088, 2015.
- [7] Z. Yang, B. Yu, J. Zhu et al., "A microfluidic method to synthesize transferrin-lipid nanoparticles loaded with siRNA LOR-1284 for therapy of acute myeloid leukemia," *Nanoscale*, vol. 6, no. 16, pp. 9742–9751, 2014.
- [8] C. Zhou, Z. Yang, and L. Teng, "Nanomedicine based on nucleic acids: pharmacokinetic and pharmacodynamic perspectives," *Current Pharmaceutical Biotechnology*, vol. 15, no. 9, pp. 829–838, 2014.
- [9] J. Xie, L. Teng, Z. Yang et al., "A polyethylenimine-linoleic acid conjugate for antisense oligonucleotide delivery," *BioMed Research International*, vol. 2013, Article ID 710502, 7 pages, 2013.
- [10] Z. Chena, A. Zhang, Z. Yang et al., "Application of DODMA and derivatives in cationic nanocarriers for gene delivery," *Current Organic Chemistry*, vol. 20, no. 17, pp. 1813–1819, 2016.
- [11] Z. Chen, M. Cong, J. Hu, Z. Yang, and Z. Chen, "Preparation of functionalized TiO₂ nanotube arrays and their applications," *Science of Advanced Materials*, vol. 8, no. 6, pp. 1231–1241, 2016.
- [12] X. Liu, D. Wei, J. Zhong et al., "Electrospun nanofibrous P(DLLA-CL) balloons as calcium phosphate cement filled containers for bone repair: in vitro and in vivo studies," *ACS Applied Materials and Interfaces*, vol. 7, no. 33, pp. 18540–18552, 2015.
- [13] N. Xu, X. Ye, D. Wei et al., "3D artificial bones for bone repair prepared by computed tomography-guided fused deposition modeling for bone repair," *ACS Applied Materials and Interfaces*, vol. 6, no. 17, pp. 14952–14963, 2014.
- [14] G. Sun, D. Wei, X. Liu et al., "Novel biodegradable electrospun nanofibrous P(DLLA-CL) balloons for the treatment of

- vertebral compression fractures,” *Nanomedicine: Nanotechnology, Biology, and Medicine*, vol. 9, no. 6, pp. 829–838, 2013.
- [15] N. Panda, A. Bissoyi, K. Pramanik, and A. Biswas, “Directing osteogenesis of stem cells with hydroxyapatite precipitated electrospun eri-tasar silk fibroin nanofibrous scaffold,” *Journal of Biomaterials Science, Polymer Edition*, vol. 25, no. 13, pp. 1440–1457, 2014.
- [16] H. R. A. Balaji Raghavendran, S. Puvaneswary, S. Talebian et al., “A comparative study on in vitro osteogenic priming potential of electron spun scaffold PLLA/HA/Col, PLLA/HA, and PLLA/Col for tissue engineering application,” *PLoS ONE*, vol. 9, no. 8, Article ID e104389, 2014.
- [17] J. Hu, Y. Zhou, L. Huang, J. Liu, and H. Lu, “Effect of nano-hydroxyapatite coating on the osteoinductivity of porous biphasic calcium phosphate ceramics,” *BMC Musculoskeletal Disorders*, vol. 15, no. 1, article 114, 2014.
- [18] Q. Lv, M. Deng, B. D. Ulery, L. S. Nair, and C. T. Laurencin, “Nano-ceramic composite scaffolds for bioreactor-based bone engineering basic research,” *Clinical Orthopaedics and Related Research*, vol. 471, no. 8, pp. 2422–2433, 2013.
- [19] A. Polini, D. Pisignano, M. Parodi, R. Quarto, and S. Scaglione, “Osteoinduction of human mesenchymal stem cells by bioactive composite scaffolds without supplemental osteogenic growth factors,” *PLoS ONE*, vol. 6, no. 10, Article ID e26211, 2011.
- [20] A. Khadka, J. Li, Y. Li, Y. Gao, Y. Zuo, and Y. Ma, “Evaluation of hybrid porous biomimetic nano-hydroxyapatite/polyamide 6 and bone marrow-derived stem cell construct in repair of calvarial critical size defect,” *Journal of Craniofacial Surgery*, vol. 22, no. 5, pp. 1852–1858, 2011.
- [21] B.-N. Lin, S. W. Whu, C.-H. Chen et al., “Bone marrow mesenchymal stem cells, platelet-rich plasma and nanohydroxyapatite-type I collagen beads were integral parts of biomimetic bone substitutes for bone regeneration,” *Journal of Tissue Engineering and Regenerative Medicine*, vol. 7, no. 11, pp. 841–854, 2013.
- [22] X. Liu, X. Li, Y. Fan et al., “Repairing goat tibia segmental bone defect using scaffold cultured with mesenchymal stem cells,” *Journal of Biomedical Materials Research Part B: Applied Biomaterials*, vol. 94, no. 1, pp. 44–52, 2010.
- [23] B. Qiao, J. Li, Q. Zhu et al., “Bone plate composed of a ternary nano-hydroxyapatite/polyamide 66/glass fiber composite: biomechanical properties and biocompatibility,” *International Journal of Nanomedicine*, vol. 9, no. 1, pp. 1423–1432, 2014.
- [24] Z.-B. Tang, J.-K. Cao, N. Wen et al., “Posterolateral spinal fusion with nano-hydroxyapatite-collagen/PLA composite and autologous adipose-derived mesenchymal stem cells in a rabbit model,” *Journal of Tissue Engineering and Regenerative Medicine*, vol. 6, no. 4, pp. 325–336, 2012.
- [25] P. J. ter Brugge, R. Torensma, J. E. De Ruijter, C. G. Figdor, and J. A. Jansen, “Modulation of integrin expression on rat bone marrow cells by substrates with different surface characteristics,” *Tissue Engineering*, vol. 8, no. 4, pp. 615–626, 2002.
- [26] S. Tetè, F. Mastrangelo, R. Quaresima et al., “Influence of novel nano-titanium implant surface on human osteoblast behavior and growth,” *Implant Dentistry*, vol. 19, no. 6, pp. 520–531, 2010.
- [27] M. Annunziata, A. Oliva, A. Buosciolo, M. Giordano, A. Guida, and L. Guida, “Bone marrow mesenchymal stem cell response to nano-structured oxidized and turned titanium surfaces,” *Clinical Oral Implants Research*, vol. 23, no. 6, pp. 733–740, 2012.
- [28] D. Khang, J. Choi, Y.-M. Im et al., “Role of subnano-, nano- and submicron-surface features on osteoblast differentiation of bone marrow mesenchymal stem cells,” *Biomaterials*, vol. 33, no. 26, pp. 5997–6007, 2012.
- [29] L. Lv, Y. Liu, P. Zhang et al., “The nanoscale geometry of TiO₂ nanotubes influences the osteogenic differentiation of human adipose-derived stem cells by modulating H3K4 trimethylation,” *Biomaterials*, vol. 39, pp. 193–205, 2015.
- [30] M. Wang, N. J. Castro, J. Li, M. Keidar, and L. G. Zhang, “Greater osteoblast and mesenchymal stem cell adhesion and proliferation on titanium with hydrothermally treated nanocrystalline hydroxyapatite/magnetically treated carbon nanotubes,” *Journal of Nanoscience and Nanotechnology*, vol. 12, no. 10, pp. 7692–7702, 2012.
- [31] M. B. Eslaminejad, M. Zandi, E. Nejati, and E. Zomorodian, “Study of mesenchymal stem cell proliferation and bone differentiation on composite scaffolds of PLLA and nano hydroxyapatite with different morphologies,” *Cell Journal*, vol. 12, no. 4, pp. 469–476, 2010.
- [32] E. García-Gareta, J. Hua, J. C. Knowles, and G. W. Blunn, “Comparison of mesenchymal stem cell proliferation and differentiation between biomimetic and electrochemical coatings on different topographic surfaces,” *Journal of Materials Science: Materials in Medicine*, vol. 24, no. 1, pp. 199–210, 2013.
- [33] Y. C. Chai, G. Kerckhofs, S. J. Roberts et al., “Ectopic bone formation by 3D porous calcium phosphate-Ti6Al4V hybrids produced by perfusion electrodeposition,” *Biomaterials*, vol. 33, no. 16, pp. 4044–4058, 2012.
- [34] H. H. K. Xu, L. Zhao, M. S. Detamore, S. Takagi, and L. C. Chow, “Umbilical cord stem cell seeding on fast-resorbable calcium phosphate bone cement,” *Tissue Engineering—Part A*, vol. 16, no. 9, pp. 2743–2753, 2010.
- [35] J. L. Moreau and H. H. K. Xu, “Mesenchymal stem cell proliferation and differentiation on an injectable calcium phosphate—chitosan composite scaffold,” *Biomaterials*, vol. 30, no. 14, pp. 2675–2682, 2009.
- [36] T. R. Nayak, H. Andersen, V. S. Makam et al., “Graphene for controlled and accelerated osteogenic differentiation of human mesenchymal stem cells,” *ACS Nano*, vol. 5, no. 6, pp. 4670–4678, 2011.
- [37] S. Kang, J. B. Park, T.-J. Lee et al., “Covalent conjugation of mechanically stiff graphene oxide flakes to three-dimensional collagen scaffolds for osteogenic differentiation of human mesenchymal stem cells,” *Carbon*, vol. 83, pp. 162–172, 2015.
- [38] S. Kumar, S. Raj, E. Kolanthai, A. K. Sood, S. Sampath, and K. Chatterjee, “Chemical functionalization of graphene to augment stem cell osteogenesis and inhibit biofilm formation on polymer composites for orthopedic applications,” *ACS Applied Materials and Interfaces*, vol. 7, no. 5, pp. 3237–3252, 2015.
- [39] G. Marletta, G. Ciapetti, C. Satriano, F. Perut, M. Salerno, and N. Baldini, “Improved osteogenic differentiation of human marrow stromal cells cultured on ion-induced chemically structured poly- ϵ -caprolactone,” *Biomaterials*, vol. 28, no. 6, pp. 1132–1140, 2007.
- [40] D. Sankar, K. T. Shalumon, K. P. Chennazhi, D. Menon, and R. Jayakumar, “Surface plasma treatment of poly(caprolactone) micro, nano, and multiscale fibrous scaffolds for enhanced osteoconductivity,” *Tissue Engineering—Part A*, vol. 20, no. 11–12, pp. 1689–1702, 2014.
- [41] C. Cunha, S. Panseri, O. Villa, D. Silva, and F. Gelain, “3D culture of adult mouse neural stem cells within functionalized self-assembling peptide scaffolds,” *International Journal of Nanomedicine*, vol. 6, pp. 943–955, 2011.
- [42] S. Shah, P. T. Yin, T. M. Uehara, S.-T. D. Chueng, L. Yang, and K.-B. Lee, “Guiding stem cell differentiation into oligodendrocytes

- using graphene-nanofiber hybrid scaffolds,” *Advanced Materials*, vol. 26, no. 22, pp. 3673–3680, 2014.
- [43] A. Polini, S. Scaglione, R. Quarto, and D. Pisignano, “Composite electrospun nanofibers for influencing stem cell fate,” in *Stem Cell Nanotechnology: Methods and Protocols*, K. Turksen, Ed., pp. 25–40, Humana Press, Totowa, NJ, USA, 2013.
- [44] O. F. Zouani, C. Chanseau, B. Brouillaud et al., “Altered nanofeature size dictates stem cell differentiation,” *Journal of Cell Science*, vol. 125, no. 5, pp. 1217–1224, 2012.
- [45] M. Manfrini, C. Di Bona, A. Canella et al., “Mesenchymal stem cells from patients to assay bone graft substitutes,” *Journal of Cellular Physiology*, vol. 228, no. 6, pp. 1229–1237, 2013.
- [46] B. Holmes, N. J. Castro, J. Li, M. Keidar, and L. G. Zhang, “Enhanced human bone marrow mesenchymal stem cell functions in novel 3D cartilage scaffolds with hydrogen treated multi-walled carbon nanotubes,” *Nanotechnology*, vol. 24, no. 36, Article ID 365102, 2013.
- [47] D. Xue, Q. Zheng, C. Zong et al., “Osteochondral repair using porous poly(lactide-co-glycolide)/ nano-hydroxyapatite hybrid scaffolds with undifferentiated mesenchymal stem cells in a rat model,” *Journal of Biomedical Materials Research—Part A*, vol. 94, no. 1, pp. 259–270, 2010.
- [48] H. H. Yoon, S. H. Bhang, T. Kim, T. Yu, T. Hyeon, and B.-S. Kim, “Dual roles of graphene oxide in chondrogenic differentiation of adult stem cells: cell-adhesion substrate and growth factor-delivery carrier,” *Advanced Functional Materials*, vol. 24, no. 41, pp. 6455–6464, 2014.
- [49] Y. Yang, J. Zhang, Y. Qian et al., “Superparamagnetic iron oxide is suitable to label tendon stem cells and track them in vivo with MR imaging,” *Annals of Biomedical Engineering*, vol. 41, no. 10, pp. 2109–2119, 2013.
- [50] G. J. Bakeine, J. Ban, G. Greci et al., “Design, fabrication and evaluation of nanoscale surface topography as a tool in directing differentiation and organisation of embryonic stem-cell-derived neural precursors,” *Microelectronic Engineering*, vol. 86, no. 4–6, pp. 1435–1438, 2009.
- [51] S. Irani, M. Zandi, N. Salamian, S. M. Saeed, M. Daliri Joupari, and S. M. Atyabi, “The study of P19 stem cell behavior on aligned oriented electrospun poly(lactic-co-glycolic acid) nano-fibers for neural tissue engineering,” *Polymers for Advanced Technologies*, vol. 25, no. 5, pp. 562–567, 2014.
- [52] M. Navaei-Nigjeh, G. Amoabedini, A. Noroozi et al., “Enhancing neuronal growth from human endometrial stem cells derived neuron-like cells in three-dimensional fibrin gel for nerve tissue engineering,” *Journal of Biomedical Materials Research. Part A*, vol. 102, no. 8, pp. 2533–2543, 2014.
- [53] A. Rahjouei, S. Kiani, A. Zahabi, N. Z. Mehrjardi, M. Hashemi, and H. Baharvand, “Interactions of human embryonic stem cell-derived neural progenitors with an electrospun nanofibrillar surface in vitro,” *The International Journal of Artificial Organs*, vol. 34, no. 7, pp. 559–570, 2011.
- [54] S. Ryu and B.-S. Kim, “Culture of neural cells and stem cells on graphene,” *Tissue Engineering and Regenerative Medicine*, vol. 10, no. 2, pp. 39–46, 2013.
- [55] A. Solanki, S.-T. D. Chueng, P. T. Yin, R. Kappera, M. Chhowalla, and K.-B. Lee, “Axonal alignment and enhanced neuronal differentiation of neural stem cells on graphene-nanoparticle hybrid structures,” *Advanced Materials*, vol. 25, no. 38, pp. 5477–5482, 2013.
- [56] Y. Wang, W. C. Lee, K. K. Manga et al., “Fluorinated graphene for promoting neuro-induction of stem cells,” *Advanced Materials*, vol. 24, no. 31, pp. 4285–4290, 2012.
- [57] H. Yoon, S. H. Ahn, and G. H. Kim, “Three-dimensional polycaprolactone hierarchical scaffolds supplemented with natural biomaterials to enhance mesenchymal stem cell proliferation,” *Macromolecular Rapid Communications*, vol. 30, no. 19, pp. 1632–1637, 2009.
- [58] D. Yang, T. Li, M. Xu et al., “Graphene oxide promotes the differentiation of mouse embryonic stem cells to dopamine neurons,” *Nanomedicine*, vol. 9, no. 16, pp. 2445–2455, 2014.
- [59] S. Y. Park, J. Park, S. H. Sim et al., “Enhanced differentiation of human neural stem cells into neurons on graphene,” *Advanced Materials*, vol. 23, no. 36, pp. H263–H267, 2011.
- [60] M. Tang, Q. Song, N. Li, Z. Jiang, R. Huang, and G. Cheng, “Enhancement of electrical signaling in neural networks on graphene films,” *Biomaterials*, vol. 34, no. 27, pp. 6402–6411, 2013.

Review Article

Peptide Self-Assembled Nanostructures for Drug Delivery Applications

Taotao Fan,¹ Xiaoyan Yu,² Bing Shen,¹ and Leming Sun³

¹*School of Basic Medical Sciences, Anhui Medical University, Hefei, Anhui 230032, China*

²*International Center for Automotive Research, Clemson University, Greenville, SC 29607, USA*

³*Department of Biomedical Engineering, College of Engineering, The Ohio State University, Columbus, OH 43210, USA*

Correspondence should be addressed to Bing Shen; shenbing@ahmu.edu.cn and Leming Sun; sun.1342@osu.edu

Received 3 February 2017; Accepted 21 February 2017; Published 24 April 2017

Academic Editor: Chuanfei Guo

Copyright © 2017 Taotao Fan et al. This is an open access article distributed under the Creative Commons Attribution License, which permits unrestricted use, distribution, and reproduction in any medium, provided the original work is properly cited.

Peptide self-assembled nanostructures are very popular in many biomedical applications. Drug delivery is one of the most promising applications among them. The tremendous advantages for peptide self-assembled nanostructures include good biocompatibility, low cost, tunable bioactivity, high drug loading capacities, chemical diversity, specific targeting, and stimuli responsive drug delivery at disease sites. Peptide self-assembled nanostructures such as nanoparticles, nanotubes, nanofibers, and hydrogels have been investigated by many researchers for drug delivery applications. In this review, the underlying mechanisms for the self-assembled nanostructures based on peptides with different types and structures are introduced and discussed. Peptide self-assembled nanostructures associated promising drug delivery applications such as anticancer drug and gene drug delivery are highlighted. Furthermore, peptide self-assembled nanostructures for targeted and stimuli responsive drug delivery applications are also reviewed and discussed.

1. Introduction

Molecular self-assembly is organizing molecules into a stable and well-defined structure under equilibrium conditions through noncovalent interactions spontaneously, which is a powerful tool in the synthesis of functional nanostructures as a bottom-up fabrication method for biomedical applications [1, 2]. Self-assembly with a variety of complex nano- and microstructures is founded in nature [3–6]. Mechanisms underlying self-assembly have been applied in many areas to prepare functional materials. In most cases, a thermodynamically stable structure is formed through enthalpic and entropic interactions that involve the basic assembling units and the reacting solvent molecules [7, 8]. Electrostatic interactions, hydrophobic interactions, hydrogen bonding, π - π stacking, and so on together make sure molecules are at stable low energy levels [9]. The self-assembly process also gives the flexibility of developing many functional materials with the desired tunable properties and structures by single molecule design and fabrication [5, 10, 11].

Recently, many self-assembly nanostructures have been synthesized from biomaterials including carbohydrates, nucleic acids, and peptides to achieve a better understanding of the self-assembly mechanism and utilize them for several biomedical applications such as tissue regeneration, drug delivery, and biosensors [12–17]. Many self-assembling systems have been developed for various biomedical applications; peptide self-assembled nanostructures remain one of the most promising directions for many reasons [18]. They are easily fabricated using solid-phase peptide methods where the peptide sequence could be specifically modified at molecular levels [19]. Custom molecular structures can be designed and synthesized through tuning the peptide basic units. Naturally occurring structures occurred in proteins such as α -helices and β -sheets that can be utilized for driving the self-assembly processes [20–22]. Moreover, the self-assembly process is also very important in the functions of cell-penetrating peptides that could play an important role in delivering the drugs inside the cell membrane and transporting genes into the nucleus [23].

Peptides consisting of natural or synthetic amino acids are basic repeating units for the construction of molecular assemblies. These simple structures help us better understand the complex biological systems and underlying mechanisms. Researchers have utilized various approaches in the synthesis of peptide building units while minimizing other possible by-products [24]. To self-assemble peptides into nanostructures, there are mainly three approaches: solid-phase peptide synthesis, ring-opening polymerization, and protein engineering [25]. The solid-phase peptide synthesis is utilized to precisely control the peptide structure with short or medium sequences. Although this method has very high yield, the synthetic sequence is less than 70 amino acids [26]. Researchers have also utilized protein engineering to fabricate peptides with longer sequences and more defined structure such as collagen and silk materials through expression in bacteria [27–29]. For large-scale production of polypeptides, people have utilized ring-opening polymerization. In this method, cyclic monomers are introduced to the end of the sequences to form a longer peptide. On the other hand, a lower accuracy of the peptide primary structure than other methods such as solid-phase peptide synthesis is noticed using this method [25].

Several reviews have been focused on the morphologies, functions, or biomedical applications of peptide self-assembled nanostructures in tissue engineering rather than drug delivery applications [24, 30–32]. There is still a need for a comprehensive review on the peptide self-assembled nanostructures for drug delivery applications. In this paper, self-assembled peptide types and structures including dipeptide, cyclic peptide, amphiphilic peptide, α -helical peptide, and β -sheet peptide as basic building blocks are introduced. Meanwhile, some relevant peptide self-assembly mechanisms are also discussed. More importantly, peptide self-assembled nanostructures for anticancer drug delivery, gene drug delivery, and targeted and stimuli responsive drug delivery applications are reviewed and discussed.

2. Peptide Types and Structures for Self-Assembly

Peptides can be assembled into different nanostructures in Figure 1 including nanotubes, nanofibers, and nanovesicles based on their design and self-assembly conditions [33]. Different types and structures of peptides including dipeptides, cyclic peptides, amphiphilic peptides, α -helical peptides, and β -sheet peptides have been utilized to self-assemble into nanostructures.

2.1. Dipeptide. Recently, researchers have claimed that short peptides have the ability to self-assemble into many different nanostructures that can minimize the difficulty and cost of the fabrication process and simultaneously enhance the stability [35, 36]. Among them, dipeptide self-assembled nanostructures are investigated intensively for various biomedical applications including drug delivery. Diphenylalanine, Phe-Phe (FF), the first reported dipeptide that has been used for the self-assembly of different nanostructures, is a core motif of the amyloid- β polypeptide segment [37]. It has been

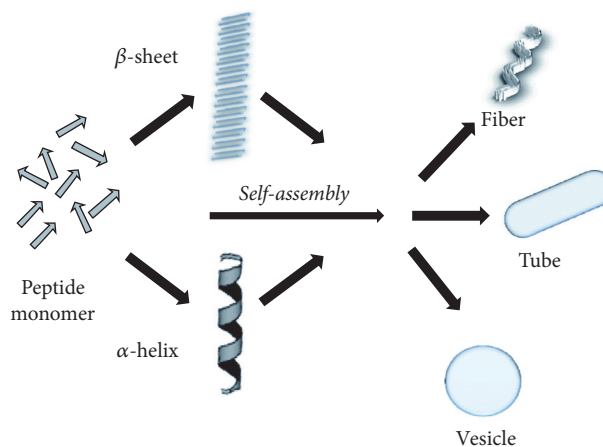


FIGURE 1: Peptides self-assembled into different nanostructures. Reproduced from [33] with permission from the Royal Society of Chemistry.

recognized as the core recognition motif to drive self-assembly in Alzheimer's disease. Many studies have been carried out to self-assemble FF dipeptides into different nanostructures including nanoparticles, nanotubes, nanovesicles, and nanowires, shown in Figure 2 [34, 38–42]. FF self-assembled nanotubes have been demonstrated to be thermally stable, which is one of the most unique properties for bioinspired materials [43]. The high yield of FF dipeptides self-assembled nanotubes was achieved through vapor deposition method, which could tune the density and length of nanotubes by controlling the monomer supply [38]. FF self-assembled nanotubes were also obtained through dissolving the dipeptides in water by sonication followed by heating. Meanwhile, FF self-assembled nanowires were achieved in water at high ionic strength. Both FF dipeptides self-assembled nanotubes and nanowires are interconvertible. These two nanostructures have been studied for mechanical applications including biosensors, nanodevices, and conducting nanomaterials [44, 45].

Hydrophobic dipeptides such as LL, LI, and LF can also self-assemble into nanotubes through hydrogen bonding. The water molecules filled nanotubes from the dipeptide WG showed negative thermal expansion, which later was utilized to form nanoporous structures from dipeptides FF, LS, IV, VI, VA, and AV [46–48]. These dipeptide self-assembled nanoporous materials have been demonstrated to absorb and store many different gasses including carbon dioxide, methane, and hydrogen [49–51]. Introducing a thiol group in FF dipeptides can change their formation from tubular to spherical nanostructures. Nanospheres, nanoplates, nanofibrils, and hydrogels were further developed from the self-assembly of several aromatic homodipeptides [52, 53]. These dipeptide self-assembled nanostructures can be applied for casting mold to fabricate conductive nanowires and for many different biomedical applications including biosensing, tissue engineering, bioimaging, and drug delivery [53–55].

Modified dipeptides also could be used as templates for self-assembling nanostructures with tunable biological

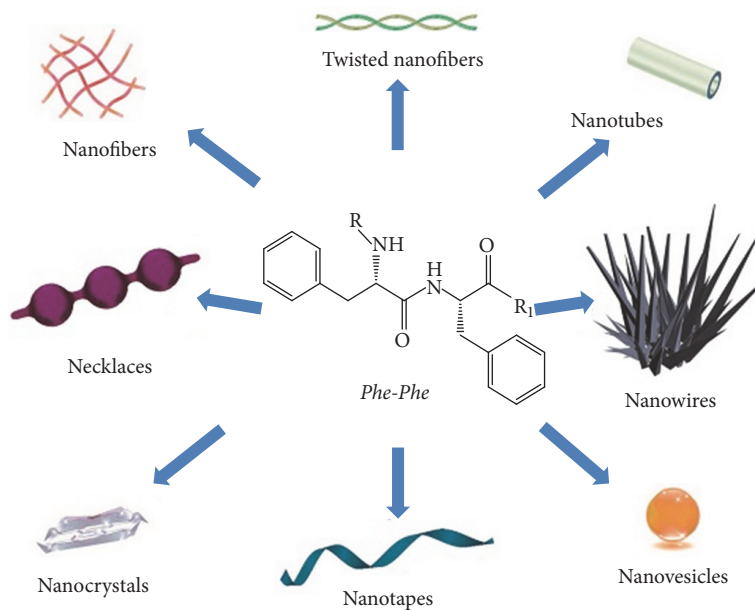


FIGURE 2: Dipeptide Phe-Phe self-assembled into diverse nanostructures. Reproduced from [34] with permission from the Creative Commons Attribution License.

functions [56]. The modified dipeptides containing an N-terminal ω -amino acid could self-assemble into nanotubes in the solid state and in aqueous solutions [57]. The morphological studies revealed the self-assembly of uniform and well-organized nanotubes with various dimensions. These modified dipeptide self-assembled nanostructures are significantly different from the solid-state or solution methods, which demonstrated that the self-assembly mechanisms in these two strategies are different [58]. Therefore, water molecules with hydrogen bonding capacities could have an important function in the self-assembly or even stabilization of the nanotubes.

Except for the dipeptides self-assembled nanostructures, there are also many other short linear peptides self-assembled nanostructures for biomedical applications including drug delivery [59, 60]. For example, KLVFF, a short peptide from amyloid-beta peptides self-assembly mechanism from Alzheimer's disease, could also self-assemble into nanofibrous structures and then hydrogel format in a concentrated phosphate buffered saline solution. The experimental results from physical and chemical characterizations have demonstrated that the linear short peptides can self-assemble into β -sheet structures and then form nanofibrillar hydrogel structures through electrostatic interactions [59]. Moreover, the short linear peptides DFNK and DFNKF both have been demonstrated to self-assemble into nanofibril structures based on the effects of pH values. These peptides have aromatic and charged side chains in the peptide sequences [60].

2.2. Cyclic Peptide. Cyclic peptides with alternating D type and L type amino acids that could self-assemble into nanotubes were determined theoretically as early as 1974 [61]. However, the first self-assembled nanotube using cyclo-(L-Gln-D-Ala-L-Glu-D-Ala)₂ cyclic peptides was achieved in

1993 based on that theory [62]. The cyclic peptide self-assembly is formed through aggregating cyclic peptides as basic building blocks to a flat conformation structure where the amino and carbonyl side chains are arranged perpendicular to the ring [63]. The cyclic peptide self-assembled nanotubes were self-assembled and stabilized by hydrogen bonding between amide groups shown in Figure 3 [64]. Due to the alternating D type and L type amino acids, the peptide side chains could be formulated on the outside area that can create a nanotube structure. There are many cyclic peptide sequences that can be used for the self-assembly, including alternating D type and L type α -amino acids, alternating α - and β -amino acids, β -amino acids, and δ -amino acids [62, 63, 65, 66].

In comparison to the other peptide self-assembled nanostructures, cyclic peptide self-assembled nanotubes have unique properties such as precise diameter controls, which could be tuned through the peptide sequences and lengths. The functions of the nanotubes could also be tuned by modifying the peptide side chains [63]. For instance, the internal diameter of the cyclic peptide could increase from 2 Å to 13 Å after increasing the peptide length from 4 to 12 amino acids [2, 66]. Moreover, the eight-residue cyclic peptides with the sequence of cyclo-(L-Gln-D-Ala-L-Glu-D-Ala)₂ can not only self-assemble into nanotube structures, but also self-assemble into nanoparticles with different methods and self-assembly parameters shown in Figure 4 [18].

For example, cyclic peptide self-assembled nanotubes have been prepared using eight-residue cyclic peptides containing Glu and Cys amino acids, which have been demonstrated for drug delivery applications [67]. The results have claimed that polyethylene glycol modified doxorubicin loaded nanotubes have high drug encapsulation ratio. More importantly, compared to free doxorubicin, the polyethylene

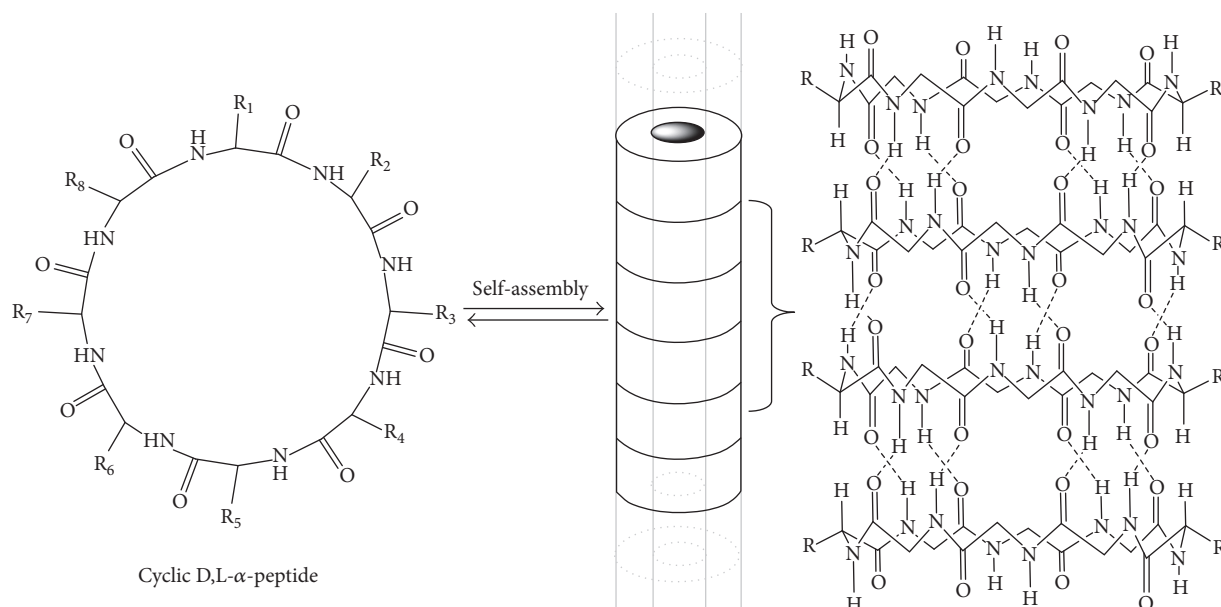


FIGURE 3: The schematic of the eight-residue cyclic D,L- α -peptide self-assembled nanotubes through hydrogen bonding. Reprinted with permission from Macmillan Publishers Ltd.: Nature [64].

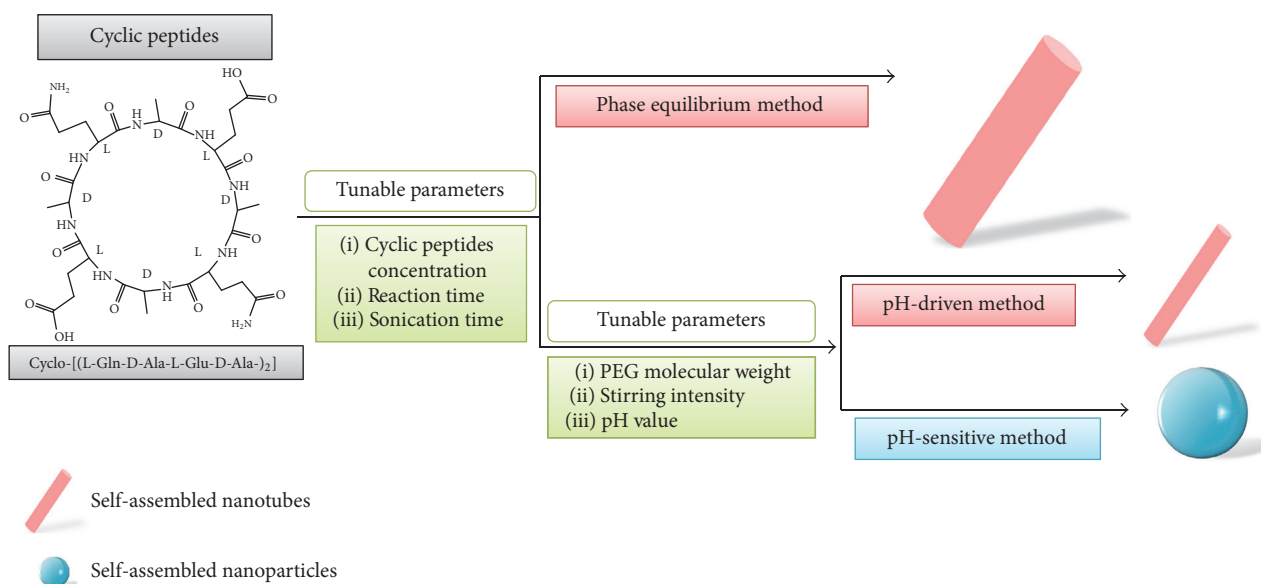


FIGURE 4: Schematic of the eight-residue cyclic peptides self-assembled nanotubes and nanoparticles. Reproduced from [18] with permission from the Royal Society of Chemistry.

glycol modified nanotubes with doxorubicin have been demonstrated to be with higher cytotoxicity and raised DOX uptake in human breast cancer MCF-7/ADR cells in vitro. Moreover, the polyethylene glycol modified nanotubes with doxorubicin have shown their potential in multidrug resistance tumor therapy [67].

2.3. Amphiphilic Peptide. Amphiphilic peptides have many different types such as linear peptides, ionic complementary peptides, peptide phospholipids, and long-chain alkylated peptides [68, 69]. Amphiphilic peptides are generally formed

from hydrophilic peptide head groups and hydrophobic tails that could be used to form various secondary and tertiary conformations [70, 71]. These peptides could self-assemble into nanostructures with many different morphological structures including nanovesicles, nanotubules, and nanomicelles [69, 72]. The electrostatic and hydrophobic interactions are thought to be the main factors that drive the self-assembly for amphiphilic peptides [73].

Linear peptides with hydrophobic tails and hydrophilic heads have the ability to self-assemble into different nanostructures depending on their chemical properties and

physical properties. For the hydrophobic tail, A, G, L, and F amino acids are good candidates. On the other hand, the amino acids D, E, H, and R are always utilized in the hydrophilic domains [74]. For example, lipid-like peptides similar to surfactants, such as G₄DD, G₆DD, G₈DD, A₆D, A₆K, and KA₆ sequences, can self-assemble into various nanostructures once they reach the critical aggregation concentration [73, 75]. Because they are very similar to phospholipids, those peptides have the potential to stabilize membrane proteins.

The ionic complementary self-assembling peptides EAK16 were first discovered in 1993 with the formation of nanofibers [76]. These peptides have charged side chains in one side group and hydrophobic chains in another side group. The hydrophobic side chains could form a sheet structure inside the nanofibers. Meanwhile, the charged side chains could be laid on the outside of the nanofibers. Therefore, a stable structure could be formed from the repeated positively and negatively charged amino acids in the peptides sequences through ionic complementary forces [77]. Finally, they can self-assemble into typical β -sheet structures and then form a hydrogel structure which is composed of nanofibers. These hydrogels could be very stable under various ranges of conditions such as pH, temperature, and organic solvents because of the hydrogen bonding and ionic force [78].

Transparent hydrogels could be formed in seconds using amphiphilic peptides as soon as they react with physiological fluids [79]. This ionic complementary self-assembled peptide hydrogel is composed of more than 99% water. Therefore, there are plenty of spaces between the nanofibers inside the hydrogels. These types of peptide self-assembled nanostructures have been utilized to advance cell growth and differentiation in bone, cartilage, heart, and neural systems [80–85].

2.4. α -Helical Peptide. For decades, it has been well known that biological and physical properties can enhance the self-assembly of peptides into helical structures. Actuarially, there are only several major molecules that have been discovered with the purpose of self-assembling these helical structures into nanostructural biomaterials. The α -helical peptides have drawn researchers' attention because they can form nanostructures that are very common in the cytoskeleton and extracellular matrix in biological systems [86]. For example, these filamentous nanostructures could be formed from α -helical peptides with 25–50 amino acids [87]. The α -helical peptides with 2–5 helices can aggregate around each other to form nanofibers [88, 89]. These α -helical peptides can also self-assemble into nanofibers using around 30-amino-acid-long peptides through helical coiled-coils structures [90]. The hydrophobic residues could promote the helix oligomerization through hydrophobic collapse. Another nanofibrous structure could also be formed using the peptides with central Glu amino acid and Lys amino acid at the end of the sequence through ionic interactions [91].

Hydrogels could also be self-assembled from helical peptides with triblock motifs that have coiled-coil blocks [92]. Through the repeated hydrophobic and charged amino acids

in the peptide sequence, coiled-coil structures could be self-assembled from α -helices [93]. Moreover, through tuning the length and structure of the basic coiled-coil units, the hydrogel properties also could be managed [94]. Therefore, these materials could be proposed to be a stimuli responsive hydrogel for drug delivery applications.

2.5. β -Sheet Peptide. The β -sheet is one of the most useful naturally occurring motifs that can be used for peptide self-assembly [95]. Tremendous peptides have been studied for self-assembling β -sheet secondary structures. The β -sheet consists of alternating hydrophilic and hydrophobic amino acids in the peptide sequence, which can provide amphiphilic property to the peptide that drives the self-assembly of β -sheets [96]. The β -sheet peptides also could be utilized to form many different nanostructures including nanotubes, monolayers in nanoscale order, and nanoribbons [97–101]. For example, β -sheet peptide QQRFEWEFEQQ can self-assemble into a pH responsive hydrogel using peptides' ionizable side chains from Glu and Arg amino acids. These peptides are soluble in neutral pH condition and transform to a hydrogel structure at low pH conditions [97]. The reason is that antiparallel β -sheet tapes were formed at lower pH values and then stacked together to form nanofibrils in hydrogels. The β -hairpin peptides were also found to self-assemble into various nanostructures at the water and air interfaces [102]. The self-assembly of β -hairpins in proteins is based on the arrangement of two β -sheets in antiparallel formats. A β -hairpin peptide with the sequence of VKVKVKVKVDPP-TKVKVKV was utilized to form responsive hydrogels. This material could be formed from the increase of the pH values. The underlying mechanism is that the hydrogels could be formed from the hairpin structure that was self-assembled from β -sheets formation after the increase of the pH values [103].

3. Peptide Self-Assembly Mechanisms

Electrostatic interaction, hydrophobic interaction, hydrogen bonding, and π - π stacking are the key contributors of peptide self-assembly [104]. Nonpolar amino acids, such as aromatic and aliphatic amino acids, are mainly responsible for hydrophobic aggregation through π - π stacking and hydrophobic interactions. Polar amino acids result in either electrostatic interactions or hydrogen bonding depending on whether they have uncharged or charged residues [105]. Besides individual amino acids, the peptide backbone itself also provides considerable stability through hydrogen bonds.

3.1. Electrostatic Interaction. Electrostatic interactions involve both attractive and repulsive forces between charged residues from amino acids in the peptide self-assembly, which also have strong effects on many other self-assembly processes. Positively charged peptides have the ability to aggregate with negatively charged peptides or even drugs by electrostatic interactions. After that, they could form a stable nanostructure that could be used for drug delivery applications [106]. For instance, a multifunctionalized peptide self-assembled nanostructure was designed and synthesized using

cRGD-BSA and KALA cell-penetrating peptides through electrostatic interaction. These nanostructures could be used for targeted and pH responsive anticancer drug delivery applications [107].

3.2. Hydrophobic Interaction. The hydrophobic interaction is one of the most important effects among various noncovalent interactions in the peptide self-assembly process. The self-assembly of amphiphilic peptides could be readily accomplished through microphase separation driven by thermodynamics because of the coexistence of polar and nonpolar regions inside the peptide sequences. In the aqueous reaction condition, the nonpolar segments of the basic units will collapse and cluster together to try to hide the hydrophobic area from water. Meanwhile, the polar areas attempt to enhance their contact with water [108, 109]. For instance, amphiphilic drugs that can be self-assembled into nanostructures were developed based on hydrophobic interactions. The amphiphilic drugs are composed of a tau protein derived peptide conjugated with a hydrophobic anticancer drug camptothecin. These materials could be self-assembled into fibril structures through hydrophobic interactions and intermolecular hydrogen bonding [110].

3.3. Hydrogen Bonding. Naturally occurring hydrogen bonding patterns such as those found in α -helices, β -sheets, and coiled coils are utilized for the design of various peptide sequences to self-assemble into nanostructures. Hydrogen bond is the electrostatic attraction between H atom and a highly electronegative atom nearby, such as N and O. Hydrogen bonding has a key role in the formation and stabilization of the peptide secondary structure and protein folding. Actually, among different noncovalent interactions, hydrogen bonding is probably the most important one in peptide self-assembly. The stabilization of multiple peptide backbone arrangements is based on hydrogen bonding interactions through the amide and carbonyls groups in the backbone. After that, they can self-assemble into β -sheet structures. These structures could be in parallel or antiparallel arrangements according to the direction of the peptide sequences. Peptide is typically designed to contain repeating amino acid residues for hydrophobic and hydrophilic regions. Therefore, the hydrophobic part will be buried within the self-assembled nanostructure while the hydrophilic region is exposed to the aqueous environment [111]. Unlike β -sheets, α -helices are formed by individual peptide chains where backbone amide components are intramolecularly hydrogen bonded. This arrangement leads to the presentation of side chains from amino acids on the surface of each helix and further facilitates the accessibility of them in the solvent.

3.4. π - π Stacking. The π - π stacking can promote the peptide self-assembly, especially for aromatic peptides. The interactions for π - π stacking can drive directional growth and they are robust in water due to their limited solubility of molecules containing aromatic groups [112]. The π - π stacking is also a more distinct driving force in pure organic solvents such as toluene and TFA. These solvents can make the π - π stacking more dominant than other self-assembly effects [40]. For the

dipeptide FF self-assembly process, π - π stacking from the aromatic groups and hydrogen bonding stabilized the self-assembled FF nanostructures, which have been demonstrated for various applications including drug delivery [43, 113].

In summary, noncovalent interactions play very important roles in the peptide self-assembly processes. As these noncovalent interactions are easily affected by the external stimuli, these factors including pH values, temperature, and reaction solvent polarity can also trigger the self-assembly and manipulate the self-assembly process and even the final formed nanostructures. For example, pH values are very important for peptides with charged amino acids such as Glu, Asp, Lys, His, and Arg. The status of these peptides with negative or positive surface charges could be sensitively affected by the pH values and then self-assembled into different nanostructures [18]. Tunable management of the physical and biological properties of peptide self-assembled nanostructures is highly desired for their successful utilization in drug delivery applications. When designing peptide self-assembled nanostructures for drug delivery, noncovalent interactions, as well as peptide types and structures, should be taken into consideration and be rationally applied in the strategies.

4. Drug Delivery Applications of Peptide Self-Assembled Nanostructures

In the past decades, peptide self-assembled nanostructures with various sizes and shapes have been fabricated and utilized for many biomedical applications such as tissue regeneration, biosensors, bioimaging, and drug delivery. In this section, peptide self-assembled nanostructures for anticancer drug and gene drug delivery as well as targeted and stimuli responsive drug delivery are illustrated and discussed in detail. The most desired properties for self-assembled nanostructures are biocompatibility, biodegradability, and multifunctionality for drug delivery applications [17, 114]. Compared to other organic materials for drug delivery, peptide self-assembled nanostructures are more suitable due to their intrinsic physical and biological properties.

4.1. Anticancer Drug Delivery. Although tumors are one of the most deadly diseases worldwide, the proper therapy strategy is still far away from the real demand. Therefore, there is still a need for new materials or methods for cancer therapy. Nanomaterials as drug delivery carriers have many advantages including high efficiency for drug loading, a low ratio for drug loss, and high stability to avoid body clearance [115]. For example, nanostructures could be used for anticancer drug delivery because they have the ability to both enhance the therapeutic efficiency and decrease unwanted negative reactions. Among various nanostructures, peptide self-assembled nanostructures have attracted increasing attention for anticancer drug delivery and are believed to be a promising strategy for cancer treatment. The peptide has the ability to self-assemble into many different nanostructures such as nanoparticles, nanotubes, nanovesicles, and nanofibers that form hydrogels [116]. All of them could be used to deliver different types of anticancer drugs

for cancer therapy. For instance, the peptide with amphiphilic properties could self-assemble into nanovesicle structures, which have been demonstrated to deliver hydrophobic anticancer agents for cancer therapy. Meanwhile, the outside layer of these nanostructures could be tuned to achieve specific drug delivery purposes [117]. Peptide self-assembled hydrogel with injectable properties could also be used to directly come into contact with the tumor sites to enhance the efficacy and safety of tumor therapy [118]. Peptide self-assembled nanotubes also could be utilized for cancer therapy through conjugation with doxorubicin in high efficiency [113]. There are many different anticancer agents including doxorubicin, curcumin, fluorouracil, and paclitaxel that have been loaded in the peptide self-assembled nanostructures and investigated in preclinical or clinical trials for cancer therapy. Recently, there is much more progress in cancer therapy from peptide self-assembled nanostructures because of their excellent biodegradability and biocompatibility.

The peptide self-assembled nanofibers that form injectable hydrogels could be the most interesting materials for anticancer drug delivery applications, because, in this way, the chemotherapeutic drugs could directly come into contact with the targeted cancer tissues at higher local concentrations compared with traditional cancer therapy methods. These peptide hydrogels could be more safe and controllable due to their slow release rates. For instance, stimuli forming hydrogels self-assembled from KLD motifs can be used to tune the release of conventional cytotoxic anticancer drugs such as doxorubicin [118].

The nanofiber structures which self-assembled from the EAK peptides have been demonstrated to deliver anticancer drug ellipticine through encapsulation method. Two methods were used for the analysis of the self-assembly and drug delivery applications. The first one is the UV-based approach. In this method, the result revealed that the conjugation between the peptide and anticancer drug ellipticine was based on electrostatic interactions. Moreover, this method also could be used to detect the efficiency of drug loading in the peptide self-assembled nanostructures. The second approach is to use fluorescence technologies, which have the ability to monitor the conjugation process and efficiency. From the results, we could detect the concentrations of anticancer drug ellipticine in the whole self-assembly and delivery process through monitoring the fluorescence properties. The *in vitro* experiments also demonstrated that the encapsulated anticancer drug ellipticine in the self-assembled nanofibers in protonated stage is more efficient than in the crystalline stage for cancer therapy. These EAK peptide self-assembled nanostructures and the two encapsulation methods could also be used for some other anticancer agents in drug delivery for cancer therapy [119].

Dendrimer tetrapeptide GFLG self-assembled into compact nanoparticles with negatively charged surfaces after conjugation with PEG and anticancer drug doxorubicin. The drug loading and releasing experiments have demonstrated the 9.62 wt% drug loading efficiency as well as the enzyme responsive drug delivery applications. Fluorescent and cell studies revealed stable and effective cancer therapy compared with free doxorubicin anticancer drugs. Moreover, this study

showed the decreased toxicities from doxorubicin anticancer drug as well as nondetectable side effects [120]. In addition to that, peptide self-assembled multifunctional nanostructures with dual-functional liposomes have also been developed for targeted drug delivery in cancer therapy. This system could be used for anticancer drug delivery through conjugation with cell-penetrating peptide and active targeting agents. In this study, R6H4 was screened for pH responsive anticancer drug delivery purposes. Hyaluronic acid was used to coat the R6H4 peptides due to their rapid degradation property. The *in vitro* and *in vivo* experiments have demonstrated that these nanocarriers could enhance the efficiency of tumor-targeted drug delivery in cancer therapy, as shown in Figure 5 [121].

Peptide-based hybrid nanostructures were also fabricated from polylactide (PLA) and VVVVVVKK (V6K2) peptides [75]. These nanostructures could conjugate with doxorubicin and paclitaxel for anticancer drug delivery in cancer therapy applications. The pure PLA nanoparticles have a diameter of around 130 nm, but the PLA-V6K2 self-assembled nanoparticles only have a diameter of around 100 nm. The encapsulation and anticancer drug releasing ratios for PLA-V6K2 nanoparticles are significantly higher and slower than the pure PLA nanoparticles. Moreover, the experiments have demonstrated that the PLA-V6K2 nanoparticles conjugated with anticancer drugs have higher toxicity to cancer cells and no toxicity to normal cells compared with free doxorubicin or paclitaxel and pure PLA nanoparticles conjugates. Therefore, this study demonstrated the higher efficacy of these PLA-V6K2 nanoparticles for anticancer drug delivery that could be potentially useful in cancer therapy [123].

4.2. Gene Drug Delivery. The great progress in biotechnology, as well as many other fields with better acknowledgment of the pathology mechanisms for various diseases from the gene levels, has promoted a big change in many different diseases' diagnosis and therapy. Researchers have used recombinant plasmid DNA as a gene drug for delivery to the specific target for gene therapy. In this way, the functional proteins from the related gene encoding could be applied to heal patients. The gene drug delivery needs cost-effective methods and noninvasive approaches for this specific gene disease therapy [124]. Although more and more attention has been paid to gene therapy, there is still huge enhancement needed for the study of nonviral gene drug delivery platforms currently. For example, the nanocarriers for gene drug delivery should be improved through different perspectives including toxicity, immunogenic response, and poor uptake into cells and the nucleus [125, 126]. Therefore, attention for the design and fabrication of nanostructures for gene drug delivery should be paid to the enhancement of cellular delivery, specific delivery, and improvement of loading efficacy. Cationic nanostructures have been intensively studied and utilized because they are easier to be delivered into cells and because of their high loading capacity for nucleic acids [127]. Most importantly, peptide self-assembled nanostructures present a very promising and efficient method for gene drug delivery due to their intrinsic properties and precisely controllable fabrication approaches. Peptide self-assembled nanotubes also could be used for gene drug delivery through the

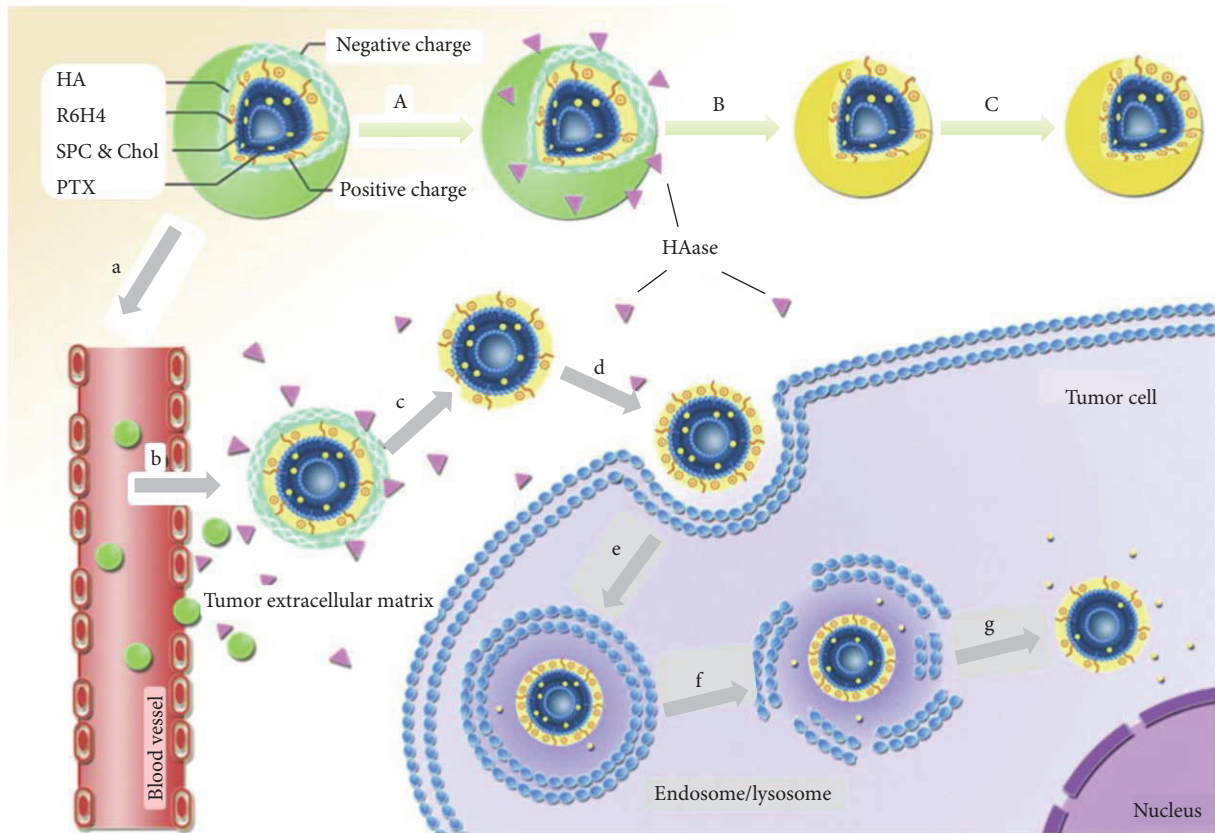


FIGURE 5: Schematic design of the multifunctional nanostructures for tumor-targeted drug delivery. Reprinted from [121] with permission from Elsevier.

transforming of nanotube structures into nanovesicles in the endocytosis process [128]. Therefore, many conjugations of gene drugs and peptide self-assembled nanostructures have been developed recently for the gene drug delivery systems [129].

The surfactant peptide could be self-assembled into nanotubes or nanovesicles with a diameter of around 50 nm. This type of surfactant peptide was designed based on the cationic lipid systems for better gene drug delivery applications. The peptide monomers are around 2 nm in length. The head of the peptide is cationic and hydrophilic with one or two Lys and His amino acids. After that, there are six amino acids including Ala, Val, or Leu to form the peptide tail with hydrophobic properties. When the pH values are higher than the pI, these nanostructures could be further self-assembled into nanosheet structures. Because of the unique self-assembly and charge properties, these cationic peptides self-assembled nanostructures could be very useful to conjugate negatively charged DNA and RNA for efficient gene drug delivery applications [75].

A peptide including four segments conjugated with the lipopeptide transfection gene drugs has been developed recently for gene drug delivery applications in gene therapy. The peptide is composed of cysteine, lysine, histidine residues, and the alkyl chains. These nanostructures were self-assembled for the delivery of gene drugs into cells

through histidine residues. The delivery of gene drugs into the nucleus was promoted by the lysine residues with charges at neutral pH values. Therefore, after the design, synthesis, and evaluation, these peptide self-assembled nanostructures have been demonstrated to be with high transfection efficiency for gene therapy through gene drug delivery [130].

A targeting peptide GE11 with branched structures has been developed and self-assembled into nanostructures with other components for gene drug delivery as shown in Figure 6; the peptide-based nanostructures were composed of the GE11 targeting peptide, branched polyethyleneimine, S-S bond, and polyethylene glycol [122]. The experimental results have demonstrated that both GE11 and branched GE11 self-assembled nanostructures have efficient capability for gene condensing and transfection. Moreover, they also have low toxicity and increased capability for targeting. Most importantly, compared to the GE11 self-assembled nanostructures, the branched one has a higher capability for targeting cancer cells with overexpressed EGFR. Therefore, this study has demonstrated that the peptide self-assembled nanostructures could be very useful for gene drug delivery in gene therapy.

One of the most important properties of peptide self-assembled nanostructures for gene drug delivery is the conjugation between these nanostructures with DNA. Moreover, because of the easier modification and tunability of the

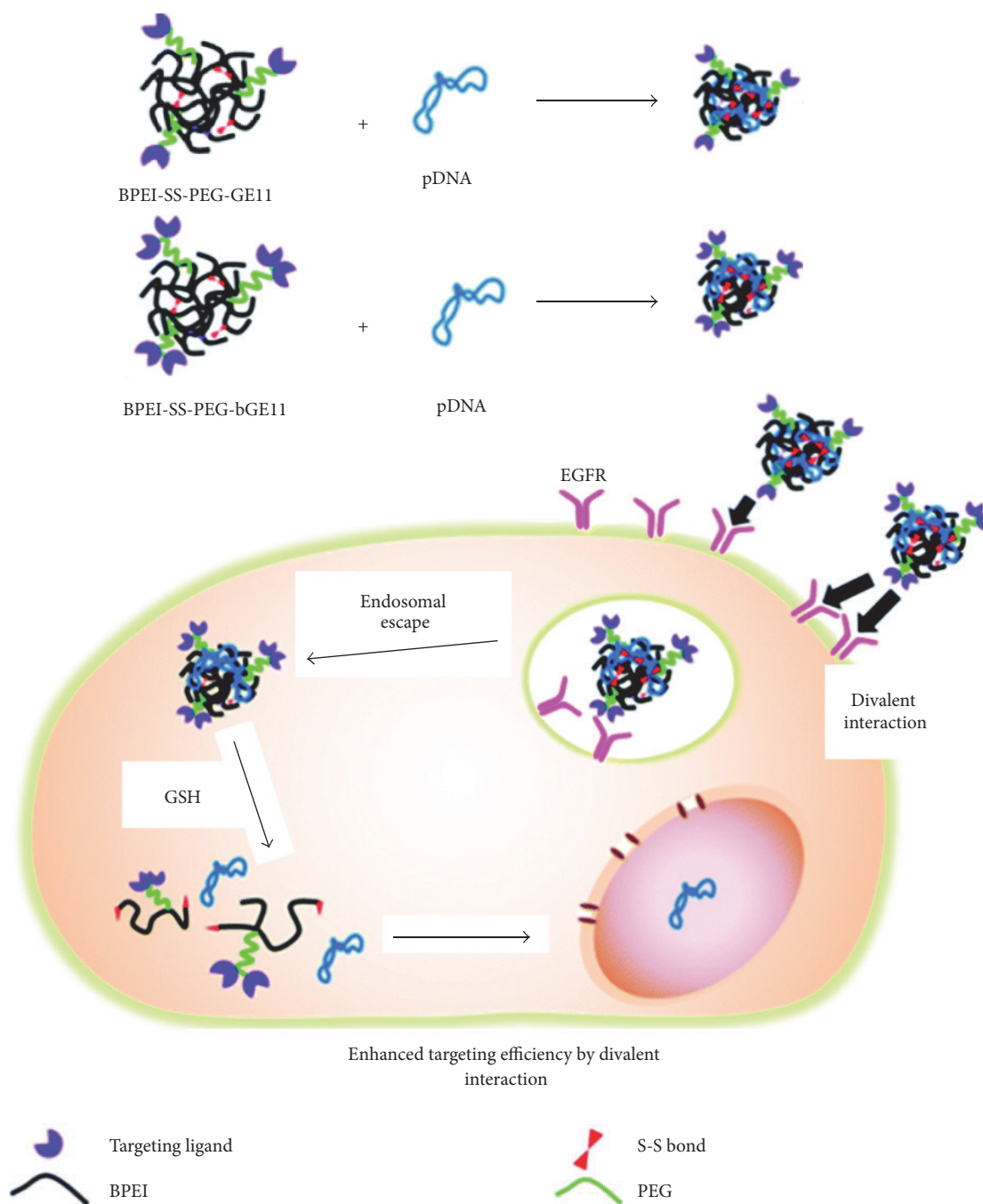


FIGURE 6: Schematic of gene drug delivery by using GE11 peptide-based self-assembled nanostructures. Reproduced from [122] with permission from the Royal Society of Chemistry.

peptide building blocks, these peptide self-assembled nanostructures could also increase the DNA uptake through cell membrane and nucleus. They also have the ability to control the gene drug release and enhance gene expression [131]. Therefore, researchers could focus on developing vectors with improved efficiency, safety, and specificity. Although there are several studies using peptide self-assembled nanostructures for gene drug delivery, it is still far away from the real demand.

4.3. Targeted Drug Delivery. For drug delivery applications, specific targeting with desired sites is very important for the nanocarriers to deliver or transport the drugs efficiently [132]. For this purpose, peptides self-assembled nanostructures have many advantages such as easier modification properties and tunable design of the recognition motifs. For example, cell-penetrating peptides are cationic peptides with less than 30 amino acids, which could be used to

promote the penetration of the cell membrane to make the drug or gene delivery more efficient [133]. Most importantly, the self-assembly mechanism is also very important for the enhanced membrane transport using cell-penetrating peptides. Besides that, there are also many other proteins or aptamers that could be used to enhance cell penetrating or specific targeting especially for cancer cells or disease sites. For example, dipeptide WF self-assembled nanoparticles have been developed for targeted drug delivery for cancer therapy [15]. These peptide self-assembled nanoparticles have visible fluorescent properties compared to amino acids' intrinsic UV range fluorescent properties. The self-assembly and fluorescence generation mechanisms are inspired from the green fluorescent protein (GFP) and yellow fluorescent protein (YFP). Through that, this dipeptide including tryptophan and phenylalanine could self-assemble into blue light fluorescent nanoparticles through π - π stacking and zinc coordination interactions. The experimental results have demonstrated that these nanostructures are biocompatible and photostable, except the blue color fluorescent properties with a narrow emission wavelength. Most importantly, these dipeptides self-assembled nanoparticles could conjugate with MUC1 aptamer and anticancer drug doxorubicin to target specific cancer cells for better delivery and cancer therapy applications [15]. These studies revealed the potential and advantages of using peptide self-assembled nanostructures for targeted drug delivery applications.

The peptide self-assembled nanostructures could be in many different formats that have the advantages of specific targeting and could conjugate with many drugs such as anticancer and gene drugs for the delivery system [134, 135]. For example, one functional nanostructure could be self-assembled with many different targeting peptides and drugs with multiple purposes. The supramolecular nanoparticles self-assembled with specific targeting motifs including cancer cells and nucleolus have been developed for targeted drug delivery in tumor therapy and gene therapy [136, 137]. The functional peptides with lots of arginines could be used to bind with RNA sites for condensed siRNA for the targeted gene drug delivery applications in this system. The tumor cell targeting peptides could also be introduced into this system for the targeted anticancer drug delivery for cancer therapy. The electrostatic interactions play the main role in the self-assembly processes. The experimental results have demonstrated that these peptide self-assembled nanostructures could specifically target the hepatocellular carcinoma cells efficiently.

A capsid-like nanostructure self-assembled from dendrimer peptides and functionalized peptides has been developed for targeted drug delivery in cancer therapy [138]. These dendritic nanostructures are designed and self-assembled using a supramolecular method to mimic the capsid-like structures and similar components. The functionalized peptides were selected for specific targeting of cancer cells. These designs have many advantages for targeted drug delivery for tumor therapy. For example, the capsid-like nanostructure could be used to promote drug penetration through many different barriers. The peptide self-assembled nanostructures with well-ordered structures also could enhance the drug

accumulation in targeted disease areas. Most importantly, the functionalized nanostructures could be used for specific delivery to the targeted tumor sites. The experimental results have confirmed the advantages and demonstrated that these nanostructures loaded with doxorubicin have the ability to treat tumors in BALB/c mice with low toxicity efficiently [138].

Functional peptides have also been used for targeted drug delivery for biomaterials such as liposomes to improve specific targeting and cell penetrating [139]. For example, the PR_b peptide, as well as polyethylene glycol, could be used to self-assemble into nanostructures with liposomes in a good manner. The PR_b peptide in this system could be used to specifically bind with the overexpressed integrin $\alpha_5\beta_1$ in colon cancer cells. The polyethylene glycol could be utilized as a steric barrier to protect the nanostructures. Therefore, these coated peptide self-assembled nanostructures could stay longer in the circulating blood system. The experimental results clearly demonstrated the capability of these functional nanostructures for targeted delivery of anticancer drugs into colon cancer cells. Therefore, they can decrease the tumor metastasis and reduce the tumor growth with limited side effects.

4.4. Stimuli Responsive Drug Delivery. Peptides have the ability to self-assemble into well-defined nanostructures which have many different formats including nanofibers or hydrogels for tissue regeneration, drug delivery, and so on [118, 140]. Peptide self-assembled hydrogels are biodegradable and biocompatible and are easier to be modified with specific materials such as small molecules or peptide ligands [92]. Therefore, biocompatibility and biodegradability could be realized through the peptide-based self-assembly due to their incorporation of biological advantages in the specific targeting and sensitive reaction sites [103]. Importantly, these peptide self-assembled nanostructures should have the capability for controlled release of the loaded drugs or other materials when they are triggered by the environmental factors. The releasing time, ratio, or many other strategies should be controlled under the requirements of the disease status. Therefore, the peptide self-assembled nanostructures with stimuli responsive properties and well-controlled releasing functions could be used to increase the drug delivery efficiency and then for therapeutic purposes [141].

Peptide self-assembled nanostructures especially the hydrogel formats are very important classes of hydrogels, which have attracted much attention recently as a drug delivery platform because of their high drug loading efficiency, controlled drug release, and responsive drug release under different stimulations such as pH value and temperature [141]. For example, a hydrogelator system has been developed based on peptides with anticancer drug curcumin. The basic building blocks are curcumin-FFE-ss-ERGD. The peptides FFE and disulfide bond have been proven to have the ability to form supramolecular hydrogelator structures. The ERGD peptides could be used for the specific targeting of cancer cells. In addition, these peptide self-assembled nanostructures could also be responsive to pH change after endocytosis and then disassembly into single molecules. The in vitro and

in vivo experimental results have demonstrated that these systems could enhance the cellular uptake and controlled and responsive drug releasing. Therefore, they have the potential to inhibit cancer cells and tumor growth through stimuli responsive drug delivery for cancer therapy.

The peptide self-assembled fiber-like nanostructures have been developed using cleavable amphiphilic peptide for stimuli responsive anticancer drug delivery application in tumor therapy [142]. These nanostructures could be formed by spherical nanoparticles after the loading of hydrophobic chemotherapeutic drugs. These nanoparticles have been demonstrated to be responsive to fibroblast activation protein α , which could be overexpressed on the surface of cancer-related fibroblasts cells. These nanoparticles could be disassembled specifically at the tumor sites with efficient and rapid release of the conjugated anticancer drugs. Therefore, this system has the ability to promote the local accumulation of drugs through the disruption of stromal barriers.

There are also many other peptides or proteins including IgG, bovine serum albumin, and lysozymes that can be used to conjugate with Ac-(RADA)₄-CONH₂ peptide hydrogel for stimuli responsive drug delivery applications [143]. The mixing of the therapeutic-based proteins and peptide solution could be utilized for drug release with the controlled manner in specific tissues. Moreover, peptide self-assembled nanostructures that are responsive to temperature or magnetic field also have been developed and validated for responsive drug delivery applications [144]. For example, the peptide self-assembled nanostructures coated with chitosan/ELR shell could be responsive to temperature for controlled drug release. The chitosan/ELR has the temperature responsive function in this system. Depsipeptide self-assembled nanostructures were also designed to overcome the resistance to degradation by protease for peptide self-assembled nanofibers [145]. These nanostructures are self-assembled using the peptide sequence with ester bonds. Therefore, the depsipeptides self-assembled nanostructures can degrade from days to weeks by the ester hydrolysis processes for the enzyme responsive drug delivery applications.

5. Conclusions and Perspectives

Peptide self-assembled nanostructures could construct well-defined structures through the noncovalent forces including electrostatic interaction, hydrophobic reaction, hydrogen bonding, and π - π stacking. The morphology and function of the peptide self-assembled nanostructures can be manipulated from the molecular level by tuning the types and structures of peptides, or external triggers such as temperature, pH value, and electric field. Recent studies have shown that these peptide self-assembled nanostructures have been utilized for many different biomedical applications. The examples presented in this paper highlight the potential role of peptide self-assembled nanostructures for drug delivery applications. One peptide self-assembled nanostructure could include multiple functions such as cell penetration, specific targeting, release responsive mechanism, and endosomal escape motifs. However, people are still facing many challenges such as predicting precise molecular or higher structures, functional

properties, and biosafety from the peptide self-assembly. Another major challenge is the high yield of the peptide nanomanufacturing. This is also very important for the clinical applications. In conclusion, with multidisciplinary efforts, peptide self-assembled nanostructures for drug delivery applications have much potential and are very promising to treat human diseases.

Conflicts of Interest

The authors declare that they have no competing interests.

References

- [1] T. H. Han, J. K. Oh, G.-J. Lee, S.-I. Pyun, and S. O. Kim, "Hierarchical assembly of diphenylalanine into dendritic nanoarchitectures," *Colloids and Surfaces B: Biointerfaces*, vol. 79, no. 2, pp. 440–445, 2010.
- [2] G. M. Whitesides and B. Grzybowski, "Self-assembly at all scales," *Science*, vol. 295, no. 5564, pp. 2418–2421, 2002.
- [3] Z. Liu, Y. Jiao, Y. Wang, C. Zhou, and Z. Zhang, "Polysaccharides-based nanoparticles as drug delivery systems," *Advanced Drug Delivery Reviews*, vol. 60, no. 15, pp. 1650–1662, 2008.
- [4] L. Sun, Y. Huang, Z. Bian et al., "Sundew-inspired adhesive hydrogels combined with adipose-derived stem cells for wound healing," *ACS Applied Materials & Interfaces*, vol. 8, no. 3, pp. 2423–2434, 2016.
- [5] L. Sun, S. Yi, Y. Wang, K. Pan, Q. Zhong, and M. Zhang, "A bio-inspired approach for in situ synthesis of tunable adhesive," *Bioinspiration and Biomimetics*, vol. 9, no. 1, Article ID 016005, 2014.
- [6] Y. Wang, S. Yi, L. Sun, Y. Huang, and M. Zhang, "Charge-selective fractions of naturally occurring nanoparticles as bioactive nanocarriers for cancer therapy," *Acta Biomaterialia*, vol. 10, no. 10, pp. 4269–4284, 2014.
- [7] N. Stephanopoulos, J. H. Ortony, and S. I. Stupp, "Self-assembly for the synthesis of functional biomaterials," *Acta Materialia*, vol. 61, no. 3, pp. 912–930, 2013.
- [8] Z. Wang, Y. Li, Y. Huang et al., "Enzyme-regulated topology of a cyclic peptide brush polymer for tuning assembly," *Chemical Communications*, vol. 51, no. 96, pp. 17108–17111, 2015.
- [9] S. I. Stupp, "Self-assembly and biomaterials," *Nano Letters*, vol. 10, no. 12, pp. 4783–4786, 2010.
- [10] L. Sun, L. Xia, S. Yi, S. C. Lenaghan, Y. Wang, and M. Zhang, "Biosynthesis of metal nanoparticles from the Peel of *Asparagus Lettuce* (*Lactuca sativa* var. *asparagine*)," *Advanced Science, Engineering and Medicine*, vol. 5, no. 11, pp. 1157–1165, 2013.
- [11] M. Ma, J. Zhong, W. Li et al., "Comparison of four synthetic model peptides to understand the role of modular motifs in the self-assembly of silk fibroin," *Soft Matter*, vol. 9, no. 47, pp. 11325–11333, 2013.
- [12] S. Zhang, "Fabrication of novel biomaterials through molecular self-assembly," *Nature Biotechnology*, vol. 21, no. 10, pp. 1171–1178, 2003.
- [13] W. Liao, T. Lai, L. Chen et al., "Synthesis and characterization of a walnut peptides-zinc complex and its antiproliferative activity against human breast carcinoma cells through the induction of apoptosis," *Journal of Agricultural and Food Chemistry*, vol. 64, no. 7, pp. 1509–1519, 2016.

- [14] Y. Wen, S. L. Roudebush, G. A. Buckholtz et al., "Coassembly of amphiphilic peptide EAK16-II with histidinylated analogues and implications for functionalization of β -sheet fibrils in vivo," *Biomaterials*, vol. 35, no. 19, pp. 5196–5205, 2014.
- [15] Z. Fan, L. Sun, Y. Huang, Y. Wang, and M. Zhang, "Bioinspired fluorescent dipeptide nanoparticles for targeted cancer cell imaging and real-time monitoring of drug release," *Nature Nanotechnology*, vol. 11, no. 4, pp. 388–394, 2016.
- [16] L. Sun, N. Wanasekara, V. Chalivendra, and P. Calvert, "Nanomechanical studies on polyglactin sutures subjected to in vitro hydrolytic and enzymatic degradation," *Journal of Nanoscience and Nanotechnology*, vol. 15, no. 1, pp. 93–99, 2015.
- [17] N. Habibi, N. Kamaly, A. Memic, and H. Shafiee, "Self-assembled peptide-based nanostructures: smart nanomaterials toward targeted drug delivery," *Nano Today*, vol. 11, no. 1, pp. 41–60, 2016.
- [18] L. Sun, Z. Fan, Y. Wang, Y. Huang, M. Schmidt, and M. Zhang, "Tunable synthesis of self-assembled cyclic peptide nanotubes and nanoparticles," *Soft Matter*, vol. 11, no. 19, pp. 3822–3832, 2015.
- [19] C. M. Rubert Pérez, N. Stephanopoulos, S. Sur, S. S. Lee, C. Newcomb, and S. I. Stupp, "The powerful functions of peptide-based bioactive matrices for regenerative medicine," *Annals of Biomedical Engineering*, vol. 43, no. 3, pp. 501–514, 2015.
- [20] L. Zhang, J. Zhong, L. Huang, L. Wang, Y. Hong, and Y. Sha, "Parallel-oriented fibrogenesis of a β -sheet forming peptide on supported lipid bilayers," *Journal of Physical Chemistry B*, vol. 112, no. 30, pp. 8950–8954, 2008.
- [21] Z. Yu, Z. Cai, Q. Chen et al., "Engineering β -sheet peptide assemblies for biomedical applications," *Biomaterials Science*, vol. 4, no. 3, pp. 365–374, 2016.
- [22] J. B. Matson, R. H. Zha, and S. I. Stupp, "Peptide self-assembly for crafting functional biological materials," *Current Opinion in Solid State & Materials Science*, vol. 15, no. 6, pp. 225–235, 2011.
- [23] S. Pujals, J. Fernández-Carneado, C. López-Iglesias, M. J. Kogan, and E. Giralt, "Mechanistic aspects of CPP-mediated intracellular drug delivery: relevance of CPP self-assembly," *Biochimica et Biophysica Acta - Biomembranes*, vol. 1758, no. 3, pp. 264–279, 2006.
- [24] E. Melis Sardan, C. Goksu, K. Mohammad Aref, and O. G. Mustafa, "Self-assembled peptide nanostructures for functional materials," *Nanotechnology*, vol. 27, no. 40, Article ID 402002, 2016.
- [25] H.-A. Klok, "Protein-inspired materials: synthetic concepts and potential applications," *Angewandte Chemie—International Edition*, vol. 41, no. 9, pp. 1509–1513, 2002.
- [26] L. Sun, C. Zheng, and T. Webster, "Self-assembled peptide nanomaterials for biomedical applications: promises and pitfalls," *International Journal of Nanomedicine*, vol. 12, pp. 73–86, 2017.
- [27] S. Frank, R. A. Kammerer, D. Mechling et al., "Stabilization of short collagen-like triple helices by protein engineering," *Journal of Molecular Biology*, vol. 308, no. 5, pp. 1081–1089, 2001.
- [28] Z. Li, Z. Zheng, Y. Yang et al., "Robust protein hydrogels from silkworm silk," *ACS Sustainable Chemistry and Engineering*, vol. 4, no. 3, pp. 1500–1506, 2016.
- [29] Y. Huang, Y.-J. Wang, Y. Wang et al., "Exploring naturally occurring ivy nanoparticles as an alternative biomaterial," *Acta Biomaterialia*, vol. 25, pp. 268–283, 2015.
- [30] V. A. Kumar, N. L. Taylor, A. A. Jalan, L. K. Hwang, B. K. Wang, and J. D. Hartgerink, "A nanostructured synthetic collagen mimic for hemostasis," *Biomacromolecules*, vol. 15, no. 4, pp. 1484–1490, 2014.
- [31] H. Cui, M. J. Webber, and S. I. Stupp, "Self-assembly of peptide amphiphiles: from molecules to nanostructures to biomaterials," *Biopolymers*, vol. 94, no. 1, pp. 1–18, 2010.
- [32] H. Lu, J. Wang, T. Wang, J. Zhong, Y. Bao, and H. Hao, "Recent progress on nanostructures for drug delivery applications," *Journal of Nanomaterials*, vol. 2016, Article ID 5762431, 12 pages, 2016.
- [33] J. J. Panda and V. S. Chauhan, "Short peptide based self-assembled nanostructures: implications in drug delivery and tissue engineering," *Polymer Chemistry*, vol. 5, no. 15, pp. 4418–4436, 2014.
- [34] S. Marchesan, A. V. Vargiu, and K. E. Styan, "The Phe-Phe motif for peptide self-assembly in nanomedicine," *Molecules*, vol. 20, no. 11, pp. 19775–19788, 2015.
- [35] C. Chen, F. Pan, S. Zhang et al., "Antibacterial activities of short designer peptides: a link between propensity for nanostructuring and capacity for membrane destabilization," *Biomacromolecules*, vol. 11, no. 2, pp. 402–411, 2010.
- [36] A. S. Veiga, C. Sinthuvanich, D. Gaspar, H. G. Franquelim, M. A. R. B. Castanho, and J. P. Schneider, "Arginine-rich self-assembling peptides as potent antibacterial gels," *Biomaterials*, vol. 33, no. 35, pp. 8907–8916, 2012.
- [37] C. H. Görbitz, "The structure of nanotubes formed by diphenylalanine, the core recognition motif of Alzheimer's β -amyloid polypeptide," *Chemical Communications*, no. 22, pp. 2332–2334, 2006.
- [38] L. Adler-Abramovich, D. Aronov, P. Beker et al., "Self-assembled arrays of peptide nanotubes by vapour deposition," *Nature Nanotechnology*, vol. 4, no. 12, pp. 849–854, 2009.
- [39] M. Wang, L. Du, X. Wu, S. Xiong, and P. K. Chu, "Charged diphenylalanine nanotubes and controlled hierarchical self-assembly," *ACS Nano*, vol. 5, no. 6, pp. 4448–4454, 2011.
- [40] P. Zhu, X. Yan, Y. Su, Y. Yang, and J. Li, "Solvent-induced structural transition of self-assembled dipeptide: from organogels to microcrystals," *Chemistry—A European Journal*, vol. 16, no. 10, pp. 3176–3183, 2010.
- [41] J. Ryu and C. B. Park, "High-temperature self-assembly of peptides into vertically well-aligned nanowires by aniline vapor," *Advanced Materials*, vol. 20, no. 19, pp. 3754–3758, 2008.
- [42] Z. Li, C. Liu, S. Ma, D. Zhang, and Y. Yamaguchi, "Analysis of the inhibition of nucleic acid dyes on polymerase chain reaction by capillary electrophoresis," *Analytical Methods*, vol. 8, no. 11, pp. 2330–2334, 2016.
- [43] L. Adler-Abramovich, M. Reches, V. L. Sedman, S. Allen, S. J. B. Tendler, and E. Gazit, "Thermal and chemical stability of diphenylalanine peptide nanotubes: implications for nanotechnological applications," *Langmuir*, vol. 22, no. 3, pp. 1313–1320, 2006.
- [44] S. Scanlon and A. Aggeli, "Self-assembling peptide nanotubes," *Nano Today*, vol. 3, no. 3–4, pp. 22–30, 2008.
- [45] N. Hendler, N. Sidelman, M. Reches, E. Gazit, Y. Rosenberg, and S. Richter, "Formation of well-organized self-assembled films from peptide nanotubes," *Advanced Materials*, vol. 19, no. 11, pp. 1485–1488, 2007.
- [46] C. H. Görbitz, "Nanotubes from hydrophobic dipeptides: pore size regulation through side chain substitution," *New Journal of Chemistry*, vol. 27, no. 12, pp. 1789–1793, 2003.

- [47] C. H. Görbitz, "Nanotube formation by hydrophobic dipeptides," *Chemistry - A European Journal*, vol. 7, no. 23, pp. 5153–5159, 2001.
- [48] Y. Pan, H. Birkedal, P. Pattison, D. Brown, and G. Chapuis, "Molecular dynamics study of tryptophylglycine: a dipeptide nanotube with confined water," *Journal of Physical Chemistry B*, vol. 108, no. 20, pp. 6458–6466, 2004.
- [49] I. Moudrakovski, D. V. Soldatov, J. A. Ripmeester, D. N. Sears, and C. J. Jameson, "Xe NMR lineshapes in channels of peptide molecular crystals," *Proceedings of the National Academy of Sciences of the United States of America*, vol. 101, no. 52, pp. 17924–17929, 2004.
- [50] D. V. Soldatov, I. L. Moudrakovski, and J. A. Ripmeester, "Dipeptides as microporous materials," *Angewandte Chemie - International Edition*, vol. 43, no. 46, pp. 6308–6311, 2004.
- [51] A. Comotti, S. Bracco, G. Distefano, and P. Sozzani, "Methane, carbon dioxide and hydrogen storage in nanoporous dipeptide-based materials," *Chemical Communications*, no. 3, pp. 284–286, 2009.
- [52] M. Reches and E. Gazit, "Formation of closed-cage nanostructures by self-assembly of aromatic dipeptides," *Nano Letters*, vol. 4, no. 4, pp. 581–585, 2004.
- [53] M. Reches and E. Gazit, "Designed aromatic homo-dipeptides: formation of ordered nanostructures and potential nanotechnological applications," *Physical Biology*, vol. 3, no. 1, pp. S10–S19, 2006.
- [54] O. Carny, D. E. Shalev, and E. Gazit, "Fabrication of coaxial metal nanocables using a self-assembled peptide nanotube scaffold," *Nano Letters*, vol. 6, no. 8, pp. 1594–1597, 2006.
- [55] L. Adler-Abramovich, M. Badihi-Mossberg, E. Gazit, and J. Rishpon, "Characterization of peptide-nanostructure-modified electrodes and their application for ultrasensitive environmental monitoring," *Small*, vol. 6, no. 7, pp. 825–831, 2010.
- [56] R. Orbach, L. Adler-Abramovich, S. Zigerson, I. Mironi-Harpaz, D. Seliktar, and E. Gazit, "Self-assembled Fmoc-peptides as a platform for the formation of nanostructures and hydrogels," *Biomacromolecules*, vol. 10, no. 9, pp. 2646–2651, 2009.
- [57] S. Guha, M. G. B. Drew, and A. Banerjee, "Dipeptide nanotubes, with N-terminally located ω -amino acid residues, that are stable proteolytically, thermally, and over a wide range of pH," *Chemistry of Materials*, vol. 20, no. 6, pp. 2282–2290, 2008.
- [58] S. Guha, M. G. B. Drew, and A. Banerjee, "Construction of helical nanofibers from self-assembling pseudopeptide building blocks: Modulating the handedness and breaking the helicity," *Small*, vol. 4, no. 11, pp. 1993–2005, 2008.
- [59] M. J. Krysmann, V. Castelletto, A. Kellarakis, I. W. Hamley, R. A. Hule, and D. J. Pochan, "Self-assembly and hydrogelation of an amyloid peptide fragment," *Biochemistry*, vol. 47, no. 16, pp. 4597–4605, 2008.
- [60] M. Reches, Y. Porat, and E. Gazit, "Amyloid fibril formation by pentapeptide and tetrapeptide fragments of human calcitonin," *Journal of Biological Chemistry*, vol. 277, no. 38, pp. 35475–35480, 2002.
- [61] P. De Santis, E. Forni, and R. Rizzo, "Conformational analysis of DNA–basic polypeptide complexes: Possible models of nucleoprotamines and nucleohistones," *Biopolymers*, vol. 13, no. 2, pp. 313–326, 1974.
- [62] M. R. Ghadiri, J. R. Granja, R. A. Milligan, D. E. McRee, and N. Khazanovich, "Self-assembling organic nanotubes based on a cyclic peptide architecture," *Nature*, vol. 366, no. 6453, pp. 324–327, 1993.
- [63] R. Chapman, M. Danial, M. L. Koh, K. A. Jolliffe, and S. Perrier, "Design and properties of functional nanotubes from the self-assembly of cyclic peptide templates," *Chemical Society Reviews*, vol. 41, no. 18, pp. 6023–6041, 2012.
- [64] S. Fernandez-Lopez, H.-S. Kim, E. C. Choi et al., "Antibacterial agents based on the cyclic D,L- α -peptide architecture," *Nature*, vol. 412, no. 6845, pp. 452–455, 2001.
- [65] Y. Ishihara and S. Kimura, "Nanofiber formation of amphiphilic cyclic tri- β -peptide," *Journal of Peptide Science*, vol. 16, no. 2, pp. 110–114, 2010.
- [66] J. D. Hartgerink, J. R. Granja, R. A. Milligan, and M. R. Ghadiri, "Self-assembling peptide nanotubes," *Journal of the American Chemical Society*, vol. 118, no. 1, pp. 43–50, 1996.
- [67] Y. Wang, S. Yi, L. Sun, Y. Huang, S. C. Lenaghan, and M. Zhang, "Doxorubicin-loaded cyclic peptide nanotube bundles overcome chemoresistance in breast cancer cells," *Journal of Biomedical Nanotechnology*, vol. 10, no. 3, pp. 445–454, 2014.
- [68] D. W. P. M. Lowik and J. C. M. van Hest, "Peptide based amphiphiles," *Chemical Society Reviews*, vol. 33, no. 4, pp. 234–245, 2004.
- [69] R. Huang, W. Qi, R. Su, J. Zhao, and Z. He, "Solvent and surface controlled self-assembly of diphenylalanine peptide: from microtubes to nanofibers," *Soft Matter*, vol. 7, no. 14, pp. 6418–6421, 2011.
- [70] R. S. Tu and M. Tirrell, "Bottom-up design of biomimetic assemblies," *Advanced Drug Delivery Reviews*, vol. 56, no. 11, pp. 1537–1563, 2004.
- [71] T. Gore, Y. Dori, Y. Talmon, M. Tirrell, and H. Bianco-Peled, "Self-assembly of model collagen peptide amphiphiles," *Langmuir*, vol. 17, no. 17, pp. 5352–5360, 2001.
- [72] L. Liu, K. Busuttill, S. Zhang et al., "The role of self-assembling polypeptides in building nanomaterials," *Physical Chemistry Chemical Physics*, vol. 13, no. 39, pp. 17435–17444, 2011.
- [73] S. Vauthey, S. Santoso, H. Gong, N. Watson, and S. Zhang, "Molecular self-assembly of surfactant-like peptides to form nanotubes and nanovesicles," *Proceedings of the National Academy of Sciences of the United States of America*, vol. 99, no. 8, pp. 5355–5360, 2002.
- [74] M. R. Caplan, E. M. Schwartzfarb, S. Zhang, R. D. Kamm, and D. A. Lauffenburger, "Control of self-assembling oligopeptide matrix formation through systematic variation of amino acid sequence," *Biomaterials*, vol. 23, no. 1, pp. 219–227, 2002.
- [75] G. Von Maltzahn, S. Vauthey, S. Santoso, and S. Zhang, "Positively charged surfactant-like peptides self-assemble into nanostructures," *Langmuir*, vol. 19, no. 10, pp. 4332–4337, 2003.
- [76] S. Zhang, T. Holmes, C. Lockshin, and A. Rich, "Spontaneous assembly of a self-complementary oligopeptide to form a stable macroscopic membrane," *Proceedings of the National Academy of Sciences of the United States of America*, vol. 90, no. 8, pp. 3334–3338, 1993.
- [77] S. Zhang, T. C. Holmes, C. M. DiPersio, R. O. Hynes, X. Su, and A. Rich, "Self-complementary oligopeptide matrices support mammalian cell attachment," *Biomaterials*, vol. 16, no. 18, pp. 1385–1393, 1995.
- [78] X. Zhao, F. Pan, H. Xu et al., "Molecular self-assembly and applications of designer peptide amphiphiles," *Chemical Society Reviews*, vol. 39, no. 9, pp. 3480–3498, 2010.

- [79] S. Zhang, "Emerging biological materials through molecular self-assembly," *Biotechnology Advances*, vol. 20, no. 5-6, pp. 321-339, 2002.
- [80] M. E. Davis, J. P. M. Motion, D. A. Narmoneva et al., "Injectable self-assembling peptide nanofibers create intramyocardial microenvironments for endothelial cells," *Circulation*, vol. 111, no. 4, pp. 442-450, 2005.
- [81] Y. Wen, W. Liu, C. Bagia et al., "Antibody-functionalized peptidic membranes for neutralization of allogeneic skin antigen-presenting cells," *Acta Biomaterialia*, vol. 10, no. 11, pp. 4759-4767, 2014.
- [82] Y. Wen and J. H. Collier, "Supramolecular peptide vaccines: Tuning adaptive immunity," *Current Opinion in Immunology*, vol. 35, pp. 73-79, 2015.
- [83] T. Sun, H. Han, G. A. Hudalla, Y. Wen, R. R. Pompano, and J. H. Collier, "Thermal stability of self-assembled peptide vaccine materials," *Acta Biomaterialia*, vol. 30, pp. 62-71, 2016.
- [84] Y. Wen, A. Waltman, H. Han, and J. H. Collier, "Switching the immunogenicity of peptide assemblies using surface properties," *ACS Nano*, vol. 10, no. 10, pp. 9274-9286, 2016.
- [85] Y. Wen, H. R. Kolonich, K. M. Kruszewski, N. Giannoukakis, E. S. Gawalt, and W. S. Meng, "Retaining antibodies in tumors with a self-assembling injectable system," *Molecular Pharmaceutics*, vol. 10, no. 3, pp. 1035-1044, 2013.
- [86] K. Beck and B. Brodsky, "Supercoiled protein motifs: the collagen triple-helix and the α -helical coiled coil," *Journal of Structural Biology*, vol. 122, no. 1-2, pp. 17-29, 1998.
- [87] R. Fairman and K. S. Åkerfeldt, "Peptides as novel smart materials," *Current Opinion in Structural Biology*, vol. 15, no. 4, pp. 453-463, 2005.
- [88] S. A. Potekhin, T. N. Melnik, V. Popov et al., "De novo design of fibrils made of short α -helical coiled coil peptides," *Chemistry and Biology*, vol. 8, no. 11, pp. 1025-1032, 2001.
- [89] D. E. Wagner, C. L. Phillips, W. M. Ali et al., "Toward the development of peptide nanofilaments and nanoropes as smart materials," *Proceedings of the National Academy of Sciences of the United States of America*, vol. 102, no. 36, pp. 12656-12661, 2005.
- [90] E. Moutevelis and D. N. Woolfson, "A Periodic Table of Coiled-Coil Protein Structures," *Journal of Molecular Biology*, vol. 385, no. 3, pp. 726-732, 2009.
- [91] C. Gribbon, K. J. Channon, W. Zhang et al., "MagicWand: a single, designed peptide that assembles to stable, ordered α -helical fibers," *Biochemistry*, vol. 47, no. 39, pp. 10365-10371, 2008.
- [92] A. S. Hoffman, "Hydrogels for biomedical applications," *Advanced Drug Delivery Reviews*, vol. 54, no. 1, pp. 3-12, 2002.
- [93] A. M. Smith, E. F. Banwell, W. R. Edwards, M. J. Pandya, and D. N. Woolfson, "Engineering increased stability into self-assembled protein fibers," *Advanced Functional Materials*, vol. 16, no. 8, pp. 1022-1030, 2006.
- [94] C. Xu, V. Breedveld, and J. Kopeček, "Reversible hydrogels from self-assembling genetically engineered protein block copolymers," *Biomacromolecules*, vol. 6, no. 3, pp. 1739-1749, 2005.
- [95] A. Aggeli, I. A. Nyrkova, M. Bell et al., "Hierarchical self-assembly of chiral rod-like molecules as a model for peptide β -sheet tapes, ribbons, fibrils, and fibers," *Proceedings of the National Academy of Sciences of the United States of America*, vol. 98, no. 21, pp. 11857-11862, 2001.
- [96] C. W. G. Fishwick, A. J. Beevers, L. M. Carrick, C. D. Whitehouse, A. Aggeli, and N. Boden, "Structures of helical β -tapes and twisted ribbons: the role of side-chain interactions on twist and bend behavior," *Nano Letters*, vol. 3, no. 11, pp. 1475-1479, 2003.
- [97] A. Aggeli, M. Bell, L. M. Carrick et al., "pH as a trigger of peptide β -sheet self-assembly and reversible switching between nematic and isotropic phases," *Journal of the American Chemical Society*, vol. 125, no. 32, pp. 9619-9628, 2003.
- [98] K. Lu, J. Jacob, P. Thiyagarajan, V. P. Conticello, and D. G. Lynn, "Exploiting amyloid fibril lamination for nanotube self-assembly," *Journal of the American Chemical Society*, vol. 125, no. 21, pp. 6391-6393, 2003.
- [99] M. Reches and E. Gazit, "Casting metal nanowires within discrete self-assembled peptide nanotubes," *Science*, vol. 300, no. 5619, pp. 625-627, 2003.
- [100] G. Xu, W. Wang, J. T. Groves, and M. H. Hecht, "Self-assembled monolayers from a designed combinatorial library of de novo β -sheet proteins," *Proceedings of the National Academy of Sciences of the United States of America*, vol. 98, no. 7, pp. 3652-3657, 2001.
- [101] N. Ashkenasy, W. S. Horne, and M. R. Ghadiri, "Design of self-assembling peptide nanotubes with delocalized electronic states," *Small*, vol. 2, no. 1, pp. 99-102, 2006.
- [102] E. T. Powers, S. I. Yang, C. M. Lieber, and J. W. Kelly, "Ordered Langmuir-Blodgett films of amphiphilic β -hairpin peptides imaged by atomic force microscopy," *Angewandte Chemie - International Edition*, vol. 41, no. 1, pp. 127-130, 2002.
- [103] J. P. Schneider, D. J. Pochan, B. Ozbas, K. Rajagopal, L. Pakstis, and J. Kretsinger, "Responsive hydrogels from the intramolecular folding and self-assembly of a designed peptide," *Journal of the American Chemical Society*, vol. 124, no. 50, pp. 15030-15037, 2002.
- [104] S. Toksoz, H. Acar, and M. O. Guler, "Self-assembled one-dimensional soft nanostructures," *Soft Matter*, vol. 6, no. 23, pp. 5839-5849, 2010.
- [105] D. M. Leite, E. Barbu, G. J. Pilkington, and A. Lalatsa, "Peptide self-assemblies for drug delivery," *Current Topics in Medicinal Chemistry*, vol. 15, no. 22, pp. 2277-2289, 2015.
- [106] Y. Li, G. H. Gao, and D. S. Lee, "Stimulus-sensitive polymeric nanoparticles and their applications as drug and gene carriers," *Advanced Healthcare Materials*, vol. 2, no. 3, pp. 388-417, 2013.
- [107] B. Chen, X.-Y. He, X.-Q. Yi, R.-X. Zhuo, and S.-X. Cheng, "Dual-peptide-functionalized albumin-based nanoparticles with pH-dependent self-assembly behavior for drug delivery," *ACS Applied Materials & Interfaces*, vol. 7, no. 28, pp. 15148-15153, 2015.
- [108] J.-H. Lee, Y. J. Choi, and Y.-B. Lim, "Self-assembled filamentous nanostructures for drug/gene delivery applications," *Expert Opinion on Drug Delivery*, vol. 7, no. 3, pp. 341-351, 2010.
- [109] Y. Wang and X. Gong, "Special oleophobic and hydrophilic surfaces: approaches, mechanisms, and applications," *Journal of Materials Chemistry A*, vol. 5, no. 8, pp. 3759-3773, 2017.
- [110] A. G. Cheetham, P. Zhang, Y.-A. Lin, L. L. Lock, and H. Cui, "Supramolecular nanostructures formed by anticancer drug assembly," *Journal of the American Chemical Society*, vol. 135, no. 8, pp. 2907-2910, 2013.
- [111] A. Brack and L. E. Orgel, " β structures of alternating polypeptides and their possible prebiotic significance," *Nature*, vol. 256, no. 5516, pp. 383-387, 1975.
- [112] J. Wang, K. Liu, R. Xing, and X. Yan, "Peptide self-assembly: thermodynamics and kinetics," *Chem. Soc. Rev.*, vol. 45, no. 20, pp. 5589-5604, 2016.

- [113] R. F. Silva, D. R. Araújo, E. R. Silva, R. A. Ando, and W. A. Alves, "L-Diphenylalanine microtubes as a potential drug-delivery system: characterization, release kinetics, and cytotoxicity," *Langmuir*, vol. 29, no. 32, pp. 10205–10212, 2013.
- [114] R. Pawar, A. Ben-Ari, and A. J. Domb, "Protein and peptide parenteral controlled delivery," *Expert Opinion on Biological Therapy*, vol. 4, no. 8, pp. 1203–1212, 2004.
- [115] J. Shi, Z. Xiao, N. Kamaly, and O. C. Farokhzad, "Self-assembled targeted nanoparticles: evolution of technologies and bench to bedside translation," *Accounts of Chemical Research*, vol. 44, no. 10, pp. 1123–1134, 2011.
- [116] Z. Yu, Q. Xu, C. Dong et al., "Self-assembling peptide nanofibrous hydrogel as a versatile drug delivery platform," *Current Pharmaceutical Design*, vol. 21, no. 29, pp. 4342–4354, 2015.
- [117] J. Boekhoven, R. H. Zha, F. Tantakitti et al., "Alginate-peptide amphiphile core-shell microparticles as a targeted drug delivery system," *RSC Advances*, vol. 5, no. 12, pp. 8753–8756, 2015.
- [118] E. Yishay-Safranchik, M. Golan, and A. David, "Controlled release of doxorubicin and Smac-derived pro-apoptotic peptide from self-assembled KLD-based peptide hydrogels," *Polymers for Advanced Technologies*, vol. 25, no. 5, pp. 539–544, 2014.
- [119] S. Lu, H. Wang, Y. Sheng, M. Liu, and P. Chen, "Molecular binding of self-assembling peptide EAK16-II with anticancer agent EPT and its implication in cancer cell inhibition," *Journal of Controlled Release*, vol. 160, no. 1, pp. 33–40, 2012.
- [120] N. Li, N. Li, Q. Yi et al., "Amphiphilic peptide dendritic copolymer-doxorubicin nanoscale conjugate self-assembled to enzyme-responsive anti-cancer agent," *Biomaterials*, vol. 35, no. 35, pp. 9529–9545, 2014.
- [121] T. Jiang, Z. Zhang, Y. Zhang et al., "Dual-functional liposomes based on pH-responsive cell-penetrating peptide and hyaluronic acid for tumor-targeted anticancer drug delivery," *Biomaterials*, vol. 33, no. 36, pp. 9246–9258, 2012.
- [122] D. Lee, Y. M. Lee, J. Kim, M. K. Lee, and W. J. Kim, "Enhanced tumor-targeted gene delivery by bioreducible polyethylenimine tethering EGFR divalent ligands," *Biomaterials Science*, vol. 3, no. 7, pp. 1096–1104, 2015.
- [123] E. Jabbari, X. Yang, S. Moeinzadeh, and X. He, "Drug release kinetics, cell uptake, and tumor toxicity of hybrid VVVVVVKK peptide-assembled polylactide nanoparticles," *European Journal of Pharmaceutics and Biopharmaceutics*, vol. 84, no. 1, pp. 49–62, 2013.
- [124] Y. Takakura, M. Nishikawa, F. Yamashita, and M. Hashida, "Development of gene drug delivery systems based on pharmacokinetic studies," *European Journal of Pharmaceutical Sciences*, vol. 13, no. 1, pp. 71–76, 2001.
- [125] C. E. Thomas, A. Ehrhardt, and M. A. Kay, "Progress and problems with the use of viral vectors for gene therapy," *Nature Reviews Genetics*, vol. 4, no. 5, pp. 346–358, 2003.
- [126] Z. Li, C. Liu, D. Zhang, S. Luo, and Y. Yamaguchi, "Capillary electrophoresis of RNA in hydroxyethylcellulose polymer with various molecular weights," *Journal of Chromatography B: Analytical Technologies in the Biomedical and Life Sciences*, vol. 1011, pp. 114–120, 2016.
- [127] B. Ballarín-González and K. A. Howard, "Polycation-based nanoparticle delivery of RNAi therapeutics: adverse effects and solutions," *Advanced Drug Delivery Reviews*, vol. 64, no. 15, pp. 1717–1729, 2012.
- [128] X. Yan, Q. He, K. Wang, L. Duan, Y. Cui, and J. Li, "Transition of cationic dipeptide nanotubes into vesicles and oligonucleotide delivery," *Angewandte Chemie—International Edition*, vol. 46, no. 14, pp. 2431–2434, 2007.
- [129] H. O. McCarthy, J. McCaffrey, C. M. McCrudden et al., "Development and characterization of self-assembling nanoparticles using a bio-inspired amphipathic peptide for gene delivery," *Journal of Controlled Release*, vol. 189, pp. 141–149, 2014.
- [130] Tarwadi, J. A. Jazayeri, R. J. Pranker, and C. W. Pouton, "Preparation and in vitro evaluation of novel lipopeptide transfection agents for efficient gene delivery," *Bioconjugate Chemistry*, vol. 19, no. 4, pp. 940–950, 2008.
- [131] M. E. Martin and K. G. Rice, "Peptide-guided gene delivery," *The AAPS Journal*, vol. 9, no. 1, article 3, pp. E18–E29, 2007.
- [132] E. Kokkoli, A. Mardilovich, A. Wedekind, E. L. Rexeisen, A. Garg, and J. A. Craig, "Self-assembly and applications of biomimetic and bioactive peptide-amphiphiles," *Soft Matter*, vol. 2, no. 12, pp. 1015–1024, 2006.
- [133] S. M. Fuchs and R. T. Raines, "Internalization of cationic peptides: The road less (or more?) traveled," *Cellular and Molecular Life Sciences*, vol. 63, no. 16, pp. 1819–1822, 2006.
- [134] L. Cai, X. Wang, W. Wang et al., "Peptide ligand and PEG-mediated long-circulating liposome targeted to FGFR overexpressing tumor in vivo," *International Journal of Nanomedicine*, vol. 7, pp. 4499–4510, 2012.
- [135] L. Cai, N. Qiu, X. Li et al., "A novel truncated basic fibroblast growth factor fragment-conjugated poly (ethylene glycol)-cholesterol amphiphilic polymeric drug delivery system for targeting to the FGFR-overexpressing tumor cells," *International Journal of Pharmaceutics*, vol. 408, no. 1–2, pp. 173–182, 2011.
- [136] H. Wang, W. Chen, H. Xie et al., "Biocompatible, chimeric peptide-condensed supramolecular nanoparticles for tumor cell-specific siRNA delivery and gene silencing," *Chemical Communications*, vol. 50, no. 58, pp. 7806–7809, 2014.
- [137] J. Wang, H. Wang, J. Li et al., "IRGD-decorated polymeric nanoparticles for the efficient delivery of vandetanib to hepatocellular carcinoma: preparation and in vitro and in vivo evaluation," *ACS Applied Materials and Interfaces*, vol. 8, no. 30, pp. 19228–19237, 2016.
- [138] Y. Li, Y. Lai, X. Xu et al., "Capsid-like supramolecular dendritic systems as pH-responsive nanocarriers for drug penetration and site-specific delivery," *Nanomedicine: Nanotechnology, Biology, and Medicine*, vol. 12, no. 2, pp. 355–364, 2016.
- [139] A. Garg, A. W. Tisdale, E. Haidari, and E. Kokkoli, "Targeting colon cancer cells using PEGylated liposomes modified with a fibronectin-mimetic peptide," *International Journal of Pharmaceutics*, vol. 366, no. 1–2, pp. 201–210, 2009.
- [140] Q. Hou, P. A. De Bank, and K. M. Shakesheff, "Injectable scaffolds for tissue regeneration," *Journal of Materials Chemistry*, vol. 14, no. 13, pp. 1915–1923, 2004.
- [141] Y. Nagai, L. D. Unsworth, S. Koutsopoulos, and S. Zhang, "Slow release of molecules in self-assembling peptide nanofiber scaffold," *Journal of Controlled Release*, vol. 115, no. 1, pp. 18–25, 2006.
- [142] Y. Zhao, T. Ji, Y. Zhao et al., "Transformable peptide nanocarriers for expeditious drug release and effective cancer therapy via cancer-associated fibroblast activation," *Angewandte Chemie—International Edition*, vol. 55, no. 3, pp. 1050–1055, 2016.
- [143] S. Koutsopoulos, L. D. Unsworth, Y. Nagai, and S. Zhang, "Controlled release of functional proteins through designer self-assembling peptide nanofiber hydrogel scaffold," *Proceedings of*

the National Academy of Sciences of the United States of America, vol. 106, no. 12, pp. 4623–4628, 2009.

- [144] I. González De Torre, M. Santos, L. Quintanilla, A. Testera, M. Alonso, and J. C. Rodríguez Cabello, “Elastin-like recombinamer catalyst-free click gels: characterization of poroelastic and intrinsic viscoelastic properties,” *Acta Biomaterialia*, vol. 10, no. 6, pp. 2495–2505, 2014.
- [145] Y. F. Tian, G. A. Hudalla, H. Han, and J. H. Collier, “Controllably degradable β -sheet nanofibers and gels from self-assembling depsipeptides,” *Biomaterials Science*, vol. 1, no. 10, pp. 1037–1045, 2013.

Research Article

Optimal Zn-Modified Ca–Si-Based Ceramic Nanocoating with Zn Ion Release for Osteoblast Promotion and Osteoclast Inhibition in Bone Tissue Engineering

Jiangming Yu,^{1,2} Lizhang Xu,¹ Ning Xie,¹ Kai Li,³ Yanhai Xi,¹ Xiling Liu,¹
Xuebin Zheng,³ Xiongsheng Chen,¹ Xiaojian Ye,¹ and Daixu Wei⁴

¹Department of Orthopaedics, Changzheng Hospital, Second Military Medical University, Shanghai 200003, China

²National Engineering Research Center for Nanotechnology, Shanghai 200241, China

³Key Laboratory of Inorganic Coating Materials, Shanghai Institute of Ceramics, Chinese Academy of Sciences, Shanghai 200003, China

⁴Tsinghua-Peking Center for Life Sciences, Tsinghua University, Beijing 100084, China

Correspondence should be addressed to Xiaojian Ye; yespine@163.com and Daixu Wei; davidxwei@163.com

Received 21 December 2016; Revised 21 January 2017; Accepted 30 January 2017; Published 9 March 2017

Academic Editor: Chuanfei Guo

Copyright © 2017 Jiangming Yu et al. This is an open access article distributed under the Creative Commons Attribution License, which permits unrestricted use, distribution, and reproduction in any medium, provided the original work is properly cited.

We investigated the slow release of Zn ion (Zn^{2+}) from nanocoatings and compared the in vitro response of osteoblasts (MC3T3-E1) and proosteoclasts (RAW 264.7) cultured on $Ca_2ZnSi_2O_7$ nanocoated with different Zn/Ca molar ratios on a Ti-6Al-4V (i.e., Ti) substrate to optimize cell behaviors and molecule levels. Significant morphology differences were observed among samples. By comparing with pure Ti and $CaSiO_3$ nanocoating, the morphology of $Ca_2ZnSi_2O_7$ ceramic nanocoatings was rough and contained small nanoparticles or aggregations. Slow Zn^{2+} release from nanocoatings was observed and Zn^{2+} concentration was regulated by varying the Zn/Ca ratios. The cell-response results showed $Ca_2ZnSi_2O_7$ nanocoating at different Zn/Ca molar ratios for osteoblasts and osteoclasts. Compared to other nanocoatings and Ti, sample Zn/Ca (0.3) showed the highest cell viability and upregulated expression of the osteogenic differentiation genes ALP, COL-1, and OCN. Additionally, sample Zn/Ca (0.3) showed the greatest inhibition of RAW 264.7 cell growth and decreased the mRNA levels of osteoclast-related genes OAR, TRAP, and HYAL. Therefore, the optimal Zn-Ca ratio of 0.3 in $Ca_2ZnSi_2O_7$ ceramic nanocoating on Ti had a dual osteoblast-promoting and osteoclast-inhibiting effect to dynamically balance osteoblasts/osteoclasts. These optimal Zn-Ca ratios are valuable for $Ca_2ZnSi_2O_7$ ceramic nanocoating on Ti-coated implants for potential applications in bone tissue regeneration.

1. Introduction

In bone tissue engineering, calcium silicate-based ceramics, such as $CaSiO_3$ and Ca_2SiO_4 , are promising as potential implant biomaterials based on their bioactive and biocompatible properties [1, 2]. Recently, novel ion-modified Ca–Si-based ceramics were developed to improve their chemical stability and biomedical properties. Introduced ions mainly include divalent (e.g., Zn, Mg, and Sr) [3–5] and tetravalent (e.g., Zr and Ti) ions [6, 7]. Compared with pure calcium silicate coatings, tetravalent Ti and Zr-incorporated Ca–Si-based ceramics have been used as stable coatings to improve biomedical properties.

Zinc (Zn), an essential trace element, has been demonstrated to play an important role in various physiological processes in humans [8]. However, Zn-modified calcium silicate ceramic coatings have not been widely investigated. Zn was shown to have a stimulatory effect on bone formation and inhibitory or biphasic effect on osteoclastic bone resorption [9]. Furthermore, Zn deficiency in the body can arrest bone growth, bone development, and overall bone health maintenance [10]. However, Zn-modified calcium silicate ($Ca_2ZnSi_2O_7$) ceramic coating Ti shows high potential as a biomaterial in bone tissue engineering but has not been investigated in detail.

Previous studies [11, 12] investigated the preparation of $\text{Ca}_2\text{ZnSi}_2\text{O}_7$ ceramic nanocoating on a Ti-6Al-4V (i.e., Ti) substrate and explored the effects on osteoblasts. The results showed that the $\text{Ca}_2\text{ZnSi}_2\text{O}_7$ nanocoating promoted the adhesion, proliferation, and osteoblast differentiation of MC3T3-E1 cells. However, the optimal Zn content in the $\text{Ca}_2\text{ZnSi}_2\text{O}_7$ nanocoating and whether abundant healthy osteoblasts grew on the Zn nanocoating were not confirmed. Various materials can affect osteoclasts when stimulating osteoblasts because of the dynamic balance between these cells [13, 14]. Moreover, we predicted that Zn ion could be released slowly from the $\text{Ca}_2\text{ZnSi}_2\text{O}_7$ ceramic nanocoating to maintain the Zn^{2+} content for MC3T3-E1 cells in the medium. Therefore, in this study, we investigated the optimal Zn/Ca ratio in $\text{Ca}_2\text{ZnSi}_2\text{O}_7$ nanocoating and the slow release of Zn from the nanocoating to promote osteogenic differentiation and inhibit osteoclastic differentiation.

2. Materials and Methods

2.1. Materials. Zinc nitrate hexahydrate was purchased from Sinopharm Chemical Reagent Co., Ltd. (Shanghai, China). Calcium nitrate tetrahydrate and tetraethyl orthosilicate were purchased from Sinopharm Chemical Reagent Co., Ltd. Ti-6Al-4V substrates were fabricated in our lab. All cell culture reagents were purchased from Life-Tech Co., Ltd. (USA), and cell culture plates were obtained from Corning (Corning, NY, USA). Other analytical grade reagents were purchased from Sigma (St. Louis, MO, USA) and Milli-Q water was produced in our lab.

2.2. Preparation of Nanocoatings. According to previous studies [11, 12], three types of zinc-modified calcium silicate ($\text{Ca}_2\text{ZnSi}_2\text{O}_7$) powders and nanocoatings were prepared. Briefly, using zinc nitrate hexahydrate, calcium nitrate tetrahydrate, and tetraethyl orthosilicate, nanoscale $\text{Ca}_2\text{ZnSi}_2\text{O}_7$ powders were synthesized by the sol-gel method. These powders had different Zn/Ca molar ratios of 0.1, 0.3, and 0.5, respectively, and were named as samples Zn/Ca (0.1), Zn/Ca (0.3), and Zn/Ca (0.5). The produced $\text{Ca}_2\text{ZnSi}_2\text{O}_7$ powders were sprayed onto Ti-6Al-4V substrates with dimensions of $10 \times 10 \times 2$ mm and $\phi 10 \times 1$ mm. To prepare all nanocoatings, the atmosphere plasma spray (APS) system (Sulzer Metco, Winterthur, Switzerland) was employed to generate a coating thickness of approximately 170 nm. CaSiO_3 coatings were prepared using pure CaSiO_3 nanopowder, named as sample Zn/Ca (0), because of the lack of the Zn element. After spraying, all samples, including Ti-6Al-4V substrates (named as sample Ti) as a control, were ultrasonically cleaned in acetone, ethanol, and distilled water for 10 min.

2.3. Characterizations of Nanocoatings. Morphological studies of all samples were performed by scanning electron microscopy (SEM) (Hitachi S-4800, Tokyo, Japan). All samples were treated by Pt spraying for 60 s prior to observation at 10x and 5000x magnification by SEM at 10 kV. In addition, the static contact angles of all nanocoatings were measured using

a contact angle analyzer (Model SL600; Solon Inform-tech Co. Ltd., Shanghai, China) at 25°C. Next, 5 ± 0.5 μL of Milli-Q water was gently added onto the surface of each sample and measured within 10 s. For statistical analysis, the static contact angles were evaluated for at least 6 random contact test points.

2.4. In Vitro Release Studies of Zn^{2+} . Two divalent ions of Zn^{2+} were studied for in vitro release from the nanocoatings. All samples were immersed in 20 mL alpha-minimum essential medium (α -MEM) for 7 days and then filtered through a 0.22 μm membrane (Millipore, Billerica, MA, USA). The test media were diluted 1/20 prior to measurement. The concentration of Zn^{2+} was detected using an inductively coupled plasma atomic emission spectrometer (ICP-AES, 710-ES, Varian Medical Systems, Palo Alto, CA, USA). Sample Ti without nanocoatings as a control was also analyzed in the same manner for release studies in vitro.

2.5. Cell Culture. Osteoblasts (MC3T3-E1) and proosteoclasts (RAW 264.7) were kindly provided by Shanghai Cell Bank in the Chinese Academy of Sciences. The MC3T3-E1 cells and RAW 264.7 cells, respectively, were cultivated in the α -MEM with penicillin/streptomycin (both 100 units/mL), and 10% of fetal beef serum (FBS) in incubator was supplied with 5% of CO_2 at 37°C. The α -MEM for RAW 264.7 cells contained 10 ng/mL RANKL for osteoclastic differentiation [13].

2.6. CCK-8 Test. In the cell proliferation test, 2×10^4 MC3T3-E1 cells and RAW 264.7 cells were, respectively, seeded onto the surface of discs sterilized with 75% v/v ethyl alcohol for 6 h and UV for 2 h. The cells on samples were cultivated in α -MEM at day 3 and day 7, respectively, and viability was assessed by the CCK-8 assay (Cell Counting Kit-8, Sigma). Briefly, the original α -MEM was replaced with 500 μL of fresh α -MEM containing 10% CCK-8. Osteoblast cells on films with CCK-8 were incubated at 37°C for 1 h to form dissoluble formazan. Next, 100 mL of dissoluble formazan was removed from each sample and added to the well in a 96-well plate, which was analyzed in a microplate reader (SpectraMax M4, Molecular Devices, Sunnyvale, CA, USA) at 450 nm.

2.7. Confocal Laser Scanning Microscope (CLSM). To analyze cell numbers, at day 3 and day 7, cells on the samples were treated with 10% (w/v) paraformaldehyde for 15 min, 0.5% (w/v) Triton X-100 for 20 min, and then DAPI and Phalloidin-Alexa Fluor® 488 (for RAW 264.7 cell) and Phalloidin-Alexa Fluor 555 (MC3T3-E1 cell) in 30 min. Next, the cells were observed by confocal laser scanning microscopy (CLSM, TCS SP5, Leica, Wetzlar, Germany).

2.8. Scanning Electron Microscopy (SEM). At day 7, the cells on samples were also dehydrated in a graded ethanol series of 50%, 60%, 70%, 80%, 85%, 90%, 95%, and 100% (v/v) for 15 min and then treated by freeze-drying to remove residual ethanol for 4 h. Finally, the cells sprayed with Pt for 120 s were evaluated by SEM at 250x magnification.

TABLE 1: Primers used for Sybr Green polymerase chain reaction (RT-PCR) in this study.

Genes	Primers
OAR	Forward: 5'-CGTGCTGACTTCACACCAACA-3' Reverse: 5'-AAGGTCACGTTGATCCCAGGAG-3'
TRAP	Forward: 5'-GTGCTGGCTGGAACCATGA-3' Reverse: 5'-GTCCAGCATAAAGATGGCCACA-3'
HYA1	Forward: 5'-CCGTAATGCCCTACGTCCAG-3' Reverse: 5'-AAGGGCCCAAGTGTGGAA-3'
COL1	Forward: 5'-GCGAAGGCAACAGTCGCT-3' Reverse: 5'-CTTGGTGGTTTTGTATTTCGATGAC-3'
ALP	Forward: 5'-TCCTGACCAAAAACCTCAAAGG-3' Reverse: 5'-TGCTTCATGCAGAGCCTGC-3'
OCN	Forward: 5'-CTCACAGATGCCAAGCCCA-3' Reverse: 5'-CCAAGGTAGCGCCGAGTCT-3'
GAPDH	Forward: 5'-TCCACTCACGGCAAATTCAACG-3' Reverse: 5'-TAGACTCCACGACATACTCAGC-3'

2.9. Real-Time Quantitative PCR (RT-qPCR). Using the Quantitect SYBR Green PCR Kit (Qiagen, Hilden, Germany), the expression of 3 osteogenic gene markers for MC3T3-E1, alkaline phosphatase (ALP), collagen type-1 (COL-1), and osteocalcin (OCN), was evaluated by real-time quantitative PCR (RT-qPCR) [15]. The primers used are shown in Table 1. First, 1 mg of the total RNA from the cells on each film was purified for the synthesis of complementary DNA according to the kit instructions. Similarly, the expression of 3 osteoclastic gene markers for RAW 264.7 cells, osteoclast-associated receptor (OAR), tartrate-resistant acid phosphatase (TRAP), and hyaluronoglucosaminidase 1 (HYA1), was evaluated by the same method. The results were reported as the relative expression normalized to the transcript level of the housekeeping gene glyceraldehyde 3-phosphate dehydrogenase (GAPDH).

2.10. Statistical Analysis. For statistical analysis, all data were expressed as the means \pm standard deviations (SD) ($n = 3-6$). Statistical comparisons were performed by Student's t -tests with $p < 0.05$ indicating statistical significance and $p < 0.01$ indicating high statistical significance.

3. Results and Discussion

3.1. Characterization of $\text{Ca}_2\text{ZnSi}_2\text{O}_7$ Nanocoatings. Metals are widely considered to be optimal materials for bone repair in bone tissue engineering because of their physical characteristics, which are similar to those of natural bone. However, traditional metallic biomaterials, for example, titanium alloy, did not show a satisfactory cellular response and ultimately did not show tissue regeneration when implanted in the body for a long period of time, limiting their applications. Thus, studies to modify the surfaces of metallic biomaterials attempted to improve their wear properties, corrosion resistance, and biocompatibility [16–18]. In previous studies [11, 12], we verified that $\text{Ca}_2\text{ZnSi}_2\text{O}_7$ nanocoating promoted

the adhesion, proliferation, and osteoblast differentiation of MC3T3-E1 cells. However, the optimal Zn content in $\text{Ca}_2\text{ZnSi}_2\text{O}_7$ nanocoating and whether healthy osteoblasts grow abundantly on Zn in the nanocoating were not confirmed. Moreover, we predicted that Zn^{2+} could be released slowly from the $\text{Ca}_2\text{ZnSi}_2\text{O}_7$ ceramic nanocoating to maintain a reasonable Zn^{2+} content for MC3T3-E1 cells in the medium, which is similar to the sustained release system of Zn^{2+} .

First, we regulated the Zn/Ca ratios in the $\text{Ca}_2\text{ZnSi}_2\text{O}_7$ ceramic nanocoating. As shown in Figure 1, the micromorphology of the samples with ceramic nanocoatings was rough (Figures 1(b)–1(e)), which was different from the Ti substrate (Figure 1(a)). Some ceramic big particles, which are labeled by blue arrows in Figure 1, were observed on surface of Zn/Ca (0) and additional nanoparticles or aggregations adhered on the nanocoatings of $\text{Ca}_2\text{ZnSi}_2\text{O}_7$ (red arrows in Figure 1). These results were similar to those of previous studies [11]. However, with increasing Zn content in the nanocoating, the surface nanoparticles decreased gradually from Zn/Ca (0.1) to Zn/Ca (0.5). Similarly, sizes distribution of surface particles also showed a decreasing tendency, and average sizes of Zn/Ca (0), Zn/Ca (0.1), Zn/Ca (0.3), and Zn/Ca (0.5) are 401 ± 195 nm, 212 ± 47 nm, 178 ± 61 nm, and 119 ± 67 nm, respectively. These results indicate that Zn content changed the structure of the ceramic nanocoatings. Interestingly, the introduction of Zn did not affect the surface hydrophilicity of the coatings, as measured by the water contact angle test. As shown in Figure 2, the water contact angles of Zn/Ca (0.1), Zn/Ca (0.3), and Zn/Ca (0.5) were 18.31° to 21.22° , which are close to 21.49° of Zn/Ca (0), representing the CaSiO_3 coating. But all nanocoatings showed lower water contact angles than control Ti of 39.86° . Thus, these nanocoatings changed the surface physical property by transforming the microstructures. However, different Zn/Ca ratios among the nanocoatings did not have a large effect on surface hydrophilicity.

3.2. Release of Zn^{2+} from Nanocoatings. Furthermore, the influence of the potential slow release of Zn from the nanocoatings was evaluated. As shown in Figure 3, Zn^{2+} showed typical slow release from the nanocoatings of $\text{Ca}_2\text{ZnSi}_2\text{O}_7$ with different Zn/Ca ratios, with a burst release in the initial 12 h. Ultimately, with increasing Zn content in the nanocoatings, the order of accumulated Zn^{2+} concentration in the medium was $\text{Ti} = \text{Zn/Ca (0)} < \text{Zn/Ca (0.1)} < \text{Zn/Ca (0.3)} < \text{Zn/Ca (0.5)}$. The contents of Zn/Ca (0.1), Zn/Ca (0.3), and Zn/Ca (0.5) were 3.12, 5.89, and 9.41 ppm, respectively. In contrast, released Zn^{2+} from sample Zn/Ca (0), representing Ca_2SiO_3 , was close to 0, similarly to sample Ti. In previous studies [19–22], Zn, an important element in cells and the body, was introduced into an inorganic compound coating, such as hydroxyapatite (HA). To improve the osseointegration properties of the hydroxyapatite-titanium substrate (HA/TiO_2), Zhang et al. prepared Zn containing hydroxyapatite titania (ZnHA/TiO_2) hybrid coatings on titanium, and the released Zn^{2+} was investigated [22]. However, Zn was only mixed into the microporous structure

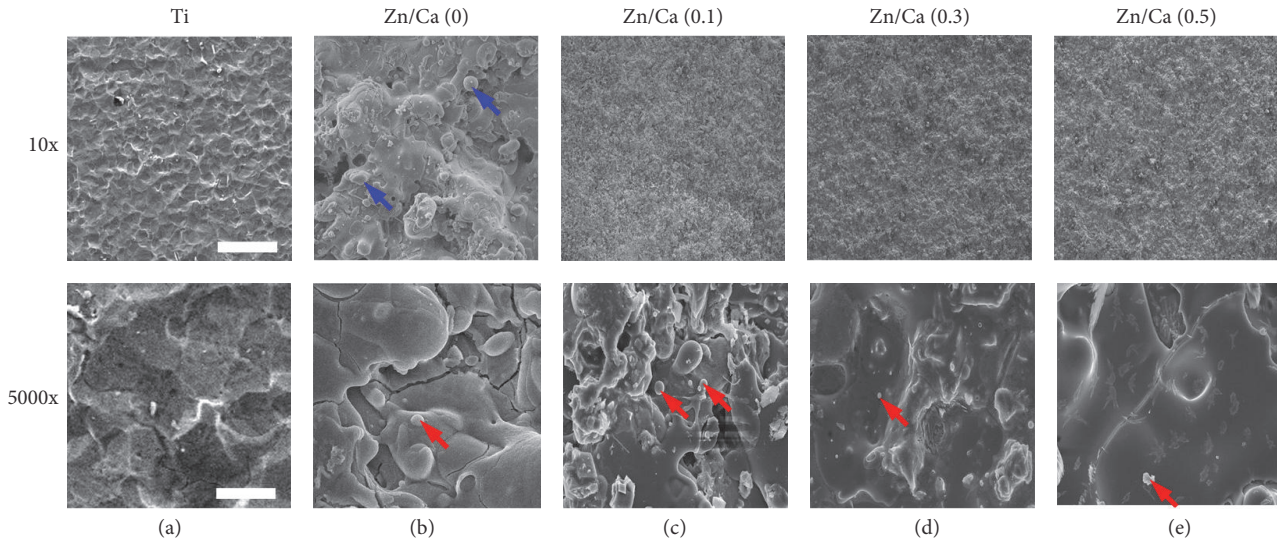


FIGURE 1: Morphology of Ti, Zn/Ca (0), Zn/Ca (0.1), Zn/Ca (0.3), and Zn/Ca (0.5), respectively. The bar is 1 mm in 10x magnification and the bar is $2\ \mu\text{m}$ in 5000x magnification, respectively.

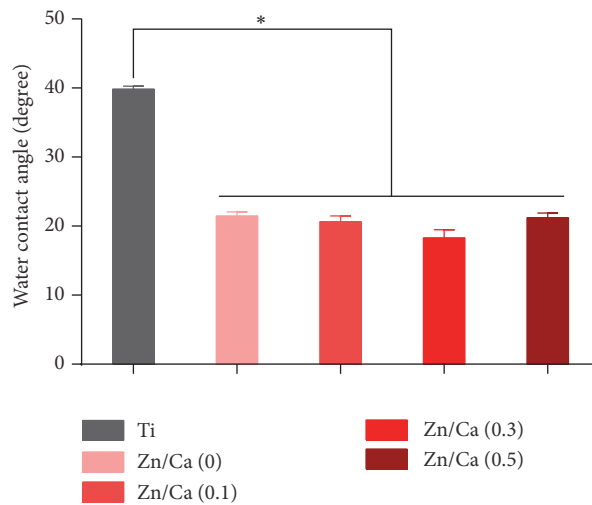


FIGURE 2: Water contact angles of samples Ti, Zn/Ca (0), Zn/Ca (0.1), Zn/Ca (0.3), and Zn/Ca (0.5) at 25°C . * $p < 0.05$; $n = 6$ for each sample.

of HA, not TiO_2 . In contrast, $\text{Ca}_2\text{ZnSi}_2\text{O}_7$, a Zn-modified Ca–Si coating, has been reported as a biometrical substrate for bone-related cell culture. However, the potential slow release of Zn^{2+} was not evaluated. We found that Zn can promote osteoblast proliferation and differentiation compared to on pure Ca–Si based coatings. Zn may have been released slowly from the hybrid nanocoating, playing an important role in the effect on osteoblasts.

3.3. Behaviors of Cells on Nanocoatings. Some materials can affect osteoclasts when stimulating osteoblasts because of the dynamic balance of these cells [13, 14]. MC3T3-E1 and RAW 264.7 cells, as cell models of osteoblasts and osteoclasts, respectively, were employed in this study and cultivated on the surface of all samples for proliferation analysis. MC3T3-E1 cells and RAW 264.7 cells grew in 7 days. As shown in

Figures 4 and 5, the numbers of RAW 264.7 cells on all nanocoatings were similar, containing Zn/Ca (0), Zn/Ca (0.1), Zn/Ca (0.3), and Zn/Ca (0.5), which were lower than on pure Ti discs at day 3. At day 7, the number of cells increased as Zn content increased and then decreased at a Zn/Ca ratio of 0.3. Attentively, the samples without Zn, Ti, and Zn/Ca (0) showed better cell growth, revealing how the nanocoatings with the Zn element inhibited osteoclast through inhibitory or biphasic effects of Zn on osteoclastic bone resorption [9]. Moreover, the formation of multinucleated cells is the main feature of osteoclast-like cells. Some multinucleated cells were found in samples Ti and Zn/Ca (0), indicated by asterisk in Figure 4. However, MC3T3-E1 cells showed the opposite growth tendency for different nanocoatings of Zn/Ca. The order of cell viability was $\text{Ti} < \text{Zn/Ca (0)} < \text{Zn/Ca (0.1)} < \text{Zn/Ca (0.3)} < \text{Zn/Ca (0.5)}$ at day 3. The viability of MC3T3-E1 cells grown on Zn/Ca (0.3) was the highest in all samples.

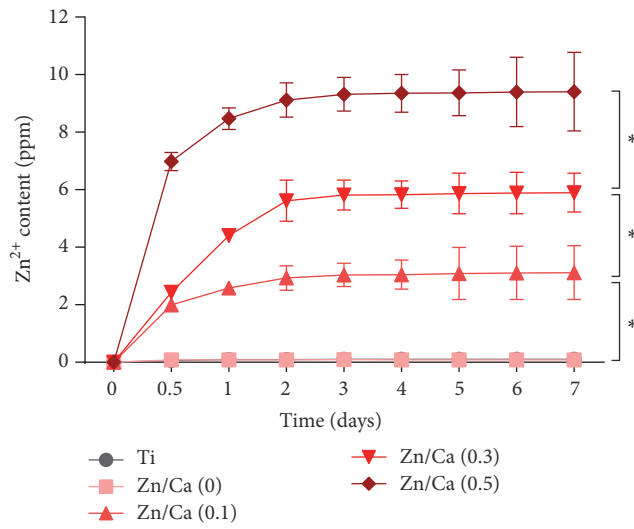


FIGURE 3: Curves of accumulated Ca²⁺ and Zn²⁺ released from Ti, Zn/Ca (0), Zn/Ca (0.1), Zn/Ca (0.3), and Zn/Ca (0.5) in 7 days. * *p* < 0.05; *n* = 4 for each sample.

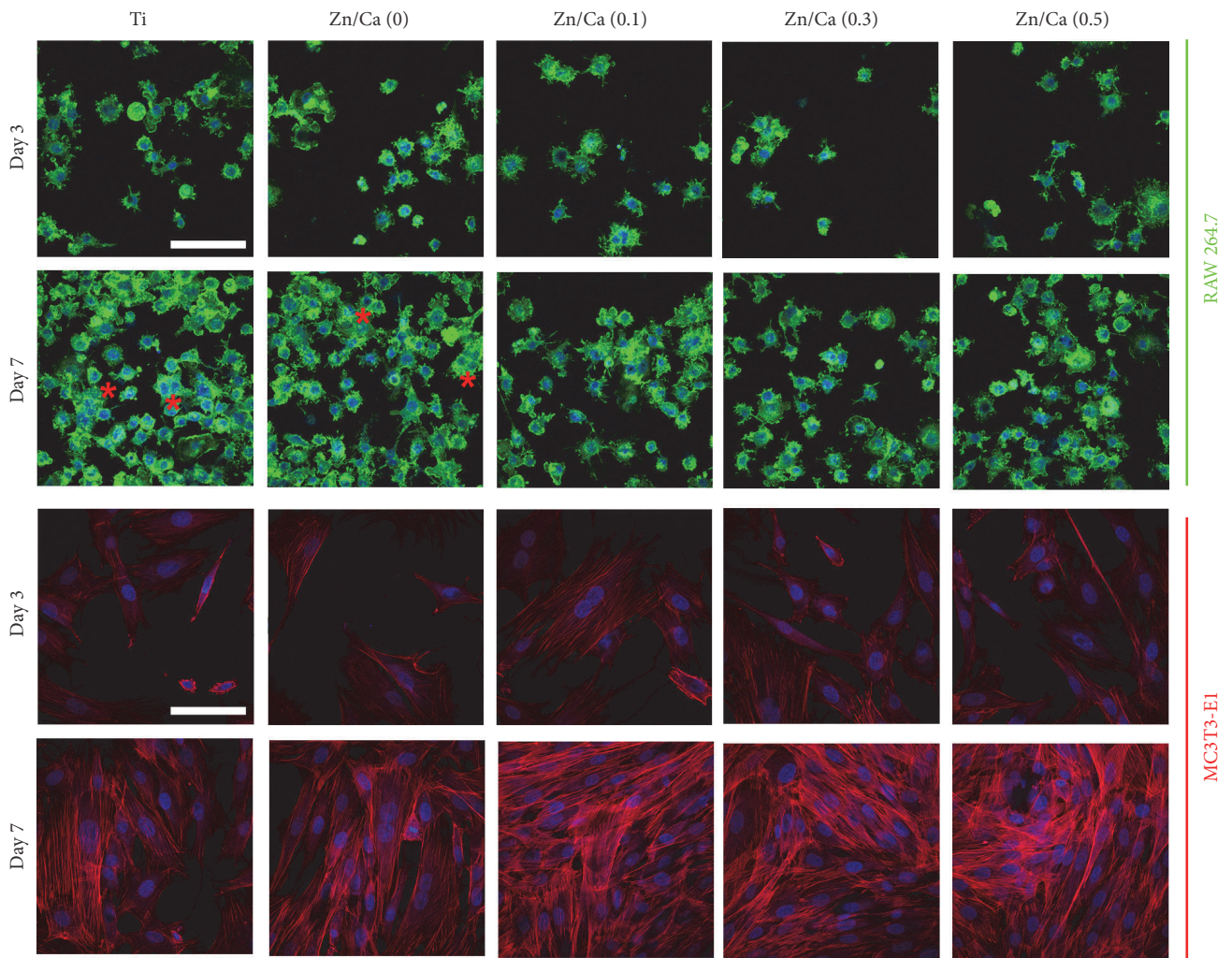


FIGURE 4: CLSM images of RAW 264.7 cells and MC3T3-E1 cells grown on Ti, Zn/Ca (0), Zn/Ca (0.1), Zn/Ca (0.3), and Zn/Ca (0.5) at day 3 and day 7. The bar is 100 μ m. The red asterisks indicate the multinucleated cells for osteoclast differentiation of RAW 264.7 cells.

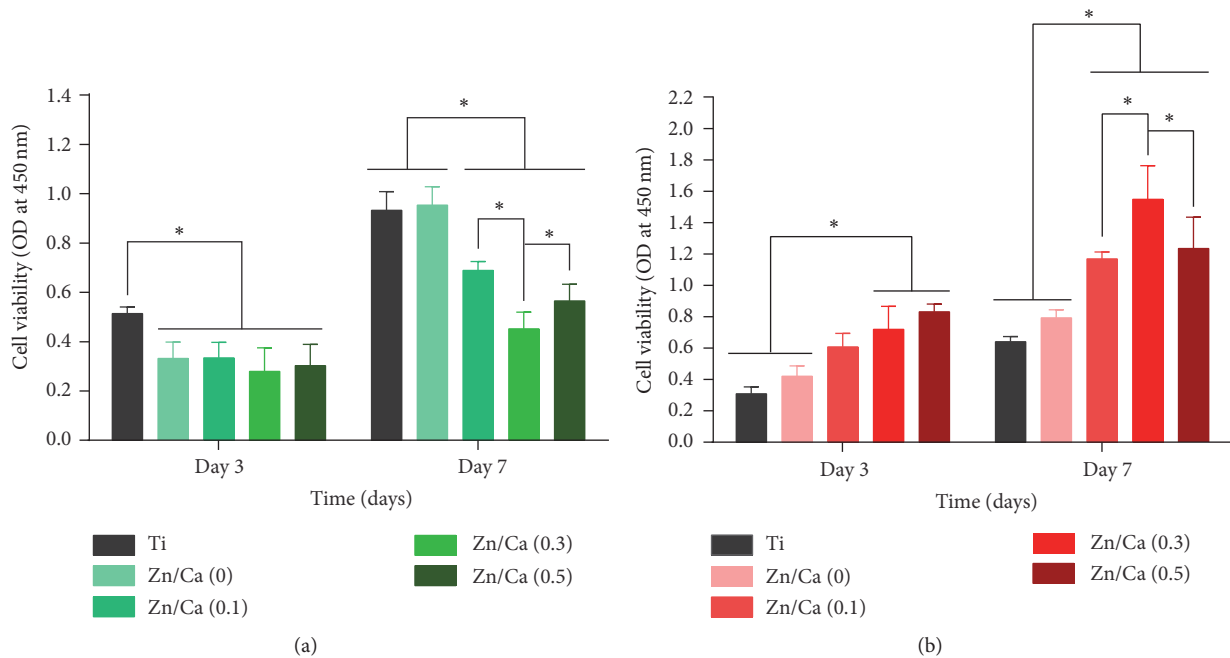


FIGURE 5: The CCK-8 assay of (a) RAW 264.7 cells and (b) MC3T3-E1 cells grown on Ti, Zn/Ca (0), Zn/Ca (0.1), Zn/Ca (0.3), and Zn/Ca (0.5) at day 3 and day 7, respectively. * $p < 0.05$; $n = 4$ for each sample.

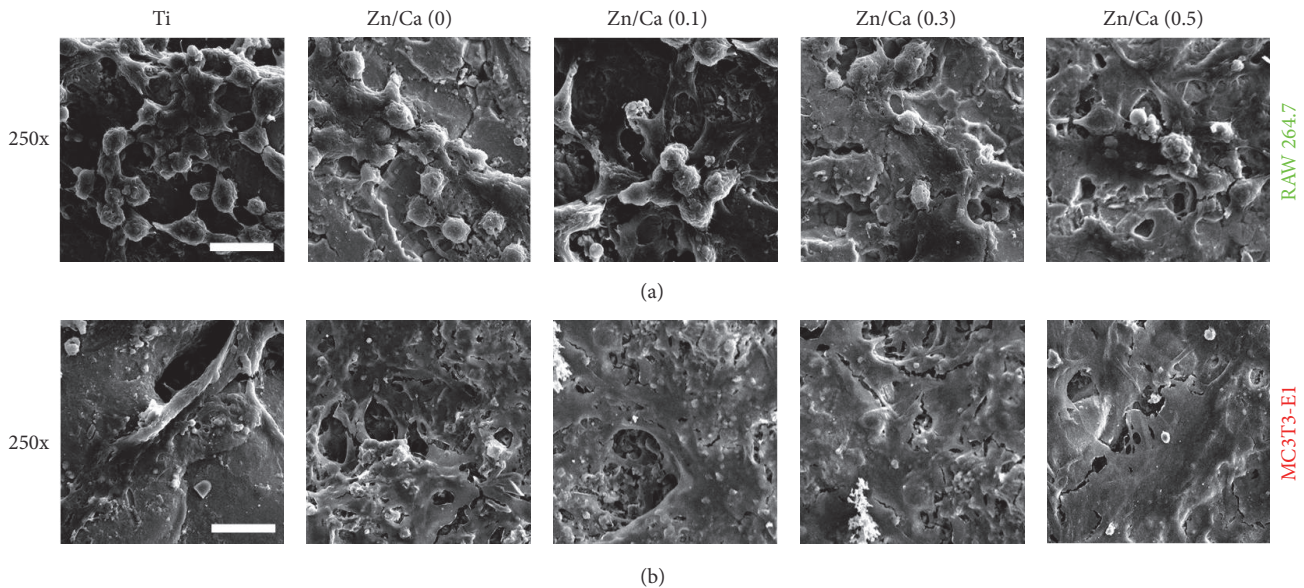


FIGURE 6: SEM images of RAW 264.7 cells (a) and MC3T3-E1 cells (b) grown on Ti, Zn/Ca (0), Zn/Ca (0.1), Zn/Ca (0.3), and Zn/Ca (0.5) at day 7. The bar is 50 μm .

In contrast to RAW 264.7 cells, MC3T3-E1 cells on the discs with Zn nanocoating showed higher viability than samples without Zn, similarly to our previous results [11]. Differences in cell number and morphology were determined by SEM as shown in Figure 6. A larger number of normal RAW 264.7 cells was found on samples Ti and Zn/Ca (0). In contrast, MC3T3-E1 cells preferred to adhere and grew well on Zn/Ca (0.1), Zn/Ca (0.3), and Zn/Ca (0.5).

These results show that nanocoating with higher Zn content promotes osteoblasts while inhibiting osteoclasts. Changes in the shape and number of MC3T3-E1 and RAW 264.7 cells were also observed by confocal laser scanning microscopy as shown in Figure 4 and SEM in Figure 6.

With in vitro release test, we discovered the accumulative release curves of Zn^{2+} for all nanocoatings samples started to be steady at day 3. Hence, day 3 is an important time point

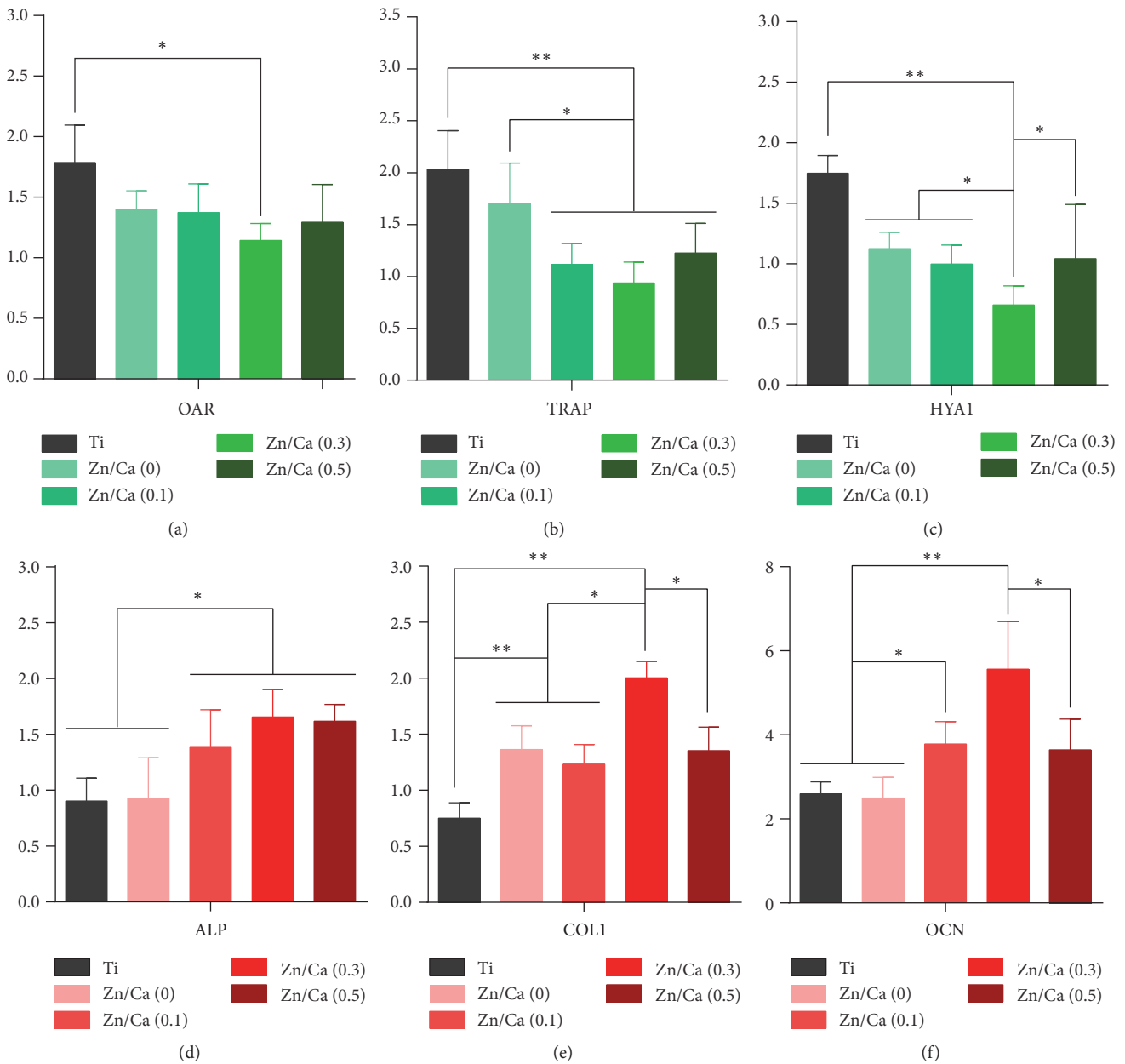


FIGURE 7: Real-time quantitative PCR analysis of gene expression for osteoclastic marker genes in RAW 264.7 cells and osteogenic marker genes in MC3T3-E1 cells grown on Ti, Zn/Ca (0), Zn/Ca (0.1), Zn/Ca (0.3), and Zn/Ca (0.5) at day 7, respectively. * $p < 0.05$; ** $p < 0.01$; $n = 3$ for each sample. The y -axis represented the relative expression ($2^{-\Delta CT}$) normalized to expression level. Osteoclastic marker genes: (a) osteoclast-associated receptor (OAR), (b) tartrate-resistant acid phosphatase (TRAP), and (c) hyaluronoglucosaminidase 1 (HYA1). Osteogenic marker genes: (d) alkaline phosphatase (ALP), (e) collagen type-1 (COL1), and (f) osteocalcin (OCN).

for cells in this study. In early stage, Zn^{2+} concentration was lacking; the concentration is maximum for cell growth for starting at day 3. Maybe it is the main reason that there is no remarkable difference of cells in all nanocoatings samples at day 3; however it was changed to be remarkable at day 7.

3.4. Response of Cells on Nanocoatings. To explore the inhibition of osteoclastic differentiation of $Ca_2ZnSi_2O_7$ ceramic nanocoating with different Zn/Ca ratios, the expression of three relative genes, OAR, TRAP, and HYA1, was assessed

by RT-qPCR. In Figures 7(a)–7(c), gene expression in RAW 264.7 cells was downregulated with increasing Zn in the nanocoating. The effect of sample Zn/Ca (0.3) was most significant, which was lower than Zn/Ca (0), Zn/Ca (0.1), Zn/Ca (0.5) and Ti discs for any osteoclastic genes. Because of the lack of Zn, the Zn/Ca (0) (i.e., $CaSiO_3$ nanocoating) showed similar expression of OAR and HYA1 on the Ti discs, but TRAP expression was slightly higher than on Ti. This demonstrates that Zn-loading of the nanocoating inhibited RAW 264.7 cell differentiation by affecting mRNA expression

related to the osteoclastogenic response, particularly for Zn/Ca (0.3). On the contrary, overmuch Zn, such as sample Zn/Ca (0.5), could also affect related gene expression, but not best. When RANKL binds to RANK, various signaling pathways (e.g., OAR, TRAP, and HYA1) in RAW 264.7 cells can be rapidly activated to facilitate osteoclast differentiation. RANKL can stimulate some transcription factors, such as AP-1, through mitogen-activated protein kinase (MAPK) activation, and NF- κ B through I κ B kinase (IKK) activation [23]. Hence, these pathways play an important role in osteoclastogenesis. In our study, suppression of these signaling pathways was thought to inhibit osteoclast differentiation on the Ca₂ZnSi₂O₇ ceramic nanocoating. However, the inhibition mechanism of Zn in osteoclast differentiation requires further analysis [2, 12].

To further evaluate the mechanism of the promotion of osteogenic differentiation of MC3T3-E1 cells, the expression of related genes was also evaluated. As shown in Figures 7(d)–7(f), sample Zn/Ca (0.3), which was modified by a ceramic nanocoating at a 0.3 Zn/Ca ratio, always showed the highest mRNA expression of ALP, COL-1, and OCN. In addition, samples loaded with higher or lower Zn content than Zn/Ca (0.3), that is, Zn/Ca (0.1) and Zn/Ca (0.5), showed higher expression of ALP and OCN in MC3T3-E1 cells than in samples Ti and Zn/Ca (0). This result is in accordance with previous results of ALP gene regulation, which indicated that the Ca₂ZnSi₂O₇ nanocoating has a greater ability to stimulate preosteoblast differentiation compared to CaSiO₃ nanocoating and Ti discs. And ALP is a Zn-dependent enzyme, illustrated in past reports, while others were secreted solely by osteoblasts and thought to play a role in cell mineralization and calcium ion homeostasis. In addition, ALP acts as initiators of biological mineralization [24, 25], which is very important for osteogenic differentiation. The results of peak-tendency for osteoblast of mRNA expression also explain why the expression of these genes was changed by Zn content in a dose-dependent manner, with the Zn/Ca ratio of 0.3 showing the best results.

Interestingly, two profiles of relevant mRNA expression, the peak-tendency for osteoblast and valley-tendency for osteoclasts, were complementary. Thus, the Zn content in the Ca₂ZnSi₂O₇ nanocoating may simultaneously regulate osteogenic-osteoclastic differentiation because of the slow release of introduced Zn.

4. Conclusions

By comparison of the Ti surface, the morphology of Ca₂ZnSi₂O₇ ceramic nanocoating with Zn/Ca (0.1), Zn/Ca (0.3), and Zn/Ca (0.5) was rough and mixed with some nanoparticles or aggregations, which differed from Zn/Ca (0) (CaSiO₃ nanocoating) and Ti. Additionally, the Ca₂ZnSi₂O₇ ceramic nanocoating showed a typical slow release of Zn²⁺ with a burst release during the initial 12 h. MC3T3-E1 cells showed the highest cell viability on sample Zn/Ca (0.3), and all the expressions of the ALP, COL-1, and OCN genes involved in osteogenic differentiation were upregulated. In contrast, for Zn/Ca (0.3), RAW 264.7 cells showed the lowest cell viability and inhibited the osteoclastic gene expressions

of OAR, TRAP, and HYA1. In summary, the optimal Zn-Ca ratio of 0.3 in the Ca₂ZnSi₂O₇ ceramic nanocoating on Ti with Zn²⁺ slow release may have osteoblast-promoting and osteoclast-inhibiting effects to form a dynamic balance between osteoblasts/osteoclasts.

Disclosure

Jiangming Yu and Lizhang Xu are co-first authors.

Competing Interests

All authors declare that there is no conflict of interests regarding the publication of this paper.

Acknowledgments

The research was supported by the National Natural Science Foundation of China (Grant no. 81301537).

References

- [1] S. Ni, J. Chang, L. Chou, and W. Zhai, "Comparison of osteoblast-like cell responses to calcium silicate and tricalcium phosphate ceramics in vitro," *Journal of Biomedical Materials Research—Part B Applied Biomaterials*, vol. 80, no. 1, pp. 174–183, 2007.
- [2] X. Liu, S. Tao, and C. Ding, "Bioactivity of plasma sprayed dicalcium silicate coatings," *Biomaterials*, vol. 23, no. 3, pp. 963–968, 2002.
- [3] C. Wu, J. Chang, J. Wang, S. Ni, and W. Zhai, "Preparation and characteristics of a calcium magnesium silicate (bredigite) bioactive ceramic," *Biomaterials*, vol. 26, no. 16, pp. 2925–2931, 2005.
- [4] M. Schumacher, A. Lode, A. Helth, and M. Gelinsky, "A novel strontium(II)-modified calcium phosphate bone cement stimulates human-bone-marrow-derived mesenchymal stem cell proliferation and osteogenic differentiation in vitro," *Acta Biomaterialia*, vol. 9, no. 12, pp. 9547–9557, 2013.
- [5] C. Wu, Y. Ramaswamy, D. Kwik, and H. Zreiqat, "The effect of strontium incorporation into CaSiO₃ ceramics on their physical and biological properties," *Biomaterials*, vol. 28, no. 21, pp. 3171–3181, 2007.
- [6] Y. Ramaswamy, C. Wu, A. Van Hummel, V. Combes, G. Grau, and H. Zreiqat, "The responses of osteoblasts, osteoclasts and endothelial cells to zirconium modified calcium-silicate-based ceramic," *Biomaterials*, vol. 29, no. 33, pp. 4392–4402, 2008.
- [7] C. Wu, Y. Ramaswamy, A. Soeparto, and H. Zreiqat, "Incorporation of titanium into calcium silicate improved their chemical stability and biological properties," *Journal of Biomedical Materials Research - Part A*, vol. 86, no. 2, pp. 402–410, 2008.
- [8] H. Tapiero and K. D. Tew, "Trace elements in human physiology and pathology: zinc and metallothioneins," *Biomedicine and Pharmacotherapy*, vol. 57, no. 9, pp. 399–411, 2003.
- [9] M. Yamaguchi, H. Oishi, and Y. Suketa, "Stimulatory effect of zinc on bone formation in tissue culture," *Biochemical Pharmacology*, vol. 36, no. 22, pp. 4007–4012, 1987.
- [10] W. Windisch, U. Wher, W. Rambeck, and R. Erben, "Effect of Zn deficiency and subsequent Zn repletion on bone mineral composition and markers of bone tissue metabolism in

- 65Zn-labelled, young-adult rats," *Journal of Animal Physiology and Animal Nutrition*, vol. 86, no. 7-8, pp. 214–221, 2002.
- [11] J. Yu, K. Li, X. Zheng, D. He, X. Ye, and M. Wang, "In Vitro and In Vivo Evaluation of Zinc-Modified Ca-Si-Based Ceramic Coating for Bone Implants," *PLoS ONE*, vol. 8, no. 3, Article ID e57564, 2013.
- [12] K. Li, J. Yu, Y. Xie, L. Huang, X. Ye, and X. Zheng, "Chemical stability and antimicrobial activity of plasma sprayed bioactive $\text{Ca}_2\text{ZnSi}_2\text{O}_7$ coating," *Journal of Materials Science: Materials in Medicine*, vol. 22, no. 12, pp. 2781–2789, 2011.
- [13] C. V. Gurban and O. Mederle, "The OPG/RANKL system and zinc ions are promoters of bone remodeling by osteoblast proliferation in postmenopausal osteoporosis," *Romanian Journal of Morphology and Embryology*, vol. 52, no. 3, supplement, pp. 1113–1119, 2011.
- [14] M. Satué, M. D. M. Arriero, M. Monjo, and J. M. Ramis, "Quercitrin and Taxifolin stimulate osteoblast differentiation in MC3T3-E1 cells and inhibit osteoclastogenesis in RAW 264.7 cells," *Biochemical Pharmacology*, vol. 86, no. 10, pp. 1476–1486, 2013.
- [15] Y. C. Chai, G. Kerckhofs, S. J. Roberts et al., "Ectopic bone formation by 3D porous calcium phosphate-Ti6Al4V hybrids produced by perfusion electrodeposition," *Biomaterials*, vol. 33, no. 16, pp. 4044–4058, 2012.
- [16] H. Güleriyüz and H. Çimenoglu, "Effect of thermal oxidation on corrosion and corrosion-wear behaviour of a Ti-6Al-4V alloy," *Biomaterials*, vol. 25, no. 16, pp. 3325–3333, 2004.
- [17] E. H. Fragal, T. S. P. Cellet, V. H. Fragal et al., "Hybrid materials for bone tissue engineering from biomimetic growth of hydroxiapatite on cellulose nanowhiskers," *Carbohydrate Polymers*, vol. 152, pp. 734–746, 2016.
- [18] H. Shin, S. Jo, and A. G. Mikos, "Biomimetic materials for tissue engineering," *Biomaterials*, vol. 24, no. 24, pp. 4353–4364, 2003.
- [19] A. Valanezhad, K. Tsuru, and K. Ishikawa, "Fabrication of strongly attached hydroxyapatite coating on titanium by hydrothermal treatment of Ti-Zn- PO_4 coated titanium in CaCl_2 solution," *Journal of Materials Science: Materials in Medicine*, vol. 26, no. 7, article 212, 2015.
- [20] Y.-W. Shang, W. Zhang, J. He, D.-N. Wang, M. Zhong, and B.-H. Zhao, "Study of relationship between (Ca+Zn)/P of pure titanium surface coating and biological activity of osteoblasts," *Shanghai kou qiang yi xue = Shanghai journal of stomatology*, vol. 24, no. 1, pp. 46–51, 2015.
- [21] T. Boonfueng, L. Axe, N. Yee, D. Hahn, and P. K. Ndiba, "Zn sorption mechanisms onto sheathed *Leptothrix discophora* and the impact of the nanoparticulate biogenic Mn oxide coating," *Journal of Colloid and Interface Science*, vol. 333, no. 2, pp. 439–447, 2009.
- [22] J. Y. Zhang, H. J. Ai, and M. Qi, "Osteoblast growth on the surface of porous Zn-containing HA/TiO₂ hybrid coatings on Ti substrate by MAO plus sol-gel methods," *Surface and Coatings Technology*, vol. 228, no. 1, pp. S202–S205, 2013.
- [23] J. Mizukami, G. Takaesu, H. Akatsuka et al., "Receptor activator of NF- κ B ligand (RANKL) activates TAK1 mitogen-activated protein kinase kinase kinase through a signaling complex containing RANK, TAB2, and TRAF6," *Molecular and Cellular Biology*, vol. 22, no. 4, pp. 992–1000, 2002.
- [24] N. Ohara, N. Ohara, K. Yanagiguchi, S. Yamada, I. L. Vilorio, and Y. Hayashi, "Expression of alkaline phosphatase induces rapid and artificial mineralization in specific transformed *Escherichia coli*," *New Microbiologica*, vol. 25, no. 1, pp. 107–110, 2002.
- [25] H. S. Sandhu and S. S. Jande, "Investigations of alkaline phosphatase Ca+2-ATPase and Na+, K+-ATPase during Beta-APN-induced initial bone mineralization inhibition," *Acta Anatomica*, vol. 112, no. 3, pp. 242–248, 1982.

Research Article

Study of the Dynamic Uptake of Free Drug and Nanostructures for Drug Delivery Based on Bioluminescence Measurements

Zhongjian Fang,^{1,2,3} Houchao Xu,⁴ Xiangjun Ji,⁵ Congbiao Liu,¹ Kai Wang,⁶ Xiaoqing Qian,⁷ and Wencong Zhou¹

¹School of Pharmacy, Shanghai University of Medicine & Health Sciences, Shanghai 200237, China

²China Pharmaceutical University, Nanjing 211198, China

³Health School Attached to Shanghai University of Medicine & Health Sciences, Shanghai 200237, China

⁴State Key Laboratory of Phytochemistry and Plant Resources in West China, Kunming Institute of Botany, Chinese Academy of Sciences, Kunming 650201, China

⁵Center for Bioinformatics and Computational Biology and the Institute of Biomedical Sciences, School of Life Science, East China Normal University, Shanghai 200241, China

⁶School of Agriculture and Biology, Shanghai Jiao Tong University, Shanghai 200240, China

⁷Institute of Nano Biomedicine and Engineering, School of Biomedical Engineering, Shanghai Jiao Tong University, Shanghai 200240, China

Correspondence should be addressed to Zhongjian Fang; shilyvip@sina.com

Received 28 October 2016; Revised 16 January 2017; Accepted 23 January 2017; Published 23 February 2017

Academic Editor: Jian Zhong

Copyright © 2017 Zhongjian Fang et al. This is an open access article distributed under the Creative Commons Attribution License, which permits unrestricted use, distribution, and reproduction in any medium, provided the original work is properly cited.

The past two decades have witnessed the great growth of the development of novel drug carriers. However, the releasing dynamics of drug from drug carriers in vivo and the interactions between cells and drug carriers remain unclear. In this paper, liposomes were prepared to encapsulate D-luciferin, which was the substrate of luciferase and served as a model drug. Based on the theoretical calculation of active loading, methods of preparation for liposomes were optimized. Only when D-luciferin was released from liposomes or taken in by the cells could bioluminescence be produced under the catalysis of luciferase. Models of multicellular tumor spheroid (MCTS) were built with 4T1-luc cells that expressed luciferase stably. The kinetic processes of uptake and distribution of free drugs and liposomal drugs were determined with models of cell suspension, monolayer cells, MCTS, and tumor-bearing nude mice. The technology platform has been demonstrated to be effective for the study of the distribution and kinetic profiles of various liposomes as drug delivery systems.

1. Introduction

Since Bangham A. D. and Standish M. M. found liposomes and put forward the concept of liposomes in the 1960s, the technology of liposomes has developed greatly [1]. Various preparation technologies are constantly emerging and gradually applied into clinical use from the laboratory. Among all sorts of research and practice of bioluminescent technology, the firefly luciferase system research is the most thorough and mature one. However, many unsolved problems exist in liposome. For example, the method for dynamically monitoring liposomes and study platform for linking the models in vivo and in vitro are still far from mature.

With the gradual development in D-luciferin research, a growing number of D-luciferin derivatives have been synthesized. These derivatives have various characteristics in molecular weight, solubility, hydrophilicity, and other physicochemical characteristics, which means that they can serve as good model drugs for small molecules [2].

According to the chemical structure and spectral characteristics, D-luciferin has an ultraviolet absorption at 333 nm, and its emission ray peak is at a wavelength of 526 nm [3]. The quantitative detection of D-luciferin can be achieved by both its spectral characteristics and enzymatic reaction with luciferase. These methods provide standards for assays of encapsulation and drug loading of liposomes, which may

also be applied to D-aminoluciferin and other D-luciferin derivatives [4].

Compared with two-dimensional models, multicellular tumor spheroids (MCTS) could serve as models which can bridge monolayer cells in vitro and tumor models in vivo [5]. MCTS are composed of core layers (necrotic layer and layer gangrene), transition layers, and surface layers. Polarity makes MCTS more similar to tumor models in vivo. Besides, since MCTS can be obtained by the method of cell culture, it is more convenient and economical than building tumor models with nude mice [6].

Methods of preparing MCTS include cell suspension dispersive cultivation, tissue engineering method, the microfluidic system, and three-dimensional printing technology. Among all the above methods, cell suspension dispersive cultivation and tissue engineering method are most commonly used. On the other hand, in order to meet the requirements to model a wide variety of tumor cells, a combination of various preparation methods is also a recent trend [7].

The main cell models are two-dimensional models with cell culture plates. It is popular for its short training period and high repeatability. However, two-dimensional plane of monolayer cells has significant limitations. For example, the basal side of cells is contracted to culture plate, and the upper side is exposed to nutrition solution. Although uniformity exists, a good simulation of tumor stroma cannot be achieved.

Therefore, we introduce a liposome encapsulation technology platform for studying the dynamic uptake of nanoparticles delivery system in vitro and in vivo with D-luciferin as a model. We plan to study the preparation of liposomes to encapsulate D-luciferin with pH gradient both theoretically and practically. We also want to investigate the kinetic uptake of free drugs and drug-loaded nanostructures in cell suspension, monolayer cells, MCTS, and tumor-bearing mice. A three-dimensional model is expected to be built to bridge tumor cells in vitro and tumor models in vivo.

2. Materials and Methods

2.1. Materials. EPC and HSPC were purchased from Lipids Corp (Japan). Cholesterol, DPPC, DSPE-PEG2k, and DPPC were purchased from Avanti Polar Lipids Inc. (US). Triton X-100, ATP, Coenzyme A, and agarose were obtained from Sigma-Aldrich (US). D-luciferin and $5 \times$ cell lysis buffer were purchased from Promega Corp (US). Sephadex G-75 was purchased from GE Corp (US). RPMI 1640 cell culture fluid, FBS, trypsin, penicillin/streptomycin solution, and microdialysis tubes were purchased from Thermo Fisher (US). 4T-luc was purchased from Shanghai Science Light Corp (China). DSPE-PEG2000-Mal-GE11 and H1299-pGL3 (C11) were obtained from School of Pharmacy, Shanghai Jiao Tong University. Nude mice (BALB/C, female, 4-week-old, 12.5~17.5 g) were purchased from Slac Laboratory Animal Corp (China). Dialysis bags (MWCO 3.5 KD) were purchased from Sangon Biotech Corp (China). Other chemical reagents for common use were purchased from Shanghai Chemical Reagent Corp (China).

2.2. Methods

2.2.1. Preparation of Liposomes. Most liposomes prepared with the method of passive loading had encapsulation efficiency lower than 15% [8]. In order to prepare liposomes that could carry enough D-luciferin for imaging in vivo and to reduce lipid costs, theoretical calculation has been studied to identify the feasibility of active loading with pH gradient.

The theoretical calculation was based on the following physicochemical parameters and hypothetical conditions:

- The surface of the head of EPC was 70 \AA^2 [8–12]. The pKa of D-luciferin was 8.6.
- The thickness of the lipid bilayer of the liposome models was uniformly 40 \AA [9–12].
- In order to obtain the oil-water partition coefficient of D-luciferin, the software of Marvin-Sketch has been applied with the computed result of $\log P = 2.24$.
- All the liposomes prepared were homogeneous SUV with diameter of 200 nm.

In this hypothetical case, liposomes were composed of EPC: cholesterol: DSPE-PEG2000 with molar ratio of 56:39:5. During the process of drug loading, 0.05 mL D-luciferin (0.725 mg, pH 5.0) was added to liposomes (2.9 mg lipid) with formed pH gradient (pH 5.0 in intrawater phase and pH 10.0 in interwater phase) [13, 14].

$1 \mu\text{mol}$ EPC can be dispersed into 4200 cm^2 lipid monolayer or 2100 cm^2 lipid bilayer.

$$V = S * h. \quad (1)$$

The volume of the oil phase of liposomes composed of $1 \mu\text{mol}$ EPC was $8.4e - 10 \text{ m}^3$. The volume of the oil phase of liposomes composed of 1 mol EPC was $8.4e - 4 \text{ m}^3$.

As shown in Figure 1, in a model of a liposome with diameter of 200 nm, the thickness of lipid bilayer is 4 nm.

$$V_{\text{water-phase}} = \frac{4}{3} \pi r^3 \quad (2)$$

$$V_{\text{oil-phase}} = \frac{4}{3} \pi (R^3 - r^3) \quad (3)$$

$$v_{(\text{water-phase})} = 3.7041e - 21 \text{ m}^3 \quad (\text{Data 1})$$

$$v_{(\text{oil-phase})} = 4.8257e - 22 \text{ m}^3. \quad (\text{Data 2})$$

In the case of liposomes composed of EPC:cholesterol: DSPE-PEG2000 with molar ratio of 56:39:5 [15], when drug:lipid (w/w) = 1:4, liposomes composed of 2.9 mg total lipid contained $2.24309e - 6 \text{ mol}$ EPC and $2.00325e - 7 \text{ mol}$ DSPE-PEG2000.

Hypothesis Condition A. The addition of cholesterol to liposomes only increases the density of membrane but makes no difference on the volume of oil phase. The volume of the oil phase is the sum of volume of EPC and DSPE-PEG2000.

Hypothesis Condition B. When 1 mol EPC and 1 mol DSPE-PEG2000 are forming liposomes, they occupy the same

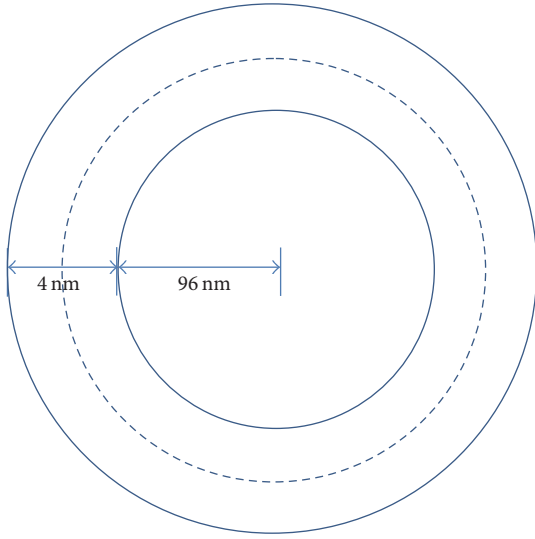


FIGURE 1: Structure schematic of liposome with diameter of 200 nm.

volume. To be specific, 1 mol EPC or 1 mol DSPE-PEG2000 forms an oil phase of $8.4e - 4 \text{ m}^3$.

Based on the hypotheses stated above, in the liposomes composed of 2.9 mg lipid

$$V_{(\text{EPC})} = 1.8842e - 9 \text{ m}^3 \quad (\text{Data 3})$$

$$V_{(\text{DSPE-PEG2000})} = 1.6827e - 10 \text{ m}^3 \quad (\text{Data 4})$$

$$V_{(\text{oil-phase})} = 2.0525e - 9 \text{ m}^3. \quad (\text{Data 5})$$

Hypothesis Condition C. All 2.9 mg lipid forms homogeneous liposomes with diameters of 200 nm.

As shown in (Data 2), in a liposomal model of SUV with diameter of 200 nm, $V_{(\text{oil-phase})} = 4.8257e - 22 \text{ m}^3$. Based on the hypothesis above, 2.9 mg lipid can form $N = 4.253269e12$ liposomes of homogeneous SUV with a diameter of 200 nm. Accordingly, as shown in (Data 1), the total volume of the water phase formed with the 2.9 mg lipid was $1.57545e - 8 \text{ m}^3$.

$$\begin{aligned} V_{(\text{water-phase})} &= N * v_{(\text{water-phase})} \\ &= 1.57545e - 8 \text{ m}^3. \end{aligned} \quad (\text{Data 6})$$

In this case [16], the total volume of liposomal solution was 0.35 mL.

$$V_{(\text{inter-water})} = V - V_{(\text{intra-water})} - V_{(\text{oil-phase})}. \quad (4)$$

Based on the above equation,

$$V_{(\text{inter-water})} = 3.3404e - 7 \text{ m}^3. \quad (\text{Data 7})$$

In order to make sure the calculation for the volume of intra-water phase, interwater phase, and oil phase was reliable and objective enough, a second computing method was applied.

In the model shown in Figure 1, the hydrophilic radicals (polar head) of lipid bilayer faced the intrawater phase

and interwater phase. The inside diameter and the outside diameter of the liposomal model were 186 nm and 200 nm, respectively.

$$S = 4\pi r^2. \quad (5)$$

Based on (5), the sum area of the inner surface and the outside surface was $S = 2.4135e - 13 \text{ m}^2$. Since the area of the polar head of EPC was 70 \AA^2 [9, 10, 17], in order to form a liposomal model with diameter of 200 nm, the number of EPC molecules needed was $3.44786e5$.

$$n_{200 \text{ nm}} = 3.44786e5. \quad (\text{Data 8})$$

Accordingly, 1 mol EPC can form $1.7466e18$ liposomal models with a diameter of 200 nm.

$$N_{200 \text{ nm}} = 1.7466e18. \quad (\text{Data 9})$$

In the case of liposomes composed of 2.9 mg lipids with molar ratio of EPC : chol : SPE-PEG2000 = 56 : 39 : 5,

$$n_{(\text{EPC})} = 2.24309e - 6 \text{ mol} \quad (\text{Data 10})$$

$$n_{(\text{DSPE-PEG2000})} = 2.00325e - 7 \text{ mol}. \quad (\text{Data 11})$$

Hypothesis Condition D. Liposomes are composed of EPC and DSPE-PEG2000 solely. Cholesterol makes no difference on forming liposomes.

Hypothesis Condition E. The head of DSPE-PEG2000 occupies an area of 70 \AA^2 when it is forming liposomes.

Based on the two hypothesis conditions stated above,

$$\begin{aligned} n_{(\text{total lipid})} &= n_{(\text{EPC})} + n_{(\text{DSPE-PEG2000})} \\ &= 2.443415e - 6 \text{ mol}. \end{aligned} \quad (\text{Data 12})$$

Based on (Data 9) and (Data 12), 2.9 mg lipid can form $4.2677e12$ liposomal models of SUV with diameter of 200 nm.

$$N = 4.2677e12. \quad (\text{Data 13})$$

Based on (Data 1) and (Data 2), in 0.35 mL liposomal solution containing 2.9 mg lipids,

$$V_{(\text{oil-phase})} = 2.0710e - 9 \text{ m}^3 \quad (\text{Data 14})$$

$$V_{(\text{intra-water phase})} = 1.5808e - 8 \text{ m}^3. \quad (\text{Data 15})$$

Based on (4)

$$V_{(\text{inter-water phase})} = 3.3212e - 7 \text{ m}^3. \quad (\text{Data 16})$$

Based on the above data, in order to identify the feasibility of active loading of pH gradient, the balanced concentration of D-luciferin in different phases was calculated.

Hypothesis Condition F. When the active loading of pH gradient finished, the pH of intrawater phase was 5.0 and the pH of interwater phase was 10.0.

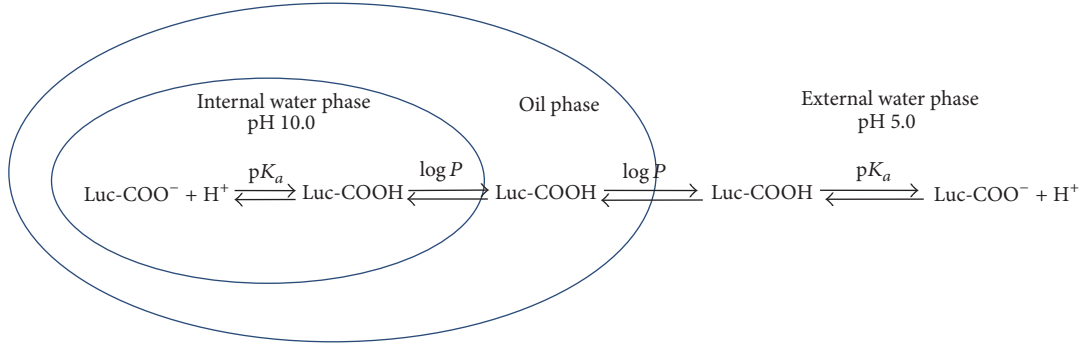


FIGURE 2: Schematic diagram of the concentration equilibrium of D-luciferin in the internal water phase, external water phase, and oil phase.

TABLE 1: Concentration of molecular and ionized D-luciferin in different phases in the model of liposomes.

Molecular or ionized D-luciferin	Concentration
Ionized D-luciferin in internal water phase (Luc-COO ⁻)	a_1
Molecular D-luciferin in internal water phase (Luc-COOH)	a_2
Molecular D-luciferin in oil phase (Luc-COOH)	a_3
Molecular D-luciferin in external water phase (Luc-COOH)	a_4
Ionized D-luciferin in external water phase (Luc-COO ⁻)	a_5
Total concentration of ionized and molecular D-luciferin	$a_{(total)}$

As shown in the liposome model in Figure 2, the distribution of D-luciferin in each phase was mainly determined by the balance of oil-water partition and molecular dissociation.

According to the definition of oil-water partition coefficient of D-luciferin and the concentration set in Table 1,

$$P = \frac{C_{oil}}{C_{water}} \quad (6)$$

$$P = \frac{a_3}{a_2} = \frac{a_3}{a_4} \quad (7)$$

$$a_2 = a_4 = \frac{a_3}{P}. \quad (8)$$

According to the definition of dissociation constant,

$$K_a = \frac{C_{(Luc-coo^-)}C_{(H^+)}}{C_{(Luc-COOH)}} \quad (9)$$

$$a_5 = \frac{K_a \cdot P \cdot a_3}{C_{(H^+ \text{ external-water-phase})}} \quad (10)$$

$$pK_a = -\lg K_a. \quad (11)$$

As the physiochemical parameters of D-luciferin, $pK_a = 8.6$ [18],

$$\begin{aligned} K_a &= 10^{-8.6} \text{ (mol/L)} \\ &= 2.5119 \times 10^{-9} \text{ (mol/L)}. \end{aligned} \quad (\text{Data 17})$$

Based on hypothesis condition F and $\log P = 2.24$,

$$a_1 = 4.3652 \times 10^3 \cdot a_3 \quad (12)$$

$$a_2 = 173.7801 \cdot a_3 \quad (13)$$

$$a_4 = 173.7801 \cdot a_3 \quad (14)$$

$$a_5 = 4.3652 \times 10^{-2} \cdot a_3. \quad (15)$$

From the above equations, we can conclude that $a_1 > a_2 = a_4 \gg a_5$.

$$\begin{aligned} a_1 \cdot V_{\text{inner-water}} + a_2 \cdot V_{\text{inner-water}} + a_3 \cdot V_{\text{oil}} + a_4 \\ \cdot V_{\text{outer-water}} + a_5 \cdot V_{\text{outer-water}} = a \cdot V \end{aligned} \quad (16)$$

$$\log P = \log \frac{C_{\text{oil-phase}}}{C_{\text{water-phase}}}. \quad (17)$$

Based on the above equations, 0.725 mg D-luciferin is equal to 2.2767×10^{-6} mol [19], and the concentration of D-luciferin in different phases can be calculated.

According to the above theoretical calculation, both pH gradient and the volume of external water phase affected the encapsulation efficiency. The following experiments were conducted to identify whether the effect of pH gradient on encapsulation efficiency in practical conditions was consistent with theoretical calculation.

In this study, lipid films composed of EPC : chol : DSPE-PEG2k with molar ratio of 56 : 39 : 5 were prepared in 4 egg-plant-shaped flasks. The 4 samples of lipid films were labeled as ①, ②, ③, and ④, respectively. TRIS buffer (300 mL, pH

10.0) was added to the flasks with lipid membranes, and the final concentration of lipid was adjusted to 10 mg/mL. After manual extrusion with polycarbonate membranes with pore size of 400 nm and 200 nm, liposomes of ① and ③ were dialyzed with dialysate of 20 mL citric acid solution (150 mL NaCl, pH 6.0). While liposomes of ② and ④ were dialyzed with dialysate of 20 mL citric acid solution (150 mL NaCl, pH 3.0). The process of dialysis lasted for 12 h with exchange of fresh dialysate every 4 h. 50 μ L purified liposomes of ①, ②, ③, and ④ with lipid concentration of 10 mg/mL was added to 950 μ L 10% Triton solution. The mixtures were kept static for 30 min after being vortexed for 30 s. 50 μ L liquid was transferred to 96-well plates in triplicate. Microplate reader was used to detect the absorption with wavelength set at 330 nm. By comparing with the standard curve, the amount of D-luciferin and the entrapment efficiency of liposomes could be calculated.

In order to further optimize the method of preparing liposomes, the relationship between pH gradient and encapsulation efficiency has been studied based on the method designed by Kheirrolomoom et al. [20].

2.2.2. Assays with Cell Suspensions

- (1) SMMC-7721-pGL3 cells were cultured according to conventional procedures (cell culture was carried out using RPMI 1640 cell culture medium containing 10% fetal bovine serum). The cells in the logarithmic growth phase of a flask (T25-sized cell culture flask) were collected using trypsin digestion.
- (2) The cells were counted by a hemocytometer, and the density of the cell suspension was adjusted to 4.0×10^5 cells/mL.
- (3) The cells were added to 24-well plates at 1.0 mL per well. Namely, the inoculation density per hole was 4.0×10^5 cells/mL.
- (4) The cells were placed in a cell incubator and incubated in a 5% CO₂ incubator at 37°C for 48 h.
- (5) The cells were cultured for 48 h. The complete medium was removed in a biological clean bench and washed twice with a PBS (pH 7.4) solution. The complete medium was removed in a biological clean bench and washed twice with a PBS (pH 7.4) solution. After digestion with trypsin for 2 min, RPMI 1640 cell culture medium containing 10% fetal bovine serum (FBS) was added to stop digestion. After centrifugation (300 \times g, 5 min for each time), the cells were washed 3 times with PBS (pH 7.4) to completely remove trypsin.
- (6) The cells were counted with a hemocytometer. And the cell density was adjusted to 1.0×10^5 cells/mL with PBS solution.
- (7) Liposomes composed of DPPC : chol : DSPE-PEG2k with molar ratio of 86 : 10 : 4 and 86 : 10 : 10 were prepared with the method of thin-film dispersion. They were purified with dialysis to separate the unloaded

D-luciferin. The concentration of encapsulated D-luciferin was diluted to 0.3 mg/mL. And free D-luciferin with the same concentration was for control.

- (8) 10 μ L cell suspension was mixed with 10 μ L 0.3 mg/mL free D-luciferin in a tube. Bioluminescence was measured with illuminance meter (FB12/Sirius Illuminance meter, Berthold Science and Technology Company, Germany) immediately after mixing. The detection mode of the illuminometer was set as single kinetics. The delay time and the measure time were set as 2.0 s and 12.0 s, respectively. The measurement was repeated for three times.

2.2.3. Assays with Monolayer Cells

- (1) Cells of H1299-pGL3 were cultured according to routine operation (the cell culture fluid of RPMI 1640 which contained 10% fetal bovine serum was used). Trypsin was used to digest and a bottle of cultured cells (T25 specification) in logarithmic growth phase was collected.
- (2) The number of the cells was counted by the blood cell counting plate, and the density of cell suspension was adjusted to 8.0×10^4 /mL.
- (3) 0.1 mL cell suspension was added to each well in 96-well plates (Corning 3610, whiteboard). In order to avoid the difference of the volume between the wells caused by the evaporation of the outer ring of the well plate of culture medium, the outermost one was not inoculated with cells; only 0.1 mL PBS was added to it. Therefore, only $10 \times 6 = 60$ wells are inoculated in every 96-well plate.
- (4) Cell culture medium was taken out after the incubation of 48 h in the incubator of 5% CO₂ at 37°C. The culture medium was absorbed by a straw and then discarded at bioclean working platform, washing them up 3 times with PBS (pH 7.4) and making every well left 100 μ L RPMI 1640 without fetal bovine serum. Three wells of them were digested trypsin, and the cell number was also counted by the blood cell counting plate. According to the calculation, the number of cells was 5.334×10^4 /mL in every well.
- (5) PBS (pH 7.4) was used to prepare the solution of D-luciferin with the concentration of 0.05 mg/mL.
- (6) 96-well plates were moved to the Multimode Detection Platform, and the automatic injector was also used to add 100 μ L of different concentrations of D-luciferin to the plates; the measure time was set as 10 ms, 100 ms, 1000 ms, and 4000 ms; then continuous determinations of biological luminescence signal were made. 100 μ L PBS (pH 7.4) was added to groups of blank control. Every measurement was repeated 3 times.
- (7) Microsoft Excel was applied to sort the data, and the figure was generated by setting time as the horizontal coordinate and setting signal intensity of bioluminescence as the vertical coordinate.

In order to elaborate the mechanism of the uptake of D-luciferin, endocytosis inhibitors have been added to the monolayer cells of H1299-pGL3. The only difference compared with the method above was that the D-luciferin solution was mixed with 50 μ l 2 μ g/ml methyl- β -cyclodextrin, 25 μ g/ml cytochalasin B, 25 μ g/ml cytochalasin B, 1 μ g/ml Filipin III, or Omeprazole, respectively.

2.2.4. Assays with MCTS. The preparation of MCTS models referred to the method used by Juergen Friedrich. Specific operations are listed as follows [14]:

- (1) Weigh 0.75 g of agarose into a 250 mL beaker and add RPMI 1640 to 1.5% (w/v) agarose. 50 mL of agarose solution was generally sufficient for about 10 plates of 96-well plates.
- (2) The beaker was sealed with aluminum foil and put into an autoclave and autoclaved according to conventional procedures.
- (3) After autoclaving, the agarose was removed from the autoclave immediately before the agarose solution had been solidified (about 90°C) and placed in a 60°C water bath prepared in a biological clean bench device in advance.
- (4) The agarose solution was added to a flat-bottomed 96-well plate. 50 L of solution was added to each well.

(Note: common transparent cell culture plate can be used for the preparation of MCTS models for routine experiments; to increase the sensitivity of bioluminescence detection with Multimode Detection Platform, 96-well plates with white wall and transparent bottom were recommended (such as Corning #3610); a transparent bottom facilitated the observation of inverted microscopes and the use of phase contrast microscopy, and a white wall can decrease the interference from adjacent wells.)

In this experiment, Eppendorf 96-well plate was chosen.

- (5) The 96-well plates were placed horizontally and allowed to stand for cell inoculation after the agarose solution was cooled and solidified. To reserve pre-coated 96-well plates for future use, they should be wrapped with plastic and aluminum foil in a sterile environment.
- (6) To investigate the effect of cell seeding density on the MCTS model, 4T1-luc cell suspension was collected and cultured according to the conventional method in the previous section. And the density of the 4T1-luc cell suspension was adjusted to 2.5×10^3 cells/mL, 3.75×10^3 cells/mL, 5.0×10^3 cells/mL, 7.5×10^3 cells/mL, 1.0×10^4 cells/mL, 1.5×10^4 cells/mL, 2.0×10^4 cells/mL, 3.0×10^4 cells/mL, 4.0×10^4 cells/mL, and 6.0×10^4 cells/mL.
- (7) The cell suspensions of each concentration were inoculated into 96-well plates and the volume of each well was 0.2 mL. Cultured for 48 h, the formed cell aggregates or MCTS were observed using a phase

contrast microscope. Cell aggregates or MCTS were photographed using phase contrast microscopy and the diameter of multicellular tumor spheres was measured using matching image processing software. Then the volume of MCTS was calculated.

- (8) The above method of agarose-coating was also applied to H1299-pGL3 (C11), A549-luc, and SMMC-7721-pGL3 to identify whether they could form MCTS.

In order to detect the dynamic uptake of nanostructures for drug delivery in MCTS, the bioluminescence produced from the reaction of liposomes encapsulating D-luciferin with MCTS models of 4T1-luc was detected.

- (1) Models of 4T1-luc were built with seeding density of 1.0×10^4 cells/mL (8.0×10^3 cells per well) following the above method.
- (2) After culture for 3 d, models of homogeneous MCTS with diameter of $776.61 \pm 22.12 \mu\text{m}$ were prepared.
- (3) Liposomes composed of HSPC:chol = 70:30 and HSPC:chol:DSPE-PEG2k-Mal-GE11 = 68.6:29.4:2 were prepared with the above method and were purified with dialysis to eliminate the D-luciferin that had not been encapsulated.
- (4) The concentration of encapsulated D-luciferin was adjusted to 6.0 mg/mL.
- (5) After 50 μ L of liposomes was added to each well containing MCTS, the final concentration of D-luciferin in each well was 1.2 mg/mL. The same volume of free D-luciferin with the same concentration was added to the control groups.
- (6) Bioluminescence was detected with small animal imaging system at 5 min, 15 min, 25 min, 40 min, 50 min, 75 min, and 720 min. The exposure time was set at 5 min. And the bioluminescence was calculated with the software attached to the instrument.
- (7) The dynamic curve was generated with Microsoft Excel.

2.2.5. Assays with Tumor-Bearing Nude Mice

- (1) 4T1-luc cells were cultured and collected. 5 μ g/mL of Blasticidin S (sterilized fungus) was added in the cell culture to obtain 4T1-luc cells which were with higher purity and could express luciferase stably.
- (2) The density of 4T1-luc cell suspension was adjusted to 1.0×10^7 cells/mL. Cancer cells were cultured under the armpit skin folds of 12 nude mice (BALB/C nude mice) with the inoculation amount being 1.0×10^6 cells each nude mouse.
- (3) The subcutaneous tumors formed after 10 days. The length and width of subcutaneous tumors were measured by Vernier calipers.
- (4) Liposomes composed of HSPC:chol = 70:30 and EPC:chol = 70 were prepared.
- (5) In order to study the dynamic uptake of nanostructures for drug delivery in tumor, the liposomes were

TABLE 2: Distribution of D-luciferin in different phases.

Molecular or ionized D-luciferin in different phases	Concentration (mol/m ³)	Amount of substance (mol)	Distribution of D-luciferin
a_1	76.7533	1.2133×10^{-6}	53.2920%
a_2	3.0556	4.8303×10^{-8} mol	2.1216%
a_3	1.7583×10^{-2}	3.6414×10^{-11} mol	0.0016%
a_4	3.0556	1.0148×10^{-6} mol	44.5146%
a_5	7.6753×10^{-4}	2.5491×10^{-10} mol	0.0112%

TABLE 3: Fraction of the amount of substance of D-luciferin in intraliposomal, extraliposomal, and oil phase.

Phase	Fraction of the amount of D-luciferin in different phases
Internal water phase	53.7969%
Oil phase	0.0029%
External water phase	46.2013%

administered by tail vein injection and intratumoral injection, respectively.

For intravenous injection, the concentration of encapsulated D-luciferin was adjusted to 15 mg/mL, and the dose was 0.2 mg/g body weight. The control group was injected with the same volume of saline. Bioluminescence was detected with ZKKS-MI-II small animal imaging system (Guangzhou Zhongke Kaisheng Medical Technology Co., Ltd). The exposure time was set as 1 min. And the images were captured continuously for 100 min after injection.

For intratumoral injection, the concentration of encapsulated D-luciferin was adjusted to 10 mg/mL, and the dose was 0.1 mg/g body weight. The control group was injected with the same volume of saline. The exposure time was set 4 min.

- (6) The data of bioluminescence was processed with the software attached to the instrument. And the dynamic curve was generated with Excel (Microsoft Office).

Animal welfare and experimental procedures were approved by the animal ethics committee of Shanghai University of Medicine and Health Sciences and Shanghai Jiao Tong University.

3. Results and Discussion

3.1. Preparation of Liposomes

3.1.1. Theoretical Calculation. The results of the theoretical calculation indicated that the active loading with pH gradient was feasible. As is shown in Tables 2 and 3, in the case of active loading designed by Kheiolomoom et al. [20], the total amount of ionized and molecular D-luciferin in internal water phase could reach 55.4136% in ideal conditions. It

should be noted that, in the above theoretical calculation, all D-luciferin in oil phase was considered to be molecular forms that did not dissociate.

The result demonstrated that, in order to achieve active loading and to sustain high concentration of D-luciferin in interwater phase, at least two factors were related. One was the pH gradient between internal and external water phase, and the other was the volume of external water phase.

It must be noted that the above theoretical calculation was based on the balance of oil-water partition and molecular dissociation. In practice, the distribution is related to time and the diffusion rate is associated with lipid components. For example, it takes time for molecular D-luciferin to pass from external water phase to oil phase, or to pass from oil phase to intrawater phase.

Practical experience and long-term exploration indicated that the leakage of encapsulate D-luciferin from liposomes could be a significant factor, especially when the process of dialysis lasted long. Compared with dialysis, glucan gel column chromatography (Sephadex G-75) was generally a better choice for the purification of liposomes.

In vivo imaging tended to cost a big amount of D-luciferin; thus column chromatography (Sephadex G-75) was recommended. While for in vitro test with cells or MCTS, dialysis was recommended because the separation of free D-luciferin was more thorough; thus the interference effect resulting from incomplete purification could be decreased.

Column chromatography often resulted in the dilution of liposomes. Three practical approaches could be applied to condense the liposomes. Firstly, ultrafiltration tubes (MWCO 3 KD) were strongly recommended. It should be noticed that liposomes with diameters less than 100 nm could not be cut off completely by ultrafiltration tubes (MWCO 10 KD). The second approach was to employ frozen centrifugation technology to evaporate water. The third approach was to put liposomes into dialysis bag (MWCO 3 KD) with PEG2k coated outside. After putting the bag into a drying oven for 24 h, liposomes could be condensed. Since the last two approaches only eliminated water, the ionic concentration tended to increase. In brief, ultrafiltration was the best choice.

3.1.2. Encapsulation Efficiency by pH Gradient Method. In Figure 3, under the condition that pH = 10.2 in internal water phase and pH = 6.0 in external water phase, the encapsulation efficiency of liposome was $5.29 \pm 1.20\%$. While in conditions that pH = 10.2 in the interwater phase and pH = 3.0 in external

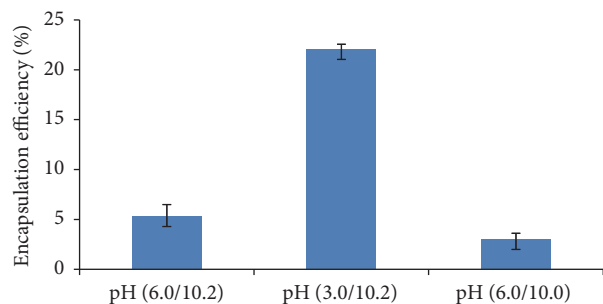


FIGURE 3: Effect of pH gradient on encapsulation efficiency of liposomes.

water phase, the encapsulation efficiency was $22.04 \pm 0.52\%$. This indicated that the increasing pH gradient was favorable for pH gradient active drug loading, which was consistent with the theoretical calculation results mentioned before.

3.2. Assays with Cell Suspensions. Figure 4 showed kinetic curves of bioluminescence produced from the reaction of cells suspensions with liposomal and free D-luciferin with concentration of 0.3 mg/mL. The bioluminescence of free D-luciferin peaked at 105 s. The curve of the liposomes with molar ratio of DPPC : chol : DSPE-PEG2k = 86 : 10 : 4 had two gentle peaks, with peaking time at 119 s and 273 s, respectively. The first peak might be resulting from the same mechanism of free D-luciferin which was released from liposomes, which needed further study. The releasing process might happen outside or near the surface of cell membrane. The second peak might be caused by the transfer of liposomes to the cells and the later reaction of released D-luciferin with cellular lysate.

The kinetic curve of liposomes with molar ratio of DPPC : chol : DSPE-PEG2k = 86 : 10 : 10 had the highest bioluminescence at 189 s, which was almost at the midpoint of the 119 s and 273 s. In other words, this curve might be the overlap of 2 peaks resulting from free D-luciferin and liposomal D-luciferin. The kinetic curve was totally lower than that of liposomes of DPPC : chol : DSPE-PEG2k = 86 : 10 : 4. It might be explained that DSPE-PEG2k increased the hydrophobicity of liposomes and thus decreased the attachment of liposomes to cell membrane.

3.3. Assays with Monolayer Cells. Figure 5 shows the kinetic curve of bioluminescence produced from the reaction of free D-luciferin and liposomal D-luciferin in different formulations with monolayer cells. The peaking value of the bioluminescence of liposomes of EPC : chol = 70 : 30 was found to be higher than that of liposomes in other formulations. It could be explained that the phase transition temperature of EPC was lower than other lipids. Thus the liposomes composed majorly of EPC would be “softer,” which made the leakage and release of D-luciferin easier than other liposomes.

Compared to the liposomes of EPC : chol = 70 : 30, both the value of bioluminescence reaching peak and the value remaining stable were higher than that of the liposomes of EPC : chol : DSPE-PEG2000 = 56 : 39 : 5. It could be explained

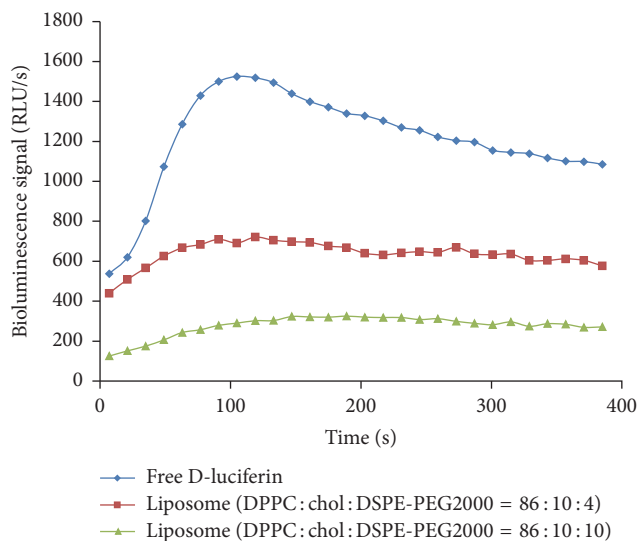


FIGURE 4: Dynamic curves of bioluminescence signal produced from the reaction of cell suspension with liposomal and free D-luciferin. (Liposomes composed of DPPC : chol : DSPE-PEG2k with molar ratio of 86 : 10 : 4 and 86 : 10 : 10 were prepared with the method of thin-film dispersion. They were purified with dialysis to separate the unloaded D-luciferin. The concentration of encapsulated D-luciferin was diluted to 0.3 mg/mL. And free D-luciferin with the same concentration was for control. The density of cell suspension was adjusted to 1.0×10^5 cells/mL. The testing mode of the illumination meter was set as single kinetic. After mixing the cell suspension with liposomal or free D-luciferin, bioluminescence was detected immediately. The delay time for each measurement was 2.0 s, and the measurement time was 10.0 s. RLU is short for relative light unit.)

that the addition of DSPE-PEG2000 increased the hydrophobicity of the liposomes, which decreased the adhesion of liposomes to cells. Similarly, the bioluminescence of liposomes of HSPC : chol = 70 : 30 was found to be lower than that of liposomes of EPC : chol = 70 : 30. It could be explained that the liposomes were composed majorly of HSPC, which had a higher phase transition temperature. Due to the increase of the phase transition temperature, the barrier effect of the “hard” liposomes could decrease the leakage and release of the encapsulated D-luciferin.

Figure 6 shows the kinetic curve of bioluminescence produced from the reaction of liposomes of EPC : chol = 70 : 30 with monolayer cells within 10,000 s. The curve had two overlapped peaks. The first peak was sharper with a value of 1,000 at 300 s, while the second peak had a value of 1200 at about 6,700 s.

The first hypothesis of the overlapped peaks was that the uptake of liposomes was via two routes. The first route of cellular uptake happened earlier with liposomes fused with cellular membranes after absorption. Thus higher concentration of D-luciferin was formed near the area of inner surface of cellular membranes. In this route, encapsulated drugs were transported into the cells in forms of free D-luciferin. In the kinetic curve, the second peak was wide with gentle slope.

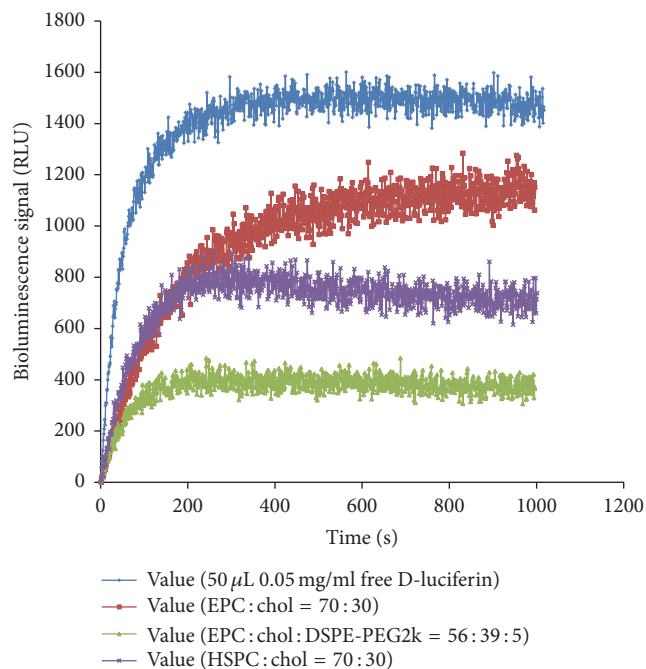


FIGURE 5: Kinetic curves of bioluminescence produced from the reaction of monolayer cells with free D-luciferin and luciferin-loaded liposomes of different formulations.

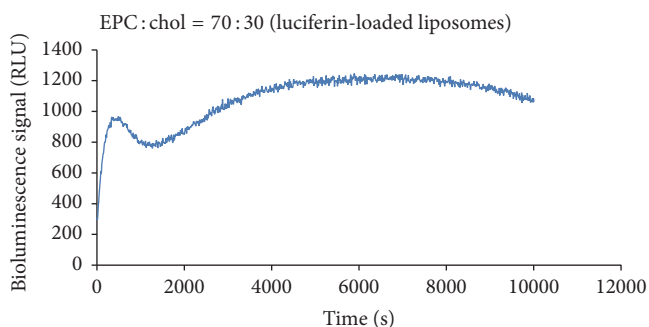


FIGURE 6: Kinetic curve of bioluminescence produced from the reaction of liposomes of EPC:chol = 70:30 and monolayer cells of H1299-pGL3 within 10,000 s. (Luciferin-loaded liposomes were separated from nonencapsulated luciferin by passing the extruded liposomal solution through a column of Sephadex G-75. To further prepare the liposomes, the released luciferin from the liposomes was separated using centrifugal ultrafiltration units with a molecular cutoff of 3 KD at 2000 \times g, 15°C for 20 min prior to detection. Interval of the measure time was set at 1000 ms.)

The uptake of liposomes might be in form of endosomes. Bioluminescence was produced after the reaction of released D-luciferin with cellular luciferase following endocytosis. However, this was only a hypothesis on the mechanism of explaining the cellular uptake of liposomes. To verify this hypothesis, further study with confocal microscope, radioactive labeling, and imaging techniques was needed.

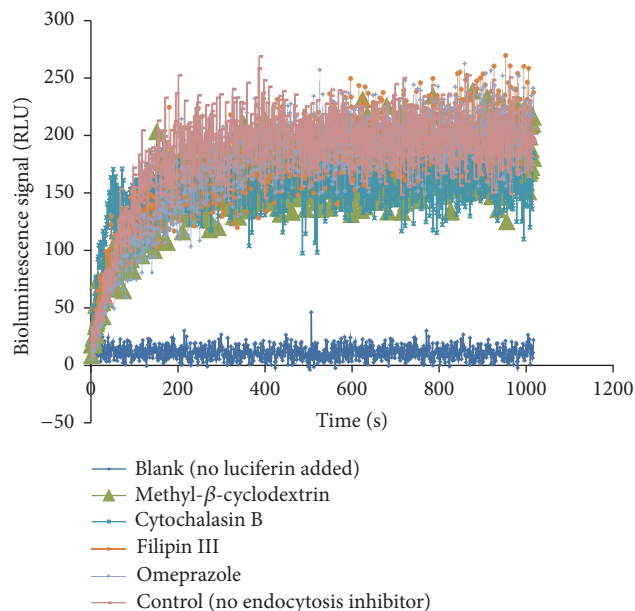


FIGURE 7: Effect of endocytosis inhibitors to the bioluminescence produced after free D-luciferin was added to monolayer cells of H1299-pGL3. (The 96-well plates had white walls with clear bottoms. Each well was seeded with 3000 cells. Bioluminescence was detected with multifunctional microplate reader. The unit of measurement time was set at 1000 ms.)

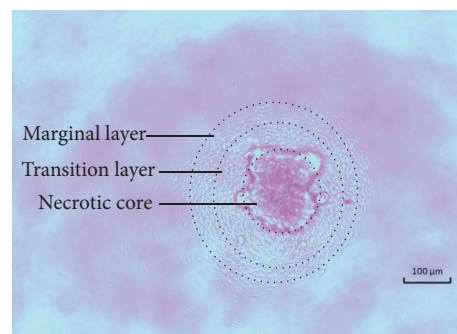


FIGURE 8: Multicellular tumor spheroid of 4T1-luc. (The picture was taken with a phase contrast microscope. The seeding density was 8.0×10^3 cells in each well. The pink background shows the color of cell culture medium of RPMI 1640.)

As shown in Figure 7, endocytosis inhibitor group and the control group did not show significant difference. It demonstrated that the uptake of D-luciferin was not related to caveolin, clathrin, or micropinocytosis.

3.4. Assays with MCTS. As shown in Figure 8, a model of MCTS (4T1-luc) was composed of marginal layer, transition layer, and a necrotic core. Table 4 showed the morphological parameters of MCTS with different seeding densities. Practical experience indicated that MCTS with a seeding density of 8,000 cells per well showed the best morphology and stable repetition in different wells and different batch.

TABLE 4: Morphological parameters of cell aggregates and MCTS of 4T1-luc with different seeding density.

Initial seeding density (cell number in each well)	Longest diameter (μm)	Shortest diameter (μm)	Diameter (μm)	Volume (mm^3)
500	411.15	319.90	365.52 ± 73.23	27.73 ± 13.05
750	475.67	418.24	446.96 ± 35.11	47.38 ± 11.13
1000	543.38	514.05	526.43 ± 30.37	76.85 ± 12.92
2000	595.81	587.67	591.74 ± 5.76	108.45 ± 3.16
3000	680.18	647.61	663.90 ± 23.03	153.41 ± 15.94
6000	757.28	706.00	736.49 ± 53.97	211.33 ± 47.64
8000	792.25	760.97	776.61 ± 22.12	245.42 ± 20.95
10000	884.82	853.48	869.15 ± 22.16	343.94 ± 262.86

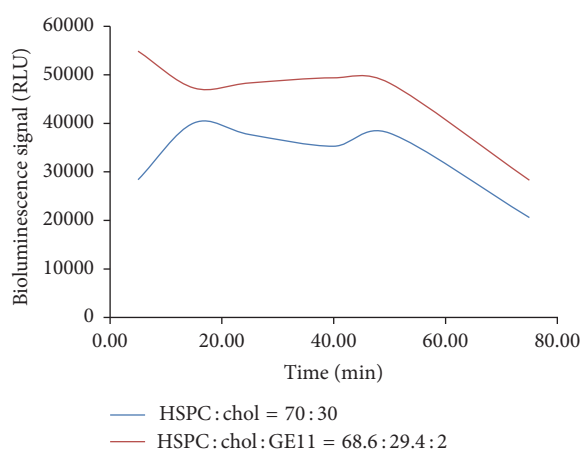


FIGURE 9: Kinetic curve of bioluminescence of luciferin-loaded liposomes of HSPC:chol = 70:30 and HSPC:chol:GE11 = 68.6:29.4:2 added to MCTS.

Except for 4T-1-luc, the other three cell lines have been studied for building models of MCTS with the method of loading agarose on the bottom of wells. Cells of H1299-pGL3 could only form loose aggregates that could not bear pipetting. Cells of SMMC-7721-pGL3 and A549-luc could not form aggregates with this method.

In Figure 9, the kinetic curve of bioluminescence of liposomes modified with GE11 was totally above the curve of the control group without modification. It was consistent with the fact that the modification with GE11, a new peptide ligand, promoted the delivery of nanoparticles to cells that had epidermal growth factor receptor (EGFR) [9, 12].

3.5. Assays with Tumor-Bearing Nude Mice. Figure 10 shows the kinetic curve of bioluminescence on the tumor area captured by the in vivo imaging system after tail vein injection of free or liposomal D-luciferin. The bioluminescence of liposomes of HSPC:chol = 70:30 peaked to a photon number of 4.14×10^7 at 41 min. Compared to free D-luciferin, the kinetic curve of the liposomes shows a certain degree of sustained releasing, which could be explained by the barrier effect of the liposomal membranes to D-luciferin.

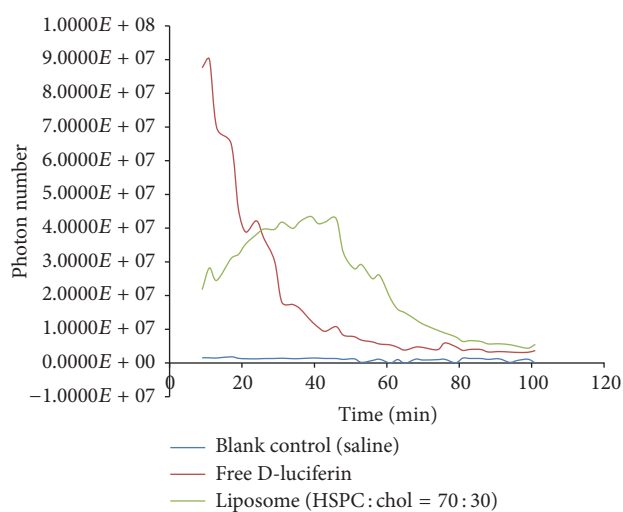
FIGURE 10: Kinetic detection of bioluminescence of the tumor region in tumor-bearing nude mice following tail vein injection of luciferin-loaded liposomes and free D-luciferin. (The volume of the subcutaneous tumor of 4T1-luc was $0.440 \pm 0.022 \text{ cm}^3$. Each mouse was injected with either liposomal or free D-luciferin with dosage of 0.2 mg/g body weight. The exposure time of the in vivo image system was set at 1 min.)

Figure 11 shows the kinetic curve of bioluminescence of the tumor region in tumor-bearing nude mice after intratumoral injection of luciferin-loaded liposomes (EPC:chol = 70:30). Compared with free D-luciferin, the kinetic curve of liposomes shows a sustained releasing effect.

4. Conclusion

Focused on the dynamic uptake of nanostructures for drug delivery based on bioluminescence measurements, this study included three parts. The first part was the preparation of liposomes to encapsulate D-luciferin, which served as a model drug. The distribution and the active loading of D-luciferin with pH gradient have been studied. Based on the theoretical calculation, the feasibility was demonstrated by experiments. The second part of this study was building

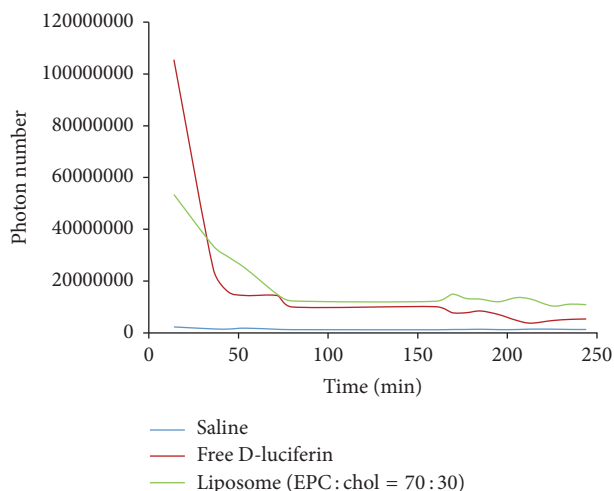


FIGURE 11: Kinetic detection of bioluminescence of the tumor region in tumor-bearing nude mice following intratumoral injection of luciferin-loaded liposomes and free D-luciferin. (The volume of the subcutaneous tumor of 4T1-luc was $0.440 \pm 0.022 \text{ cm}^3$. Each mouse was injected with either liposomal or free D-luciferin with dosage of 0.1 mg/g body weight. The exposure time of the in vivo image system was set to 4 min.)

three-dimensional models to bridge tumor cells in vitro to tumor models in vivo. The third part of this study focused on kinetic uptake on free drugs and drug-loaded nanostructures in cell suspension, monolayer cells, MCTS and tumor-bearing mice. This paper laid a solid foundation for establishing a technology platform for tracking and analyzing the dynamic uptake of luciferin and luciferin-loaded nanoparticles.

5. Prospective

This study offered a technology platform for studying the dynamic uptake of luciferin and luciferin-loaded nanostructures in vitro and in vivo.

First of all, scientists have synthesized dozens of derivatives of D-luciferin and D-aminoluciferin [2, 14, 15, 21, 22]. Due to the various groups modified to the core structure, these derivatives could have vastly different characteristics on molecular weight, solubility, hydrophobicity, hydrophilicity, and so on. The differences on their characteristics make them quite suitable to serve as model drugs for small molecules. By modifying D-luciferin with grand organs like peptides or polysaccharide, Mäger et al. have tried to study the uptake mechanism of small molecules and to identify the effect of cell penetrating peptides on cellular endocytosis [22]. Besides, radioactively labeled D-luciferin is also popular for studying the mechanism of cellular uptake [23].

Except for liposomes, the development of other novel nanostructures has attracted more and more scientists. Li et al. have tried to prepare nanostructures by caging luciferin and to apply ultrasound to promote the release of caged luciferin [24, 25].

Targeting modification has been applied to the preparation of nanostructures for loading D-luciferin. The nanostructures prepared in this study could also be applied to screen membrane-targeting peptides and cell penetrating peptide. Luciferin-loaded nanostructures might also play a role in explaining their mechanism on promoting membrane targeting and cell penetrating [20]. In order to increase the mechanical strength of MCTS and to maintain their morphology during pipetting, combination of Matrigel, centrifuge tube culture, cell suspension, and agarose-coating was expected [17, 18].

Building postoperation models for the study of mutual reaction between nanostructures and tumor stroma is expected to be a research hotspot. Thermal therapy and the digestion of collagenase to collagen fibers are two good tools. The luciferin-loaded nanostructures in this study have great potential for studying the difference of nanostructures and tumor stroma after operation, thermal therapy, or treatment with collagenase [26, 27].

Nanostructures that load two or more kinds of drugs are shown to be a novel direction. These findings are expected to have a great potential in therapies of drug combinations. The extension of this study also includes the fluorescence modification of nanostructures encapsulating D-luciferin or D-aminoluciferin. By detecting both fluorescence and bioluminescence, further study of their dynamic uptake and distribution with models both in vitro and in vivo is expected. The tracing of these dual labeled nanostructures may yield more interesting results in the near future [28–30].

Competing Interests

The authors declare that they have no competing interests.

Acknowledgments

The project is funded by grants from Shanghai Program for Young College Teachers' Training (no. ZZJKYX15010/A1-5201-16-311015). The authors thank Zeyu Zhong, Junjie Xu, Yanqing Ma, Kunnan Chen, Jing Ge, ZhenYu Zhang, Fanbai Qi, and Jing Wei for their generous help and support.

References

- [1] E. Faure-Fremet, "Mitochondria and liposomes," *Comptes Rendus des Seances de la Societe de Biologie et de ses Filiales*, vol. 68, pp. 537–539, 1910.
- [2] W. Miska and R. Geiger, "Synthesis and characterization of luciferin derivatives for use in bioluminescence enhanced enzyme immunoassays. New ultrasensitive detection systems for enzyme immunoassays," *Journal of Clinical Chemistry and Clinical Biochemistry*, vol. 25, no. 1, pp. 23–30, 1987.
- [3] Z. Zheng, L. Wang, W. Tang et al., "Hydrazide d-luciferin for in vitro selective detection and intratumoral imaging of Cu^{2+} ," *Biosensors and Bioelectronics*, vol. 83, pp. 200–204, 2016.
- [4] Y. Yuan, F. Wang, W. Tang et al., "Intracellular self-assembly of cyclic d-luciferin nanoparticles for persistent bioluminescence imaging of fatty acid amide hydrolase," *ACS Nano*, vol. 10, no. 7, pp. 7147–7153, 2016.

- [5] Y. Chen, D. Gao, H. Liu, S. Lin, and Y. Jiang, "Drug cytotoxicity and signaling pathway analysis with three-dimensional tumor spheroids in a microwell-based microfluidic chip for drug screening," *Analytica Chimica Acta*, vol. 898, pp. 85–92, 2015.
- [6] R. Akasov, D. Zaytseva-Zotova, S. Burov et al., "Formation of multicellular tumor spheroids induced by cyclic RGD-peptides and use for anticancer drug testing in vitro," *International Journal of Pharmaceutics*, vol. 506, no. 1-2, pp. 148–157, 2016.
- [7] S. Däster, N. Amatruda, D. Calabrese et al., "Insight of 3D multicellular tumor spheroids for innovative culture models of potential relevance for the screening of anti-CRC compounds," *Cancer Research*, vol. 74, no. 19, 2014.
- [8] G. Meroni, M. Rajabi, and E. Santaniello, "D-Luciferin, derivatives and analogues: synthesis and in vitro/in vivo luciferase-catalyzed bioluminescent activity," *Arkivoc*, vol. 2009, no. 1, pp. 265–288, 2009.
- [9] H. Patel, "Liposomes: a practical approach," *FEBS Letters*, vol. 275, no. 1-2, pp. 242–243, 1990.
- [10] P. Balgavý, M. Dubničková, N. Kučerka, M. A. Kiselev, S. P. Yaradaikin, and D. Uhríková, "Bilayer thickness and lipid interface area in unilamellar extruded 1,2-diacylphosphatidylcholine liposomes: A Small-Angle Neutron Scattering Study," *Biochimica et Biophysica Acta—Biomembranes*, vol. 1512, no. 1, pp. 40–52, 2001.
- [11] Y. Tahara and Y. Fujiyoshi, "A new method to measure bilayer thickness: cryo-electron microscopy of frozen hydrated liposomes and image simulation," *Micron*, vol. 25, no. 2, pp. 141–149, 1994.
- [12] Y. Tahara, M. Murata, S.-I. Ohnishi, Y. Fujiyoshi, M. Kikuchi, and Y. Yamamoto, "Functional signal peptide reduces bilayer thickness of phosphatidylcholine liposomes," *Biochemistry*, vol. 31, no. 37, pp. 8747–8754, 1992.
- [13] Z. Li, R. Zhao, X. Wu et al., "Identification and characterization of a novel peptide ligand of epidermal growth factor receptor for targeted delivery of therapeutics," *FASEB Journal*, vol. 19, no. 14, pp. 1978–1985, 2005.
- [14] R. Shinde, J. Perkins, and C. H. Contag, "Luciferin derivatives for enhanced in vitro and in vivo bioluminescence assays," *Biochemistry*, vol. 45, no. 37, pp. 11103–11112, 2006.
- [15] Y.-Q. Sun, J. Liu, P. Wang, J. Zhang, and W. Guo, "D-luciferin analogues: a multicolor toolbox for bioluminescence imaging," *Angewandte Chemie—International Edition*, vol. 51, no. 34, pp. 8428–8430, 2012.
- [16] S. Song, D. Liu, J. Peng et al., "Peptide ligand-mediated liposome distribution and targeting to EGFR expressing tumor in vivo," *International Journal of Pharmaceutics*, vol. 363, no. 1-2, pp. 155–161, 2008.
- [17] A. Ivascu and M. Kubbies, "Rapid generation of single-tumor spheroids for high-throughput cell function and toxicity analysis," *Journal of Biomolecular Screening*, vol. 11, no. 8, pp. 922–932, 2006.
- [18] J. Friedrich, C. Seidel, R. Ebner, and L. A. Kunz-Schughart, "Spheroid-based drug screen: considerations and practical approach," *Nature Protocols*, vol. 4, no. 3, pp. 309–324, 2009.
- [19] H. Song, O. David, S. Clejan et al., "Spatial composition of prostate cancer spheroids in mixed and static cultures," *Tissue Engineering*, vol. 10, no. 7-8, pp. 1266–1276, 2004.
- [20] A. Kheirloomoom, D. E. Kruse, S. Qin et al., "Enhanced in vivo bioluminescence imaging using liposomal luciferin delivery system," *Journal of Controlled Release*, vol. 141, no. 2, pp. 128–136, 2010.
- [21] S. Ioka, T. Saitoh, S. Iwano et al., "Synthesis of firefly luciferin analogues and evaluation of the luminescent properties," *Chemistry*, vol. 22, no. 27, pp. 9330–9337, 2016.
- [22] I. Mäger, K. Langel, T. Lehto, E. Eiríksdóttir, and Ü. Langel, "The role of endocytosis on the uptake kinetics of luciferin-conjugated cell-penetrating peptides," *Biochimica et Biophysica Acta—Biomembranes*, vol. 1818, no. 3, pp. 502–511, 2012.
- [23] K.-H. Lee, S. S. Byun, J.-Y. Paik et al., "Cell uptake and tissue distribution of radioiodine labelled D-luciferin: Implications for luciferase based gene imaging," *Nuclear Medicine Communications*, vol. 24, no. 9, pp. 1003–1009, 2003.
- [24] J. Li, L. Chen, L. Du, and M. Li, "Cage the firefly luciferin!—a strategy for developing bioluminescent probes," *Chemical Society Reviews*, vol. 42, no. 2, pp. 662–676, 2013.
- [25] Y. Yang, Q. Shao, R. Deng et al., "In vitro and in vivo uncaging and bioluminescence imaging by using photocaged upconversion nanoparticles," *Angewandte Chemie - International Edition*, vol. 51, no. 13, pp. 3125–3129, 2012.
- [26] J. Dong, P. Liu, A. Zhang, and L. X. Xu, "Immunological response induced by alternated cooling and heating of breast tumor," in *Proceedings of the 29th Annual International Conference of IEEE-EMBS, Engineering in Medicine and Biology Society (EMBC '07)*, pp. 1491–1494, Lyon, France, August 2007.
- [27] T. T. Goodman, P. L. Olive, and S. H. Pun, "Increased nanoparticle penetration in collagenase-treated multicellular spheroids," *International Journal of Nanomedicine*, vol. 2, no. 2, pp. 265–274, 2007.
- [28] G. Van Den Bogaart, J. T. Mika, V. Krasnikov, and B. Poolman, "The lipid dependence of melittin action investigated by dual-color fluorescence burst analysis," *Biophysical Journal*, vol. 93, no. 1, pp. 154–163, 2007.
- [29] W. J. M. Mulder, G. J. Strijkers, G. A. F. Van Tilborg, D. P. Cormode, Z. A. Fayad, and K. Nicolay, "Nanoparticulate assemblies of amphiphiles and diagnostically active materials for multimodality imaging," *Accounts of Chemical Research*, vol. 42, no. 7, pp. 904–914, 2009.
- [30] D.-E. Lee, H. Koo, I.-C. Sun, J. H. Ryu, K. Kim, and I. C. Kwon, "Multifunctional nanoparticles for multimodal imaging and theragnosis," *Chemical Society Reviews*, vol. 41, no. 7, pp. 2656–2672, 2012.

Research Article

Functional Surface Coating on Cellulosic Flexible Substrates with Improved Water-Resistant and Antimicrobial Properties by Use of ZnO Nanoparticles

Xiaofei Tian,^{1,2} Yaping Li,^{2,3} Sikang Wan,² Zhenqiang Wu,¹ and Zhiwei Wang^{2,3,4}

¹School of Bioscience and Bioengineering, South China University of Technology, Guangzhou 510640, China

²Guangxi Key Laboratory of Clean Pulp & Papermaking and Pollution Control, College of Light Industry and Food Engineering, Guangxi University, Nanning 530004, China

³State Key Laboratory of Pulp and Paper Engineering, South China University of Technology, Guangzhou 510640, China

⁴Collaborative Innovation Center for Guangxi Sugar Industry, Guangxi, Nanning 530004, China

Correspondence should be addressed to Zhiwei Wang; wangzhiwei@gxu.edu.cn

Received 28 October 2016; Accepted 14 December 2016; Published 19 January 2017

Academic Editor: Siya Huang

Copyright © 2017 Xiaofei Tian et al. This is an open access article distributed under the Creative Commons Attribution License, which permits unrestricted use, distribution, and reproduction in any medium, provided the original work is properly cited.

It is of significant interest to create functional flexible surfaces that simultaneously exhibit high water-resistance and antimicrobial performances for medical or packaging applications. This study reported a synthesis of functional surface coating on flexible cellulose materials (filter papers) with ZnO nanoparticles and binds of renewable soybean oil-based polymers. Self-aggregation of ZnO nanoparticles could form ZnO particles with two regular morphological patterns. Rather than a rod-like morphology, a flower-like ZnO benefited a promotion of surface hydrophobicity. Moreover, surface with the flower-like ZnO showed a 51.6% promotion on antimicrobial activities against Gram-negative bacteria (*E. coli*) than the rod-like ZnO. A low binder/ZnO ratio of 0.2 led to a remarkable improvement on water repelling performances without negative effects on a coating adhesion of ZnO. Under this condition, a hydrophobic surface was achieved with a large static contact angle of 138° when applying ZnO nanoparticles at a dosage of 3 g m⁻².

1. Introduction

Introduction of flexible cellulose materials such as microfibrillated cellulose or cellulose nanofibers as functional membrane, supporting component or papers in medicinal and electronic and packaging applications, attracts people's great attentions [1–4]. For a nature of existence of -OH group on cellulose surfaces, the ease of absorbing moisture or directly contacting with water during distribution, storage, and application is of great challenge to mechanical durabilities or antidegradability of these cellulose materials. Moreover, additional functional properties such as good antibacterial activity were also usually preferred for preparing functional cellulose materials. Surface modification possessed a great promise for a controlled wettability or hydrophobicity of the functional cellulose materials.

The creation or development of hydrophobic surfaces with (or without) antibacterial function on cellulose materials uses a number of technologies, such as, chemical coating methods using a mixture of 1H,1H,2H,2H-perfluorooctyltriethoxysilane, 3-(trimethoxysilyl)-propyldimethyloctadecyl ammonium chloride, and P,P-diphenyl-N-(3-(trimethoxysilyl) propyl) phosphinic amide [5] or fluoroalkyl-functional siloxane [6] through a sol-gel process; laccase-catalyzed hydrophobization with lauryl gallate [7] and grafting with eugenol [8] or ferulic acid [9]; thermochemical fabrication and impregnation of silver nanoparticles with starch [10]; sonochemical cohydrolysis and cocondensation with tetraethyl orthosilicate and alkyltrialkoxysilanes [11]; and physical pad-dry-cure method with MgO/methyl silicate nanocomposites [12].

Other methods such as internal sizing and surface sizing only provide a first barrier for cellulosic substrates against water penetration but often cannot meet the requirements for modern applications [13]. Nowadays, artificial water-resistant surfaces have been fabricated on cellulosic substrate based on selection of appropriate methods to create roughness and/or low surface energy on local surfaces [14]. Fluorinated polymers together with nanoparticles, for example, silica [15] or ZnO [16], were believed to be effective chemicals in building up water-resistant structure on cellulosic surface [17]. However, if an environment concern was taken into consideration, coating with no-fluorinated materials is preferable technology for preparation of highly hydrophobic surface [18].

ZnO is an attractive candidate for surface coating application [19, 20] due to its considerable antibacterial efficiency [21], stability [22], tunable structure [23], and low toxicity [24]. ZnO nanoparticles are promising additives for further improving the hydrophobicity through dedicated surface modification [18] such as stearic-acid modification [25, 26]. On the other hand, preventing undesirable microbial spoilage was also an important property for coating materials [19, 27]. ZnO finds increasing application as an antibacterial material for its promise of withstanding a harsh physical or chemical processing [21], compared to organic antibiotics that were conventionally used [22]. For instance, incorporate ZnO in hygienic coating for sterile packaging use [28].

Because of the promising functional properties, ZnO was introduced in this study for creating functional flexible surfaces that simultaneously exhibit high water-resistance and antimicrobial performances that could be subject to medical or packaging applications. ZnO nanoparticles were applied to build functional layers hierarchically on filter papers as a model of flexible substrate through a surface coating method. Soybean oil-based polymers were used as a green binding reagent for assembling the ZnO particles with cellulosic fibers. With an optimal coating formulation and application dosages, water repelling properties and antibacterial activities of the composite surface were determined for evaluating its feasibility for medical or packaging applications.

2. Materials and Methods

2.1. Materials. Rod-like ZnO were obtained from Aladdin Biochemical Technology, Co. Ltd. (Shanghai, China). Flower-like ZnO were synthesized by a typical hydrothermal method according to the reported method [26]. The average intensity-based hydrodynamic size of ZnO particles was measured using a Zeta Potential analyzer (ZetaPlus, Instruments Corporation, NY, USA). Cellulose filter paper (Whatman #2, 106 g m⁻², GE healthcare Life Sciences, Buckinghamshire, UK) was used as the cellulose substrate. Soybean oil-based polymer for binding ZnO nanoparticles on the paper surface was prepared according to the procedure reported in our previous study [29]. The chemicals of acrylated epoxidized soybean oil (AESO), 3-aminopropyltriethoxysilane (APTS), benzoyl peroxide (BPO), and anhydrous acetone were mixed with a weight ratio of 1/0.3/0.004/1. All of the chemicals were

purchased from Sigma-Aldrich Corporation (St. Louis, MO, USA).

2.2. Methods

2.2.1. Coating ZnO on Paper Surface. Coating slurry was prepared by mixing ZnO particles with binder together. In a typical method, 1 g ZnO particles (dry mass) was dispersed in 5 mL ethanol. All the prepared coating slurry was in an equal volume of 5 mL. The binder was gently added into the slurry at the ratio of 0.2–0.6/1 (binder/ZnO, w/w).

The paper was coated by a rod coater (K303 Multicoater, RK. Print Coat Instruments Ltd., UK) with the coating slurry at a velocity of 3 m min⁻¹. After coating, the paper was immediately transferred for curing at 80°C for 30 min to finalize the bonding of ZnO particles. Coating weight of the ZnO varied from 1.5 g m⁻² to 4.5 g m⁻².

2.2.2. Characterization of Morphologies and Surface Wettability. The aggregation patterns of the commercial and synthesized ZnO particles and distributions of ZnO particles on surface were characterized using a JEOL 6400 scanning electron microscope (JEOL Ltd., Tokyo, Japan). To determine the surface wettability, static contact angles (SCA) of water droplets (3 μL) on the surface coating were measured using an optical tensiometer (Attension Theta, Biolin scientific, Stockholm, Sweden) [30]. Measurement was performed for 10 times on each sample.

2.2.3. Antibacterial Assays. Minimum inhibition concentration (MIC) of ZnO particles against *E. coli* ATCC 11229 was measured by a dilution method [31]. ZnO particles with different concentrations were serially diluted in LB broth. The ZnO dilution and fresh bacterial culture (10⁶ CFU mL⁻¹) were equally mixed by volume and incubated at 37°C for 18 h. MIC was determined as the lowest effective concentration of ZnO in inhibiting a visible growth of bacteria.

The antibacterial activity of the ZnO surface coating was quantitatively examined through a cultivation method in shaking flasks. A 0.10 g of paper sample was soaked in a 25 mL flask containing 5 mL culture of *E. coli* (10⁵ CFU mL⁻¹). Shaken at 200 rpm, the mixture was incubated at 37°C for 60 min. After cultivation, 0.5 mL culture was successively diluted with 4.5 mL PBS solution to prepare bacterial dilutions. Finally, 0.1 mL of the dilution was coated on LB agar plate. After an incubation at 37°C for 24 h, the number of bacterial colonies formed was counted. Each paper sample was tested in triplicate. Filter paper without surface coating was used as the paper blank.

A reduction rate of bacterial reproduction was calculated to determine the antibacterial efficiency of the surface coatings by

$$\text{Reduction rate (\%)} = 100\% \times \frac{(A - B)}{A}, \quad (1)$$

where *A* and *B* were the numbers of bacterial colonies formed from the cultures with paper blank and coated papers, respectively.

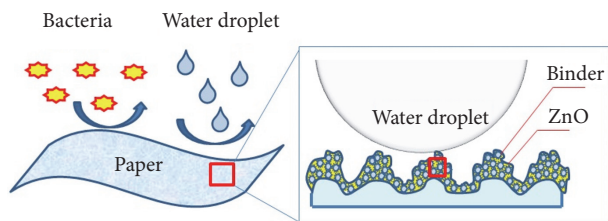


FIGURE 1: Schematic diagram of the surface coating structure.

3. Results and Discussion

3.1. Structure of the Surface Coating. The surface wettability of the surface coating was usually determined by two important factors: surface energy and surface roughness [32]. Natural cellulosic surfaces are hydrophilic or highly affiliative to water. In this work, change in hydrophobicity of cellulosic surface was realized due to the hydrophobic properties of soybean oil-based binder [33]. Low surface energy was achieved after incorporating the hydrophobic binder on cellulosic surfaces. At the mean time, the micro- or nanoscale hierarchical structures of ZnO particles could control the surface roughness (Figure 1).

The use of soybean oil-based polymer in the coating formula as binders relied on its bifunctional roles in the surface coating [34]. On one hand, AESO, the main constituent in the binder, could distribute through chain propagation to form a hydrophobic substance through free-radical reactions. On the other hand, the APTS which attached on AESO through a Michael addition reaction [35] could efficiently provide reactive silanol groups to render covalent bonds between $-OH$ and \ddot{O}_2^- on cellulosic surface and metallic oxide, respectively [33]. The binder was predominantly made up of triglyceride structures and probably possesses a potential degradability [36].

The original pore structure on natural cellulosic surface and ZnO particles contributed to the increase of water-resistant property of the coated cellulosic surfaces. The interlaced network of cellulose fibers provided basic microstructure of paper surfaces. ZnO nanoparticles coating could lead to three-dimensional structural patterns in micro- and nanoscale to form a hierarchical roughness on cellulosic surface. This specific morphology was believed to be more effective in creating air pockets [37] and increasing the water contact angles of the cellulose materials [38].

3.2. Aggregation of Patterns of ZnO Nanoparticles. In this study, two aggregation patterns of ZnO nanoparticles, that is, rod-like ZnO and flower-like ZnO, were introduced and tested separately (Figure 2). With an average diameter of $\sim 2 \mu m$, the 3D structure of the flower-like ZnO was observed by assembling a large number of 15 nm-thick nano-ZnO sheets. The nanosheets intersected with each other to form special porous structures on the flower-like ZnO.

Table 1 demonstrates the average diameters of the ZnO particles with two different aggregation patterns. The hydrodynamic size for both ZnO particles was relatively lower than that estimated by SEM imaging method.

3.3. Factors Affecting the Water Repelling Efficiency of Surface Coating

3.3.1. Patterns of ZnO Particles. Figure 3 shows that the cellulosic surface is superhydrophilic as the SCA is almost 0° . It could be explained by the existing of free hydroxyl groups that had a strong affinity for water. It demonstrated a strong hydrophobicity of the polymer binder was demonstrated as the hydrophilic cellulosic surface became hydrophobic with a SCA of 106° when a 0.3 g m^{-2} binding polymer was applied (Figure 3(b)). With introducing of two ZnO into the coating formula, the SCA of paper was further promoted over 125° (Figures 3(c) and 3(d)). It could be explained by a formation of hydrophobic substance over the cellulosic substrate followed by a decrease of the surface energy with ZnO particles. Additionally, the coverage of hydrophobic ZnO particles introduced micro- and nanoscale roughness, which was able to trap air for forming a solid-air-liquid interface. The multiscale structures, combining micro- and nanometric structuration would provide a remarkable promotion on water-droplet repellency [39]. The use of ZnO particles and polymer binder realized an improved antiwetting property through a surface morphological modification.

Interestingly, differences of the SCA between ZnO particles with distinct morphologies were observed. The flower-like ZnO was more effective in promoting SCA than the rod-like ZnO. As mentioned above, the flower-like ZnO particles tended to form a regular three-dimensional pattern full of micro- and nanostructures (Figure 3(d)) that were believed to be more effective in creating air pockets for an increase of SCA [40]. In contrast, the rod-like ZnO only deposited a flat structure through the surface coating (Figure 3(c)).

3.3.2. Ratio of Polymer Binder and ZnO in the Formula. The dosages of soybean oil-based binder in the coating agent needs to be adjusted to provide sufficient hydrophobicity as well as to ensure a solid affinity of ZnO particles on the cellulosic surface. Figure 4 shows that an increase of binder/ZnO ratio always leads to a decrease of SCA on the surface either with the lower-like ZnO or the rod-like ZnO. Lower ratio benefited a high SCA. The negative effect of an overuse of polymer binder on the SCA could refer to the AESO composition which had caused a loss of surface nanostructures induced by engulfing of ZnO particles and thus a reduction in roughness in the coating layers [15]. In addition, the reduction of the surface roughness was also attributed to the ease of aggregation of ZnO particles.

Even with an increased ratio of binder/ZnO, the flower-like ZnO still showed better performances on improving the water repelling efficiency than the rod-like ZnO did (Figure 4). As all porous structures on the ball-shaped particles could be well filled with the adsorbed binding chemicals, the flower-like ZnO showed an even distribution pattern on the coating surface. The smaller rod-like ZnO tended to gather together with the binding chemicals on the cellulosic surface. Considering a firm adhesion of ZnO particles, a ratio no less than 0.2 should be selected as the optimal level for further application.

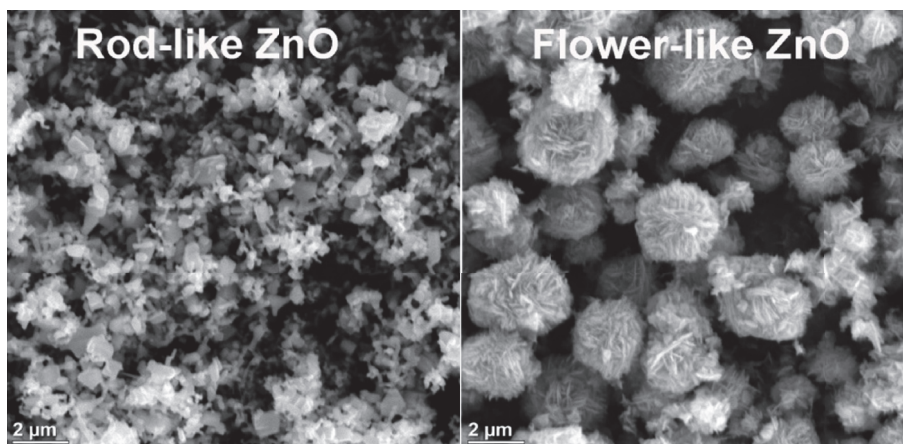


FIGURE 2: SEM images of the nano-ZnO aggregation.

TABLE 1: Particle size and polydispersity of the nano-ZnO aggregation.

Aggregation patterns	Hydrodynamic size		SEM observable size	
	Effective diameter (nm)	Polydispersity	Average diameter (nm)	Polydispersity
Rod-like ZnO	124.5	0.13	372.1	0.49
Flower-like ZnO	521.7	0.18	2374.1	0.30

3.3.3. Coating Weight. An increase application of the coating formula from 1.5 to 3 g m^{-2} promotes the SCA with either of the flower-like ZnO or the rod-like ZnO (Figure 5). However, an intensive application of coating weight had a negative effect on the SCA of the cellulosic surfaces. In Figure 6, it is revealed that the coating weight has influenced the surface morphology directly. At a coating weight of 1.5 g m^{-2} , the cellulosic surface was only partially coated by the ZnO particles with binding polymers, leaving the valley area of fiber networks hydrophilic to water. As the increase of the coating weight to 3 g m^{-2} , the cellulosic surface was well covered by the hydrophobic coating with a mixture of micro- or nanostructures exposed on the air-water interface. Upon further increasing the coating weight to 4.5 g m^{-2} , the cellulosic surface is covered by densely packed layers with a significant loss of micro- or nanohierarchical structures (Figure 6). As the fabrication of micro- or nanostructures on the coating surface would reflect the hydrophobicity performances of materials, choosing proper coating weight as well as a premodification of morphologies of the coating substrate would be possible method to adjusting the SCA on the coating surface.

3.4. Antimicrobial Efficiency of the Surface Coating with ZnO Nanoparticles. Besides regulating the surface roughness, the ZnO particles also played a key role in introducing the antimicrobial function to the cellulosic surfaces. Depending on the differences in particle sizes, the bacterial types, and experimental assays, the reported antimicrobial efficiency of ZnO differed with an effective concentrations ranging from 81 to $2835 \mu\text{g mL}^{-1}$ [41].

Determination of antibacterial activity of ZnO particles was performed homogeneously as it ensured that ZnO particles could be well distributed in the bacterial culture [42]. In this study, we also measured a relative inhibating rate for *E. coli* reproduction (reduction rate) alternatively using the filter papers with immobilized-ZnO-polymer coatings. In this study, the flower-like ZnO-polymer coating shows higher antibacterial activity than that of the rod-like ZnO-polymer coating (Table 2). The result was consistent with the reported literature [43]. Nevertheless we did not find an obvious difference in the MIC between using flower-like and the rod-like ZnO (Table 2).

A coating weight of 3 g m^{-2} led to a 51.6% of reduction rate *E. coli* reproduction by coating with flower-like ZnO particles. The reduction rate was comparable to that with the dispersion of free ZnO particles and the reduced antibacterial efficiencies of the surface coating were mainly from the barrier effects caused by binding polymers [43].

Defect sites could be formed on the flower-like ZnO with a typical structural pattern of 15 nm-thick nanoplates (Figure 2); that was believed to be responsible for the production of reactive oxygen species (ROS) in antibiosis of *E. coli*. In addition, an increase of coating weight resulted in an improvement of antibacterial activities for the coating surfaces. Clearly, a higher availability of ZnO from applying intensive coating weights on cellulosic surfaces corresponded to the promotion on release of ROS [44].

4. Conclusion

Functional flexible cellulosic surfaces with water-resistant and antimicrobial properties were prepared through a coating

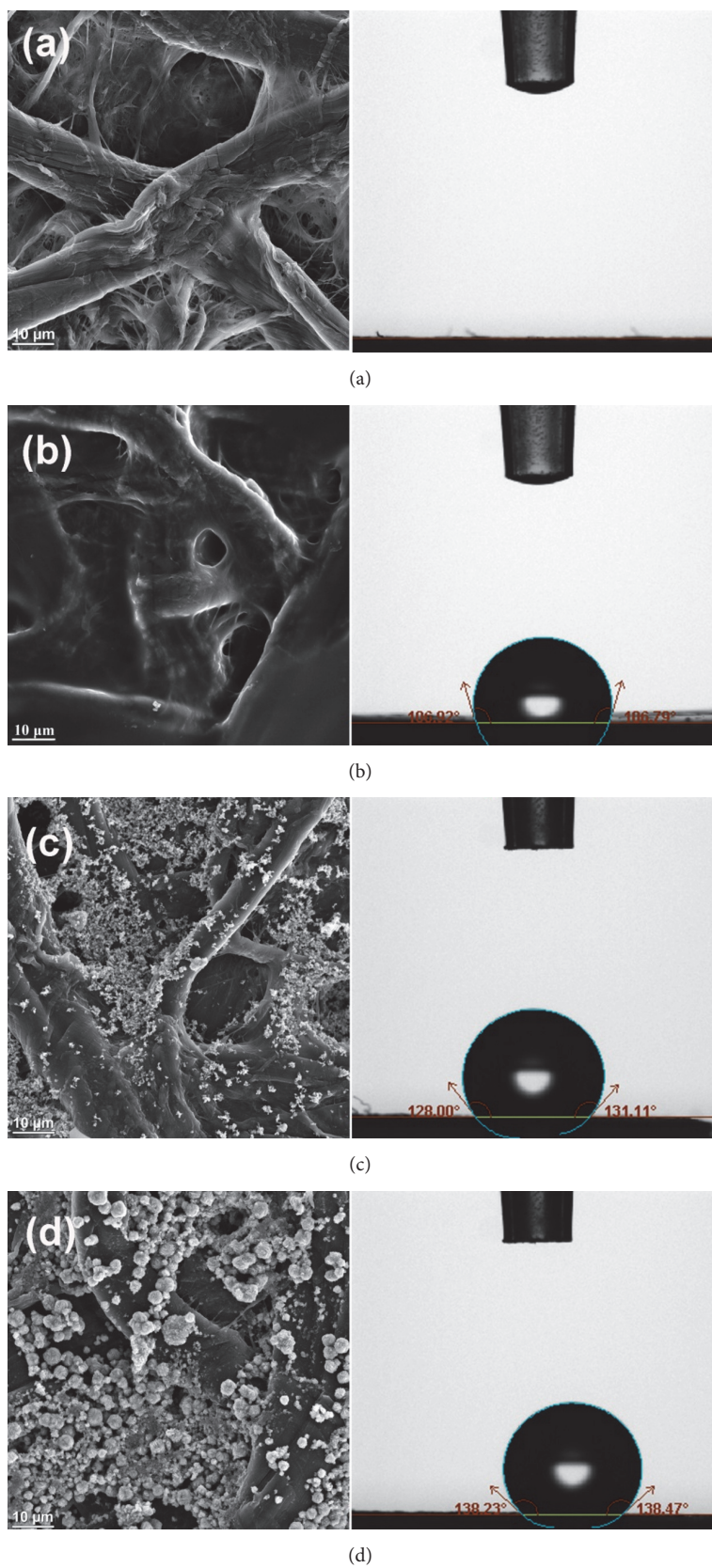


FIGURE 3: SEM images and SCA of (a) cellulosic surface; (b) cellulosic surface + binder; (c) cellulosic surface + binder + rod-like ZnO; and (d) cellulosic surface + binder + flower-like ZnO (with binder/ZnO ratio = 0.2).

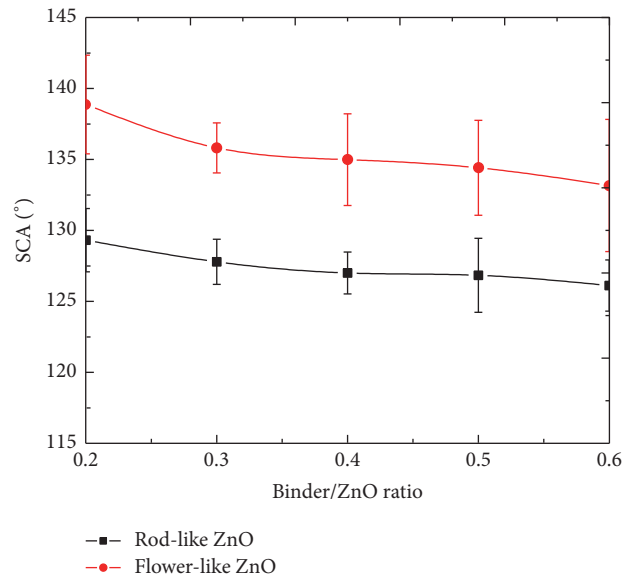


FIGURE 4: Effect of the binder/ZnO ratio on the SCA of coating surfaces.

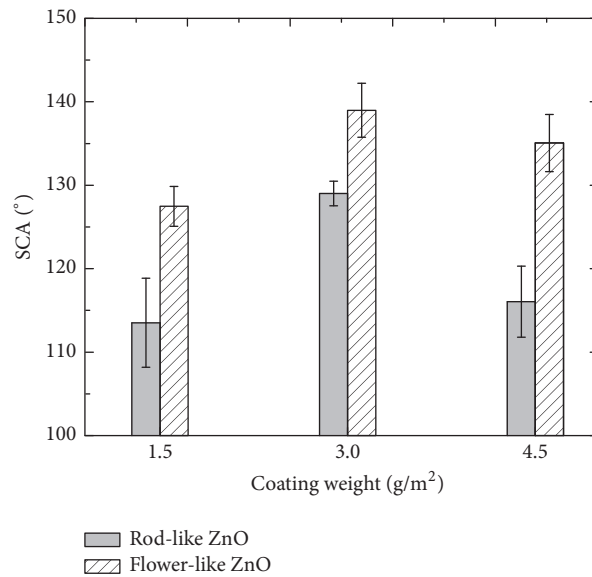


FIGURE 5: Effect of coating weight on the SCA of coating surfaces (with binder/ZnO ratio = 0.2).

TABLE 2: Antimicrobial performances of the surface coating with different ZnO aggregations.

	MIC ($\mu\text{g mL}^{-1}$)	Reduction of <i>E. coli</i> reproduction (%)	
		*Coating weight of 1.5 g m ⁻²	*Coating weight of 3 g m ⁻²
Control	0	0	0
Rod-like ZnO	312.5	34.0	45.3
Flower-like ZnO	312.5	44.9	51.6

*Binder/ZnO ratio = 0.2.

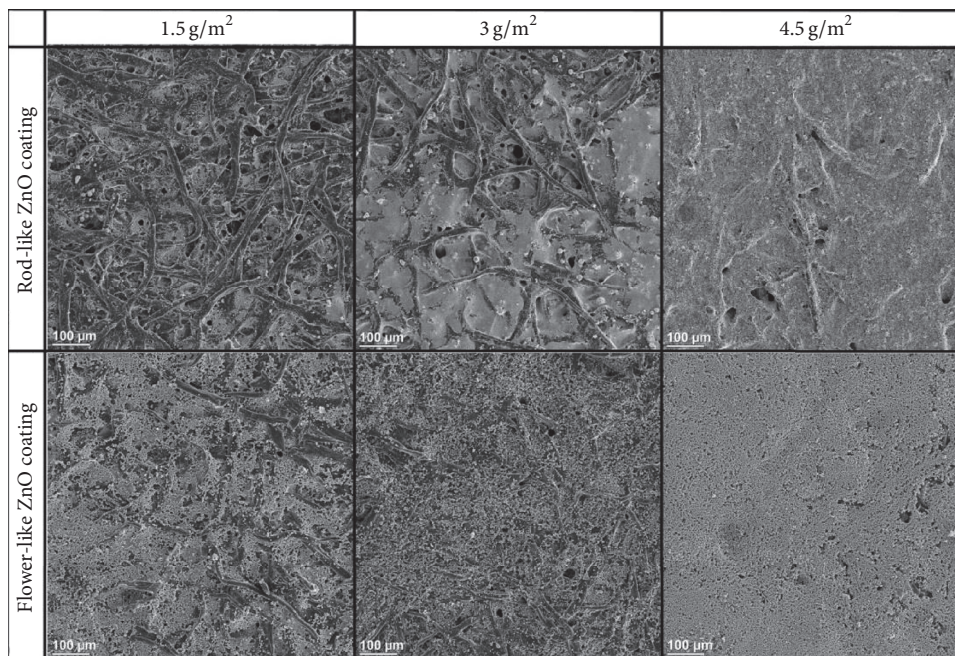


FIGURE 6: SEM images of the coating surface at different coating weight (with binder/ZnO ratio = 0.2).

method with ZnO nanoparticles and soybean oil-based polymers. The flower-like structural pattern of ZnO effectively promoted the SCA and antimicrobial activities. Under the optimal conditions with a binder/ZnO ratio of 0.2 and coating weight of 3 g m^{-2} , the prepared functional surfaces showed improved hydrophobic and antibacterial advantages with a SCA value of 138° and a 51.6% reduction rate for inhibiting *E. coli* reproduction.

Competing Interests

The authors declare that there is no conflict of interests regarding the publication of this paper.

Acknowledgments

The authors acknowledge the financial support from Scientific Research Foundation of Guangxi University (Grant no. XGZ160294), the Research Fund of State Key Laboratory of Pulp and Paper Engineering (no. 201351), and the National Science Foundation of Guangxi (no. 2015GXNSFB139042). This research was also supported by the Opening Project of Guangxi Key Laboratory of Clean Pulp & Papermaking and Pollution Control, Nanning 530004, China (KF201603).

References

- [1] S. Liu, T. Yu, Y. Wu, W. Li, and B. Li, "Evolution of cellulose into flexible conductive green electronics: a smart strategy to fabricate sustainable electrodes for supercapacitors," *RSC Advances*, vol. 4, no. 64, pp. 34134–34143, 2014.
- [2] Y. H. Jung, T.-H. Chang, H. Zhang et al., "High-performance green flexible electronics based on biodegradable cellulose nanofibril paper," *Nature Communications*, vol. 6, article 7170, 2015.
- [3] H. G. de Oliveira Barud, R. R. da Silva, H. da Silva Barud et al., "A multipurpose natural and renewable polymer in medical applications: bacterial cellulose," *Carbohydrate Polymers*, vol. 153, pp. 406–420, 2016.
- [4] H. P. S. Abdul Khalil, Y. Davoudpour, C. K. Saurabh et al., "A review on nanocellulosic fibres as new material for sustainable packaging: process and applications," *Renewable and Sustainable Energy Reviews*, vol. 64, pp. 823–836, 2016.
- [5] J. Vasiljević, B. Tomšič, I. Jerman, B. Orel, G. Jakša, and B. Simončič, "Novel multifunctional water- and oil-repellent, antibacterial, and flame-retardant cellulose fibres created by the sol-gel process," *Cellulose*, vol. 21, no. 4, pp. 2611–2623, 2014.
- [6] J. Vasiljević, M. Gorjanc, B. Tomšič et al., "The surface modification of cellulose fibres to create super-hydrophobic, oleophobic and self-cleaning properties," *Cellulose*, vol. 20, no. 1, pp. 277–289, 2013.
- [7] J. Garcia-Ubasart, J. F. Colom, C. Vila, N. G. Hernández, M. Blanca Roncero, and T. Vidal, "A new procedure for the hydrophobization of cellulose fibre using laccase and a hydrophobic phenolic compound," *Bioresource Technology*, vol. 112, pp. 341–344, 2012.
- [8] K. Thakur, S. Kalia, B. S. Kaith et al., "The development of antibacterial and hydrophobic functionalities in natural fibers for fiber-reinforced composite materials," *Journal of Environmental Chemical Engineering*, vol. 4, no. 2, pp. 1743–1752, 2016.
- [9] K. Thakur, S. Kalia, D. Pathania, A. Kumar, N. Sharma, and C. L. Schauer, "Surface functionalization of lignin constituent of coconut fibers via laccase-catalyzed biografting for development of antibacterial and hydrophobic properties," *Journal of Cleaner Production*, vol. 113, pp. 176–182, 2016.
- [10] Z. A. Raza, A. Rehman, M. Mohsin et al., "Development of antibacterial cellulosic fabric via clean impregnation of silver

- nanoparticles," *Journal of Cleaner Production*, vol. 101, pp. 377–386, 2015.
- [11] M. Shateri-Khalilabad and M. E. Yazdanshenas, "One-pot sonochemical synthesis of superhydrophobic organic-inorganic hybrid coatings on cotton cellulose," *Cellulose*, vol. 20, no. 6, pp. 3039–3051, 2013.
 - [12] N. R. Dhineshbabu, P. Manivasakan, A. Karthik, and V. Rajendran, "Hydrophobicity, flame retardancy and antibacterial properties of cotton fabrics functionalised with MgO/methyl silicate nanocomposites," *RSC Advances*, vol. 4, no. 61, pp. 32161–32173, 2014.
 - [13] P. Samyn, "Wetting and hydrophobic modification of cellulose surfaces for paper applications," *Journal of Materials Science*, vol. 48, no. 19, pp. 6455–6498, 2013.
 - [14] H.-B. Jo, J. Choi, K.-J. Byeon, H.-J. Choi, and H. Lee, "Superhydrophobic and superoleophobic surfaces using ZnO nano-in-micro hierarchical structures," *Microelectronic Engineering*, vol. 116, pp. 51–57, 2014.
 - [15] H. Ogihara, J. Xie, J. Okagaki, and T. Saji, "Simple method for preparing superhydrophobic paper: spray-deposited hydrophobic silica nanoparticle coatings exhibit high water-repellency and transparency," *Langmuir*, vol. 28, no. 10, pp. 4605–4608, 2012.
 - [16] D. Ebert and B. Bhushan, "Transparent, superhydrophobic, and wear-resistant coatings on glass and polymer substrates using SiO₂, ZnO, and ITO nanoparticles," *Langmuir*, vol. 28, no. 31, pp. 11391–11399, 2012.
 - [17] G. Gonçalves, P. A. A. P. Marques, T. Trindade, C. P. Neto, and A. Gandini, "Superhydrophobic cellulose nanocomposites," *Journal of Colloid and Interface Science*, vol. 324, no. 1–2, pp. 42–46, 2008.
 - [18] J. Li, Z. Jing, F. Zha, Y. Yang, Q. Wang, and Z. Lei, "Facile spray-coating process for the fabrication of tunable adhesive superhydrophobic surfaces with heterogeneous chemical compositions used for selective transportation of microdroplets with different volumes," *ACS Applied Materials and Interfaces*, vol. 6, no. 11, pp. 8868–8877, 2014.
 - [19] V. Chaurasia, N. Chand, and S. K. Bajpai, "Water sorption properties and antimicrobial action of zinc oxide nanoparticles-loaded cellulose acetate films," *Journal of Macromolecular Science Part A: Pure and Applied Chemistry*, vol. 47, no. 4, pp. 309–317, 2010.
 - [20] F. Fu, L. Li, L. Liu et al., "Construction of cellulose based ZnO nanocomposite films with antibacterial properties through one-step coagulation," *ACS Applied Materials & Interfaces*, vol. 7, no. 4, pp. 2597–2606, 2015.
 - [21] N. C. T. Martins, C. S. R. Freire, C. P. Neto et al., "Antibacterial paper based on composite coatings of nanofibrillated cellulose and ZnO," *Colloids and Surfaces A: Physicochemical and Engineering Aspects*, vol. 417, pp. 111–119, 2013.
 - [22] G. Applerot, J. Lellouche, N. Perkas, Y. Nitzan, A. Gedanken, and E. Banin, "ZnO nanoparticle-coated surfaces inhibit bacterial biofilm formation and increase antibiotic susceptibility," *RSC Advances*, vol. 2, no. 6, pp. 2314–2321, 2012.
 - [23] K. Han, Z. H. Zhao, Z. Xiang, C. Wang, J. Zhang, and B. Yang, "The sol-gel preparation of ZnO/silica core-shell composites and hollow silica structure," *Materials Letters*, vol. 61, no. 2, pp. 363–368, 2007.
 - [24] P. Joshi, S. Chakraborti, P. Chakraborti et al., "Role of surface adsorbed anionic species in antibacterial activity of ZnO quantum dots against *Escherichia coli*," *Journal of Nanoscience and Nanotechnology*, vol. 9, no. 11, pp. 6427–6433, 2009.
 - [25] A. B. Gurav, S. S. Latthe, R. S. Vhatkar et al., "Superhydrophobic surface decorated with vertical ZnO nanorods modified by stearic acid," *Ceramics International*, vol. 40, no. 5, pp. 7151–7160, 2014.
 - [26] Y. Wang, B. Li, and C. Xu, "Fabrication of superhydrophobic surface of hierarchical ZnO thin films by using stearic acid," *Superlattices and Microstructures*, vol. 51, no. 1, pp. 128–134, 2012.
 - [27] T. K. Sontakke, R. N. Jagtap, A. Singh, and D. C. Kothari, "Nano ZnO grafted on MAA/BA/MMA copolymer: an additive for hygienic coating," *Progress in Organic Coatings*, vol. 74, no. 3, pp. 582–588, 2012.
 - [28] T. J. Athauda, R. R. Ozer, and J. M. Chalker, "Investigation of cotton functionalized with ZnO nanorods and its interaction with *E. coli*," *RSC Advances*, vol. 3, no. 27, pp. 10662–10665, 2013.
 - [29] P. Lu, X. Tian, Y. Liu, and Z. Wang, "Effects of cellulosic base sheet pore structure and soybean oil-based polymer layer on cellulosic packaging performance as a barrier for water and water vapor," *BioResources*, vol. 11, no. 4, pp. 8483–8495, 2016.
 - [30] M. Yu, Z. Wang, H. Liu et al., "Laundering durability of photocatalyzed self-cleaning cotton fabric with TiO₂ nanoparticles covalently immobilized," *ACS Applied Materials & Interfaces*, vol. 5, no. 9, pp. 3697–3703, 2013.
 - [31] M. He, H. Xiao, Y. Zhou, and P. Lu, "Synthesis, characterization and antimicrobial activities of water-soluble amphiphilic copolymers containing ciprofloxacin and quaternary ammonium salts," *Journal of Materials Chemistry B*, vol. 3, no. 18, pp. 3704–3713, 2015.
 - [32] M. Ma and R. M. Hill, "Superhydrophobic surfaces," *Current Opinion in Colloid & Interface Science*, vol. 11, no. 4, pp. 193–202, 2006.
 - [33] M. Marquez, B. P. Grady, and I. Robb, "Different methods for surface modification of hydrophilic particulates with polymers," *Colloids & Surfaces A: Physicochemical & Engineering Aspects*, vol. 266, no. 1–3, pp. 18–31, 2005.
 - [34] P. Lu, H. Xiao, W. Zhang, and G. Gong, "Reactive coating of soybean oil-based polymer on nanofibrillated cellulose film for water vapor barrier packaging," *Carbohydrate Polymers*, vol. 111, pp. 524–529, 2014.
 - [35] S. Çolak and S. H. Küsefoğlu, "Synthesis and interfacial properties of aminosilane derivative of acrylated epoxidized soybean oil," *Journal of Applied Polymer Science*, vol. 104, no. 4, pp. 2244–2253, 2007.
 - [36] H.-M. Kim, H.-R. Kim, and B. S. Kim, "Soybean oil-based photo-crosslinked polymer networks," *Journal of Polymers and the Environment*, vol. 18, no. 3, pp. 291–297, 2010.
 - [37] E. Bormashenko, "Progress in understanding wetting transitions on rough surfaces," *Advances in Colloid and Interface Science*, vol. 222, pp. 92–103, 2015.
 - [38] T. P. N. Nguyen, R. Boukherroub, V. Thomy, and Y. Coffinier, "Micro- and nanostructured silicon-based superomniphobic surfaces," *Journal of Colloid and Interface Science*, vol. 416, pp. 280–288, 2014.
 - [39] N. J. Shirtcliffe, G. McHale, S. Atherton, and M. I. Newton, "An introduction to superhydrophobicity," *Advances in Colloid and Interface Science*, vol. 161, no. 1–2, pp. 124–138, 2010.
 - [40] D. E. Weibel, A. F. Michels, A. F. Feil, L. Amaral, S. R. Teixeira, and F. Horowitz, "Adjustable hydrophobicity of Al substrates by chemical surface functionalization of nano/microstructures," *The Journal of Physical Chemistry C*, vol. 114, no. 31, pp. 13219–13225, 2010.

- [41] V. B. Schwartz, F. Thétiot, S. Ritz et al., “Antibacterial surface coatings from zinc oxide nanoparticles embedded in poly(N-isopropylacrylamide) hydrogel surface layers,” *Advanced Functional Materials*, vol. 22, no. 11, pp. 2376–2386, 2012.
- [42] M. Li, L. Zhu, and D. Lin, “Toxicity of ZnO nanoparticles to *Escherichia coli*: mechanism and the influence of medium components,” *Environmental Science & Technology*, vol. 45, no. 5, pp. 1977–1983, 2011.
- [43] J. T. Seil and T. J. Webster, “Antimicrobial applications of nanotechnology: methods and literature,” *International Journal of Nanomedicine*, vol. 7, no. 1, pp. 2767–2781, 2012.
- [44] M. Ramani, S. Ponnusamy, and C. Muthamizhchelvan, “From zinc oxide nanoparticles to microflowers: a study of growth kinetics and biocidal activity,” *Materials Science and Engineering C*, vol. 32, no. 8, pp. 2381–2389, 2012.

Research Article

Binding Affinity, Cellular Uptake, and Subsequent Intracellular Trafficking of the Nano-Gene Vector P123-PEI-R13

Yaguang Zhang, Hongmei Shu, Jing Hu, Min Zhang, Junweng Wu, Kehai Liu, and Qing Zhu

Department of Biopharmaceutics, College of Food Science and Technology, Shanghai Ocean University, Shanghai 201306, China

Correspondence should be addressed to Kehai Liu; khliu@shou.edu.cn

Received 26 July 2016; Revised 8 September 2016; Accepted 4 October 2016

Academic Editor: Liqian Gao

Copyright © 2016 Yaguang Zhang et al. This is an open access article distributed under the Creative Commons Attribution License, which permits unrestricted use, distribution, and reproduction in any medium, provided the original work is properly cited.

A nano-gene vector PEI-P123-R13 was synthesized by cross-linking low molecular weight PEI with P123 and further coupling bifunctional peptide R13 to the polymer for targeting tumor and increasing cellular uptake. The binding assessment of R13 to $\alpha v\beta 3$ positive cells was performed by HRP labeling. The internalization pathways of P123-PEI-R13/DNA complexes were investigated based on the effect of specific endocytic inhibitors on transfection efficiency. The mechanism of intracellular trafficking was investigated based on the effect of endosome-lysosome acidification inhibitors, cytoskeleton, and dynein inhibitors on transfection efficiency. The results indicated that the bifunctional peptide R13 had the ability of binding to $\alpha v\beta 3$ positive cells *in vitro*. The modification of P123-PEI-R13 with R13 made it display new property of internalization. P123-PEI-R13/DNA complexes were conducted simultaneously via clathrin-mediated endocytosis, caveolin-mediated endocytosis, macropinocytosis, and possible energy-independent route. After internalization, P123-PEI-R13/DNA complexes could escape from the endosome-lysosome system because of its acidification and further took microtubule as the track and dynein as the dynamic source to be transported toward the microtubule (+) end, to wit nucleus, under the action of microfilament, and with the aid of intermediate filament.

1. Introduction

Cancer is the main reason of death worldwide, while gene therapy is the most potential way to eradicate cancer. A high efficiency and low toxicity gene vector plays a key role in gene therapy. Nonviral gene vectors, especially polyethyleneimine (PEI), have recently attracted remarkable interests. A targeting vector P123-PEI-R13 was once successfully synthesized. At first we synthesized a kind of high molecular weight PEI derivate (P123-PEI) by cross-linking low molecular weight PEI with Pluronic P123. Integrin $\alpha v\beta 3$ can be highly expressed on cancer cells, and RGD is the $\alpha v\beta 3$ -targeting peptide. Cell-penetrating peptides can directly carry macromolecule substance to pass through the cell membrane. In order to improve cell selection and increase cellular uptake, we coupled $\alpha v\beta 3$ -targeting peptide RGDC with the cell-penetrating peptide TAT to obtain a bifunctional peptide RGDC-TAT (named R13) and then used R13 to modify the PEI derivate P123-PEI. Thus a new polymeric gene vector (P123-PEI-R13) was prepared. The purpose of this study was to solve the efficiency-versus-cytotoxicity and tumor-targeting

problems of PEI as a nonviral gene delivery vector. The new nonviral gene vector P123-PEI-R13 could reduce cytotoxicity of PEI under the circumstance that PEI showed high transfection efficiency, increase the cell selection, and then improve the curative effect of gene therapy. This study could find an available way to gene therapy on cancer [1]. However, the binding affinity, cellular uptake, and subsequent intracellular trafficking of this vector should be clarified.

For gene therapy, an appropriate gene vector is necessary for its efficient binding to cells, cellular uptake, and intracellular trafficking. Binding to the target cells is an essential precondition for cell transfection. The internalization of macromolecules is achieved through endocytosis. Endocytosis is divided into phagocytosis and pinocytosis, in which phagocytosis exists in specialized cells while pinocytosis is involved in all kinds of cells. During the endocytosis, plasma membrane is internalized into cells to form a vesicle firstly and then enter the endolysosomal environment by fusing with endosomes [2]. Phagocytosis can be classified into the following: clathrin-mediated endocytosis, caveolin-mediated

endocytosis, macropinocytosis, and clathrin- and caveolae-independent endocytosis [3]. After the complex is taken up by cells via endocytosis, the further intracellular transport from endosome to the nucleus appears to be particularly important. Endosome-lysosome system is the main pathway. As a highway to transport the cargoes, the cytoskeleton is made of three kinds of protein filaments: microfilaments, intermediate filaments, and microtubules [4].

Chemical inhibitors have an enormous impact on the intracellular components and structures, and the major intracellular pathways of macromolecules are usually distinguished on the basis of their differential sensitivity to chemical inhibitors. In this study, inhibitors were applied to determine the internalization mode and intracellular routing of P123-PEI-R13/DNA complexes. Chlorpromazine hydrochloride (CPZ), glucose, and C9 (competitive peptide RGD, CYGGRGDTP) were used as inhibitors of clathrin-mediated endocytosis. CPZ was said to inhibit clathrin-mediated endocytosis by translocating clathrin and adaptin from membrane to vesicles [5]. Glucose might lead to the shedding of clathrin [6]. The inhibition of C9 was competitive. It blocked the combination between P123-PEI-R13/DNA and adaptin, which regulated clathrin-mediated endocytosis [7]. Genistein was used as an inhibitor of caveolin-mediated endocytosis. It restrained the formation of intracellular vesicles [8]. 5-(N,N-Dimethyl) amiloride hydrochloride (DMA) was used as an inhibitor of macropinocytosis. It could inhibit Na^+/H^+ exchange protein on the plasma membrane [9]. NH_4Cl and monensin were used as inhibitors of endosome-lysosome system. They prevented the acidification of endosome and inhibited their fuse and maturation [10]. Cytochalasin B (Cyto B) caused the depolymerization of the actin and inhibited the function of microfilaments [11]. Colchicine (Col) and paclitaxel (PTX) were used as inhibitors of microtubules. Col could stimulate polymerization of microtubules and PTX could inhibit mitosis [12, 13]. Having determined suitable inhibitors, the efficiency of inhibitors was assessed quantitatively in HeLa cells by pGL3-Control reporter gene so as to investigate the internalization pathways and intracellular trafficking of P123-PEI-R13/DNA complexes based on the effect of specific inhibitors on transfection efficiency. Understanding the intracellular transport can provide researchers with more ideas for improving current nonviral gene vectors. This study investigated the intracellular transport of gene delivery system for cancer gene therapy with the purpose of developing an optimal prototype for tumor cell transfection.

2. Materials and Methods

2.1. Materials. HRP, SMCC, BSA, genistein, monensin, cytochalasin B, glucose, colchicine, paclitaxel (PTX), and 5-(N,N-dimethyl) amiloride hydrochloride (DMA) were obtained from Sigma Aldrich (St. Louis, MO). The competitive peptide RGD C9 (CYGGRGDTP), dimethylsulfoxide (DMSO), formaldehyde, H_2O_2 , EDTA, NH_4Cl , acrylamide, and the absolute ethyl ethanol were obtained from China National Medicines Corporation Ltd. RPMI 1640 culture

medium, fetal bovine serum (FBS), and trypsin were purchased from Invitrogen (Carlsbad, CA). Luciferase assay system for *in vitro* transfection assay and pGL3-Control vector with SC-40 promoter and enhancer encoding firefly (*Photinus pyralis*) luciferase were obtained by Promega (Madison, WI). Chlorpromazine hydrochloride (CPZ) and sodium orthovanadate (SOV) were provided by TCI (Shanghai) Development Co., Ltd.

2.2. Preparation of P123-PEI-R13/DNA Complexes and Morphologic Observation. The charge ratio of P123-PEI-R13/DNA was controlled by regulating weight ratio of P123-PEI-R13 and DNA. DNA solution and polymer solution were mixed to form self-assembly complexes with desired w/w ratio. The complexes were allowed to stand at 4°C for 30 minutes before they were used in the next experiments.

The concentration of DNA was $50\ \mu\text{g}/\text{mL}$ and the w/w ratio of the polymer to DNA was 10. A drop of the complex solution was placed on a copper grid. Transmission electron microscope (JEM 2100F; JEOL Ltd., Tokyo, Japan) was used to observe the morphological characteristics of the micelle after the sample was dried.

2.3. Binding Affinity of R13 to Integrin Receptor

2.3.1. Conjugation of R13 with HRP. N-Succinimidyl-4-(N-maleimido-methyl) cyclo-hexane-carboxylate (SMCC) was used as heterobifunctional agent to combine R13 with HRP enzyme. After SMCC was dissolved in dimethyl sulfoxide solution ($3.33\ \text{mg}/\text{mL}$) and HRP was dissolved in PBS arriving at a concentration of $10\ \text{mg}/\text{mL}$, $0.1\ \text{mL}$ of SMCC solution was slowly added to $0.4\ \text{mL}$ of HRP solution (1:10, n/n). The reaction mixture was incubated at 25°C for 30 min. The superfluous nonreacted cross-linker was removed by gel chromatography (Sephadex G-25, Pharmacia). Then $10\ \text{mg}/\text{mL}$ R13 PBS solution was mixed with the maleimide-activated HRP solution (1:10, n/n) and kept at 4°C in shade for 12 hours. Amicon Ultra-4 centrifugal filter device (Millipore) was used to remove the nonreacted R13.

2.3.2. Evaluation of Binding Affinity. As we know, the integrin $\alpha\text{v}\beta3$ receptors can be highly expressed on HeLa cells and B16 cells. Two kinds of cells were seeded in RPMI 1640 medium in 6-well plates (Costar, Corning Corp, New York) and incubated for one day to 70–80% confluence. After the medium was removed, the cells were washed by PBS once. $1\ \text{mL}$ of fixative solution (2% formaldehyde and 0.05% glutaral in PBS buffer) was added to each well and the cells were fixed for 15 minutes. The cells were washed by $1\ \text{mL}$ $0.01\ \text{M}$ PBS three times, treated with 3% H_2O_2 aqueous solution, and then washed by $3\ \text{mL}$ of $0.01\ \text{M}$ PBS three times, each time for 3 minutes. $1\ \text{mL}$ of 1% BSA was added in each well to block the protein binding site. After 20 minutes, the excess liquid was blotted. The cells were randomly divided into test groups and control groups, which were cultivated with the diluted R13-HRP solutions and HRP solutions for 60 minutes at 37°C , respectively, and then washed by $3\ \text{mL}$ $0.01\ \text{M}$ PBS three times. Finally, the cells were stained with DAB and observed by microscopy (AE-31, Motic Corporation, Germany).

2.4. Effect of Specific Endocytic Inhibitors on Transfection Efficiency. The effects of different inhibitors on the transfection efficiency of P123-PEI-R13/DNA in HeLa cells were investigated using the pGL3-Control reporter gene. After being dispersed by trypsin, 3×10^4 cells were added to each well of a 24-well plate and cultured with RPMI 1640 medium containing 10% serum for 24 h to 70–80% confluence. Before transfection, the culture medium was removed and then washed by 1 mL 0.01 M PBS three times. 400 μ L of serum-free RPMI 1640 medium containing different concentrations of inhibitors was added to each well and incubated for 30 minutes. Cells were incubated for 2 h at 37°C in 5% CO₂ atmosphere after 100 μ L of complex solution with 0.8 μ g pDNA at w/w ratio of 30 was appended to each well. Then the medium was replaced with 500 μ L of medium containing 10% FBS and cells were incubated for another 48 h.

Luciferase was detected in accordance with Operation Manual (Promega, Madison, WI). The culture medium was removed and 200 μ L of cell culture lysis reagent (CCLR) was added. After 0.5 h shaking, the cell lysis solution was centrifuged (8000 rpm, 5 min, 4°C). 20 μ L of cell culture supernate was added to 100 μ L of the luciferin substrate before luciferase activity was examined immediately by a luminometer (Turner Designs Luminometer model TD-20/20; Promega, USA). The content of protein was detected by BCA protein assay kit (Pierce, Rockford, IL). The relative light unit (RLU) against the corresponding protein contents was applied to calculate the transfection efficiency for pGL3-Control. Six replicates were counted for each sample.

2.5. Effect of Incubation Time and Temperature on Transfection Efficiency. The effect of incubation temperature and time on the transfection efficiency of P123-PEI-R13/DNA complexes was also investigated in HeLa cells using the pGL3-Control reporter gene. The cells were cultured according to 2.4. After the culture medium was removed, cells were incubated with 400 μ L of serum-free RPMI 1640 medium and 100 μ L of complex solution with 0.8 μ g pDNA at w/w ratio of 30 at 4°C and 37°C, respectively. Then the culture medium was removed at different time point and the cells were washed by PBS once. A fresh medium containing 10% FBS was added and cells were further incubated for 48 hours. Luciferase activity was measured according to Section 2.4.

2.6. Effect of Endosome-Lysosome Acidification Inhibitors, Cytoskeleton, and Dynein Inhibitors on Transfection Efficiency. The effects of endosome-lysosome acidification inhibitors, cytoskeleton, and dynein inhibitors on the transfection efficiency of P123-PEI-R13/DNA in HeLa cells were investigated. All the experiments using the pGL3-Control as reporter gene were performed according to Section 2.4.

2.7. Statistical Analysis. Data was showed in the form of the mean \pm standard deviation. Assigning the value of significant level as 0.05, two-sample Student's *t*-tests and analysis of variance were used to determine statistically significant differences between these groups.

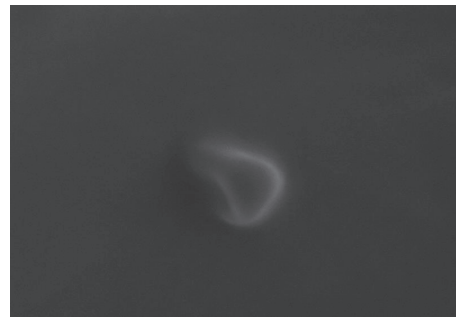


FIGURE 1: Transmission electron micrograph of P123-PEI-R13/DNA complexes.

3. Results and Discussion

3.1. Morphological Characteristics of P123-PEI-R13/DNA Complexes. From Figure 1, the P123-PEI-R13 polymer could condense pDNA into nanoparticles with spherical structure. The particle size and electric potential of P123-PEI-R13/DNA complex under different mass ratios were measured previously. The particle sizes of the complexes with range from 100 to 400 nm were inversely proportional to its w/w ratios, which was suitable for cell transfection. As the w/w ratio of cationic polymer increases, the zeta potential of the complex also increases. An appropriate amount of positive charges helps to bind successfully to cell membranes with negative charges, but too high concentration of cationic charges will be toxic to cells. The zeta potential of P123-PEI-R13/DNA complexes was around 5–40 mV.

3.2. Binding of R13 Coupled with HRP to α v β 3 Positive Cells. PEI used as gene vector was limited due to its poor cells selection. PEI was positively charged and body cells were negatively charged, which result in that there was no binding selectivity between them. HeLa cells were cocultured with HRP-labeled R13 and HRP, and staining was conducted with DAB, followed by an observation under an inverted microscope. In Figure 2, the cells in test groups were stained strongly positive, but negative in control groups. The results indicated that R13 was capable of binding to α v β 3 positive cells *in vitro*, HeLa cells, and B16 cells and heralded excellent tumor targeting.

3.3. Mechanism of Cellular Uptake of P123-PEI-R13/DNA Complexes

3.3.1. Effects of Clathrin-Mediated Endocytosis Inhibitors on Cell Uptake of P123-PEI-R13/DNA Complexes. As shown in Figure 3, different concentration of CPZ, glucose, and C9 inhibited transfection efficiency of P123-PEI-R13/DNA complexes more or less. The inhibitive effect became more significant as the dose increased (except glucose). 20 μ M of CPZ showed the most notable inhibition (>85%), followed by 250 ng/mL C9 (>50%), which affected the transfection efficiency through competitively combination with receptors on the cell surface. The inhibition rate of 0.4 M glucose is about 42%. Clathrin-mediated endocytosis is the primarily

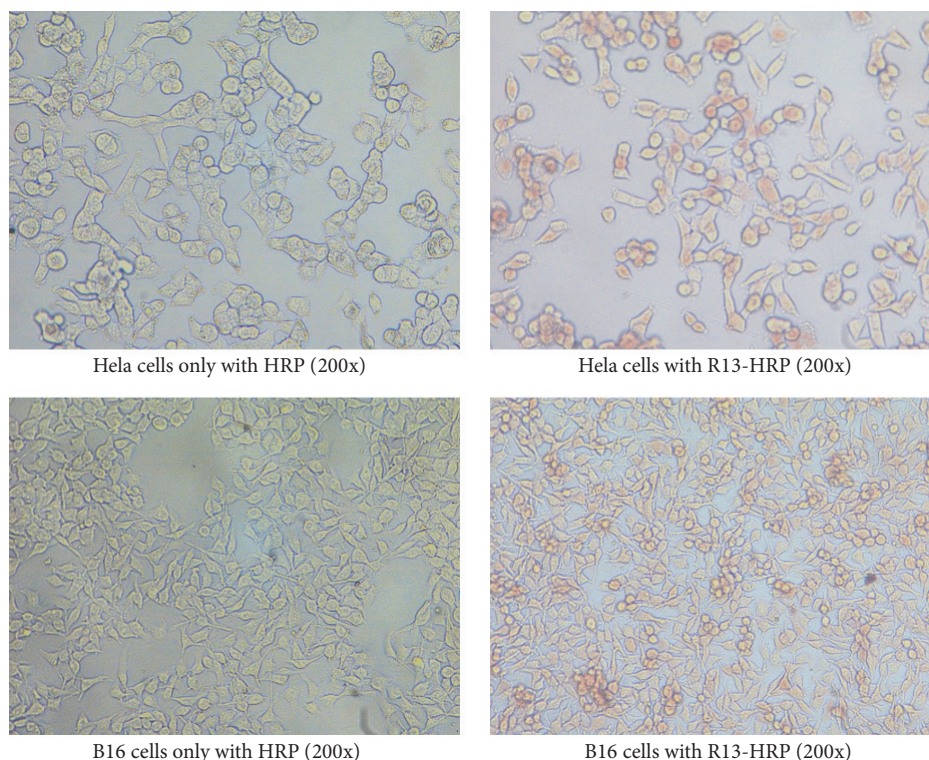


FIGURE 2: Binding affinity of R13 to HeLa cells and B16 cells.

and explicitly recognized uptake pathway of cells. Almost all mammalian cells adopt this approach for continuous endocytosis of important substances. The results demonstrated that clathrin-mediated endocytosis was one of the efficient approaches for P123-PEI-R13/DNA complexes to pass into cells.

3.3.2. Effects of Caveolin-Mediated Endocytosis Inhibitor on Cell Uptake of P123-PEI-R13/DNA Complexes. The inhibition of genistein to caveolin-mediated endocytosis was shown in Figure 4. No inhibition was found at low concentration of genistein; the inhibitive effect increased with increasing concentration. The inhibition rate is as high as 70% at the concentration of 200 μM . It revealed that caveolin-mediated endocytosis also caused difference in the internalization, as one of the efficient pathways employed by P123-PEI-R13/DNA complexes.

3.3.3. Effect of Macropinocytosis Inhibitor on Cell Uptake of P123-PEI-R13/DNA Complexes. The inhibition of DMA to macropinocytosis was shown in Figure 5. No inhibition was found at low concentration of DMA. Higher concentration of DMA could inhibit the transfection efficiency of P123-PEI-R13/DNA complexes. The inhibitive effect was dose-dependent and the inhibition rate is about 65% at the concentration of 20 μM . It is worth mentioning that the macropinocytosis is often neglected, and few cationic complexes get into cells through this way. However, the transfection of

P123-PEI-R13/DNA complexes was significantly inhibited in the presence of high concentration of DMA; that is to say, macropinocytosis participated in the endocytosis of P123-PEI-R13/DNA complexes, which showed the different endocytosis characteristics of this complex. It may be associated to the modification of P123-PEI-R13 with cell-penetrating peptide (CPP) TAT (49–57) [14].

3.3.4. Effect of Incubation Time and Temperature on Transfection Efficiency of P123-PEI-R13/DNA Complexes. HeLa cells were incubated with P123-PEI-R13/pGL3-Control complexes at 4°C and 37°C, respectively, and culture medium containing compound was removed at a certain time point. The culture medium was replaced by fresh medium with 10% FBS and cells were further incubated for 48 hours. Transfection efficiency of P123-PEI-R13/pGL3-Control complexes at different temperature and incubation time was measured, shown in Figure 6.

From Figure 6, the transfection effect of compound on cell will increase over time under 37°C, but it did not reach a maximum after 4 h incubation. It also increased with time under 4°C but gradually leveled off after 2 h incubation. In addition, the complex had a higher transfection efficiency under 37°C than under 4°C at different time point, which meant that transfection of P123-PEI-R13/DNA complexes was an energy consuming process. It is worth noting that the transfection of the complex under 4°C was not completely restrained by the low temperature and had the time-dependent characteristic, demonstrating that the internalization of this complex

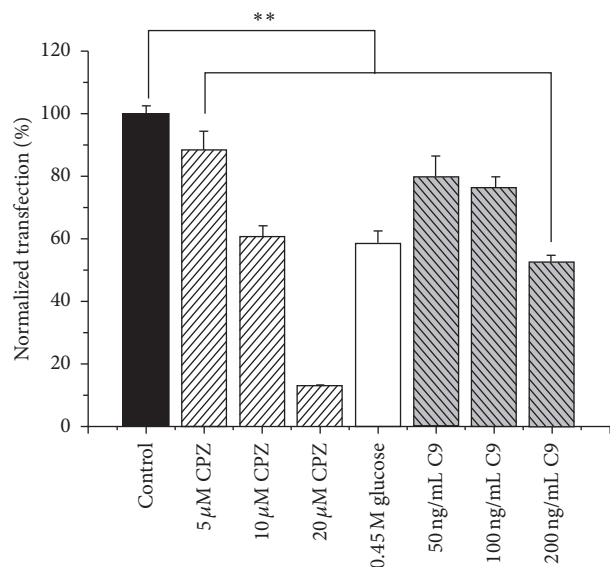


FIGURE 3: Effect of chlorpromazine hydrochloride (CPZ), glucose, and C9 on transfection efficiency of P123-PEI-R13/DNA complexes in Hela cells at w/w ratio of 30. CPZ and glucose were used as the inhibitors of clathrin-mediated endocytosis. C9 was the competitor of P123-PEI-R13/DNA complexes for clathrin-mediated endocytosis. The RLU/mg protein in control cells was set to 100%. Each data point represents the mean \pm standard deviation ($n = 6$, $**P < 0.01$).

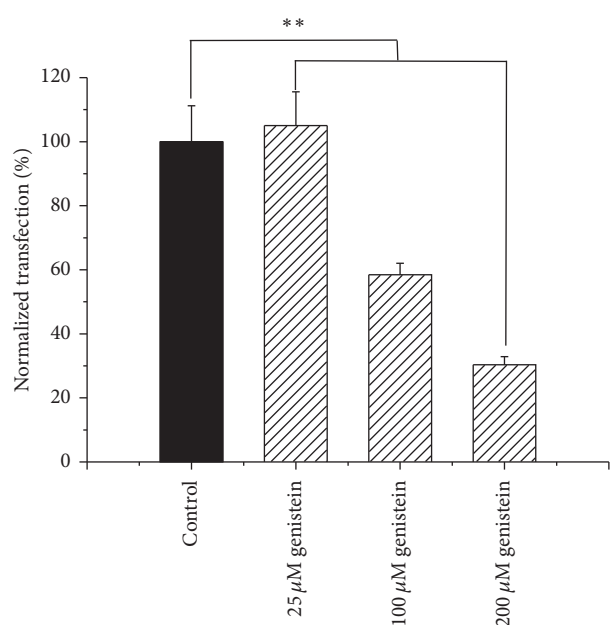


FIGURE 4: Effect of different concentration of genistein on transfection efficiency of P123-PEI-R13/DNA complexes in Hela cells at w/w ratio of 30. Genistein was used as the inhibitor of caveolin-mediated endocytosis. The RLU/mg protein in control cells was set to 100%. Each data point represents the mean \pm standard deviation ($n = 3$, $**P < 0.01$).

was not simply an active transport process that needed energy consumption, but there also might be other forms

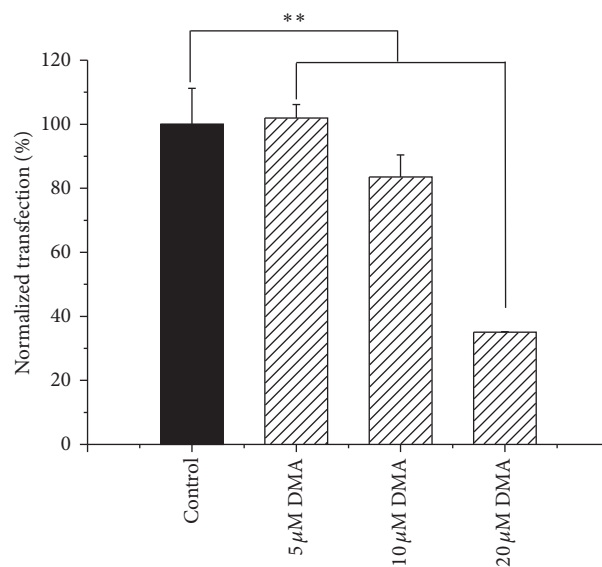


FIGURE 5: Effect of different concentration of 5-(N,N-dimethyl)amiloride hydrochloride (DMA) on transfection efficiency of P123-PEI-R13/DNA complexes in Hela cells at w/w ratio of 30. DMA was used as the inhibitor of macropinocytosis. The RLU/mg protein in control cells was set to 100%. Every data point represents the average value of integrated data ($n = 3$, $**P < 0.05$).

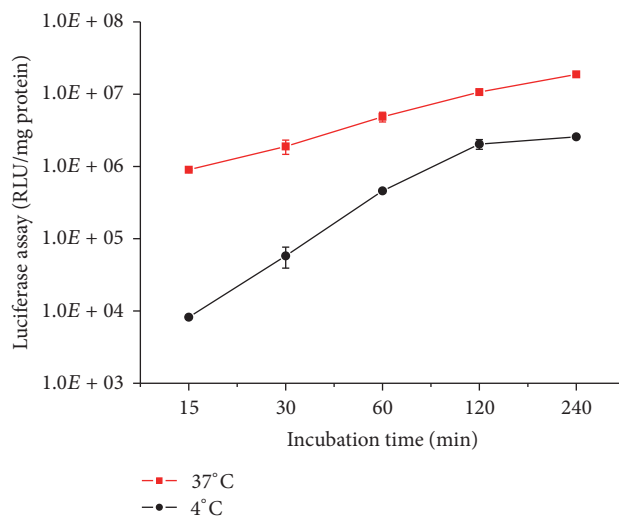


FIGURE 6: Effect of incubation time and temperature on transfection efficiency of P123-PEI-R13/DNA complexes in Hela cells at w/w ratio of 30. Each data point represents the mean \pm standard deviation ($n = 5$).

of nonendocytosis. P123-PEI-R13 was modified using the TAT (49–57) peptide. This kind of cell-penetrating peptide can carry macromolecule substance into cells directly independently of the energy consumption. Compared with the energy-dependent endocytosis, energy-independent internalization did not seem to play a dominant role, because the transfection gradually tended to balance after incubation for 2 h at 4°C, and transfection ability was much weaker than that at the corresponding time point under 37°C.

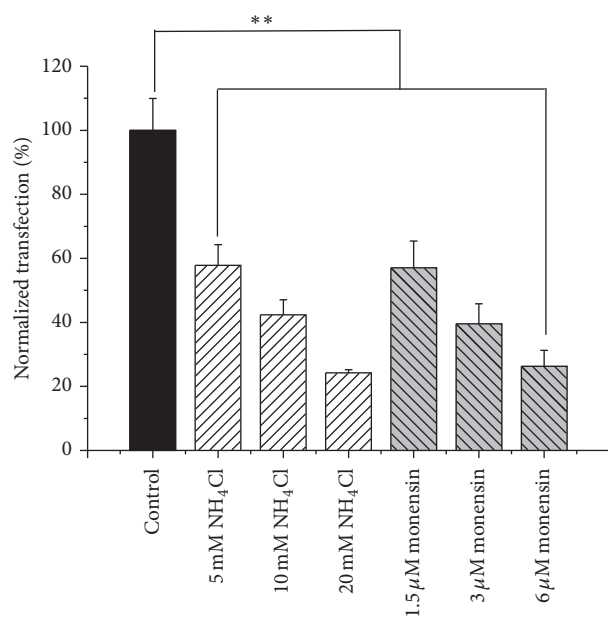


FIGURE 7: Effect of NH_4Cl and monensin on transfection efficiency of P123-PEI-R13/DNA complexes in HeLa cells at w/w ratio of 30. NH_4Cl and monensin were used as the acidification inhibitors of endosome-lysosome system. The RLU/mg protein in control cells was set to 100%. Each data point represents the mean \pm standard deviation ($n = 6$, $**P < 0.01$).

3.4. Mechanism of Intracellular Trafficking of P123-PEI-R13/DNA Complex

3.4.1. Effect of Acidification Inhibitors of Endosome-Lysosome System on Intracellular Transport of P123-PEI-R13/DNA Complexes. After endocytosis, the complex was delivered to lysosomes from endosomes, which was a cytosol acidification process. In Figure 7, the inhibition of NH_4Cl and monensin increased as the doses were increasing; they reduced the transfection efficiency by 76% and 74%, respectively, at the highest dose. These results demonstrated that part of the complex indeed underwent endosome-lysosome system in cells and acidification process is advantageous to gene transfection. It caused protonation of P123-PEI-R13 and helped the complex escape from lysosome. The acidification process of endosome-lysosome system is the basis and ensures complex transport to the nucleus [15].

3.4.2. Effect of Cytoskeleton Inhibitors on Intracellular Transport of P123-PEI-R13/DNA Complexes. As important roles in cellular activities, microtubules function as routes along which organelles can move. The assembly of microtubules is a dynamic equilibrium process of polymerization-depolymerization. Col could cause depolymerization of microtubules, but PTX stimulated excessive polymerization. They both disrupted the balance of dynamic equilibrium process [16]. In Figure 8, 50 mM of PTX and 20 $\mu\text{g}/\text{mL}$ of Col reduced transfection efficiency by 50% and 80%, respectively. The results revealed that the dynamic equilibrium process of microtubules was necessary for the intracellular trafficking of

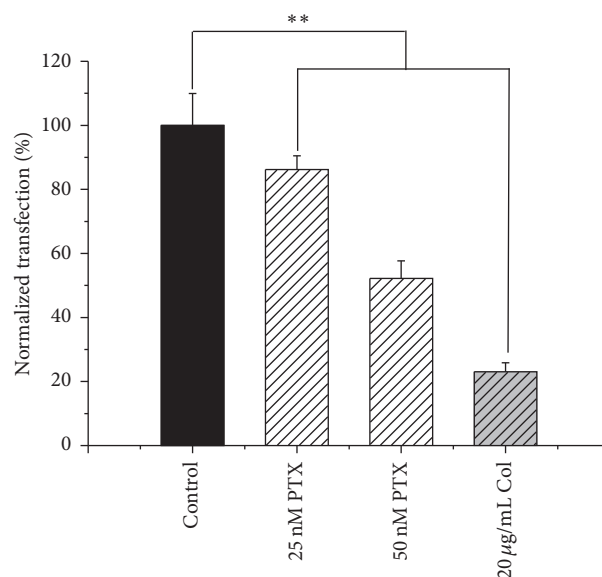


FIGURE 8: Effect of paclitaxel (PTX) and colchicine (Col) on transfection efficiency of P123-PEI-R13/DNA complexes in HeLa cells at w/w ratio of 30. PTX and Col were used as the inhibitors of microtubule. The RLU/mg protein in control cells was set to 100%. Each data point represents the mean \pm standard deviation ($n = 3$, $**P < 0.01$).

P123-PEI-R13/DNA complexes. The polymerization process stimulated the complexes tracking toward the microtubule (-) end, to wit nucleus, and depolymerization process stimulated the complexes getting into nucleus through mitosis. Once the balance was broken, gene transfection efficiency would decrease.

Microfilaments are the thinnest filaments of the cytoskeleton and they function in cell movement and generate locomotion in cells. Cyto B can interrupt cell activities as it binds with the (+) end of microfilaments, resulting in the depolymerization of actin filaments and the disappearance of F-actin skeleton [17]. In Figure 9, the transfection efficiency of Cyto B-treated cells was reduced considerably. The transfection process almost ground to a halt at the concentration of 18 μM . This result proved that microfilaments involved in the intracellular trafficking of P123-PEI-R13/DNA complexes in cells, intimately associated with cytokinesis in mitosis telophase.

The intermediate filaments have various functions during the cellular life cycle. One end of an intermediate filament is connected to cell membrane or microtubules and microfilaments, while the other end is attached to nuclear membrane and connected to nuclear skeleton through a nuclear pore. Therefore, a complete structural supporting system is formed, which has a fixation effect on the nucleus and allows it to occupy certain space within the cell. In the process of mitosis, the intermediate filaments experience depolymerization and remodeling, envelope the spindle, and conduct a spatial orientation of the spindle and the chromosome. In addition, intermediate filaments collaborate with microtubules to participate in the transportation of intracellular materials.

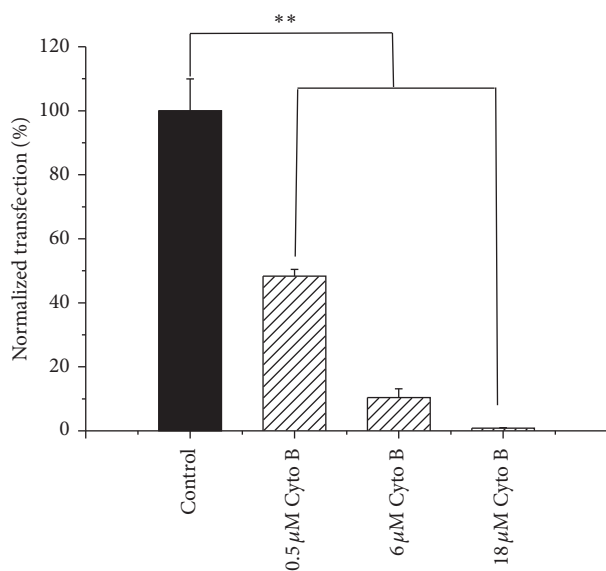


FIGURE 9: Effect of cytochalasin B (Cyto B) on transfection efficiency of P123-PEI-R13/DNA complexes in HeLa cells at w/w ratio of 30. Cyto B was used as the inhibitors of microfilament. The RLU/mg protein in control cells was set to 100%. Each data point represents the mean \pm standard deviation ($n = 3$, $**P < 0.01$).

Therefore, intermediate filaments are also an important part of intracellular transport of complexes, whose process will be greatly restricted without the support and assistance of intermediate filaments. It can be seen from Figure 10 that, after the treatment with acrylamide that has an inhibitory effect on skeleton structure of intermediate fibers, the transfection efficiency of complexes in HeLa cell significantly decreased and the inhibition rate was up to 82%. Thus it can be seen that intermediate filaments have a significant influence on P123-PEI-R13 transfection.

3.4.3. Effect of Cytoplasmic Dynein Inhibitors on Intracellular Transport of P123-PEI-R13/DNA Complexes. The side of a microtubule close to the plasma membranes is the “+” end, while the side near microtubule organizing center of nuclear membranes is the “-” end. Microtubules are distributed in the cells in a radiative way toward the periphery. Studies have indicated that microtubules are related to intracellular transport of membrane vesicles and organelles, providing both a path for the transport of materials and a guiding role in its direction. The driving force for transport comes from two types of motor proteins. Materials in cells are driven by the dynein to move from “+” to “-” while kinesin has the opposite effect.

The complexes are transferred to the “-” end of intracellular canaliculus, namely, near-nucleus end, with the power source mainly from dynein. Therefore, this experiment chose sodium orthovanadate (SOV) to treat cells and study the influence of dynein on the transfection efficiency of P123-PEI-R13. From Figure 10, with the increase of the inhibitor concentration, the inhibitory effect gradually increased. The inhibition rate was approximately 90% when the sodium

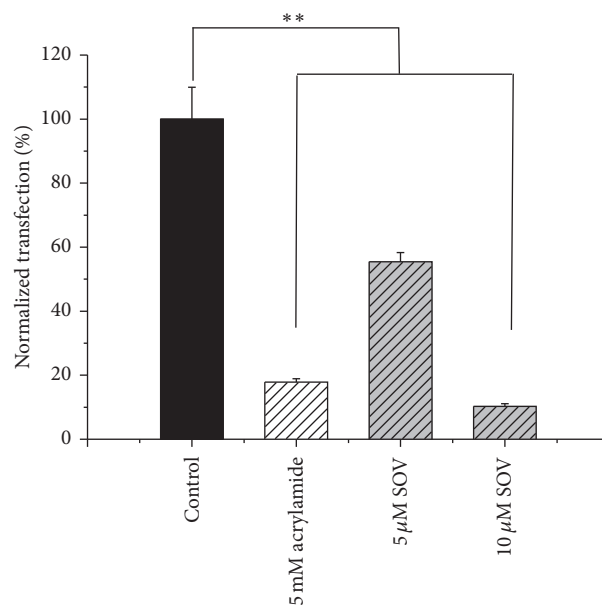


FIGURE 10: Effect of acrylamide and sodium orthovanadate (SOV) on transfection efficiency of P123-PEI-R13/DNA complexes in HeLa cells at w/w ratio of 30. Acrylamide was used as the inhibitors of intermediate filament (IF). SOV was used as the inhibitors of cytoplasmic dynein. The RLU/mg protein in control cells was set to 100%. Each data point represents the mean \pm standard deviation ($n = 3$, $**P < 0.01$).

orthovanadate (SOV) concentration was 10 μ M. According to the above results, dynein provides complexes with motivation to be transported toward the “-” end, namely, the cell nucleus within the cells. After the dynein was inhibited by sodium orthovanadate, its capability to carry the complexes was weakened, which significantly decreased the transfection efficiency.

4. Conclusion

In this paper, the binding affinity, cellular uptake, and subsequent intracellular trafficking of the nano-gene vector P123-PEI-R13 were investigated. The bifunctional peptide R13 had the ability of binding to $\alpha v \beta 3$ positive cells *in vitro*. The modification of P123-PEI-R13 with R13 made it display a new property of internalization. P123-PEI-R13/DNA complexes were mainly endocytosed by clathrin-mediated endocytosis, caveolin-mediated endocytosis, and macropinocytosis. These three kinds of classical endocytic pathways simultaneously contributed to efficient gene delivery, which was in accordance with other researchers [18, 19]. Macropinocytosis has attracted more attentions as a medicine and gene input pathway. There were reports that the endocytosis of TAT peptides and its cargo was achieved by macropinocytosis. It could be a more efficient endocytic pathway for the transfection process. In addition, there was a possible energy-independent route during the internalization for the modification of the cell-penetrating peptide TAT (49–57).

After internalization, P123-PEI-R13/DNA complexes could escape from the endosome-lysosome system because of the protonation caused by its acidification and further took microtubule as the track and dynein as the dynamic source to be transported toward the microtubule (-) end, to wit nucleus, under the action of microfilament, and with the aid of intermediate filament.

Competing Interests

The authors declare that they have no competing interests.

Acknowledgments

This work was supported by National Natural Science Foundation of China under Grants nos. 81001024 and 81572989; Scientific Research Innovation Project of the Shanghai Municipal Education Commission under Grant no. 13YZ097.

References

- [1] K. H. Liu, X. Y. Wang, W. Fan et al., "Degradable polyethyleneimine derivate coupled to a bifunctional peptide R13 as a new gene-delivery vector," *International Journal of Nanomedicine*, vol. 7, pp. 1149–1162, 2012.
- [2] C. Vaquette, S. Fawzi-Grancher, P. Lavalley et al., "In vitro biocompatibility of different polyester membranes," *Bio-Medical Materials and Engineering*, vol. 16, no. 4, pp. S131–S136, 2006.
- [3] S. D. Conner and S. L. Schmid, "Regulated portals of entry into the cell," *Nature*, vol. 422, no. 6927, pp. 37–44, 2003.
- [4] M. Torres and T. D. Coates, "Function of the cytoskeleton in human neutrophils and methods for evaluation," *Journal of Immunological Methods*, vol. 232, no. 1-2, pp. 89–109, 1999.
- [5] V. Rai, N. Dayan, and B. Michniak-Kohn, "A comparative evaluation of photo-toxic effect of fractionated melanin and chlorpromazine hydrochloride on human (dermal fibroblasts and epidermal keratinocytes) and mouse cell line/s (fibroblast Balb/c 3T3)," *Toxicology in Vitro*, vol. 25, no. 2, pp. 538–544, 2011.
- [6] A. I. Ivanov, "Pharmacological inhibition of endocytic pathways: is it specific enough to be useful?" *Methods in Molecular Biology*, vol. 440, pp. 15–33, 2008.
- [7] Z. Yu, Q. Xu, C. Dong et al., "Self-assembling peptide nanofibrous hydrogel as a versatile drug delivery platform," *Current Pharmaceutical Design*, vol. 21, no. 29, pp. 4342–4354, 2015.
- [8] R. Peltier, G. Chen, H. Lei et al., "The rational design of a peptide-based hydrogel responsive to H₂S," *Chemical Communications*, vol. 51, no. 97, pp. 17273–17276, 2015.
- [9] M. Walsh, M. Tangney, M. J. O'Neill et al., "Evaluation of cellular uptake and gene transfer efficiency of pegylated poly-L-lysine compacted DNA: implications for cancer gene therapy," *Molecular Pharmaceutics*, vol. 3, no. 6, pp. 644–653, 2006.
- [10] G. Misinzio, P. L. Delputte, and H. J. Nauwynck, "Inhibition of endosome-lysosome system acidification enhances porcine circovirus 2 infection of porcine epithelial cells," *Journal of Virology*, vol. 82, no. 3, pp. 1128–1135, 2008.
- [11] D. C. Lovelady, J. Friedman, S. Patel, D. A. Rabson, and C.-M. Lo, "Detecting effects of low levels of cytochalasin B in 3T3 fibroblast cultures by analysis of electrical noise obtained from cellular micromotion," *Biosensors and Bioelectronics*, vol. 24, no. 7, pp. 2250–2254, 2009.
- [12] Y. X. Chen, J. L. Li, Q. Q. Li et al., "Enhanced water-solubility, antibacterial activity and biocompatibility upon introducing sulfobetaine and quaternary ammonium to chitosan," *Carbohydrate Polymers*, vol. 143, pp. 246–253, 2016.
- [13] Y. Solak, H. Atalay, I. Polat, and Z. Biyik, "Colchicine treatment in autosomal dominant polycystic kidney disease: many points in common," *Medical Hypotheses*, vol. 74, no. 2, pp. 314–317, 2010.
- [14] J. S. Wadia, R. V. Stan, and S. F. Dowdy, "Transducible TAT-HA fusogenic peptide enhances escape of TAT-fusion proteins after lipid raft macropinocytosis," *Nature Medicine*, vol. 10, no. 3, pp. 310–315, 2004.
- [15] P. E. G. Thorén, D. Persson, P. Isakson, M. Goksör, A. Önfelt, and B. Nordén, "Uptake of analogs of penetratin, Tat(48–60) and oligoarginine in live cells," *Biochemical and Biophysical Research Communications*, vol. 307, no. 1, pp. 100–107, 2003.
- [16] Y.-X. Sun, W. Xiao, S.-X. Cheng, X.-Z. Zhang, and R.-X. Zhuo, "Synthesis of (Dex-HMDI)-g-PEIs as effective and low cytotoxic nonviral gene vectors," *Journal of Controlled Release*, vol. 128, no. 2, pp. 171–178, 2008.
- [17] M. Arrio-Dupont, G. Foucault, M. Vacher, P. F. Devaux, and S. Cribier, "Translational diffusion of globular proteins in the cytoplasm of cultured muscle cells," *Biophysical Journal*, vol. 78, no. 2, pp. 901–907, 2000.
- [18] L. Bromberg, V. Y. Alakhov, and T. A. Hatton, "Self-assembling Pluronic®-modified polycations in gene delivery," *Current Opinion in Colloid & Interface Science*, vol. 11, no. 4, pp. 217–223, 2006.
- [19] I. M. Kaplan, J. S. Wadia, and S. F. Dowdy, "Cationic TAT peptide transduction domain enters cells by macropinocytosis," *Journal of Controlled Release*, vol. 102, no. 1, pp. 247–253, 2005.

Review Article

Recent Progress on Nanostructures for Drug Delivery Applications

Haijiao Lu,^{1,2} Jinkang Wang,^{1,2} Ting Wang,^{1,2} Jian Zhong,³
Ying Bao,^{1,2} and Hongxun Hao^{1,2}

¹National Engineering Research Center of Industry Crystallization Technology, School of Chemical Engineering and Technology, Tianjin University, Tianjin 300072, China

²Collaborative Innovation Center of Chemical Science and Engineering, Tianjin 300072, China

³College of Food Science and Technology, Shanghai Ocean University, Shanghai 201306, China

Correspondence should be addressed to Hongxun Hao; hongxunhao@tju.edu.cn

Received 31 May 2016; Accepted 30 August 2016

Academic Editor: Christian Brosseau

Copyright © 2016 Haijiao Lu et al. This is an open access article distributed under the Creative Commons Attribution License, which permits unrestricted use, distribution, and reproduction in any medium, provided the original work is properly cited.

With the rapid development of nanotechnology, the convergence of nanostructures and drug delivery has become a research hotspot in recent years. Due to their unique and superior properties, various nanostructures, especially those fabricated from self-assembly, are able to significantly increase the solubility of poorly soluble drugs, reduce cytotoxicity toward normal tissues, and improve therapeutic efficacy. Nanostructures have been successfully applied in the delivery of diverse drugs, such as small molecules, peptides, proteins, and nucleic acids. In this paper, the driving forces for the self-assembly of nanostructures are introduced. The strategies of drug delivery by nanostructures are briefly discussed. Furthermore, the emphasis is put on a variety of nanostructures fabricated from various building materials, mainly liposomes, polymers, ceramics, metal, peptides, nucleic acids, and even drugs themselves.

1. Introduction

In the past few decades, nanostructures have attracted intensive research interest due to their unique and superior properties as compared with conventional bulk materials. They have been applied in a wide range of fields, such as materials, electronics, sensing, catalysis, environment, and drug delivery. In drug delivery systems, some of the challenges which need to be faced include bioavailability, *in vivo* stability, solubility, absorption, sustained and targeted delivery to site of action, therapeutic efficacy, side effects, and fluctuation of drug concentration in plasma [1]. To surmount these challenges, large quantities of studies have been carried out to explore the fabrication and application of various nanostructures in drug delivery.

Generally, nanostructures used in drug delivery are constructed via “bottom-up” approach, which is achieved by growing or assembling of building blocks [2]. It is noteworthy that a considerable proportion of nanostructures are obtained

via the self-assembly of building blocks. Based on the properties and structures of building blocks, various kinds of noncovalent interactions play significant roles in the self-assembly processes and contribute to the stability of resultant nanostructures.

In the delivery process, passive delivery of drugs as “cargoes” by nanocarriers is the most common strategy. The association between drugs and nanocarriers is achieved by either physical encapsulation or chemical conjugation. Meanwhile, self-delivery is another alternative which builds nanostructures with drug molecules themselves instead of drug molecules only being “cargoes” needed to be delivered.

The fabrication of well-defined nanostructures with distinct properties, especially through self-assembly process, has been an extremely active field in drug delivery. A large variety of nanostructures, including liposomes, polymeric, ceramic, metallic, peptides-based, nucleic acid-based, and drug-based nanostructures, have already emerged and found

their applications in the delivery of various drugs, including small molecules, peptides, proteins, and nucleic acids.

2. Driving Forces for Self-Assembly of Nanostructures

In drug delivery system, many nanostructures are formed by self-assembly, which is a force balance process in which well-defined structures or patterns are spontaneously formed from building blocks without human intervention [3]. The most important driving forces in self-assembly process are noncovalent interactions, including van der Waals interactions, hydrophobic effect, electrostatic interactions, hydrogen bonding, π - π stacking interactions, steric and depletion forces, coordination bonding, and solvation and hydration forces [3]. Compared with covalent bonds, noncovalent interactions are much weaker, which involve more dispersed variations of electromagnetic interactions between molecules or within a molecule [4]. However, noncovalent interactions possess the ability to significantly influence the detailed structures of self-assembled nanostructures, separately or synergistically.

2.1. Hydrophobic Effect. Among various noncovalent interactions in self-assembly process, hydrophobic effect is the most important. A wide range of building blocks for self-assembly are amphiphilic molecules, including many synthetic building blocks and biomolecules such as proteins and lipids. Due to the coexistence of polar and nonpolar regions, the self-assembly of amphiphilic molecules can be readily accomplished through microphase separation driven by thermodynamics. In aqueous solutions, the nonpolar regions of the building blocks will collapse and cluster together to expose the smallest possible hydrophobic area to water while the polar regions attempt to maximize their interaction with water [3]. Taking amphiphilic diblock copolymers as an example, when the concentration is higher than the critical micelle concentration (CMC), the hydrophobic block will assemble into a core, and the hydrophilic block stretches itself in water and thus forms a shell surrounding the hydrophobic core.

2.2. Electrostatic Interactions. Electrostatic interactions, which involve both attractive and repulsive forces between charged atoms, ions, or molecules, also have a strong effect on many self-assembly processes. Cationic polymers can interact with anionic proteins or genes through electrostatic interactions, forming stable nanoparticles in aqueous solutions [5]. For example, according to Xia et al. [6], water-soluble cationic conjugated polymer can bind to DNA by both electrostatic interactions and hydrophobic effect in the delivery of DNA. Upon reducing the strength of the hydrophobic effect, electrostatic attractions became the important interaction that regulated the binding between the water-soluble conjugated polymer and DNA.

2.3. Hydrogen Bond. Hydrogen bond is the electrostatic attraction between H atom and a highly electronegative atom nearby, such as N, O, or F. Hydrogen bond attractions can

occur both between molecules (intermolecular) and within different parts of a single molecule (intramolecular). It is very common both in inorganic molecules (e.g., water) and in organic molecules (e.g., DNA and proteins). For instance, hydrogen bond exists between the amides and carbonyls in the backbone of β -sheets formed by the self-assembly of peptides and enhances the stability of the self-assembled nanostructures [7].

2.4. π - π Staking. In addition, π - π staking can also play a role in maintaining the nanostructures from self-assembly. In the multiscale self-assembly of diphenylalanine (FF), the backbone hydrogen bonds and π - π interactions from the aromatic peptide side-chains hold the self-assembled FF structures together [8]. In alkaline solution, folic acid can self-assemble via the formation of Hoogsteen-bonded nanoscale tetrameric discs, which then stack through π - π interactions and interdisc hydrogen bonding to form chiral columns [9, 10]. However, due to the lack of hydrogen bond, methotrexate was unable to form any well-defined nanostructures with similar treatment [11].

In summary, noncovalent interactions play important roles in the formation of nanostructures, separately or synergistically. Good control of physical properties of nanostructures is highly important for their successful utilization in drug delivery. When designing nanostructures for drug delivery, noncovalent interactions should be taken into consideration and be rationally applied in the strategies.

3. Strategies of Drug Delivery by Nanostructures

3.1. Passive Delivery. In drug delivery by nanostructures, drugs are frequently associated with nanocarriers by either physical encapsulation or chemical conjugation [12] and thus passively delivered as “cargoes” by nanocarriers.

In the former method, drugs are physically incorporated into the internal cavity and stabilized by noncovalent interactions between drugs and nanocarriers, especially hydrophobic effect [13, 14]. Many nanostructures such as nanomicelles, nanocapsules, and porous nanoparticles have a net hydrophobicity to stabilize the entrapped drug molecules [15]. When the nanostructures are disassembled at target sites of action, drugs will be released as a consequence. However, physical encapsulation into hydrophobic compartments often results in very low drug loading contents (DLC), typically on the order of 2–5% by weight [16]. It is one of the crucial challenges posed by nanostructures on drug delivery.

The second method is to attach cargo drugs to the nanocarriers by direct chemical conjugation. In order to have a good control over the triggered release of drugs, the conjugation between nanocarriers and drugs should be cleavable at target sites. If drugs cannot be cleaved from their nanocarriers in time, their bioactivity and efficacy will be reduced. On the other hand, if drugs tend to be dissociated from their nanocarriers too quickly, they will fail to reach the target sites of action in a significant dose. This is so-called “burst release,” which will lead to rapid clearance of the drugs from the body

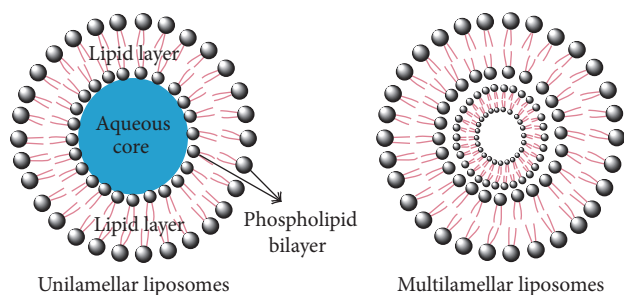


FIGURE 1: Schematic representation of basic structures and different types of liposomes [19]. Copyright © 2011, Mishra et al.

[13]. Therefore, rational design of the chemical conjugation between a drug and its nanocarrier is of great importance.

3.2. Self-Delivery. Apparently, the common strategies mentioned above merely consider drugs as active pharmaceutical compounds which need to be delivered. However, their properties, such as self-assembly ability and solubility, are ignored. In recent years, there is a growing trend to build well-defined nanostructures with drug molecules as building units. Through this strategy, the distribution and content of drugs in the nanostructures can be accurately controlled. Via rational analysis, design, and fabrication, lots of self-delivering nanostructures with high and fixed drug contents have been created. Detailed illustration and examples will be given in Section 4.8.

4. Various Nanostructures for Drug Delivery

In the past few decades, nanostructures with various shapes and sizes have been fabricated and applied for many drugs. In this section, various nanostructures fabricated by different materials and their applications in drug delivery are illustrated and discussed in detail.

4.1. Liposomes Nanostructures. Liposomes have been under extensive investigation and have become a common nanocarrier for drug delivery since 1965. Nanostructures fabricated with liposome are the first drug delivery system on the nanoscale to make the transition from concept to clinical application and have become a well-established technology platform with considerable clinical acceptance [17].

Liposomes are small artificial vesicles developed from phospholipids such as phosphatidylglycerol, phosphatidylserine, and phosphatidylcholine [18]. On the basis of lipid bilayers, liposomes can be classified into unilamellar vesicles (UVs) and multilamellar vesicles (MLVs), as shown in Figure 1. UVs consist of an aqueous core surrounded by a lipid bilayer, separating the inner aqueous core from the outside. As metastable energy configurations, MLVs are composed of various layers of lipid bilayers [19].

Due to the structures described above, liposomes have the ability to compartmentalize and solubilize both hydrophilic and hydrophobic materials by nature. This unique feature, along with biocompatibility and biodegradability, makes

liposomes attractive as drug delivery vehicles. Particularly, hydrophobic drugs can place themselves inside the bilayer of liposomes and hydrophilic drugs are entrapped within the aqueous core or at the bilayer interface [20].

Besides, liposomes have the functions to prevent drug degradation, reduce side effects, and target drugs to site of action [18, 21]. Hydrophobic drugs such as cyclosporin and paclitaxel are usually formulated in surfactants and organic cosolvents to increase their solubility in water. However, these solubilizers may cause toxicity at the doses needed to deliver the drug. In contrast, liposomes, which are nontoxic, biocompatible, and biodegradable, can deliver water-insoluble drugs with much less side effects. For example, they have been successfully applied in transdermal drug delivery to enhance skin permeation of drugs with high molecular weight and poor water solubility [22]. Besides, liposomes can accumulate at sites of increased vasculature permeability, when their average diameter is in the ultrafilterable range (<200 nm) [17].

However, the membrane of liposomes is generally thin, fragile, and thus inherently not stable [23]. Liposomes are also limited by their low encapsulation efficiency, rapid leakage of water-soluble drug in the presence of blood components, and poor storage stability [21, 24].

In the past five decades, many important technical breakthroughs, such as remote drug loading, extrusion for homogeneous size, long-circulating (PEGylated) liposomes (stealth liposomes), triggered release liposomes, liposomes containing nucleic acid polymers, ligand-targeted liposomes, and liposomes containing combinations of drugs, have led to numerous clinical trials in the delivery of diverse drugs, such as anticancer, antifungal, and antibiotic drugs, gene medicines, anesthetics, and anti-inflammatory drugs [17].

4.2. Polymeric Nanostructures. In the field of drug delivery, various polymeric nanostructures have been a hot topic of research for a long time. Generally speaking, polymer-based drug nanocarriers can significantly increase the solubility of hydrophobic drugs, reduce their cytotoxicity toward normal tissues, prolong the circulation time of drugs in blood, facilitate the entry of nanoparticles, and improve the utilization efficiency [25].

It is widely acknowledged that polymers used for drug delivery should be nontoxic and biocompatible. Natural polymers, such as chitosan [26], dextran [27], heparin [28], and hyaluronan [29], have been well investigated for drug delivery in the past few decades. However, research on using synthetic polymers to build various nanostructures is more prevalent in the field of drug delivery. Polyesters, polycarbonates, polyamides, polyphosphazenes, and polypeptides are among the most commonly used synthetic polymers [5].

4.2.1. Polymeric Nanomicelles and Nanovesicles. Owing to a great diversity of polymers, nanostructures of different sizes and morphologies have been obtained. As mentioned above, amphiphilic molecules are prone to self-assemble into various nanostructures driven by hydrophobic effect. Therefore, amphiphilic polymers containing both hydrophilic and hydrophobic blocks have been extensively studied for use in drug delivery. By controlling the hydrophilic/hydrophobic

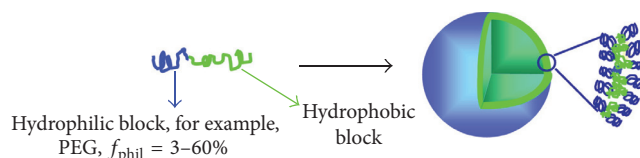


FIGURE 2: Polymeric vesicles derived from asymmetric block copolymers [23]. Copyright © 2009, American Chemical Society.

balance, various nanostructures, such as spherical micelles, cylindrical micelles, and vesicles, can be formed from amphiphilic polymers. According to Won et al. [30], the weight fraction of the hydrophilic block (f_{phil}) can play a vital role in controlling the shapes of nanostructures from amphiphilic polymers in a pure water medium. At $f_{\text{phil}} = 55\text{--}70\%$, spherical micelles are predominant; at $f_{\text{phil}} = 45\text{--}55\%$, spherical vesicles tend to form; at $f_{\text{phil}} = 20\text{--}40\%$, vesicles are favoured. Both polymeric micelles and vesicles are the most common and stable morphological structures of amphiphiles in water [23]. Polymeric micelles are nanostructures with a hydrophilic core and a hydrophilic shell (see Figure 2). Generally, hydrophilic drug molecules are encapsulated in the core of nanomicelles. Meanwhile, polymeric nanovesicles possess bilayer structures with an aqueous interior core, isolating the core from the external medium [31]. Polymeric vesicles can encapsulate hydrophilic molecules within the aqueous interior and also integrate hydrophobic molecules within the membrane. Therefore, polymeric vesicles have the capability to deliver hydrophilic as well as hydrophobic drugs such as anticancer drugs, genes, and proteins.

4.2.2. Polymeric Nanogels. However, polymeric nanomicelles and nanovesicles can only be maintained above the critical micelle concentration (CMC). Below CMC, they will dissociate into single polymer chains and thus lose the function as drug carriers. In order to avoid the dissociation of the self-assembled nanostructures, linking the polymers to obtain nanogels which are more stable in different conditions has become a common and effective approach. In recent years, nanogels have drawn increasing attention because of their high loading capacity and good stability [5].

4.2.3. Polymeric Nanocapsules. Hollow polymeric nanocapsules have also been developed by miniemulsion polymerization in the past few decades. Drugs are confined in the cavities of nanocapsules and surrounded by external polymer membranes [32]. Nanocapsules are able to improve the oral bioavailability of proteins and peptides, including insulin, elcatonin, and salmon calcitonin [32, 33]. Nanocapsules can protect the degradation of drugs, reduce systemic toxicity, provide controlled release, and mask unpleasant taste [34]. Nevertheless, due to high stability and low permeability of nanocapsules, drugs carried by nanocapsules have trouble both in encapsulation into the capsules after formulation and in the release at target site [18].

4.2.4. Polymeric Dendrimers. Apart from these nanostructures, dendrimers with three-dimensional, hyperbranched

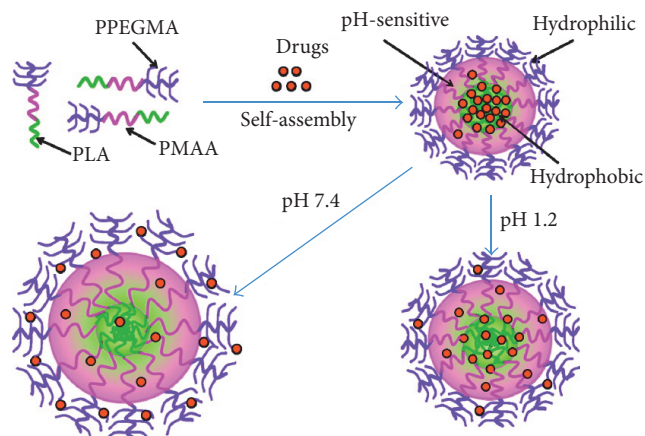


FIGURE 3: Schematic illustration of drug loading and pH-dependent release from PPEGMA-b-PMAA-b-PLA micelles [51]. Copyright © 2012, American Chemical Society.

globular nanopolymeric architectures have been the research focus of many scientists these years. Due to their attractive features like nanoscale size, narrow polydispersity index, excellent control over molecular structures, and availability of multiple functional groups at the periphery and cavities in the interior [35], dendrimers have been explored to be used in the delivery of different bioactive agents such as drugs [36], oligonucleotides [37], enzymes [38], vaccines [39], and genes [40]. Drugs can be either incorporated into the interior or attached on the surface. Due to their versatility, both hydrophilic and hydrophobic drugs can be associated with dendrimers [18].

4.2.5. Polymeric Stimulus-Sensitive Nanostructures. Particularly, recent research has focused on stimulus-sensitive (smart) nanostructures for drug delivery because it is a superior approach for delivering and releasing drugs to specific site at the desired time. Many kinds of stimuli, including chemical (e.g., redox, pH), physical (e.g., temperature, light), and biological (e.g., enzymes) ones, have been exploited in the design of smart drug delivery systems [5]. Figure 3 represents a drug delivery system based on pH-sensitive PPEGMA-b-PMAA-b-PLA micelles.

4.3. Ceramic Nanostructures. Ceramic nanostructures refer to the porous structures of nanoparticles, which are fabricated from biocompatible inorganic compounds, such as silica, calcium phosphate, alumina, and titania. In the biomedical field, ceramic nanostructures are considered to be excellent carriers for drugs, genes, and proteins.

4.3.1. Mesoporous Silica Nanostructures. Mesoporous silica nanoparticles (MSN) have been the most extensively studied ceramic nanoparticles for drug delivery in the last twenty years. MSN possesses a lot of favourable properties, including monodispersity, high specific surface area, tunable pore size and diameter, and versatile functionalization [41, 42]. A large variety of drugs have been successfully loaded in MSN or

covalently grafted at MSN, such as camptothecin [42], paclitaxel [43], doxorubicin [44], cysteine [45], telmisartan [46], and chlorambucil [47]. Generally speaking, MSN are often functionalized to achieve a better delivery of drugs. For example, mannose or galactose functionalized MSN have been reported to induce a higher cytotoxicity of cancer cells than unfunctionalized ones and target to cancer cells more efficiently [48, 49]. Folate, a targeting ligand, has been covalently attached to amino-functionalized silica nanoparticles loaded with a hydrophobic small molecule anticancer drug. Folate-functionalized nanoparticles turned out to be significantly cytotoxic to tumor cells, whereas normal cells were much less affected by the presence of these structures [50].

4.3.2. Calcium Phosphate Nanostructures. Calcium phosphate systems, including hydroxyapatite and tricalcium phosphates, are soluble under acidic conditions ($\text{pH} \leq 5$) during bone remodelling. After cellular uptake, calcium phosphate systems are soluble under the conditions of lysosomal degradation [52]. The variable stoichiometry, functionality, and dissolution properties make these ceramic nanoparticles suitable for drug delivery. Their chemical similarity to bone and thus biocompatibility as well as variable surface charge density contribute to their controlled release properties [53].

4.3.3. Alumina and Titania Ceramic Nanostructures. In addition, much progress has also been made in the development of alumina and titania ceramic nanoparticles for drug delivery. Water dispersible, highly stable, and fluorescent alumina nanoparticles have been capped with natural proteins [54]. Diverse spherical titania nanostructures, including mesoporous spheres, spherical flaky assemblies, and dendritic particles of variable diameter and monodispersity in size, have been demonstrated in recent years [55].

However, there are concerns on the application of non-biodegradable ceramic nanoparticles, such as hydroxyapatite, alumina, and titania, because they will accumulate in the body and cause harmful effects [56].

4.4. Metallic Nanostructures. Metallic nanostructures generally mean the spherical metallic nanoparticles, such as gold, silver, gadolinium, and iron oxide, which have also been studied for targeted drug delivery.

4.4.1. Gold and Silver Nanostructures. Gold nanoparticles have been frequently used in drug delivery due to their favourable optical and chemical properties, including tunable sizes in the range of 0.8 to 200 nm, easy surface modification with different functional groups, good biocompatibility, and visible light extinction behaviour [57]. They can be conjugated with polyethylenimine (PEI) to deliver genes [58] and be modified and conjugated with suitable proteins/peptides to target the cell nucleus [59]. Folate-functionalized Au or Ag nanoparticles have been demonstrated to be able to lower the unwanted toxicity of diminazene aceturate and improve its selectivity and therapeutic efficacy [60]. In many cases, gold nanoparticles are covalently bounded to polymers, greatly enhancing the stability of polymeric nanoparticles for drug

delivery [61]. The cytotoxicity of gold nanoparticles is quite low [62], and they have served as scaffolds for drug delivery. In contrast, silver nanoparticles are relatively not favoured for drug delivery due to their toxicity to eukaryotic cells.

4.4.2. Gadolinium Nanostructures. Due to the large neutron capture cross-section area and emission of photons with long flight ranges, gadolinium is a potential agent for neutron capture therapy of tumors [57]. Gadolinium has been studied for enhanced tumor targeted delivery by modification of the nanoparticles with folate. The recognition, internalization, and retention of gadolinium nanoparticles in tumor cells were enhanced, indicating a high potential of gadolinium nanoparticles in tumor-targeted delivery [63].

4.4.3. Superparamagnetic Oxide Nanostructures. Superparamagnetic oxide nanoparticles, such as magnetite (Fe_3O_4) and maghemite (Fe_2O_3), have been also proposed for target delivery by using magnetic force. Drug molecules are conjugated onto the surface modified magnetic nanoparticles, and then the organic/inorganic superparamagnetic nanohybrids are concentrated at a specific target site within the body by an external, high-gradient magnetic field [57, 64]. Efficient delivery of genes has been realized by the modification of the magnetic nanoparticles. They can be positively charged by polymers and thus bound to the negatively charged DNA by electrostatic attractions and also protect the DNA [65].

4.4.4. Two-Dimensional Transition Metal Dichalcogenides. Two-dimensional transition metal dichalcogenides (2D TMDCs) are planar crystals consisting of one or a limited number of TMDC unit cells. Single-layered TMDCs can be described by the formula MX_2 , where M is the transition metal from groups 4–10 of the periodic table and X is a chalcogen (S, Se, or Te) [66]. Various combinations of transition metals and chalcogens as well as their different arrangements in the 2D crystals can lead to a wide variety of favourable properties [67, 68], making these materials suitable for applications in drug delivery. For example, the drug loading capability of 2D MoS_2 systems has turned out to be even better than that of graphene oxide due to their surface adsorption effect caused by hydrophobic interactions [69, 70]. Their properties of photothermal and photosynthesis can also be combined with drug carrying property to deliver specific drugs [70, 71].

4.5. Peptides-Based Nanostructures. One of the most promising areas of research in drug delivery is the utilization of peptides as biodegradable, physiologically sensitive, inherently “tunable” and remarkably facile design platform for highly sophisticated drug delivery systems [13].

Peptides have many unique advantages for use in drug delivery: (1) biocompatibility and biodegradability make peptide-based nanostructures suitable for drug delivery [72]; (2) naturally occurring self-assembly motifs present in proteins such as α -helices, β -sheets, and coiled-coils can be used to drive the self-assembly process [73]; (3) peptides can form well-defined nanostructures of any size and shape [72];

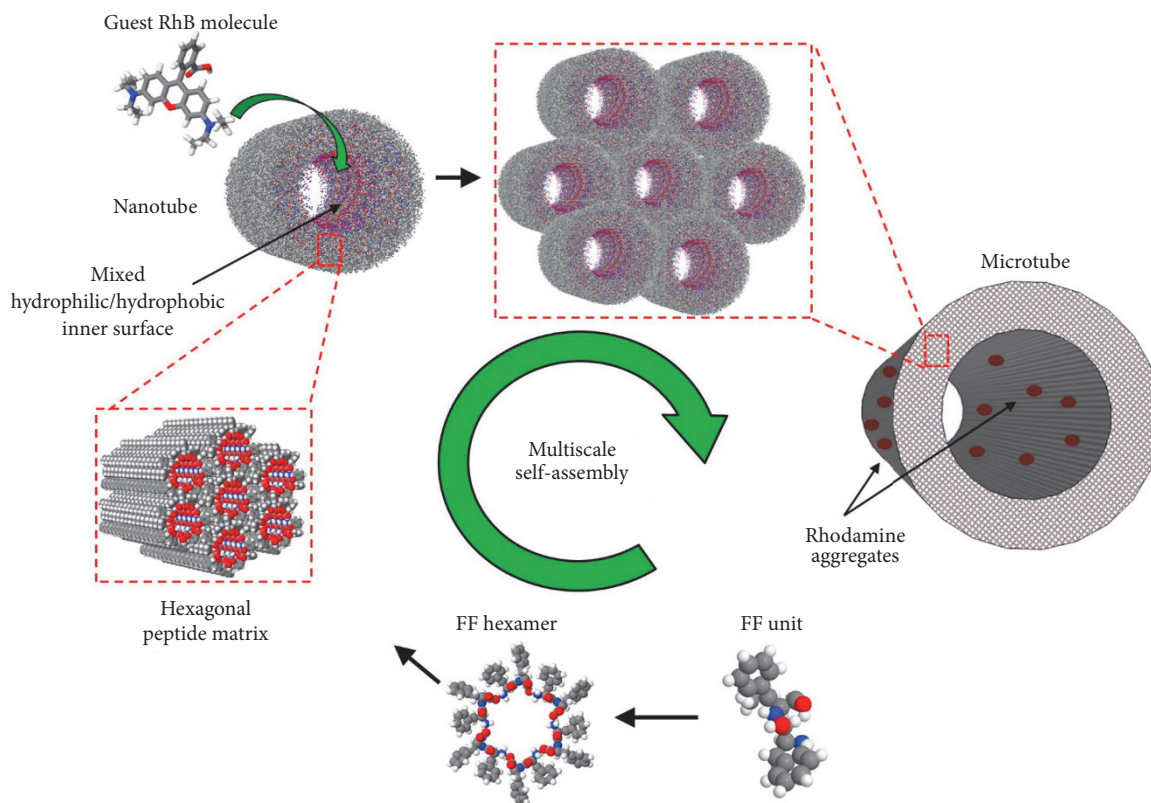


FIGURE 4: Schematic representation of the multiscale self-assembly of the FF-microtubes and their conjugation to rhodamine. Stacked FF hexamers form honeycomb-like arrays, which give rise to nanotubes. Subsequently, these nanotubes cluster into larger microtubes. The inner surfaces of the nanotubes exhibit both hydrophobic and hydrophilic groups, with the latter being able to trap polar species [8]. Copyright © 2013, American Chemical Society.

(4) additional peptide functionalization can easily be performed by introducing various compounds to the peptide structure [72]; (5) oligopeptides can be easily produced in large scale via standard solid-phase synthesis at a relatively low cost [13].

In recent years, a wide range of self-assembled peptides have been put forward for drug delivery, such as diphenylalanine (FF), various peptide amphiphiles (PA), and collagen mimetic self-assembled peptides [74]. For instance, on the basis of FF, a variety of functional nanostructures have been fabricated, such as nanotubes, spherical vesicles, nanofibrils, nanowires, ordered molecular chains, and hybrid nanoparticles [75]. As Figure 4 shows, FF peptide nanotubes have been utilized to load rhodamine (RhB) and have been found to have the ability to conjugate both hydrophobic and hydrophilic compounds due to their highly hydrophobic aromatic rings and hydrophilic peptide matrix [8]. Peptide amphiphiles are prone to self-assemble to form nanofibers, micelles and vesicles, nanotapes, nanotubes, and ribbons. The sizes, shapes, and morphologies of nanostructures can be altered simply by changing the structural elements of the peptide amphiphiles [76].

Since most chemotherapeutic drugs are hydrophobic, they suffer from poor water solubility. Besides, they are toxic to organisms to some extent [77, 78]. Conjugation of these drugs to hydrophilic peptides would create an amphiphilic

system necessary for self-assembly, reduce their side effects, and improve their efficiency via their incorporation into a drug delivering nanocarrier [13]. Peptide-based drug delivery systems are currently of wide scientific interest. Rational design of the peptide-based nanostructures can improve their drug loading capacities (DLC). For example, due to the high internal packing of hydrophobic segments, previous utilization of peptide amphiphiles as drug carriers was generally limited by low DLC (about 2–5%) [78]. However, by incorporating multiple short hydrophobic tails, the nanostructure's inner domain has been obviously enlarged and thus the loading efficiency has remarkably increased to 7% [79].

More and more novel nanostructures with various peptide motifs, stimuli-responsive function, and triggered drug delivery at disease sites are constantly emerging. The well-defined nanostructures produced by the self-assembly of peptides are highly promising for drug delivery.

4.6. Nucleic Acid-Based Nanostructures. As we all know, nucleic acid can be divided into two categories: DNA and RNA. In recent years, nucleic acid nanotechnology has progressed rapidly, especially DNA nanotechnology. A great variety of nucleic acid-based nanostructures with various dimensions, sizes, geometries, and shapes have been well investigated for drug delivery.

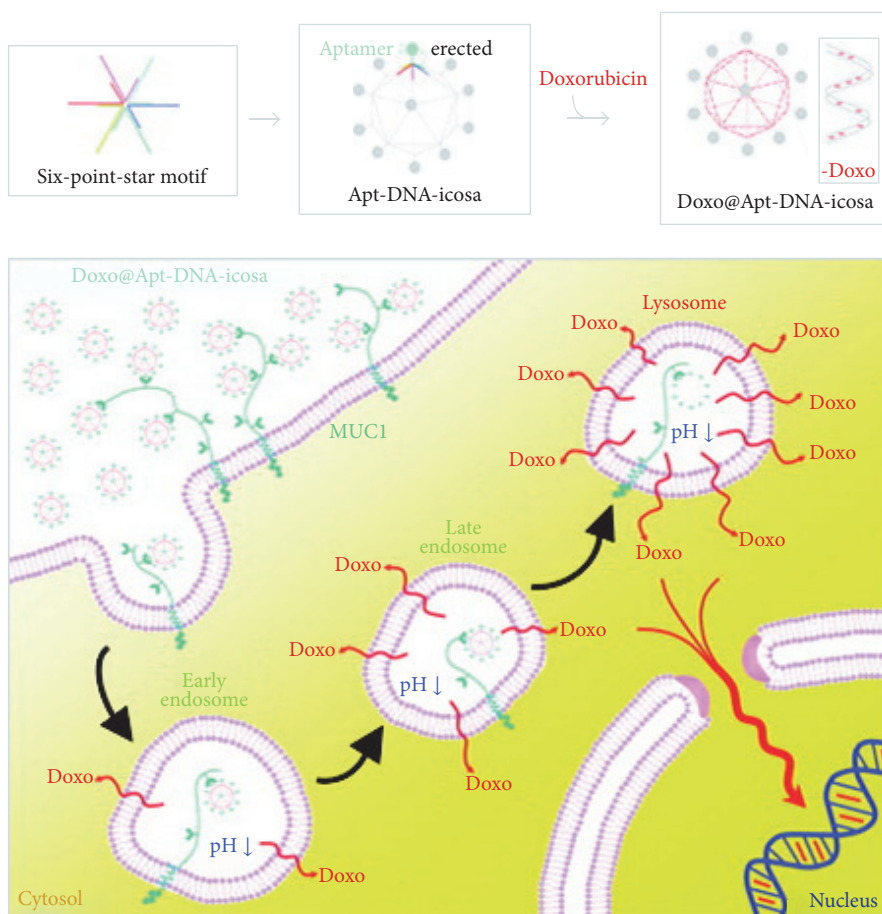


FIGURE 5: Schematic representation of aptamer-conjugated DNA icosahedral nanoparticles as a carrier of doxorubicin (DOX) [81]. Copyright © 2011, American Chemical Society.

4.6.1. DNA-Based Nanostructures. DNA-based nanostructures are quite appealing in drug delivery applications for many reasons: (1) they can be decorated with a multitude of functionalities and become multifunctional carriers; (2) they can be easily fabricated by self-assembly; (3) they are of low immunogenicity; (4) they have large flexibility of how drugs can be loaded into the DNA carrier; (5) they allow superb control over release [80].

Oligonucleotides have been successfully applied in the creation of many types of structures such as nanotubes, dendrimer-like DNA nanostructures, polypods, tetrahedra, icosahedra, and many other polyhedral structures [81]. For instance, Figure 5 gives a schematic representation of aptamer-conjugated DNA icosahedral nanoparticles as a carrier of doxorubicin (DOX) for cancer therapy.

In the last decade, an approach for constructing various DNA structures, named as DNA origami, has emerged [83]. It folds a long stranded bacteriophage through the use of more than 200 complementary staple strands to fold the backbone [84]. Various nanostructures, both 2D and 3D, such as smiley faces, tetrahedrons, DNA nanotubes, DNA barrels, and DNA “dolphins,” have been fabricated through DNA origami [83, 85–89]. As Figure 6 shows, DNA tube and DNA triangle

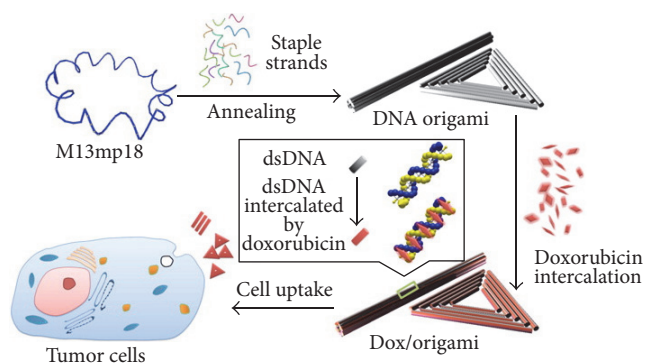


FIGURE 6: Schematic representation of DNA origami systems, DNA tube and DNA triangle, for doxorubicin (DOX) delivery [82]. Copyright © 2012, American Chemical Society.

obtained from DNA origami can be used for DOX delivery. DNA origami structures allow for either controlled or triggered release of drugs through either the intercalation of positively charged molecules or the linking of certain peptides or proteins onto the surface of the DNA origami [84].

Besides, DNA nanotubes, nanoballs, nanobelts, and nanoclews have also been produced by another innovative approach—rolling circle amplification, which creates long stranded structures with repeating DNA sequences through the use of a circular template and DNA polymerase [84]. They can be used as precise delivery vehicles for drugs and genes.

In addition, many other unique DNA nanostructures have also been put forward for drug delivery, such as DNA nanofilms [90] and hydrogels [91]. A DNA block copolymer system consisting of polypropylene oxide (PPO) and DNA has been utilized for the delivery of hydrophobic drugs [92]. The obtained hybrid particles were about 10 nm, with a hydrophobic PPO core to incorporate DOX and a DNA shell functionalized by folate to target cells.

However, there are some obstacles to be tackled in the applications of DNA-based nanostructures for drug delivery. For example, the expense of the starting materials is high and the *in vivo* pharmacokinetic bioavailability of the DNA-based structures needs to be improved [93].

4.6.2. RNA-Based Nanostructures. Due to the impression that RNA seems unstable, the potential of RNA in drug delivery has been overlooked for many years. However, with the development of RNA nanotechnology, RNA-based nanostructures, especially those based on phi29 pRNA, have been utilized in drug delivery in recent years.

According to Heoprich et al. [94], targeted hammerhead ribozymes delivery has been achieved by using ligand conjugated RNA nanoparticles based on phi29 pRNA. Besides, RNA nanoparticles can also deliver CpG DNA to macrophages specifically [95]. What is more, RNA origami nanostructures have also been reported [96]. With excellent thermodynamic stability and plasma stability after chemical modifications, RNA origami is expected to be more favourable than its counterpart DNA origami as a drug carrier for achieving controlled drug release [97].

4.7. Carbon Nanostructures. With the rapid development of carbon nanostructures, many attempts have been made to investigate their applications in drug delivery in the past twenty years. A variety of carbon nanostructures, including carbon nanotubes, graphene, and fullerenes, have been utilized. Graphene can be wrapped into spherical structures (zero-dimensional fullerenes), rolled into one-dimensional (1D) structures (carbon nanotubes, CNTs), or stacked into three-dimensional (3D) layered structures (graphite) [98]. Therefore, CNTs, graphene, and fullerenes are analogous but vary in wall number, diameter, length, and surface chemistry. Although they are all insoluble by nature, they can be modified into water-soluble species and realize drug delivery in organisms.

4.7.1. Graphene. Graphene is an atomic-scale honeycomb lattice made of carbon atoms. Due to the favourable properties, such as good biocompatibility, low cytotoxicity, and unique physicochemical properties in chemistry, electrics, optics, and mechanics, graphene has been explored as one of the most promising carbon nanostructures for drug delivery.

Compared with CNTs, graphene exhibits some important qualities such as low cost, facile fabrication and modification, and a higher drug loading ratio with two external surfaces [99]. Thus, graphene and its derivatives (e.g., graphene oxide) have been widely explored in the past decade for drug delivery applications.

4.7.2. Carbon Nanotubes. Carbon nanotubes (CNTs) have shown promise for the targeted delivery of drugs, proteins, and genes because of their favourable properties similar to graphene. More importantly, CNTs offer some interesting advantages over spherical nanoparticle. For instance, their large inner volume allows the loading of small drug molecules while their outer surface can be chemically modified to load proteins and genes for effective drug delivery. In recent years, both single-walled CNTs and multiwalled CNTs have been modified and turned out to be effective in the delivery of drugs, proteins, peptides, and nuclear acids [100–102].

4.7.3. Fullerenes. As nanomolecular carbon cages, fullerenes can also serve as drug vectors or drug delivery scaffolds with noncovalent linkages or with covalent linkages between the fullerene and a bioactive moiety [103]. After proper functionalization, such as attaching hydrophilic moieties, fullerenes have turned out to be able to work as drug carriers [57, 103].

4.8. Drug-Based Nanostructures. As mentioned above, drug molecules can also be used as building units to deliver themselves. Through rational design of the number and type of the drugs incorporated, the obtained nanostructures can exhibit various morphologies, such as nanospheres, rods, nanofibers, or nanotubes, to facilitate their delivery to particular sites [104].

4.8.1. Small Molecule Drugs. Some small molecule drugs have shown reversible self-assembly behaviour, which can be used to form supramolecular nanostructures of well-defined size and shape [104]. For example, nanofibers or lozenge-like platelets have been obtained by the self-assembly of folic acid in methanol/water mixtures [11]. As a result of the self-assembly of quinoline alkaloid camptothecin (CPT), 100–400 nm wide helical nanoribbon structures have been fabricated from the injection of an organic solution of CPT into water [105].

4.8.2. Hydrophobic Drugs. Hydrophobic drug molecules can be conjugated to hydrophilic polymers to form amphiphilic prodrugs which can spontaneously self-assemble into stable nanostructures. For example, cisplatin and PEG-P(Glu) can form coordination bonds by the coordination between Pt and P(Glu) carboxylate side-chains and then self-assemble into micelles (about 28 nm in diameter). In this way, a self-delivery system can be obtained and it can provide a sustained drug release [106]. With the evolution of self-delivering drugs, various supramolecular nanostructures have been formed from the self-assembly of amphiphilic prodrugs, such as one-dimensional filamentous structures, nanofilaments, nanospheres, and hydrogels [107].

5. Conclusions and Future Perspectives

Due to their unique and valuable properties, nanostructures have been more and more widely used in drug delivery these years. They have the advantages of increasing solubility of poorly soluble drugs, reducing side effects, improving efficacy of the existing drugs, and so on. What is more, owing to the great diversity of nanostructures, the range of choices of nanostructures for drug delivery system has been significantly broadened.

However, nanostructures for drug delivery are also faced with many challenges, such as scaling up, cost issue, and safety concerns. The fabrication method and process of many nanostructures are rather complicated compared with traditional drug delivery vehicles. Although nanostructures consume much less materials than bulk delivery materials, the whole expense of production is often uneconomic, which is another great obstacle. More importantly, only limited information about the influence of nanostructural properties on organisms is available at present. The utilization of nanostructures in drug delivery has aroused concerns all over the world.

To surmount all these problems and challenges, active research on nanostructures in drug delivery is underway. It is a common belief that future development will overcome current problems of nanostructures in the applications of drug delivery. Despite the fact that people are always reluctant to accept new technologies, numerous benefits brought about by nanotechnology will contribute to change the mind of the general public.

Competing Interests

The authors declare that they have no competing interests.

Acknowledgments

This work was financially supported by National Natural Science Foundation of China (no. 21376165) and Program of International S&T Cooperation from China Ministry of Science and Technology (no. 2013DFE43150).

References

- [1] N. A. Ochekepe, P. O. Olorunfemi, and N. C. Ngwuluka, "Nanotechnology and drug delivery—part 1: background and applications," *Tropical Journal of Pharmaceutical Research*, vol. 8, no. 3, pp. 265–274, 2009.
- [2] E. Gazit, "Self-assembled peptide nanostructures: the design of molecular building blocks and their technological utilization," *Chemical Society Reviews*, vol. 36, no. 8, pp. 1263–1269, 2007.
- [3] J.-H. Lee, Y. J. Choi, and Y.-B. Lim, "Self-assembled filamentous nanostructures for drug/gene delivery applications," *Expert Opinion on Drug Delivery*, vol. 7, no. 3, pp. 341–351, 2010.
- [4] E. V. Anslyn and D. A. Dougherty, *Modern Physical Organic Chemistry*, Palgrave Macmillan, Sausalito, Calif, USA, 2005.
- [5] Y. Li, G. H. Gao, and D. S. Lee, "Stimulus-sensitive polymeric nanoparticles and their applications as drug and gene carriers," *Advanced Healthcare Materials*, vol. 2, no. 3, pp. 388–417, 2013.
- [6] F. Xia, X. Zuo, R. Yang et al., "On the binding of cationic, water-soluble conjugated polymers to DNA: electrostatic and hydrophobic interactions," *Journal of the American Chemical Society*, vol. 132, no. 4, pp. 1252–1254, 2010.
- [7] R. V. Ulijn and A. M. Smith, "Designing peptide based nano-materials," *Chemical Society Reviews*, vol. 37, no. 4, pp. 664–675, 2008.
- [8] R. F. Silva, D. R. Araújo, E. R. Silva, R. A. Ando, and W. A. Alves, "L-Diphenylalanine microtubes as a potential drug-delivery system: characterization, release kinetics, and cytotoxicity," *Langmuir*, vol. 29, no. 32, pp. 10205–10212, 2013.
- [9] G. Gottarelli, E. Mezzina, G. P. Spada et al., "The self-recognition and self-assembly of folic acid salts in isotropic water solution," *Helvetica Chimica Acta*, vol. 79, no. 1, pp. 220–234, 1996.
- [10] Y. Kamikawa, M. Nishii, and T. Kato, "Self-assembly of folic acid derivatives: induction of supramolecular chirality by hierarchical chiral structures," *Chemistry—A European Journal*, vol. 10, no. 23, pp. 5942–5951, 2004.
- [11] L. L. Lock, M. Lacombe, K. Schwarz et al., "Self-assembly of natural and synthetic drug amphiphiles into discrete supramolecular nanostructures," *Faraday Discussions*, vol. 166, no. 5, pp. 285–301, 2013.
- [12] K. Y. Choi, G. Liu, S. Lee, and X. Y. Chen, "Theranostic nano-platforms for simultaneous cancer imaging and therapy: current approaches and future perspectives," *Nanoscale*, vol. 4, no. 2, pp. 330–342, 2012.
- [13] D. P. Keith and H. Cui, "Fabrication of drug delivery systems using self-assembled peptide nanostructures," in *Micro and Nanofabrication Using Self-Assembled Biological Nanostructures*, pp. 91–111, Elsevier, 2014.
- [14] M. Liu and J. M. J. Fréchet, "Designing dendrimers for drug delivery," *Pharmaceutical Science & Technology Today*, vol. 2, no. 10, pp. 393–401, 1999.
- [15] E. J. Chung, Y. Cheng, R. Morshed et al., "Fibrin-binding, peptide amphiphile micelles for targeting glioblastoma," *Biomaterials*, vol. 35, no. 4, pp. 1249–1256, 2014.
- [16] R. Lin, A. G. Cheetham, P. Zhang, Y.-A. Lin, and H. Cui, "Supramolecular filaments containing a fixed 41% paclitaxel loading," *Chemical Communications*, vol. 49, no. 43, pp. 4968–4970, 2013.
- [17] T. M. Allen and P. R. Cullis, "Liposomal drug delivery systems: from concept to clinical applications," *Advanced Drug Delivery Reviews*, vol. 65, no. 1, pp. 36–48, 2013.
- [18] N. A. Ochekepe, P. O. Olorunfemi, and N. C. Ngwuluka, "Nanotechnology and drug delivery part 2: nanostructures for drug delivery," *Tropical Journal of Pharmaceutical Research*, vol. 8, no. 3, pp. 275–284, 2009.
- [19] G. P. Mishra, M. Bagui, V. Tamboli, and A. K. Mitra, "Recent applications of liposomes in ophthalmic drug delivery," *Journal of Drug Delivery*, vol. 2011, Article ID 863734, 14 pages, 2011.
- [20] M. Çağdaş, A. D. Sezer, and S. Bucak, *Liposomes as Potential Drug Carrier Systems for Drug Delivery*, Application of Nanotechnology in Drug Delivery, InTech, 2014.
- [21] K. S. Soppimath, T. M. Aminabhavi, A. R. Kulkarni, and W. E. Rudzinski, "Biodegradable polymeric nanoparticles as drug delivery devices," *Journal of Controlled Release*, vol. 70, no. 1–2, pp. 1–20, 2001.
- [22] Y. Qiu, Y. Gao, K. Hu, and F. Li, "Enhancement of skin permeation of docetaxel: a novel approach combining microneedle and elastic liposomes," *Journal of Controlled Release*, vol. 129, no. 2, pp. 144–150, 2008.

- [23] F. H. Meng, Z. Y. Zhong, and F. J. Jan, "Stimuli-responsive polymeric vesicles for programmed drug delivery," *Biomacromolecules*, vol. 10, no. 2, pp. 197–209, 2009.
- [24] H. J. Lim, E. C. Cho, J. Shim, D.-H. Kim, E. J. An, and J. Kim, "Polymer-associated liposomes as a novel delivery system for cyclodextrin-bound drugs," *Journal of Colloid and Interface Science*, vol. 320, no. 2, pp. 460–468, 2008.
- [25] K. Habiba, D. P. Bracho-Rincon, J. A. Gonzalez-Feliciano et al., "Synergistic antibacterial activity of PEGylated silver-graphene quantum dots nanocomposites," *Applied Materials Today*, vol. 1, no. 2, pp. 80–87, 2015.
- [26] M. Garcia-Fuentes and M. J. Alonso, "Chitosan-based drug nanocarriers: where do we stand?" *Journal of Controlled Release*, vol. 161, no. 2, pp. 496–504, 2012.
- [27] G. Mocanu, M. Nichifor, and L. Sacarescu, "Dextran based polymeric micelles as carriers for delivery of hydrophobic drugs," *Current Drug Delivery*, vol. 13, no. 8, 2016.
- [28] S. E. Sakiyama-Elbert, "Drug delivery via heparin conjugates," *Comprehensive Biomaterials*, vol. 4, pp. 333–338, 2011.
- [29] J. Drobnik, "Hyaluronan in drug delivery," *Advanced Drug Delivery Reviews*, vol. 7, no. 2, pp. 295–308, 1991.
- [30] Y.-Y. Won, A. K. Brannan, H. T. Davis, and F. S. Bates, "Cryogenic transmission electron microscopy (cryo-TEM) of micelles and vesicles formed in water by poly(ethylene oxide)-based block copolymers," *Journal of Physical Chemistry B*, vol. 106, no. 13, pp. 3354–3364, 2002.
- [31] G. Battaglia and A. J. Ryan, "Bilayers and interdigitation in block copolymer vesicles," *Journal of the American Chemical Society*, vol. 127, no. 24, pp. 8757–8764, 2005.
- [32] F. Tiarks, K. Landfester, and M. Antonietti, "Preparation of polymeric nanocapsules by miniemulsion polymerization," *Langmuir*, vol. 17, no. 3, pp. 908–918, 2001.
- [33] C. Prego, D. Torres, E. Fernandez-Megia, R. Novoa-Carballal, E. Quiñoá, and M. J. Alonso, "Chitosan-PEG nanocapsules as new carriers for oral peptide delivery: effect of chitosan pegylation degree," *Journal of Controlled Release*, vol. 111, no. 3, pp. 299–308, 2006.
- [34] J. Whelan and J. Whelan, "Nanocapsules for controlled drug delivery," *Drug Discovery Today*, vol. 6, no. 23, pp. 1183–1184, 2001.
- [35] P. Kesharwani, K. Jain, and N. K. Jain, "Dendrimer as nanocarrier for drug delivery," *Progress in Polymer Science*, vol. 39, no. 2, pp. 268–307, 2014.
- [36] D. Bhadra, A. K. Yadav, S. Bhadra, and N. K. Jain, "Glycodendrimeric nanoparticulate carriers of primaquine phosphate for liver targeting," *International Journal of Pharmaceutics*, vol. 295, no. 1-2, pp. 221–233, 2005.
- [37] K. Kono, M. Liu, and J. M. J. Fréchet, "Design of dendritic macromolecules containing folate or methotrexate residues," *Bioconjugate Chemistry*, vol. 10, no. 6, pp. 1115–1121, 1999.
- [38] T. Dutta, H. B. Aghase, P. Vijayarajkumar, M. Joshi, and N. K. Jain, "Dendrosome-based gene delivery," *Journal of Experimental Nanoscience*, vol. 1, no. 2, pp. 235–248, 2006.
- [39] A. J. Khopade, F. Caruso, P. Tripathi, S. Nagaich, and N. K. Jain, "Effect of dendrimer on entrapment and release of bioactive from liposomes," *International Journal of Pharmaceutics*, vol. 232, no. 1-2, pp. 157–162, 2002.
- [40] S. P. Chaplot and I. D. Rupenthal, "Dendrimers for gene delivery—a potential approach for ocular therapy?" *Journal of Pharmacy and Pharmacology*, vol. 66, no. 4, pp. 542–556, 2014.
- [41] I. I. Slowing, J. L. Vivero-Escoto, B. G. Trewyn, and V. S.-Y. Lin, "Mesoporous silica nanoparticles: structural design and applications," *Journal of Materials Chemistry*, vol. 20, no. 37, pp. 7924–7937, 2010.
- [42] J. Lu, E. Choi, F. Tamanoi, and J. I. Zink, "Light-activated nanoimpeller-controlled drug release in cancer cells," *Small*, vol. 4, no. 4, pp. 421–426, 2008.
- [43] J. L. Vivero-Escoto, I. I. Slowing, C.-W. Wu, and V. S.-Y. Lin, "Photoinduced intracellular controlled release drug delivery in human cells by gold-capped mesoporous silica nanosphere," *Journal of the American Chemical Society*, vol. 131, no. 10, pp. 3462–3463, 2009.
- [44] J. E. Lee, N. Lee, H. Kim et al., "Uniform mesoporous dye-doped silica nanoparticles decorated with multiple magnetite nanocrystals for simultaneous enhanced magnetic resonance imaging, fluorescence imaging, and drug delivery," *Journal of the American Chemical Society*, vol. 132, no. 2, pp. 552–557, 2010.
- [45] R. Mortera, J. Vivero-Escoto, I. I. Slowing, E. Garrone, B. Onida, and V. S.-Y. Lin, "Cell-induced intracellular controlled release of membrane impermeable cysteine from a mesoporous silica nanoparticle-based drug delivery system," *Chemical Communications*, vol. 297, no. 22, pp. 3219–3221, 2009.
- [46] Y. Zhang, Z. Zhi, T. Jiang, J. Zhang, Z. Wang, and S. Wang, "Spherical mesoporous silica nanoparticles for loading and release of the poorly water-soluble drug telmisartan," *Journal of Controlled Release*, vol. 145, no. 3, pp. 257–263, 2010.
- [47] Q. Lin, Q. Huang, C. Li et al., "Anticancer drug release from a mesoporous silica based nanophotocage regulated by either a one- or two-photon process," *Journal of the American Chemical Society*, vol. 132, no. 31, pp. 10645–10647, 2010.
- [48] D. Brevet, M. Gary-Bobo, L. Raehm et al., "Mannose-targeted mesoporous silica nanoparticles for photodynamic therapy," *Chemical Communications*, no. 12, pp. 1475–1477, 2009.
- [49] M. Gary-Bobo, O. Hocine, D. Brevet et al., "Cancer therapy improvement with mesoporous silica nanoparticles combining targeting, drug delivery and PDT," *International Journal of Pharmaceutics*, vol. 423, no. 2, pp. 509–515, 2012.
- [50] L. F. D. Oliveira, K. Bouchmella, K. D. A. Gonçalves, J. Bettini, J. Kobarg, and M. B. Cardoso, "Functionalized silica nanoparticles as an alternative platform for targeted drug-delivery of water insoluble drugs," *Langmuir*, vol. 32, no. 13, pp. 3217–3225, 2016.
- [51] Y. Q. Yang, W. J. Lin, B. Zhao, X. F. Wen, X. D. Guo, and L. J. Zhang, "Synthesis and physicochemical characterization of amphiphilic triblock copolymer brush containing pH-sensitive linkage for oral drug delivery," *Langmuir*, vol. 28, no. 21, pp. 8251–8259, 2012.
- [52] V. Sokolova and M. Epple, "Bioceramic nanoparticles for tissue engineering and drug delivery," in *Tissue Engineering Using Ceramics and Polymers*, pp. 633–647, Elsevier, 2nd edition, 2014.
- [53] S. Bose, S. Tarafder, J. Edgington, and A. Bandyopadhyay, "Calcium phosphate ceramics in drug delivery," *Journal of the Minerals*, vol. 63, no. 4, pp. 93–98, 2011.
- [54] M. Sana, S. E. Ahmad, and A. Absar, "Nanoalumina bioleaching from bauxite ore by *Humicola* sp.," *Advanced Science*, vol. 8, no. 4, pp. 298–305, 2016.
- [55] D. Chen and R. A. Caruso, "Recent progress in the synthesis of spherical titania nanostructures and their applications," *Advanced Functional Materials*, vol. 23, no. 11, pp. 1356–1374, 2013.
- [56] C. Medina, M. J. Santos-Martinez, A. Radomski, O. I. Corrigan, and M. W. Radomski, "Nanoparticles: pharmacological and

- toxicological significance," *British Journal of Pharmacology*, vol. 150, no. 5, pp. 552–558, 2007.
- [57] Z. P. Xu, Q. H. Zeng, G. Q. Lu, and A. B. Yu, "Inorganic nanoparticles as carriers for efficient cellular delivery," *Chemical Engineering Science*, vol. 61, no. 3, pp. 1027–1040, 2006.
- [58] M. Thomas and A. M. Klibanov, "Conjugation to gold nanoparticles enhances polyethylenimine's transfer of plasmid dna into mammalian cells," *Proceedings of the National Academy of Sciences of the United States of America*, vol. 100, no. 16, pp. 9138–9143, 2003.
- [59] A. G. Tkachenko, H. Xie, Y. Liu et al., "Cellular trajectories of peptide-modified gold particle complexes: comparison of nuclear localization signals and peptide transduction domains," *Bioconjugate Chemistry*, vol. 15, no. 3, pp. 482–490, 2004.
- [60] O. S. Adeyemi and F. A. Sulaiman, "Evaluation of metal nanoparticles for drug delivery systems," *The Journal of Biomedical Research*, vol. 29, no. 2, pp. 145–149, 2015.
- [61] S. Aryal, S. Pilla, and S. Gong, "Multifunctional nano-micelles formed by amphiphilic gold-polycaprolactone-methoxy poly(ethylene glycol) (Au-PCL-MPEG) nanoparticles for potential drug delivery applications," *Journal of Nanoscience and Nanotechnology*, vol. 9, no. 10, pp. 5701–5708, 2009.
- [62] D. Bechet, P. Couleaud, C. Frochot, M.-L. Viriot, F. Guillemin, and M. Barberi-Heyob, "Nanoparticles as vehicles for delivery of photodynamic therapy agents," *Trends in Biotechnology*, vol. 26, no. 11, pp. 612–621, 2008.
- [63] M. O. Oyewumi and R. J. Mumper, "Engineering tumor-targeted gadolinium hexanedione nanoparticles for potential application in neutron capture therapy," *Bioconjugate Chemistry*, vol. 13, no. 6, pp. 1328–1335, 2002.
- [64] Q. A. Pankhurst, J. Connolly, S. K. Jones, and J. Dobson, "Applications of magnetic nanoparticles in biomedicine," *Journal of Physics D: Applied Physics*, vol. 36, no. 13, pp. R167–R181, 2003.
- [65] J.-J. Xiang, J.-Q. Tang, S.-G. Zhu et al., "IONP-PLL: a novel non-viral vector for efficient gene delivery," *Journal of Gene Medicine*, vol. 5, no. 9, pp. 803–817, 2003.
- [66] K. Kalantar-Zadeh, J. Z. Ou, T. Daeneke, M. S. Strano, M. Pumera, and S. L. Gras, "Two-dimensional transition metal dichalcogenides in biosystems," *Advanced Functional Materials*, vol. 25, no. 32, pp. 5086–5099, 2015.
- [67] M. Chhowalla, H. S. Shin, G. Eda, L.-J. Li, K. P. Loh, and H. Zhang, "The chemistry of two-dimensional layered transition metal dichalcogenide nanosheets," *Nature Chemistry*, vol. 5, no. 4, pp. 263–275, 2013.
- [68] S. Z. Butler, S. M. Hollen, L. Cao et al., "Progress, challenges, and opportunities in two-dimensional materials beyond graphene," *ACS Nano*, vol. 7, no. 4, pp. 2898–2926, 2013.
- [69] B. Tian, C. Wang, S. Zhang, L. Feng, and Z. Liu, "Photothermally enhanced photodynamic therapy delivered by nanographene oxide," *ACS Nano*, vol. 5, no. 9, pp. 7000–7009, 2011.
- [70] T. Liu, C. Wang, X. Gu et al., "Drug delivery with PEGylated MoS₂ nano-sheets for combined photothermal and chemotherapy of cancer," *Advanced Materials*, vol. 26, no. 21, pp. 3433–3440, 2014.
- [71] Y. Yong, L. Zhou, Z. Gu et al., "WS₂ nanosheet as a new photosensitizer carrier for combined photodynamic and photothermal therapy of cancer cells," *Nanoscale*, vol. 6, no. 17, pp. 10394–10403, 2014.
- [72] J. Castillo-León, K. B. Andersen, and W. E. Svendsen, *Self-Assembled Peptide Nanostructures for Biomedical Applications: Advantages and Challenges*, Biomaterials Science and Engineering, InTech, Shanghai, China, 2011.
- [73] J. B. Matson, R. H. Zha, and S. I. Stupp, "Peptide self-assembly for crafting functional biological materials," *Current Opinion in Solid State & Materials Science*, vol. 15, no. 6, pp. 225–235, 2011.
- [74] T. Jiang, C. F. Xu, Y. Liu et al., "Structurally defined nanoscale sheets from self-assembly of collagen-mimetic peptides," *Journal of the American Chemical Society*, vol. 136, no. 11, pp. 4300–4308, 2014.
- [75] X. Yan, P. Zhu, and J. Li, "Self-assembly and application of diphenylalanine-based nanostructures," *Chemical Society Reviews*, vol. 39, no. 6, pp. 1877–1890, 2010.
- [76] N. Habibi, N. Kamaly, A. Memic, and H. Shafiee, "Self-assembled peptide-based nanostructures: smart nanomaterials toward targeted drug delivery," *Nano Today*, vol. 11, no. 1, pp. 41–60, 2016.
- [77] S. E. McNeil, "Nanoparticle therapeutics: a personal perspective," *Wiley Interdisciplinary Reviews Nanomedicine & Nanobiotechnology*, vol. 1, no. 1, pp. 264–271, 2009.
- [78] S. Soukasene, D. J. Toft, T. J. Moyer et al., "Antitumor activity of peptide amphiphile nanofiber-encapsulated camptothecin," *ACS Nano*, vol. 5, no. 11, pp. 9113–9121, 2011.
- [79] P. Zhang, A. G. Cheetham, Y.-A. Lin, and H. Cui, "Self-assembled tat nanofibers as effective drug carrier and transporter," *ACS Nano*, vol. 7, no. 7, pp. 5965–5977, 2013.
- [80] J. W. D. Vries, F. Zhang, and A. Herrmann, "Drug delivery systems based on nucleic acid nanostructures," *Journal of Controlled Release*, vol. 172, no. 2, pp. 467–483, 2013.
- [81] M. Chang, C.-S. Yang, and D.-M. Huang, "Aptamer-conjugated DNA icosahedral nanoparticles as a carrier of doxorubicin for cancer therapy," *ACS Nano*, vol. 5, no. 8, pp. 6156–6163, 2011.
- [82] Q. Jiang, C. Song, J. Nangreave et al., "DNA origami as a carrier for circumvention of drug resistance," *Journal of the American Chemical Society*, vol. 134, no. 32, pp. 13396–13403, 2012.
- [83] A. R. Chandrasekaran and R. Zhuo, "A 'tile' tale: hierarchical self-assembly of DNA lattices," *Applied Materials Today*, vol. 2, pp. 7–16, 2016.
- [84] C. Angell, S. Xie, L. F. Zhang, and Y. Chen, "DNA nanotechnology for precise control over drug delivery and gene therapy," *Small*, vol. 12, no. 9, pp. 1117–1132, 2016.
- [85] D. M. Smith, V. Schüller, C. Forthmann, R. Schreiber, P. Tinnefeld, and T. Liedl, "A structurally variable hinged tetrahedron framework from DNA origami," *Journal of Nucleic Acids*, vol. 2011, Article ID 360954, 9 pages, 2011.
- [86] Y.-X. Zhao, A. Shaw, X. Zeng, E. Benson, A. M. Nyström, and B. Högberg, "DNA origami delivery system for cancer therapy with tunable release properties," *ACS Nano*, vol. 6, no. 10, pp. 8684–8691, 2012.
- [87] E. S. Andersen, M. Dong, M. M. Nielsen et al., "DNA origami design of dolphin-shaped structures with flexible tails," *ACS Nano*, vol. 2, no. 6, pp. 1213–1218, 2008.
- [88] P. W. K. Rothemund, "Folding DNA to create nanoscale shapes and patterns," *Nature*, vol. 440, no. 7082, pp. 297–302, 2006.
- [89] Q. Zhang, Q. Jiang, N. Li et al., "DNA origami as an in vivo drug delivery vehicle for cancer therapy," *ACS Nano*, vol. 8, no. 7, pp. 6633–6643, 2014.
- [90] Y. Cho, J. B. Lee, and J. Hong, "Controlled release of an anti-cancer drug from DNA structured nano-films," *Scientific Reports*, vol. 4, article 4078, 2014.
- [91] J. Li, C. Zheng, S. Cansiz et al., "Self-assembly of DNA nanohydrogels with controllable size and stimuli-responsive property for targeted gene regulation therapy," *Journal of the American Chemical Society*, vol. 137, no. 4, pp. 1412–1415, 2015.

- [92] F. E. Alemdaroglu, N. C. Alemdaroglu, P. Langguth, and A. Herrmann, "DNA block copolymer micelles—a combinatorial tool for cancer nanotechnology," *Advanced Materials*, vol. 20, no. 5, pp. 899–902, 2008.
- [93] V. Linko, A. Ora, and M. A. Kostianen, "DNA nanostructures as smart drug-delivery vehicles and molecular devices," *Trends in Biotechnology*, vol. 33, no. 10, pp. 586–594, 2015.
- [94] S. Heoprich, Q. Zhou, S. Guo et al., "Bacterial virus phi29 pRNA as a hammerhead ribozyme escort to destroy hepatitis B virus," *Gene Therapy*, vol. 10, no. 15, pp. 1258–1267, 2003.
- [95] E. F. Khisamutdinov, H. Li, D. L. Jasinski, J. Chen, J. Fu, and P. Guo, "Enhancing immunomodulation on innate immunity by shape transition among RNA triangle, square and pentagon nanovehicles," *Nucleic Acids Research*, vol. 42, no. 15, pp. 9996–10004, 2014.
- [96] C. Geary, P. W. K. Rothmund, and E. S. Andersen, "A single-stranded architecture for cotranscriptional folding of RNA nanostructures," *Science*, vol. 345, no. 6198, pp. 799–804, 2014.
- [97] H. Li, T. Lee, T. Dziubla et al., "RNA as a stable polymer to build controllable and defined nanostructures for material and biomedical applications," *Nano Today*, vol. 10, no. 5, pp. 631–655, 2015.
- [98] A. K. Geim and K. S. Novoselov, "The rise of graphene," *Nature Materials*, vol. 6, no. 3, pp. 183–191, 2007.
- [99] J. Liu, L. Cui, and D. Losic, "Graphene and graphene oxide as new nanocarriers for drug delivery applications," *Acta Biomaterialia*, vol. 9, no. 12, pp. 9243–9257, 2013.
- [100] D. Pantarotto, J.-P. Briand, M. Prato, and A. Bianco, "Translocation of bioactive peptides across cell membranes by carbon nanotubes," *Chemical Communications*, vol. 10, no. 1, pp. 16–17, 2004.
- [101] D. Pantarotto, R. Singh, D. McCarthy et al., "Functionalized carbon nanotubes for plasmid DNA gene delivery," *Angewandte Chemie-International Edition*, vol. 43, no. 39, pp. 5242–5246, 2004.
- [102] X. Zheng, T. Wang, H. Jiang et al., "Incorporation of Carvedilol into PAMAM-functionalized MWNTs as a sustained drug delivery system for enhanced dissolution and drug-loading capacity," *Asian Journal of Pharmaceutical Sciences*, vol. 8, no. 5, pp. 278–286, 2013.
- [103] R. D. Bolskar, "Fullerenes for drug delivery," in *Encyclopedia of Nanotechnology*, pp. 898–911, Springer, Amsterdam, The Netherlands, 2012.
- [104] W. Ma, A. G. Cheetham, and H. Cui, "Building nanostructures with drugs," *Nano Today*, vol. 11, no. 1, pp. 13–30, 2016.
- [105] M. Ma, P. Xing, S. Xu, S. Li, X. Chu, and A. Hao, "Reversible pH-responsive helical nanoribbons formed using camptothecin," *RSC Advances*, vol. 4, no. 80, pp. 42372–42375, 2014.
- [106] N. Nishiyama, S. Okazaki, H. Cabral et al., "Novel cisplatin-incorporated polymeric micelles can eradicate solid tumors in mice," *Cancer Research*, vol. 63, no. 24, pp. 8977–8983, 2003.
- [107] H. M. Wang, C. H. Yang, L. Wang, D. Kong, Y. Zhang, and Z. Yang, "Self-assembled nanospheres as a novel delivery system for taxol: a molecular hydrogel with nanosphere morphology," *Chemical Communications*, vol. 47, no. 15, pp. 4439–4441, 2011.

Research Article

Nanostructured Surface with Tunable Contact Angle Hysteresis for Constructing *In Vitro* Tumor Model

Kang Sun,^{1,2} Mingliang Yang,¹ Yue Xu,¹ Lelun Jiang,^{1,2} Rong Song,^{1,2}
Yang Liu,^{1,2} Qing Jiang,^{1,2} and Chao Zhang^{1,2}

¹School of Engineering, Sun Yat-Sen University, Guangzhou 510006, China

²Guangdong Provincial Key Laboratory of Sensor Technology and Biomedical Instruments, Sun Yat-Sen University, Guangzhou, Guangdong 510006, China

Correspondence should be addressed to Chao Zhang; zhchao9@mail.sysu.edu.cn

Received 13 May 2016; Accepted 26 May 2016

Academic Editor: Liqian Gao

Copyright © 2016 Kang Sun et al. This is an open access article distributed under the Creative Commons Attribution License, which permits unrestricted use, distribution, and reproduction in any medium, provided the original work is properly cited.

Contact angle hysteresis (CAH) is an important phenomenon in surface chemistry. In this paper, we fabricated nanostructured substrates and investigated the relationship between roughness and CAH. We demonstrated that by patterning well-tuned CAH in superhydrophobic background, we can pattern droplets with controlled sizes. We further showed that our system could be used in fabricating complex hydrogel architecture, allowing coculture of different types of cells in three-dimensional way. This CAH-based patterning strategy would provide *in vitro* models for tissue engineering and drug delivery.

1. Introduction

Contact angle hysteresis (CAH), defined as the difference between advancing and receding contact angles, has continuously been one of important topics in surface chemistry. Enormous theoretical and experimental efforts have been devoted to how CAH correlates to topographical or chemical surface heterogeneities [1, 2]. Topological heterogeneities, for example, nanoscale roughness, have shown to largely affect surface CAH. Many studies have been devoted to mechanisms underlying CAH [3]. However, the applications of CAH are yet to be explored. In nature, CAH is crucial during feeding of water by shore birds, as it can overcome the gravity on the water droplet in the beak of birds [4]. Thus, the exploration of CAH could be beneficial in controlling the liquid behavior on surface.

Herein, we propose a CAH-based strategy to control the size of droplets in patterns and further constructed complex hydrogel architecture for three-dimensional (3D) cell coculture. Patterning droplets have been an important issue in many fields, such as biochips, microlens, and digital microfluidics [5–7]. Among various techniques developed for droplet patterning, wettability contrast-based method is

widely employed. In this case, a hydrophilic/hydrophobic (or superhydrophilic/superhydrophobic) patterned substrate is fabricated. During dip-coating, hydrophilic area can capture liquid droplets [8, 9]. In our study, we show that CAH can be utilized for patterning droplets. By tailoring the CAH, we fabricated patterned droplets with various sizes. We further fabricated hydrogel droplets with complex architecture. We constructed an *in vitro* tumor model using cell-encapsulated prehydrogel solutions. We believe that the tumor model could find potential applications in mimicking tissue *in vivo* and could serve as an *in vitro* model for drug delivery.

2. Materials and Methods

2.1. Preparing CAH-Varied Surface. Silicon wafer was cut and cleaned in ethanol and acetone solution and boiled in H₂SO₄/H₂O₂ solution (3:1, v/v. *Caution! The harmful solution should be treated carefully!*). The substrates were dried under nitrogen gun and etched in five different etching solutions in AgNO₃ and HF solution [10]. The original etching solution was prepared by dissolving 0.15 g AgNO₃ in 15 mL HF and 55 mL deionized water mixed solution and further diluted in different ratios (i.e., 0-, 0.2-, 0.4-, 0.6-, 0.8-, and

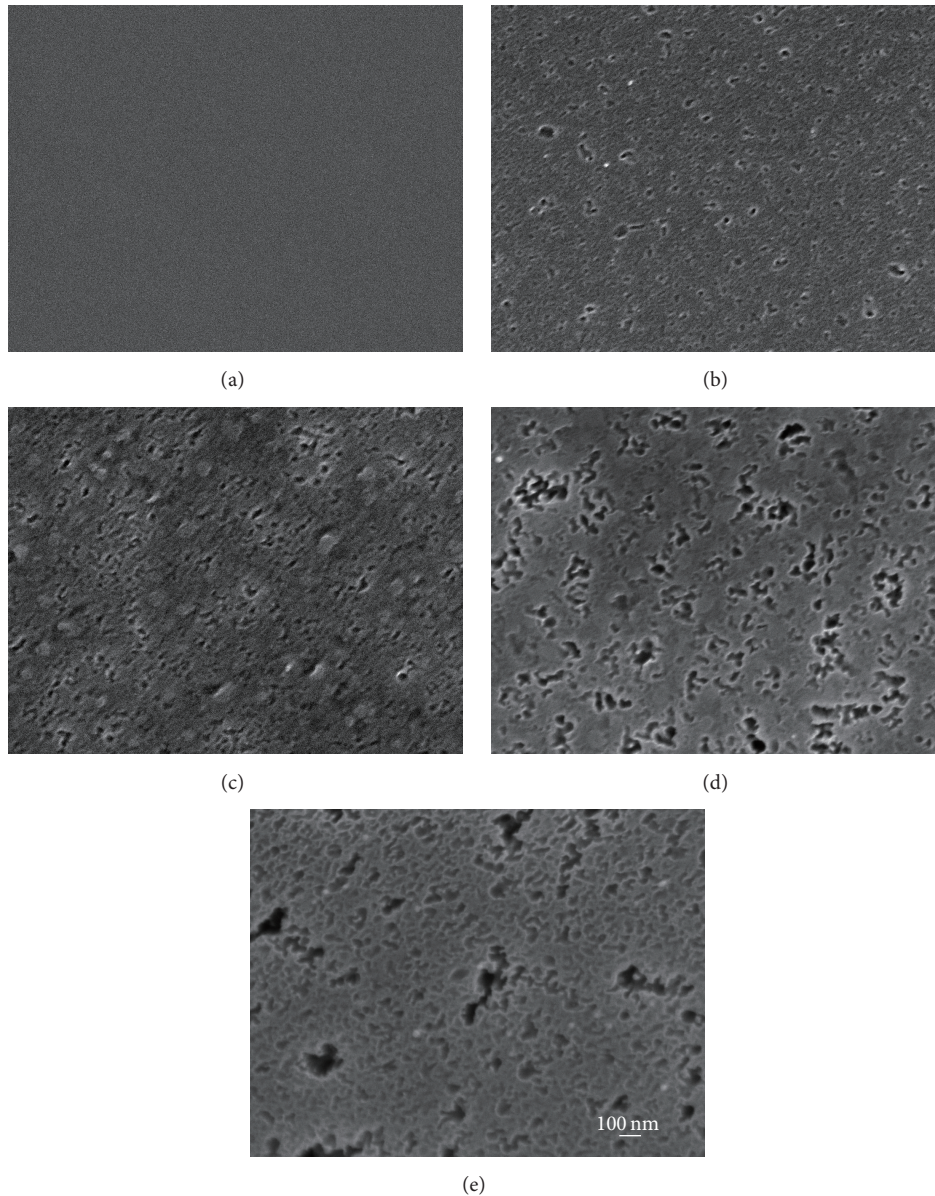


FIGURE 1: Scanning electron microscopy images of silicon substrates with increasing nanoscale roughness by various etching solutions.

1-fold). The substrates were immersed in various etching solutions for 20 s. HNO_3 solution (30%, v/v) was employed to dissolve the silver. Finally, silicon substrates were dried in oven.

2.2. Fabrication of CAH-Variied Substrates with Superhydrophobic Background. Silicon substrates with various roughness were achieved using the methods above. The substrates were patterned using photolithography and further etched (photoresist-patterned regions were protected from etching) in the original etching solution. By modifying substrates using octadecyltrichlorosilane (OTS), the background of substrate was rendered superhydrophobic. Finally, the substrates were rinsed in acetone to remove the patterned photoresist.

2.3. Fabrication of In Vitro Tumor Model. Hela cancer cells and NIH 3T3 fibroblasts were suspended in alginate solution

(1 wt% in PBS). To visualize the cells in the model, Hela cells were prestained in green and NIH 3T3 cells in red. The substrates were immersed firstly in Hela cell solution for 30 s and pulled out. The cell-encapsulated droplets captured in substrates were gelled by calcium chloride solution (5 wt%). Subsequently, the substrates were immersed in NIH 3T3 cell solution for 30 s and pulled out. Also the solution on substrates was gelled by calcium chloride solution.

3. Results and Discussions

3.1. Characterization of Surface Morphology and Calculation of CAH. We modified the surface CAH by varying surface roughness. We observed the morphologies using scanning electron microscopy (SEM). From Figure 1, we obtained that the roughness of silicon increases with the increase of the

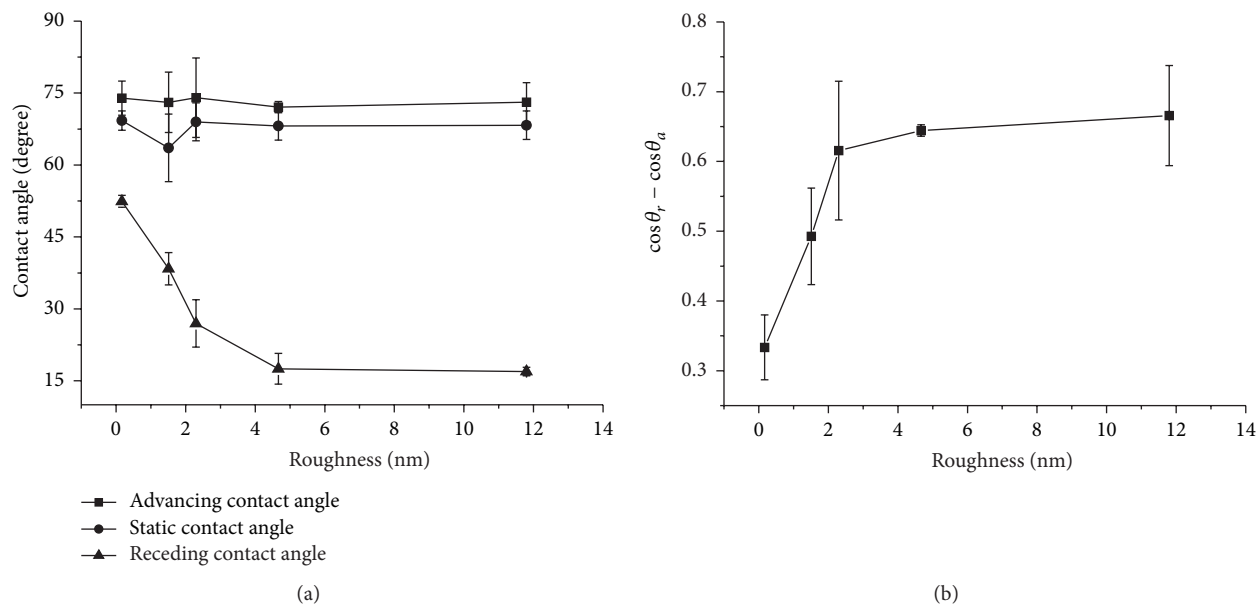


FIGURE 2: (a) Static contact angles, advancing contact angles, and receding contact angles measured on substrates with different roughness. (b) The calculated cosine values of contact angle hysteresis increased with the increase of surface roughness.

reaction concentration. We obtained the root-mean-square roughness 0.20, 1.30, 2.03, 3.87, 6.23, and 9.40 nm for solutions between 0-, 0.2-, 0.4-, 0.6-, 0.8-, and 1-fold of original solution. The high concentration of etching solutions provided more deposited Ag^+ ions as etching sites compared to low ones, resulting in a rougher surface. We calculated the CAH of different substrates after etching. For static contact angle and advancing contact angle (θ_a) of substrates, the values did not vary much in response to different roughness. However, receding contact angles (θ_r) decreased with the increase of roughness. As a result, the calculated CAH increased in response to surface roughness. The decreasing receding contact angle is implied from theoretical predictions. In their theory, receding contact angle is more sensitive to the proportion of surface defects [11]. We also calculated the difference between the cosine of values of advancing and receding contact angle $\cos(\theta_r) - \cos(\theta_a)$ and obtained that $\cos(\theta_r) - \cos(\theta_a)$ was positively related to surface roughness (Figure 2).

3.2. Controlling Liquid Size. The tunable CAH can be utilized to control liquid size on substrate. We fabricated substrates with CAH-controlled patterns in superhydrophobic background (Figure 3(a)) and examined the size of water droplets that were captured in patterns. We obtained patterned water droplets by dip-coating. We immersed the substrates in deionized water and pulled them out vertically at a speed of about 1 mm/s. For convenience, we measured the projected area of droplets just after pulling out substrates. For substrates with CAH ($\cos(\theta_r) - \cos(\theta_a)$) smaller than 0.4, sizes of droplets were close to zero. Some of the patterns contained no droplets after dip-coating (for droplets smaller than 0.02 mm^2 , some evaporated quickly before imaging). For CAH larger than 0.4, larger droplets were obtained in

the patterns. In previous studies, for patterning water, high wettability contrast between patterns and background was employed, for example, superhydrophilic/superhydrophobic patterns. In our experiment, we show that making patterns with CAH contrast is also effective in patterning droplets, with even more capabilities to control droplet sizes.

3.3. Patterning Hydrogel Droplets with Complex Architecture. Based on the control over liquid size using CAH, we constructed hydrogel droplets with complex architecture by dual dip-coating and gelling cell-encapsulated prehydrogel solutions. For prehydrogel solution, we employed 1% sodium alginate solution. Sodium alginate is a natural macromolecule and its hydrogel can be used for cell culturing [12]. Alginate solutions can be rapidly turned into hydrogel by adding Ca^{2+} ions as the cross-linking reagent. According to this, we fabricated complex hydrogel structure by performing primary dip-coating, gelation, secondary dip-coating, and gelation. After secondary dip-coating, the size of droplet from second pulling was almost equal to the size of patterns. We believe that after primary dip-coating, gelled droplets contributed to the adhesion force of the whole patterns. As a result, the whole pattern areas were covered by the secondary alginate solutions.

3.4. Construction of In Vitro Tumor Model. To construct an *in vitro* tumor model, we employed two types of cells, cancer cells (Hela cell) and normal cells (NIH 3T3 fibroblast). We suspended the cells in separate alginate solutions. We used Hela cells for the primary solution and NIH 3T3 fibroblasts for the secondary. By serially dip-coating two solutions and gelation, we obtained the coculture of different cells with Hela cells in the inner part and fibroblasts in the outer part of the hydrogel droplet (Figure 4). Controlling spatial distribution

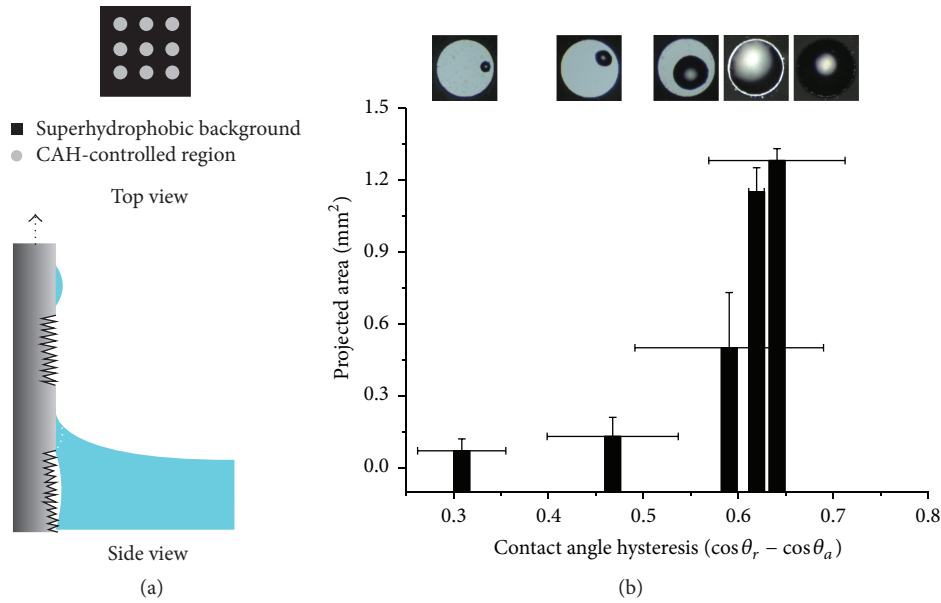


FIGURE 3: (a) The design of substrates with superhydrophobic background and CAH-controlled patterns (top view). The schematic of dip-coating process of substrates (side view). (b) Sizes of water droplets captured after dip-coating the substrates with various CAH.

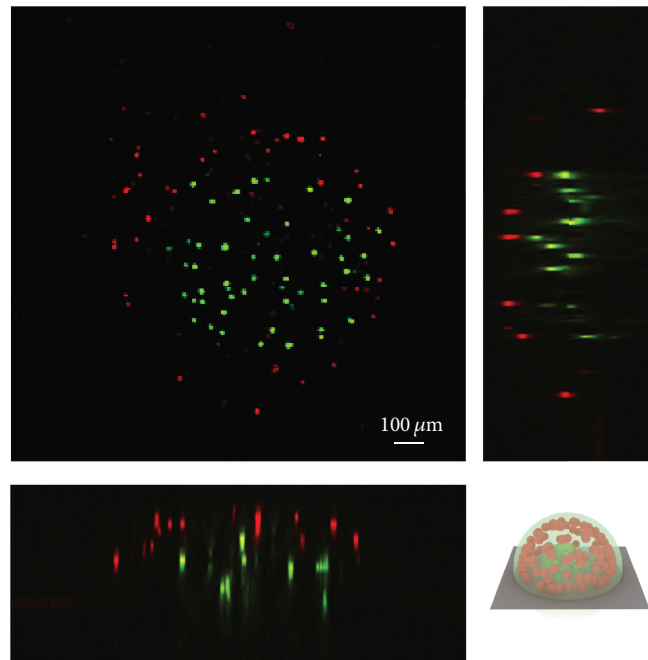


FIGURE 4: Confocal image of tumor models. Two types of cells were employed. Red cells were NIH 3T3 cells and green ones were Hela cells. Inset was the schematic of three-dimensional tumor model.

of heterogeneous types of cells is an important issue in tissue engineering and regenerative medicine. Our method provides a convenient method to fabricate complex structures for 3D cell coculture, with less dependence on functional materials and equipment and minimal harm to cells. We believe that our method could be applied in studying cell performance in tissue-level, mimicking microenvironments

in tumor, and constructing models for drug delivery and screening [13, 14].

In conclusion, we examined the relationship between contact angle hysteresis and surface roughness and demonstrated a CAH-based patterning strategy for patterning droplets with controlled sizes. We showed that droplets sizes were affected by the CAH of the surface. We fabricated

complex architecture and patterned different cells in spatially controlled way. We believe that our work would provide useful tools for tissue engineering and drug delivery.

Competing Interests

The authors declare that there are no competing interests related to this paper.

Acknowledgments

The authors are grateful to the financial supports from the Natural Science Foundation of China (Grant no. 21004080), the Program for New Century Excellent Talents in University of the Ministry of Education of China (Grant no. NCE-09-0818), the Guangdong Innovative Research Team Program (Grant no. 2009010057), the Science and Technology Planning project of Guangdong Province (Grants nos. 2011A06090101, 2015B010125004, and 2016A030313819).

References

- [1] C. Priest, R. Sedev, and J. Ralston, "Asymmetric wetting hysteresis on chemical defects," *Physical Review Letters*, vol. 99, no. 2, Article ID 026103, 2007.
- [2] D. Bonn, J. Eggers, J. Indekeu, and J. Meunier, "Wetting and spreading," *Reviews of Modern Physics*, vol. 81, no. 2, pp. 739–805, 2009.
- [3] D. Quéré, "Wetting and roughness," *Annual Review of Materials Research*, vol. 38, pp. 71–99, 2008.
- [4] M. Prakash, D. Quéré, and J. W. M. Bush, "Surface tension transport of prey by feeding shorebirds: the capillary ratchet," *Science*, vol. 320, no. 5878, pp. 931–934, 2008.
- [5] K. Choi, A. H. C. Ng, R. Fobel, and A. R. Wheeler, "Digital microfluidics," *Annual Review of Analytical Chemistry*, vol. 5, pp. 413–440, 2012.
- [6] D. Kang, C. Pang, S. M. Kim et al., "Shape-controllable microlens arrays via direct transfer of photocurable polymer droplets," *Advanced Materials*, vol. 24, no. 13, pp. 1709–1715, 2012.
- [7] H. Ren and S.-T. Wu, "Tunable-focus liquid microlens array using dielectrophoretic effect," *Optics Express*, vol. 16, no. 4, pp. 2646–2652, 2008.
- [8] E. Ueda and P. A. Levkin, "Emerging applications of superhydrophilic-superhydrophobic micropatterns," *Advanced Materials*, vol. 25, no. 9, pp. 1234–1247, 2013.
- [9] S. D. Gillmor, A. J. Thiel, T. C. Strother, L. M. Smith, and M. G. Lagally, "Hydrophilic/hydrophobic patterned surfaces as templates for DNA arrays," *Langmuir*, vol. 16, no. 18, pp. 7223–7228, 2000.
- [10] K.-Q. Peng, Y.-J. Yan, S.-P. Gao, and J. Zhu, "Synthesis of large-area silicon nanowire arrays via self-assembling nanoelectrochemistry," *Advanced Materials*, vol. 14, no. 16, pp. 1164–1167, 2002.
- [11] B. M. Mognetti and J. M. Yeomans, "Modeling receding contact lines on superhydrophobic surfaces," *Langmuir*, vol. 26, no. 23, pp. 18162–18168, 2010.
- [12] J. A. Rowley, G. Madlambayan, and D. J. Mooney, "Alginate hydrogels as synthetic extracellular matrix materials," *Biomaterials*, vol. 20, no. 1, pp. 45–53, 1999.
- [13] D. R. Albrecht, G. H. Underhill, T. B. Wassermann, R. L. Sah, and S. N. Bhatia, "Probing the role of multicellular organization in three-dimensional microenvironments," *Nature Methods*, vol. 3, no. 5, pp. 369–375, 2006.
- [14] A. Dolatshahi-Pirouz, M. Nikkhah, A. K. Gaharwar et al., "A combinatorial cell-laden gel microarray for inducing osteogenic differentiation of human mesenchymal stem cells," *Scientific Reports*, vol. 4, article 3896, 2015.